Organic-inorganic hybrid materials based on phthalocyanine, calix[4]arene and polyoxometalate scaffolds

Von der Fakultät für Mathematik, Informatik und Naturwissenschaften der RWTH Aachen
University zur Erlangung des akademischen Grades einer
Doktorin der Naturwissenschaften genehmigte Dissertation

vorgelegt von

Sidra Sarwar, Master of Science
aus
Attock, Pakistan

Berichter: Univ.-Prof. Dr. rer.nat. Paul Kögerler
Univ.-Prof. Dr. rer.nat. Iris Oppel

Tag der mündlichen Prüfung: 11.05.2021

Declaration of Authorship

I, Sidra Sarwar
declare that this thesis and the work presented in it are my own and has been generated by me as the result of my own original research work conducted between January 2017 and December 2020 in the research group of Prof. Dr. Paul Kögerler at the Institute of Inorganic Chemistry, RWTH Aachen University and Peter Grünberg Institute (PGI-6) Forschungszentrum Jülich.

I do solemnly swear that:

- This work was completely or mainly done while in candidature for the doctoral degree at this faculty and university;
- Where any part of this thesis has previously been submitted for a degree or any other qualification at this university or any other institution, this has been clearly stated;
- Where any part of this thesis has previously been submitted for a degree or any other qualification at this university or any other institution, this has been clearly stated;
- Where I have consulted the published work of others or myself, this is always clearly attributed;
- Where I have quoted from the work of others or myself, the source is always given. This thesis is entirely my own work, with the exception of such quotations;
- I have acknowledged all major sources of assistance;
- Where the thesis is based on work done by myself jointly with others, I have made clear exactly what was done by others and what I have contributed myself;
- Part of this work (in chapter 2) has been published before as:
  S. Sarwar, S. Sanz, J. van Leusen, G. S. Nichol, E. K. Brechin and P. Kögerler, "Phthalocyanine-polyoxotungstate lanthanide double deckers", *Dalton Trans.*, **2020**, *49*, 16638-16642. (I contributed to this paper in its conceptualization, synthesis and chemical analysis, writing the original draft and designing the visualization).

Date
Sidra Sarwar

Abstract

The versatile coordination chemistry of lanthanide ions has allowed to develop complexes with interesting optical and magnetic properties, including the single-molecule magnet (SMM) behavior. A key factor behind the properties of these compounds is the ligand-field, in which subtle modifications lead to remarkable changes in the physical properties. The anisotropy of the lanthanide ion is influenced by the crystal field in highly axial symmetries like D_{4d}, D_{5h} and sandwiched type D_{∞}, as this minimizes quantum tunneling of magnetization (QTM) leading to a high energy barrier to magnetic relaxation (U_{eff}) and blocking temperature - all ingredients for SMM behavior. However, despite the exquisite results and control of coordination chemistry, the realization of organic-inorganic hybrid complexes of lanthanide ions in such symmetries remains practically unexplored. These hybrid functional materials are particularly interesting as they combine the properties of tunable organic ligands and the robust inorganic ligands and offer potential applications in diverse fields such as optics, electronics, energy storage, and medicine among others.

The focus of this thesis involves the generation of new families of monometallic hybrid complexes of lanthanides involving monolacunary Keggin-phosphotungstate as an inorganic ligand, and phthalocyanine or *p*-*tert*-butyl-calix[4]arene as organic ligands. These tetradentate ligands have been selected based on the excellent coordination abilities and interesting physical properties of their coordination compounds, behaving as catalysts, single-molecule magnets, and molecular qubits.

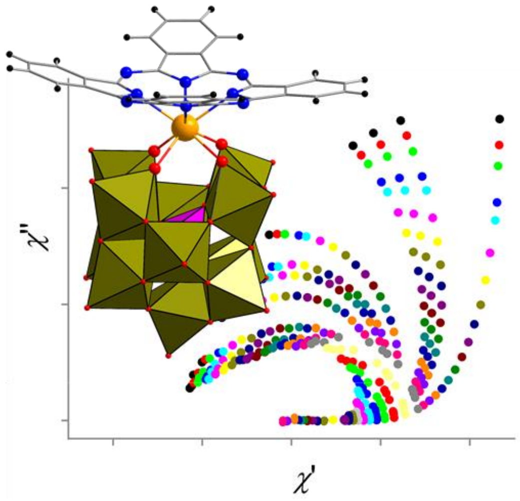

Chapter 2 describes the synthesis of a new family of hybrid structures $[Ln^{III}(H_{16}Pc)(PW_{11}O_{39})]^{6-}$ (Ln = Y, Tb, and Dy), featuring a phthalocyanate $[H_{16}Pc]^{2-}$ and a monolacunary phosphotungstate $[PW_{11}O_{39}]^{7-}$ around the single rare-earth ion. Initial characterization of yttrium-complex by NMR reveals the synthetic conditions for paramagnetic lanthanide (Tb(III) and Dy(III)) derivatives, which have been characterized by high-resolution mass spectrometry, synchrotron-based single-crystal X-ray diffraction, various spectroscopic and electrochemical methods. To study the impact of peripherally substituted phthalocyanine ring

on the properties of hybrid complexes, Pc-ring has been decorated with electron-donating (2,6-di-*iso*-propylphenoxy) and electron-withdrawing (fluorine) groups. Characterization by UV-Vis spectroscopy and cyclic voltammetry shows the impact of substituents on the electronic structure of hybrid complexes. The magnetic studies reveal the significant slow magnetic relaxation in all synthesized Dy-complexes. The peripheral groups on the Pc-ring show their impact on the magnetic properties by preferring different relaxation mechanisms.

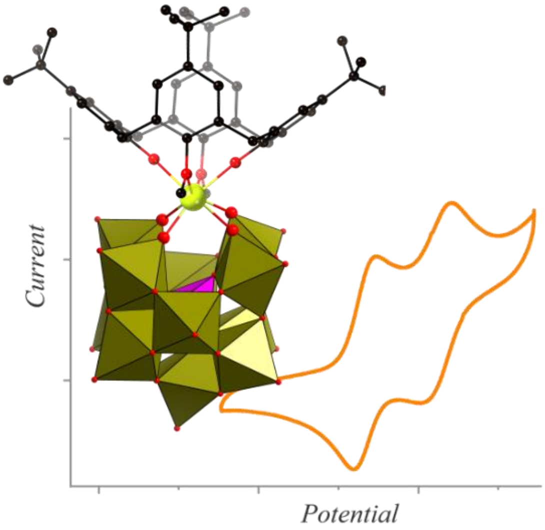

Chapter 3 describes the integration of *p*-*tert*-butylcalix[4](OMe)$_2$(OH)$_2$arene {(TBC[4](OMe)$_2$(OH)$_2$} and monolacunary phosphotungstate [PW$_{11}$O$_{39}$]$^{7-}$ into hybrid structures [M^{IV}(TBC[4](OMe)$_2$O$_2$)(PW$_{11}$O$_{39}$)]$^{5-}$ (M = Ce and Zr). The complexes represent the first example of a hybrid system comprising of calix[4]arene and polyoxotungstate moieties linked through a single-metal ion, whose synthetic approach could be extended to paramagnetic lanthanides and other lacunary POMs. Hybrid structures have been identified by nuclear magnetic resonance, high-resolution mass spectrometry, and electrochemical methods. The percentage of trivalent cerium in [Ce^{IV}(TBC[4](OMe)$_2$O$_2$)(PW$_{11}$O$_{39}$)]$^{5-}$ complex has been evaluated using XPS and SQUID magnetometry. The voltammograms of complexes show TBC[4]-centered two reversible redox waves and represent the first example of a redox-active calix[4]arene mediated by metal-ligand bonding. Future investigations will study their potential as electroactive materials in single-molecule switches.

Table of contents

Symbols and abbreviations

acac	Acetylacetonate
ac	Alternating current
B	Magnetic flux density
CV	Cyclic voltammetry
COSY	Correlation spectroscopy
dc	Direct current
D	Uniaxial anisotropy
***o*-DCB**	*o*-Dichlorobenzene
DBU	Diazabicylo[5.4.0]undec-7-ene
DCM	Dichloromethane
EA	Elemental analysis
ESI-MS	Electrospray ionization mass spectrometry
e.g.	For example
f	Frequency
HSQC	Heteronuclear single quantum coherence
HMBC	Heteronuclear multiple bond correlation
HOMO	Highest occupied molecular orbitals
IR	Infrared
***i*Pr**	*Iso*-propylphenoxy
i.e.	That is
J	Coupling constant
LUMO	Lowest unoccupied molecular orbitals
MALDI	Matrix-assisted laser desorption ionization
MeOH	Methanol
Me	Methyl
MPc	Metallophthalocyanine
m/z	Mass-to-charge ratio
mmol	Millimolar
mg	Milligram
mL	Milliliter
M	Molar (moles per liter)
NMR	Nuclear magnetic resonance
OAc	Acetate

Oe	Oersted
ppm	Parts per million
Pc	Phthalocyanine
POM	Polyoxometalate
POT	Polyoxotungstate
QTM	Quantum tunneling of magnetization
SMM	Single-molecule magnet
SQUID	Superconducting Quantum Interference Device
S	Spin ground state
T	Temperature
T	Tesla
TBC[4]	*tert*-Butylcalix[4]arene
TBA	Tetra-*n*-butylammonium
TGA	Thermogravimetric analysis
U_{eff}	Effective energy barrier for magnetization reversal
UV-Vis	Ultraviolet-visible
vs.	*Verses*
XPS	X-ray photoelectron spectroscopy
XRD	X-ray diffraction
δ	Chemical shift in parts per million
°C	Degree Celsius
χ	Magnetic susceptibility
ε	Molar extinction coefficient
τ	Relaxation time
ν	Wavenumber
λ	Wavelength

Chapter 1.

Introduction

This work aims at the development of hybrid double-decker complexes combining organic and inorganic ligands through a single-metal ion. To achieve that, phthalocyanine and *p-tert*-butylcalix[4]arene are chosen as organic ligands and a monolacunary Keggin-type phosphotungstate as an inorganic ligand. The coordination nature of these ligands and numerous electronic and magnetic properties of their complexes are the important characteristics making them excellent candidates for the construction of hybrid materials. This chapter presents an overview of the aforementioned ligands with a special focus on the synthetic procedures, their reactivity and properties.

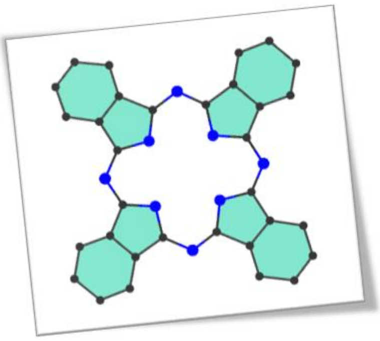

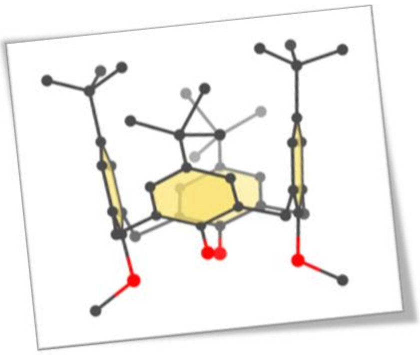

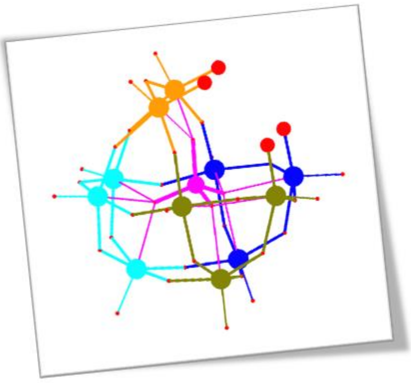

1.1 Phthalocyanine

Phthalocyanine (Pc) is a planar macrocyclic ligand containing four coordinating nitrogen centers. The first synthesis of Pc was serendipitous when two scientists Braun and Tcherniac observed a blue colored by-product during the synthesis of o-cyanobenzamide in 1907.[1] However, the industrial application of Pc emerged upon another accidental formation of insoluble blue-green material during the synthesis of phthalimide from phthalic anhydride by Grangemouth plant of Scottish Dyes Ltd in 1928.[2] After a series of investigations from 1929 to 1939, Linstead and co-workers described the molecular structure of Pc and improved methods for the synthesis of metal phthalocyanine (MPcs). The term "phthalocyanine" was also given by Linstead based on the origin and color of these compounds; Greek *cyanine* "blue".[3-5] The most common precursors for the synthesis of Pc are phthalic acid, phthalic anhydride, and phthalonitrile.[6,7]

The structure of Pc-ring is similar to the naturally occurring porphyrin (Por) with four additional benzo-units and four nitrogen atoms at meso-positions, hence they are also termed as tetrabenzotetraazaporphyrin[8] **(Fig 1.1)**. Pc binds to metal centers through four isoindole nitrogen atoms acting as a tetradentate ligand. Four nitrogen atoms at meso-positions increase the stability of Pc and additionally fused benzene rings extend the conjugation in these macrocycles leading to intense absorption in the visible region of the spectrum in comparison to porphyrin.[9]

Up to 1940, all synthesized phthalocyanine complexes had very poor solubility in common organic solvents. The structural modification of Pc-ring changes the solubility of compounds, which includes several possible ways, such as changing the coordinated metal or decorating Pc-ring with different substituents on the axial or peripheral sites.[10,11] The central cavity of Pc-ring has sufficient size to accommodate metal atoms from every group of the periodic table. Almost 70 different elements have been used to coordinate with Pc by the abstraction of two central protons. Besides, sixteen possible substitution sites at the benzene moiety of Pc-ring influence solubility and changes the chemical and physical properties of these compounds.[12,13] Usually, the term "peripheral" is used for substitution at β-positions, while the functionalization of α-positions is described as "non-peripheral".[14]

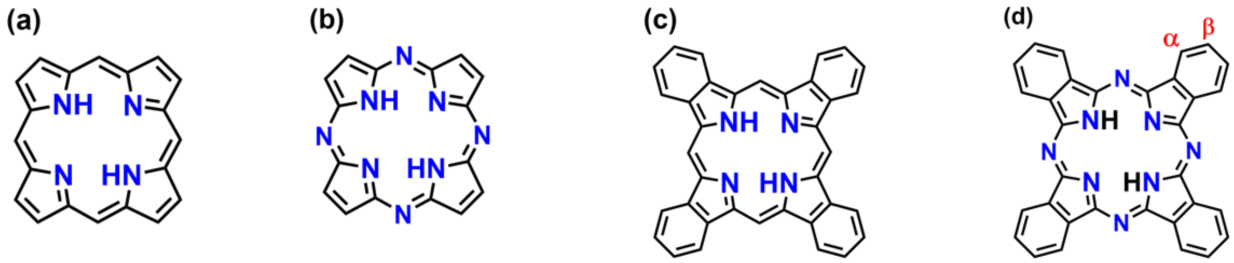

Fig 1.1 General structure of **(a)** porphyrin, **(b)** tetraazaporphyrin, **(c)** tetrabenzoporphyrin, and **(d)** phthalocyanine.

The opposite nitrogen atoms in the Pc-ring cavity are separated by ~3.9 Å and the distance between adjacent nitrogen atoms is ~2.7 Å.[15] **Fig 1.2** shows the structural representation of MPcs with different metal centers. Metal atoms with smaller ionic radii reside inside the cavity and make planar complexes with tetradentate Pc-ligand (MPc).[16] Lanthanides Ln(III)] with larger van der Waals radii cannot fit into the coordination space of Pc-ring cavity and support the formation of [Ln(Pc)(X)] type complexes in which additional ligands (chloride, acetate, or acetylacetonate) bind to the axial position to fulfill higher coordination number.[17] Ln(III) also forms double-decker [Ln(Pc)$_2$] type complexes, where one Ln(III) is confined between two Pc-rings in a square antiprismatic geometry. These double-decker complexes can exist as a neutral radical form [Ln(Pc)$_2$]$^\bullet$, in which one Pc is dianionic and the other is monoanionic, a reduced form [Ln(Pc)$_2$]$^-$ with double negatively charged both Pc-rings and an oxidized version [Ln(Pc)$_2$]$^+$.[18] Recently, multiple-decker complexes have been reported with up to six Pc-rings and two Ln-ions located at the periphery with heterometal ion in the center.[19-21] Multiple-decker complexes with identical Pc-rings are called homoleptic, while those having different substituents on different Pc-rings are named as heteroleptic complexes.

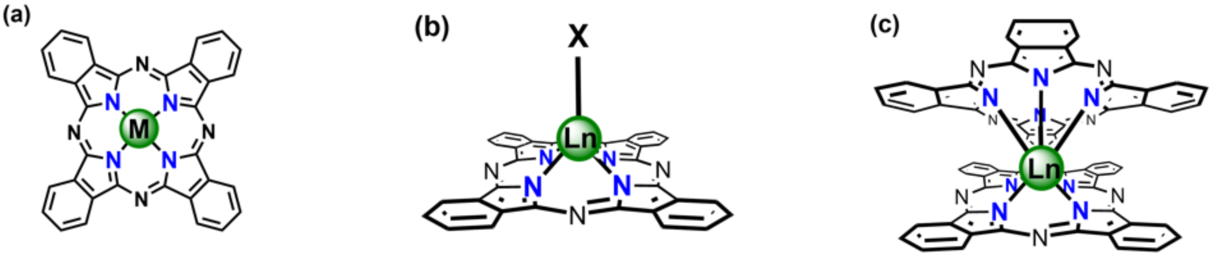

Fig 1.2 Structural representation of **(a)** transition metal MPc, **(b)** single-decker [Ln(Pc)(X)] (X = acetate, acetylacetonate, or chloride), and **(c)** double-decker [Ln(Pc)$_2$].

1.1.1 UV-Vis absorption and electrochemical properties

Electronic delocalization in Pcs gives rise to unique spectral properties, making them interesting candidates in different fields of research. In general, all Pcs exhibit an intense Q-band between 600–750 nm and a weaker Soret- or B-band between 300–400 nm. These bands are associated with HOMO to LUMO transitions. The absorption coefficient of Q-band is very large with values as high as 10^5 L mol^{-1} cm^{-1}, creating a characteristic blue-green color, with use as dyes and electrochromic material. H_2Pc also termed as free-base and its complexes exhibit different types of spectra **(Fig 1.3**, left**)** due to the transitions arising from different electronic levels. The electronic transitions responsible for Q- and B-bands in H_2Pc and MPcs are shown in **Fig 1.3** (right). Mostly the planar MPcs are D_{4h} symmetric with degenerate excited states and show a Q-band at ~650 nm and B-band at ~300 nm. In free-base Pc, the presence of proton on two of the four isoindole-nitrogen atoms reduces the symmetry to D_{2h}. Therefore, the Q-band in their spectra appears as a doublet due to the transitions from HOMO to non-degenerate LUMO states.[22,23]

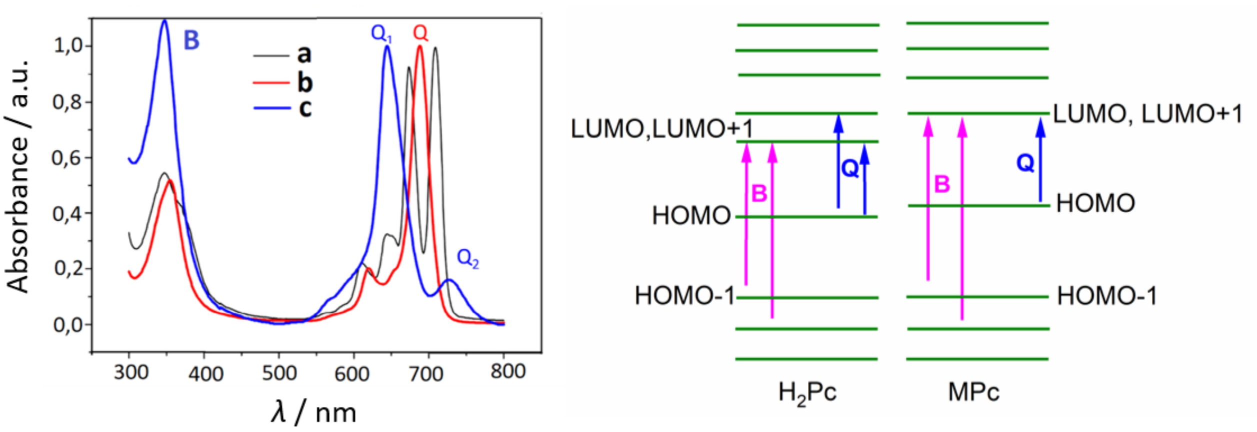

Fig 1.3 (Left) Generalized UV-Vis spectra of **(a)** free-base H_2Pc, **(b)** single-decker [Ln(Pc)(X)], and **(c)** triple-decker [Ln_2Pc_3], Ln = Lu (III). Reproduced with permission from Ref. 24, © 2016 Elsevier B. V. **(Right)** Representation of energetic levels of H_2Pc and MPc highlighting the main electronic transitions.

Lanthanide(III) single-decker phthalocyanines [Ln(Pc)(X)] show similar spectra as MPcs due to doubly degenerate LUMO levels. However, the spectra of neutral radical double-decker complexes $[Ln(Pc)_2]^\bullet$ show some additional features, which are the presence of π-radical bands (blue-valence between 400–500 nm and red-valence between 900–950 nm) and an intervalence band in near IR-region (1200–1600 nm) as shown in **Fig 1.4**. These bands arise from the transitions involving semi-occupied molecular orbital (SOMO) in these complexes.[25]

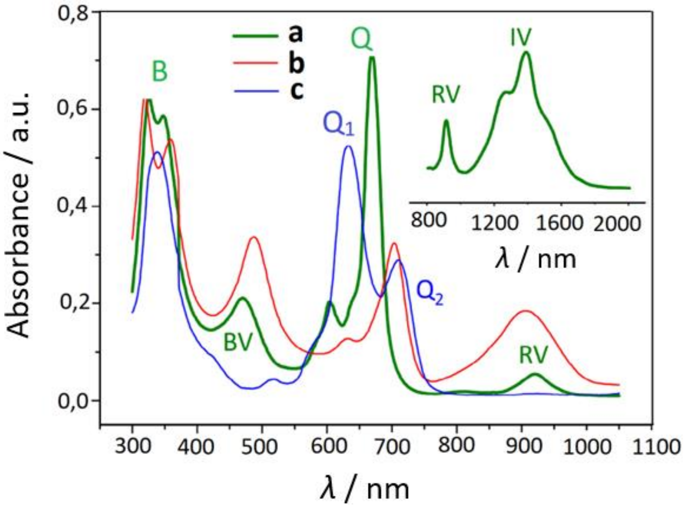

Fig 1.4 Generalized UV-Vis spectra of double-decker [Ln(Pc)$_2$] **(a)** neutral radical, **(b)** oxidized, and **(c)** reduced forms, Ln = Lu(III). Reproduced with permission from Ref. 24, © 2016 Elsevier B. V.

The electronic coupling between Pc-rings in multiple-decker complexes depends on ring-to-ring distance. The size of metal ion and the nature of peripheral substituents on Pc-ring have a profound effect on the position of absorption bands. On decreasing the ionic size of lanthanide center, stronger π-π interaction between the rings shift of Q-band to shorter wavelength.[25] Likewise, electron-withdrawing groups stabilize the frontier energy levels and shift the Q-band to shorter wavelength, while the opposite trend is observed for electron-donating peripheral substituents.[26,27]

Free-base H_2Pc and MPcs exhibit versatile redox reactions, up to two oxidation and four reduction processes. When coordinated to a redox-inactive metal center, these electrochemical reactions are associated with the addition and removal of electrons from the Pc-ring. The first and second electrochemical oxidation results in the loss of electrons from HOMO (a_{1u}) giving Pc^{1-} and Pc^{0}, whereas the successive addition of four electrons in LUMO (e_g) gives Pc^{3-}, Pc^{4-}, Pc^{5-} and Pc^{6-} species. The effect of metal ionic radius and peripheral substituents can be observed in cyclic voltammetry of MPcs. Usually decreasing the size of metal ion brings a small negative shift of first oxidation and first reduction.[25] Similarly, electron-donating groups decrease the oxidation potential of complexes while electron-withdrawing groups stabilize their reduced forms and make them harder to oxidize.[28]

1.1.2 Synthetic strategies

1.1.2.1 Phthalocyanine

Pcs can be synthesized by reductive cyclotetramerization of differently substituted *o*-phthalic acid derivatives containing nitrogen functional groups such as nitrile, amide, imide, and anhydride.[6] Among them, phthalonitrile is most commonly used for the laboratory-scale synthesis of Pc due to the resulting good yields. Phthalonitrile is converted to Pc-ring in presence of metal source in high boiling solvents. Cyclization can also be achieved under mild conditions using an organic base such as 1,8-Diazabicyclo[5.4.0]undec-7-ene (DBU) in refluxing alcohol solvents. DBU promotes the formation of alkoxide that attacks the cyano group of dinitrile to make isoindoline. This intermediate attacks the cyano group of another dinitrile to from dimeric species, which undergoes cyclization to form a phthalocyanine ring **(Scheme 1.1)**.[29]

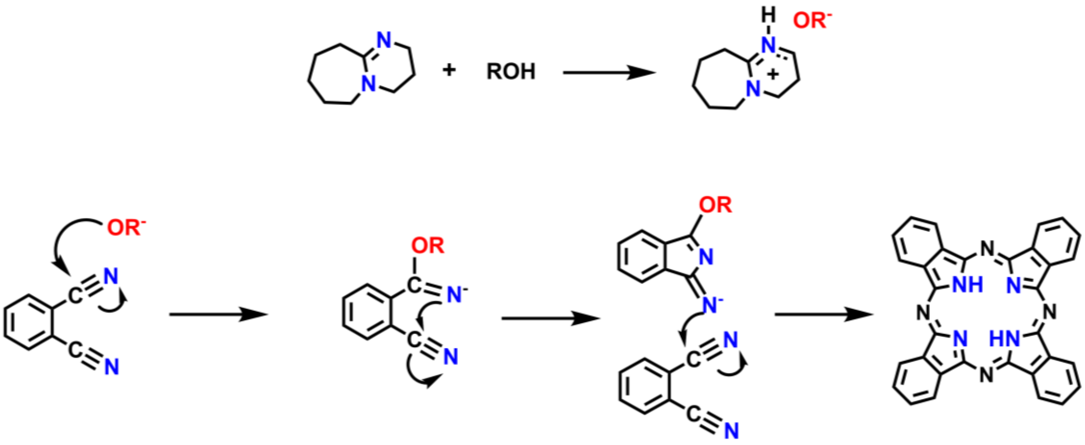

Scheme 1.1 Synthetic mechanism of phthalocyanine.

1.1.2.2 Single-decker phthalocyanine

Planar transition metal phthalocyanine complexes (MPcs) are synthesized by reacting phthalonitrile with metal(II) salts under certain conditions in which metal ion act as a template during the formation of the macrocycle complex. **Scheme 1.2** shows the different possible ways to obtain planar MPcs.

The classical method of MPc synthesis involves refluxing phthalonitrile or free-base H_2Pc and metal(II) salts (acetate, chloride, or acetylacetonate) with a catalytic amount of DBU in high boiling solvents like pentanol, *o*-dichlorobenzene, or 1-chloronaphthalene.[30] MPcs can also be prepared using microwave radiations which speed up the reaction and provide the energy required for its completion.[31] Another way of synthesis of MPcs is the fusion of phthalonitrile with a metal(II) salt at high temperature in the absence of any solvent.[32]

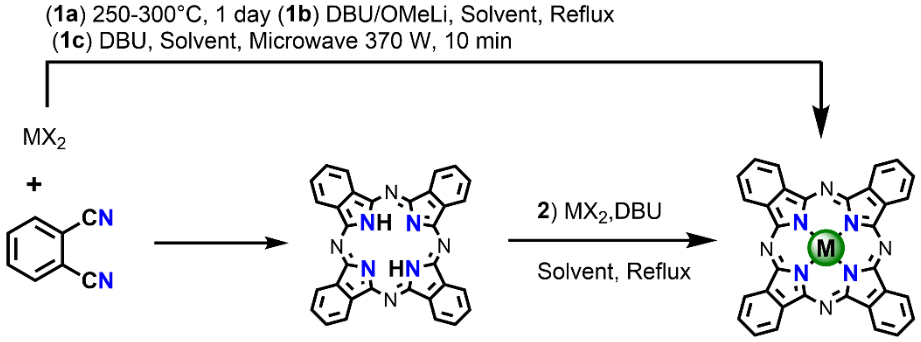

Scheme 1.2 Synthetic approaches to transition metal(II) phthalocyanine.

Template synthesis involving phthalonitrile and Ln(III) salt in the absence of solvent or using high boiling solvents renders single-decker complexes [Ln(Pc)(X)]; the drawback of this approach includes the low yield of target complexes due to the formation of a mixture of products.[33,34]

An alternative to obtaining [Ln(Pc)(X)] (X = acetate or chloride) type complexes is the use of H_2Pc and Ln(III) salts in the presence of strong bases such as DBU, or *n*-Butyllithium, which in-situ generates the dianion of Pc, in *o*-dichlorobenzene or dimethyl sulfoxide solvent.[35] The reaction of Ln(III) β–diketonates with H_2Pc produces single-decker complexes without use of a base **(Scheme 1.3)**.[36] Alkali metal (usually lithium) phthalocyanine also reacts with Ln(III) to give single-decker complex. They have more solubility in comparison to free-base Pc, so reaction proceeds under the mild condition without using additional base.[37]

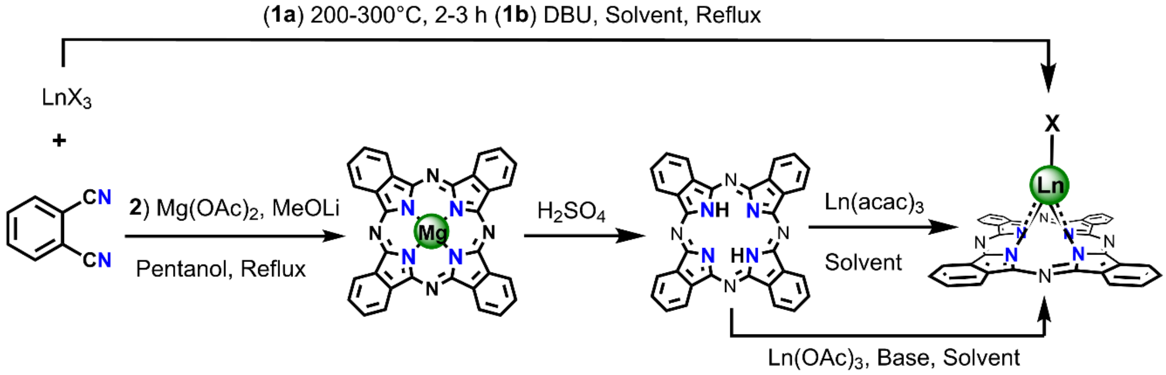

Scheme 1.3 Synthetic approaches to lanthanide(III) single-decker phthalocyanine.

1.1.2.3 Double-decker phthalocyanine

The first synthesis of a double-decker lanthanide(III) phthalocyanine [Ln(Pc)$_2$] was achieved by a template method involving a thermal fusion of a mixture of phthalonitrile and Ln(III) salt in a molar ratio of 1: (4–8) at a longer time and higher temperature than with single-decker complexes **(Scheme 1.4)**. The yield of these reactions can be increased by heating the reactants in a vacuum-sealed tube.[34] Another way of template synthesis involves irradiating phthalonitrile and Ln(III) salts with microwave radiation for a few minutes; reaction time and the power of radiation depend on the ring substitution.[38] Similarly, double-decker complexes can also be synthesized by the reaction of phthalonitrile and Ln(III) salts using DBU and mostly pentanol or hexanol.[33] The reaction of H$_2$Pc or lithium derivative with Ln(III) salts in basic medium avoid the side products during the reaction and give corresponding double-decker complexes in a good yield.[39,40] In the aforementioned synthetic procedures, the crude of the reaction mixture needs to be purified using chromatographic separation or sublimation.

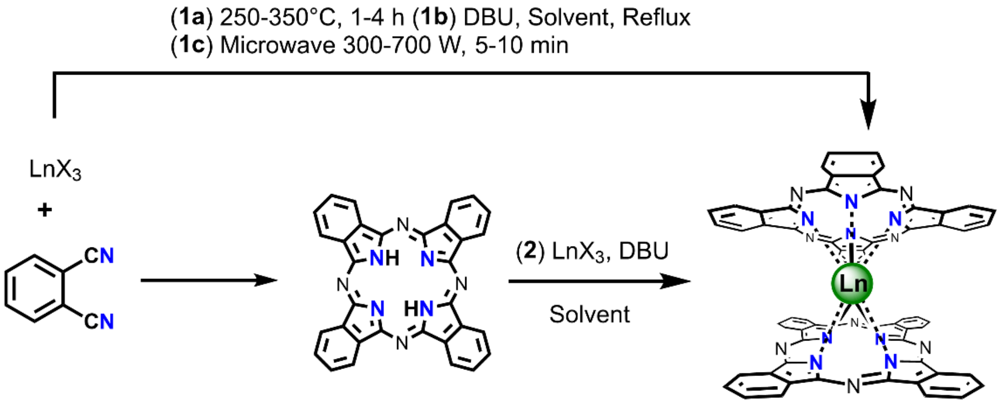

Scheme 1.4 Synthetic approaches to homoleptic lanthanide(III) double-decker phthalocyanine.

Heteroleptic double-decker lanthanide(III) phthalocyanine complexes [Ln(Pc)(Pc')] can be prepared by reacting two phthalonitrile having different substituents with Ln(III) salts.[41] The result of this reaction gives a multicomponent mixture that includes unreacted starting phthalonitrile, single-decker complexes, homoleptic and heteroleptic double-decker complexes. These products are difficult to separate and the yields are very low. Alternatively, an efficient route to synthesize heteroleptic complexes in better yield is reacting Ln(III) salt with two differently substituted Pc-rings.[42] An improved strategy, with higher yields and selectivity, entails the reaction of [Ln(Pc)(X)] with another H$_2$Pc having different substituents in trichlorobenzene or 1-chloronaphthalene solvents.[43] This is also called raise-by-one-story method as the synthesis of heteroleptic complex is done in a single step **(Scheme 1.5)**. The same strategy is also used to synthesize heteroleptic mixed ligand Ln(III) complexes [Ln(Pc)(L)] in which one lanthanide ion is sandwiched between one Pc-ring and another organic ligand.[44,45]

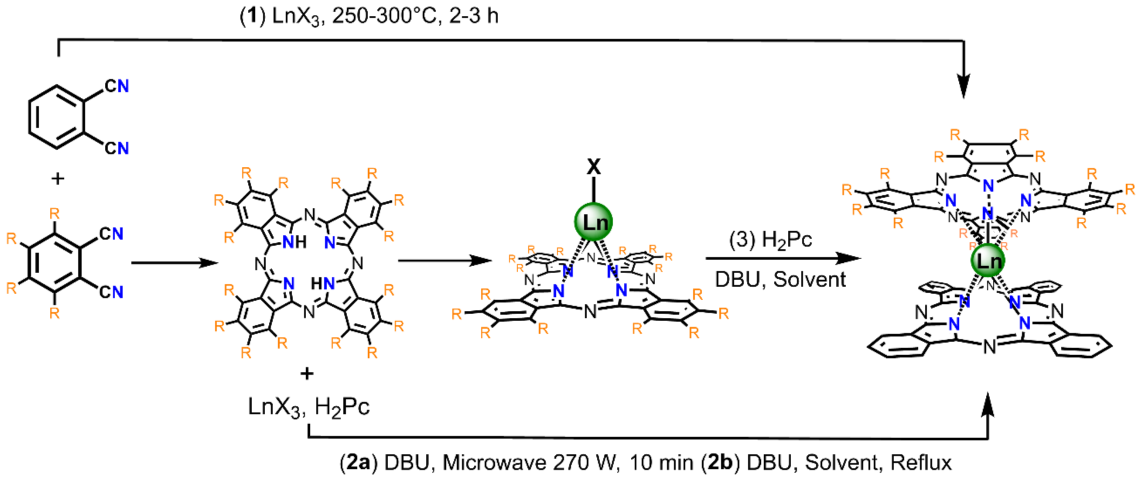

Scheme 1.5 Synthetic approaches to heteroleptic lanthanide(III) double-decker phthalocyanine.

1.1.3 Applications

Phthalocyanines are important functional materials and highly studied class of compounds in multidisciplinary fields due to their excellent thermal, chemical, and photo-stability. Extensive delocalization, conductivity, and magnetic behavior make them most interesting candidates from the traditional application as colorants to active components in technological areas such as field-effect transistors, photovoltaic cells, information storage systems, catalysts, gas sensors, electrochromic and electronic devices.[46,47]

1.1.3.1 Pc-based molecular functional materials

Due to their extended conjugated structure, Pcs play the role of charge carriers in electronic or optoelectronic devices such as organic light-emitting diodes (OLEDs), organic field-effect transistors (OFETs), and organic photovoltaic devices (OPVs).[48]

In OLEDs, Pcs can act as mediating layers in order to decrease the potential difference between electrodes and the emissive layer. Several groups have employed Cu^{II}Pc as hole-transport layer and found the higher device stabilities. Additionally, the multilayers of Cu^{II}Pc, Zn^{II}Pc, and Ni^{II}Pc, arranged in decreasing order of their ionization potential, have shown the enhancement of luminescent properties due to the breaking of initial high potential barrier into small ones.[49]

Several advantageous features of MPcs such as excellent stability, good film properties, and ease of functionalization to get n- or p-type conductivity make them a suitable candidate for the utilization in OFETs. In this context, most of the complexes ($Cu^{II}Pc$, $Ni^{II}Pc$, $Zn^{II}Pc$, $Tb^{III}Pc_2$, $Lu^{III}Pc_2$) displayed p-type conductivity whereas, few complexes ($Cu^{II}Pc$, $Zn^{II}Pc$, $Fe^{II}Pc$) with electron-withdrawing [F_{16}, Cl_{16} or $(CN)_8$] groups revealed n-type conductivity.[50-52] High charge-transfer mobility of thin film of $Ti^{IV}OPc$ (3.31 cm^2/Vs), single crystals of $Cu^{II}Pc$ (1 cm^2/Vs), and $F_{16}Zn^{II}Pc$ (1.1 cm^2/Vs) indicates the high potential of MPcs as organic field-effect transistor materials.[53-55]

The development of dye-sensitized solar cells (DSSCs), which involves the use of sensitizer along with semiconductor electrode material to achieve high power efficiency, is one of the hot topics in organic photovoltaics. A general requirement for the cells with higher power conversion efficiency includes the use of sensitizer with a large extinction coefficient in the near-IR region, high thermal, photo and redox stability, and anchoring groups for attachment to the semiconductor surface. Following this, H_2Pc and MPcs ($Zn^{II}Pc$, $Co^{II}Pc$, $Mg^{II}Pc$, $Fe^{II}Pc$, $Ti^{IV}OPc$) with similar photophysical properties have been found as perfect candidates for utilization in DSSCs. Peripheral or axial substitution in these compounds can tune the energy of LUMO, which should be higher than conduction band of TiO_2 for efficient electron injection.[56,57] So far, the maximum power efficiency of ~6 % has been reported with Pc-based sensitizers,[58] the number is less than ruthenium polypyridyl complexes but still higher than a lot of other dyes, and the possibility of shifting their LUMO by structural changes provide a great potential of these compounds in DSSCs.

MPcs also exhibit optical limiting properties due to efficient absorption in the visible and near-IR region. Optical limiters are the materials that show high transmission at a normal light intensity and low transmission for an intense beam and hence can protect sensitive elements from highly intense light.[59] Pc containing heavy metal atoms (*e.g.* $Pb^{II}Pc$ and $In^{III}ClPc$) displayed efficient optical limiting properties.[60,61] In the case of [$Ln^{III}(Pc)(OAc)$] complexes, the optical limiting properties have been improved upon derivatization of the Pc-ring with sixteen electron-withdrawing chlorine atoms.[62] Additionally, the linear optical properties of Pcs make them suitable active agents in photodynamic therapy (PDT), which is a rapidly developing area for cancer treatment. Light activation of these sensitizers produces reactive oxygen species (particularly singlet oxygen $O_2^{\cdot}$), by transferring the energy of photoexcited state to molecular oxygen in tissues, which causes cytotoxicity of malignant cells higher than normal cells. To date, various water-soluble MPcs [$Zn^{II}Pc$, $Al^{III}ClPc$, and $Si^{IV}Pc(OSi(CH_3)_2(CH_2)_3N(CH_3)_2)$] have been examined against several tumor models. Among them, axially substituted $[Si^{IV}Pc(OR)_2]$ has shown the most promising results and is in phase 1 clinical trials for the treatment of cutaneous neoplasms.[63-65]

MPcs are electrochromic material displaying different colors in different oxidation states with the possibility of their use as chemical sensors. This method involves the rapid and economic detection of toxic metal ions, which affect the electrochemical properties of complexes accompanied by a color change of solution. For example, ruthenium(II) phthalocyanine exhibited the colorimetric sensing of Cu(II) ions. The process involves one-electron oxidation of RuPc by Cu(II), resulting in a dramatic change of color from cyan to violet.[66]

Besides MPcs, the tautomerization behavior of single dehydrogenated HPc/Ag(111) has been investigated by scanning tunneling microscopy. The authors demonstrated the reversible switching of the central proton between different nitrogen atoms by applying a suitable voltage.[67,68] In general, different tautomers exhibit different conductivities, therefore, reversible switching in HPcs offers their applicability in tautomerization-induced molecular switches.

1.1.3.2 Pc in catalysis

Pcs show structural similarity to porphyrins, which are used in the active sites of enzymes for catalytic aerobic oxidation-reduction, transport of O_2, and destruction of reactive oxygen species.[69] High accessibility, structural diversity, and tunable redox properties enable MPcs to act as homogeneous and heterogeneous catalysts in electrochemical, photochemical, and several other reactions involving the preparation of nitrogen-containing compounds and C–C bond formation.[44] For example, perfluorinated-$Co^{II}Pc$ has shown efficient catalytic activity for simultaneous electrochemical oxidation and reduction of H_2O and CO_2.[70]

MPcs are also known for catalytic oxidation of mercaptans to disulfide. On an industrial scale, tetrasulphonated-$Co^{II}Pc$ is used as a catalyst for this process in the refining of petroleum also referred to as sweetening or Merox-process. Mercaptans should be low in concentration in natural gas as sulfur causes foul smell and has corrosive properties that reduce the efficiency of petroleum products.[71]

$M^{III}Pcs$ (Cr, Fe, and Mn) with azide ligands catalyzed the aerobic oxidation of alkanes to alcohol. Among them, $F_{16}Fe(N_3)Pc$ showed the highest turnover number (TON) as electron-withdrawing groups make the complexes more resistant towards electrophilic and nucleophilic attack and increase their catalytic activity.[72] Similarly, $Cl_{16}M^{II}Pc$ (M = Cu, Fe, Co) encapsulated in zeolites exhibited high activity for ambient temperature oxidation of methane in presence of *tert*-butyl hydroperoxide as an oxidant.[73] Several reports can be found on MPc-based catalytic oxidation of olefins to epoxides and diols or alcohol and ketone (depending on the site of oxidation).[74,75] The efficiency of these reactions can be tailored by appropriate design of MPcs presenting a great promise for their use as catalysts.

1.1.3.3 Pc-based magnetic material

Planar MPcs exhibit spontaneous magnetization due to intermolecular magnetic exchange interaction below a critical temperature. This ferromagnetic ordering results from the stacking of crystals along the crystallographic axis with different interplanar distances and tilting angles. MPcs-based ferromagnets include β-$Mn^{II}Pc$ and α-$Fe^{II}Pc$.[76,77] They both follow Curie-Weiss law at high temperature and exhibit ferromagnetic exchange interactions between metal centers below the transition temperature. $Cr^{II}Pc$ and $Co^{II}Pc$ display anti-ferromagnetic interaction below critical temperature, while $Cu^{II}Pc$ behaves as paramagnet with no magnetic ordering down to 1.8 K.[76]

Another class of magnets, called single-molecule magnets (SMMs), are the materials exhibiting magnetization without intermolecular interaction and collective ordering below a certain temperature known as blocking temperature. These molecules resist the reorientation of magnetic moment upon removal of the magnetic field due to the large spin-reversal energy barrier (U_{eff}) which is determined by uniaxial anisotropy and spin ground state.[78,79] Initially, SMMs research was focused on polymetallic complexes possessing a large spin ground state achieved by spin-coupling of individual metal ions in the single molecule. In recent years, the development of SMMs based on single rare-earth element (also known as single ion-magnets) has been a hot topic due to their large intrinsic magnetic anisotropy and usually large spin ground state. The use of a single rare-earth element is advantageous as spin located on just one metal center can be easily controlled.[80,81] In 2003, Ishikawa and co-workers reported the magnetic properties of double-decker phthalocyanato-terbium(III) complex $(NBu_4)[TbPc_2]$, functioning as the first monometallic SMM. The complex containing a central Tb(III) ion encapsulated by two staggered phthalocyanine rings, exhibited a large anisotropy barrier (230 cm^{-1}) and higher blocking temperature in comparison to previously described SMMs.[82]

Following that, considerable attention has been focused on synthesizing new homoleptic and heteroleptic double-decker phthalocyanato-lanthanide(III) complexes by varying the peripheral substituents on Pc-ring to investigate how structural changes could influence the ligand-field and, therefore, the magnetic properties.[83-88] The ligand-field of these complexes can also be modified by redox reactions on the Pc-ring. In this regard, removal of one or two electrons from HOMO-orbital of $[Ln(Pc)_2]^-$, which has an anti-bonding character, resulted in significant enhancement of energy barrier in $[Ln(Pc)_2]^\bullet$ or $[Ln(Pc)_2]^+$ complexes.[89]

The influence of ligand-field on magnetic properties of these complexes has been studied by comparing the homoleptic- and heteroleptic complexes with the same substitutions. Generally, heteroleptic complexes display higher spin reversal energy barriers in comparison to their homoleptic derivatives. This is explained based on the different Ln–N bonding distances of functionalized Pc-ring that result in pushing the lanthanide(III)-ion closer to the other ring, enhancing its ligand-field. To date, the highest energy barrier of 652 cm^{-1} has been achieved in this class for heteroleptic $[Tb(Pc)(Pc')]^\bullet$ complexes, in which one of the Pc-ring is modified by *p*-*tert*-butylphenoxy or dibutylamino groups on the periphery.[84,85]

The next step for the implementation of these SMMs in magneto-electronic devices depends on the retention of their properties upon surface deposition. In this field of research, Pc-based magnetic complexes have great potential due to their interesting magnetic properties, robustness, exceptional stability, and ease of deposition on the surfaces.[90] Indeed, $[Tb(Pc)_2]$ is one of the most studied SMM on a wide range of substrates and the results of different measurements indicated the strong influence of chosen substrate on the electronic and magnetic properties of molecules, leading to enhancement or preclusion of intrinsic properties.[91-95]

Another promising feature of Pc-based magnets is their potential use in magnetic refrigeration. This is characterized by a large magnetocaloric-effect (MCE) in which the magnetic entropy of a system decreases on the application of a magnetic field and to compensate that, lattice entropy increases leading to a rise in temperature. The reversible effect is observed upon the removal of magnetic field achieving very low temperatures. This energy-efficient and environment-friendly technique is promising for refrigeration in the ultra-low temperature region and provides a valid alternative to the use of rare and expensive liquid ^3He. Due to the large MCE of gadolinium(III) at room temperature, its complexes are good candidates as molecular coolants. For example, the magnetothermal properties of [Gd(Pc)(OAc)] revealed the large MCE, *i.e.* 0.47 K at room temperature by changing the field from 0 to 1 T. These results present a potential alternative to more toxic compounds in cooling devices.[96]

1.2 Calix[n]arene

Calix[n]arenes are an attractive class of macrocycles in supramolecular chemistry with a distinctive concave-like molecular framework. The first synthesis of calixarene was described in 1872 by Adolph von Bayer who reported the formation of (kittartige Substanz) cement-like substance on heating formaldehyde and phenol in the presence of a strong acid.[97] Thirty years later in 1907, Leo Baekeland converted these formaldehyde-phenol products to crystalline solid and obtained the patent for the first production of synthetic plastic "Bakelite".[98] Later on, in 1944, Zinke and his co-worker Zeigler developed the formation of cyclic tetramer as a result of condensation of *p*-*tert*-butylphenol with formaldehyde in the presence of a base.[99] In 1972, Carl David Gutsche started the exploration of these cyclic compounds for constructing enzyme mimics and specified Zinke mixture consisting of cyclic tetramers, hexamers, and octamers. He also named these compounds as "calixarene"; *calix,* the Latin word for a chalice (religious wine cup) and, *arene* due to the presence of aromatic-rings.[100]

These macrocyclic compounds are of immense interest due to their synthetic accessibility and thermal stability. They are extensively used in host-guest chemistry and as sensors for the recognition of neutral molecules and ions.[101,102] A range of calix[n]arenes of different sizes can be synthesized by judicious choice of reaction conditions, where 'n' corresponds to the number of aromatic rings in the structure **(Fig 1.5)**. In general, calix[n]arenes with minimum 3 and maximum of 20 aryl units are reported so far, but the most common are with n = 4, 6, 8. These can be produced on multigram scale by acid or base-catalyzed condensation of phenol and formaldehyde.[103]

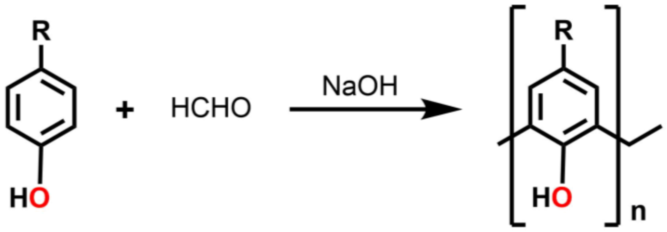

Fig 1.5 Synthesis of calix[n]arene.

Among calixarene of different sizes, calix[4]arene are the most exciting one, due to their ease of synthesis and characteristic bowl-shape molecular framework. These tetramers consist of four phenolic units bridged by methylene groups (–CH_2–) in the meta positions, resulting in a bowl-shaped cavity as shown in **Fig 1.6**. Calix[4]arenes have two rims in their structure: an upper hydrophobic and a lower hydrophilic rim containing phenolic oxygen atoms. These macrocycles can be readily functionalized at the upper and lower ends, making a very versatile class of macrocycles suitable for the incorporation of different molecules and ions.[101]

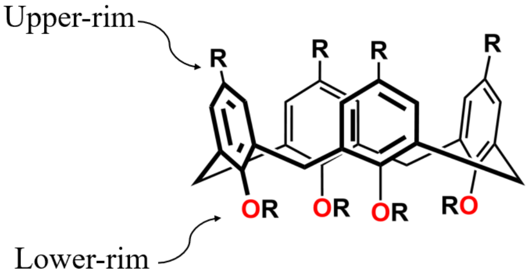

Fig 1.6 Structure of calix[4]arene highlighting the upper and lower rim.

1.2.1 Conformations and symmetry

Parent calix[4]arene with hydroxyl groups at the lower rim have a perfect bowl-like structure, but the term calixarene cannot be justified in the case of derivatized compounds if no longer remains bowl-shape. For the first time, Cornforth described their capability of existing as different conformers due to the upward or downward projection of aryl units.[104] Gutsche named these different conformations as the cone, partial-cone, 1,2-alternate, and 1,3-alternate **(Fig 1.7)**.[105] Interconversion of these isomers is possible by rotation of aromatic units around their axis. Temperature-dependent ^{1}H-NMR and 2D-NMR are the standard techniques used to differentiate between isomers. For example, ^{1}H-NMR of calix[4]arene in $CDCl_3$ shows two doublets of methylene protons at room temperature while a sharp singlet appears at high temperature due to the rapid interconversion of its conformers.[106]

The NMR spectra of symmetrically substituted calix[4]arenes are usually consistent with C_{4v} symmetry, however, some of them also adopt a pinched-cone conformation (C_{2v} isomer) **(Fig 1.8)**. Regen and coworkers reported the interconversion of cone conformation of tetracarboxylic acid substituted calix[4]arenes to pinched-cone conformation, which, in this case, is possibly stabilized due to the formation of internal hydrogen bonds.[107] The stereochemistry of calix[4]arenes is significantly affected by the reaction conditions such as temperature and solvent.[108]

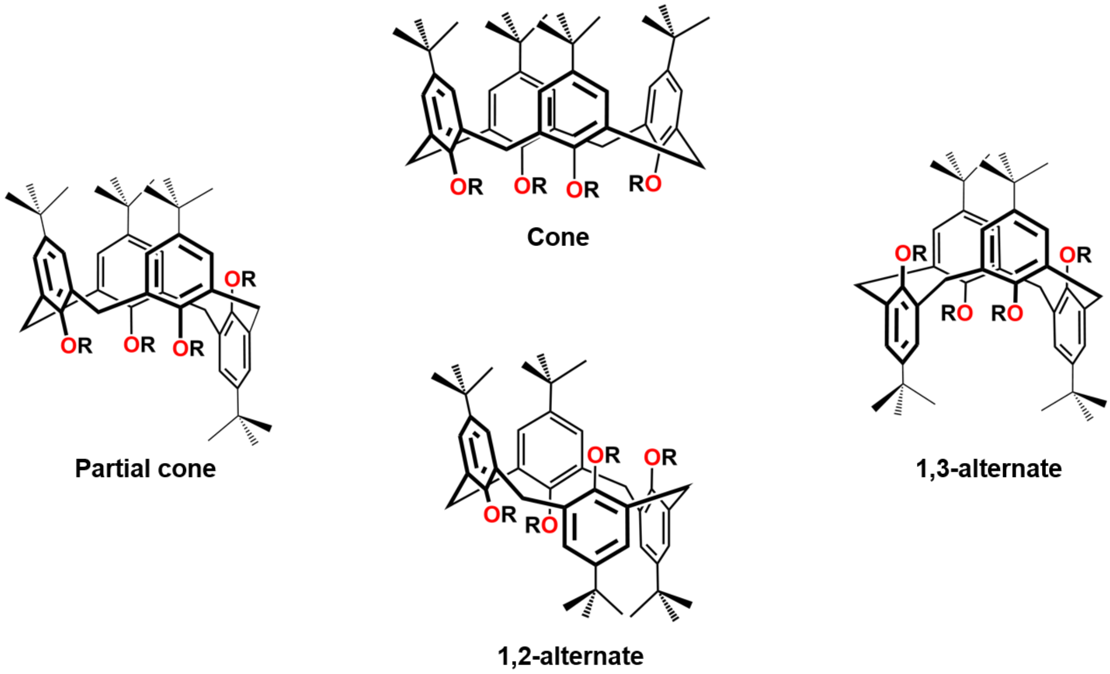

Fig 1.7 Different conformations of calix[4]arenes (R = methyl, ethyl, benzyl, or acetate at lower rim).

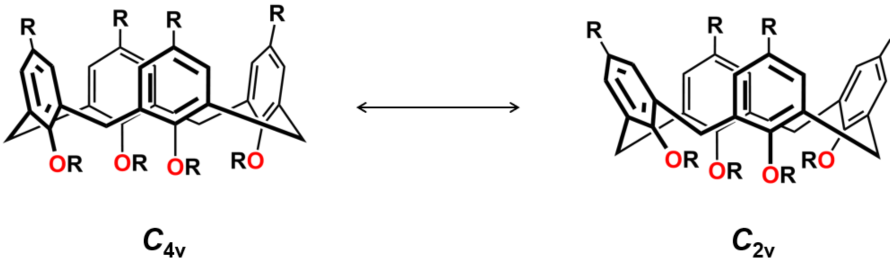

Fig 1.8 Cone and pinched-cone symmetries of calix[4]arenes (R = carboxylic acid and amide on the upper rim and octyl at lower rim).

1.2.2 Synthesis and reactivity of *p-tert*-butylcalix[4]arene (TBC[4])

For many years, the synthesis of TBC[4] under identical reaction conditions was resulting in a variable amount of product. The procedure described by Zinke involved the use of an excess of a base in the first step, which needed to be neutralized before refluxing in the second step. The neutralization process was changing the composition of the reaction mixture, therefore, giving different yields of the product. After a series of investigations, careful control of the amount of base and temperature outlined the conditions to get reproducible results.[109] The modified Zinke-Cornforth procedure for the synthesis TBC[4] involves the heating at 120 °C of 1 equivalent of *p-tert*-butylphenol, 37 % formaldehyde solution, 0.045 equivalents of NaOH and elimination of water by Dean-Stark apparatus. This produces a thick viscous solid that is further heated at 260 °C after the addition of toluene and diphenyl ether. Precipitation with ethyl acetate yields the crude as a white powder. Recrystallization from toluene provides a pure product in high yield. The best yield of calix[4]arene is obtained using 0.03–0.04 equivalents of the base, whereas the higher amount yields calix[6]arene as a major product.[100,110]

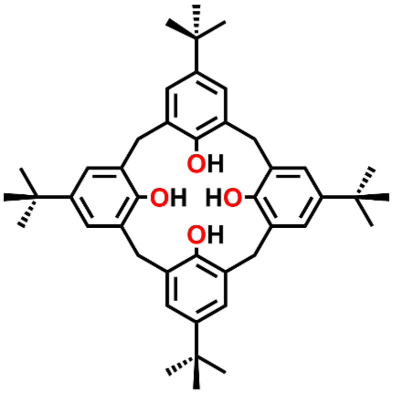

***p-tert*-butylcalix[4]arene**

To achieve their applications in multiple fields of science, a variety of functional groups have been appended at different positions of TBC[4]. These include upper/lower rim and bridging groups of the skeleton. Conformational mobility of different isomers is lost upon derivatization of parent calix[4]arene, as a result, a single stable conformation is favored depending on the derivatizing agent and reaction conditions.[111,112]

Replacement of phenolic moiety at the lower rim of TBC[4] with alkyl groups is the most common and easy reaction in the chemistry of calix[4]arene **(Scheme 1.6)**. The strength of base and reaction conditions specify the partial or full alkylation of the lower rim. For example, the use of sodium hydride with an excess of acid or aryl/alkyl-halide results in the etherification of all four phenolic sites, while partial alkylation is accomplished using a weaker base.[105,113] Use of sodium or potassium carbonate selectively deprotonates (distal) 1,3-positions of calix[4]arene. The proximal (1,2-position) dialkylation is achieved using a stronger base and stoichiometric amount of alkyl halide.[114] In general, the product of alkylation reaction depends on the nature of the alkylating agent, strength of base, solvent, and temperature of the reaction.

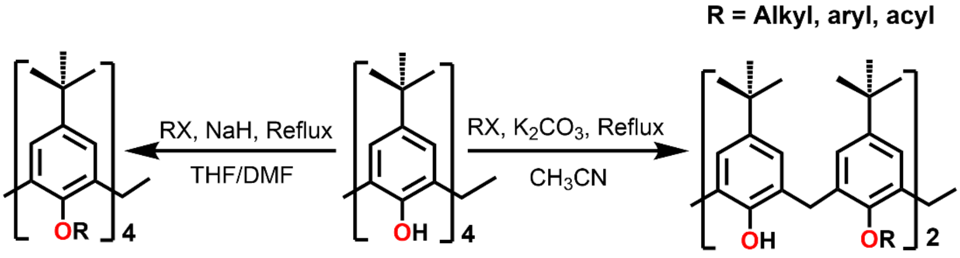

Scheme. 1.6 Partial or complete alkylation at lower-rim of calix[4]arene.

Derivatization of the upper-rim of TBC[4] can be achieved by electrophilic substitution. To introduce different functionalities on *p*-position, debutylation of *p*-*tert*-butyl groups is the first step that can be readily achieved by reverse Friedel-Crafts, followed by subsequent reactions on the unmask positions.[115] The rate of dealkylation depends on the type of substituent on phenolic moiety. Generally, *p*-*tert*-butylphenols can be easily dealkylated in comparison to ethers or esters.[116] Using this strategy, the *p*-position of debutylated calix[4]arene has been explored for various functionalization, some of them are highlighted in **Scheme 1.7**. Bromination is extensively used, due to the possibility for subsequent C–C coupling reactions or, reaction with *n*-BuLi resulting in *p*-lithiated-calix[4]arene, that can be further converted to *p*-carboxylato- and *p*-hydroxy-calix[4]arene.[117-119] Direct sulfonation of debutylated-calix[4]arenes produces water-soluble *p*-sulfonated-derivatives. These molecules display very good activity for selective removal of ions from sea-water and are also potential synthetic intermediates for introducing some other functionalization. For example, the synthesis of *p*-nitro-calix[4]arene can be achieved by the replacement of these sulfonate groups.[120]

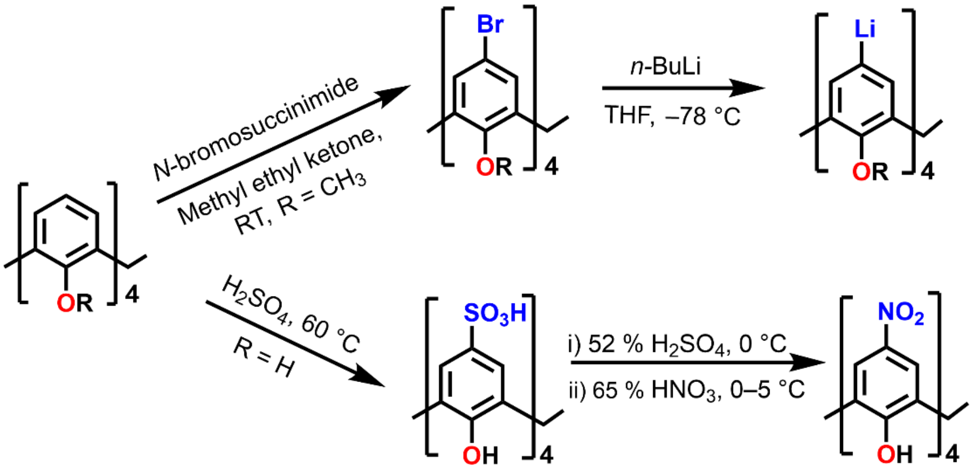

Scheme. 1.7 Electrophilic substitution at the upper-rim of calix[4]arene.

Other examples of upper-rim substitution include the synthesis of *p*-aryl-calix[4]arene, also called deep-cavity calixarene, by introducing phenyl units on the *p*-position of halogenated-calix[4]arene employing palladium-catalyzed cross-coupling reactions.[121]

Besides upper and lower-rim of calix[4]arene, bridging (–CH_2–) groups provide another potential site for modification of the skeleton **(Scheme 1.8)**. Several reports show the replacement of methylene bridged-parent calix[4]arene to brominated, lithiated, and carbonated analogues.[122,123]

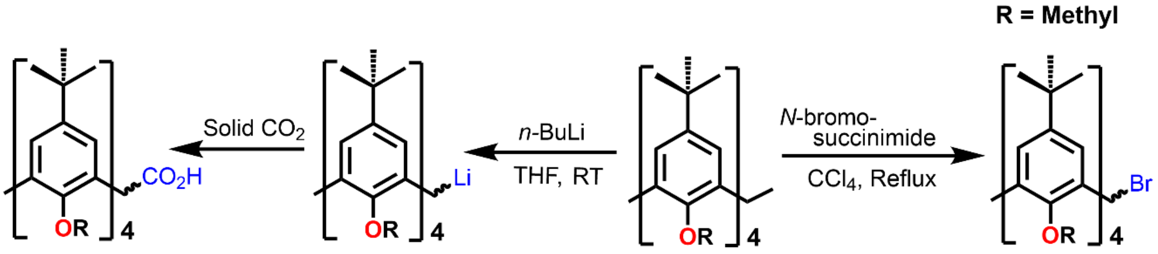

Scheme. 1.8 Modification on the bridging-positions of calix[4]arene.

Furthermore, oxidation and reduction of calix[4]arenes produce calix[4]diquinone and calix[4]arene diethers respectively as shown in **Scheme 1.9**.[124,125] Therefore, the tool of selective substitution on calix[4]arene moiety can be used to modify the parent structure and to get the compounds with multiple capabilities.

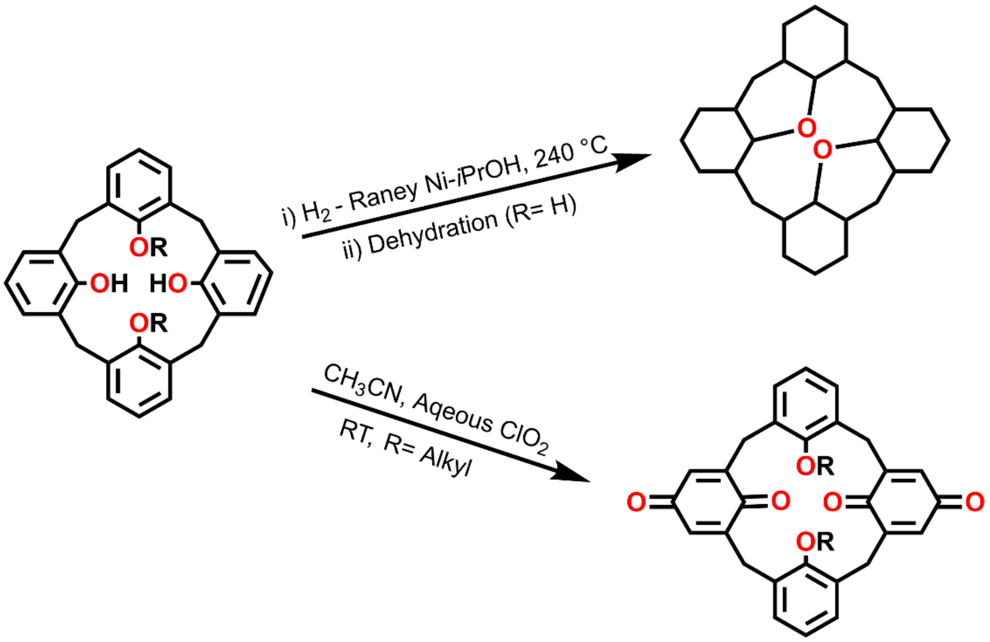

Scheme. 1.9 Oxidation and reduction of calix[4]arene.

The polyphenolic lower-rim of TBC[4] presents the perfect pocket for the coordination and inclusion of transition metal (TM) and lanthanide metal ions (Ln). Among transition metals, a mixed-valence hexavanadate cluster $[V^{III}V^{IV}_5O_6(OCH_3)_8(TBC[4])(CH_3OH)]^–$ has been obtained under solvothermal reaction conditions by reacting $VOSO_4$ and TBC[4] in methanol in presence of a base (NEt_3, NEt_4OH, or NH_4OH). The cluster represents the first example of TBC[4] coordinated to a Lindqvist $[V_6O_{19}]$ structure. The negative charge on the overall structure is balanced by a countercation from the base used in the reaction.[126] Another example of mixed-valence cluster includes $[Mn^{III}_2Mn^{II}_2(OH)_2(TBC[4])_2(DMF)_6]$, produced by reacting $MnBr_2$ with TBC[4] in presence of NEt_3 in a solvent mixture of DMF/MeOH. The cluster consists of a central $[Mn^{III}_2Mn^{II}_2(OH)_2]$ core sandwiched between two TBC[4] units, forming a butterfly-shaped molecular structure.[127]

The reaction of TBC[4] with $[Ti^{IV}(OBu)_4]$ produced a dinuclear $[Ti^{IV}_2(OBu)_2(TBC[4])_2]$ complex in which both titanium centers are coordinated to three oxygen of each TBC[4] units and bridged by two butoxide-ligands. The reaction under the same conditions with $[Zr^{IV}(OBu)_4]$ resulted in a trinuclear $[Zr^{IV}_3(OBu)_8(TBC[4])]$ structure, due to the larger size and different reactivity of zirconium.[128] Replacement of methylene bridges of TBC[4] with thia- or sulfonyl-groups produced several other polymetallic clusters with transition metals [Co(II), Ni(II), Cu(II)].[129,130]

The first family of TBC[4] supported lanthanide clusters $[Ln^{III}_6(TBC[4])_2O_2(OH)_{3.32}Cl_{0.68}(HCO_2)_2(DMF)_8(H_2O)_{0.5}]$ (Ln = Gd, Tb, Dy, and Ho) have been generated in 2012 by the reaction of hydrated lanthanide(III) chlorides with TBC[4]. In these clusters, the Ln-ions are linked to each other by two central μ_4-$O^{2–}$ ions. Each apical Ln-ion is coordinated to one TBC[4] through four oxygen atoms, each of these oxygen atoms are also bonded to a Ln-ion in the central square. The edges of the square are bridged by disordered formate/$OH^–$ and $Cl^–$/$OH^–$. The additional sites are filled with solvent (DMF) molecules resulting in octacoordinated Ln-centers in square antiprismatic geometries.[131] The examples of TBC[4]-based mononuclear complexes are quite limited. Among them, a cerium(IV)-based complex $[Ce^{IV}TBC[4](OMe)_2O_2)(acac)_2]$ has been produced by the reaction of cerium(IV) acetylacetonate with $[TBC[4](OMe)_2(OH)_2]$.[132] The complex can act as a suitable precursor for further reactions to get TBC[4]-based hybrid complexes. Another series of mononuclear hybrid complexes consists of seven coordinated lanthanide(III) (Tb, Dy, Ho) center encapsulated by $(TBC[4](OMe)_2O_2)$ and Kläui′s tripodal ligand. The Dy(III) analogue of these hybrid systems displayed a field-induced SMM behavior.[133]

A library of TM-Ln mixed compounds of TBC[4] has also been achieved in the last years. For example, the reaction of hydrated iron(II) and lanthanide(III) chloride salts with TBC[4] afforded the 3d-4f mixed clusters $[Fe^{III}_2Ln^{III}_2(O)(OH)(TBC[4])_2(DMF)_4(MeOH)_2(H_2O)_2]Cl$

(Ln = Gd, Tb, and Dy), in which two TBC[4] units encapsulate the metallic core. Each iron is binded to a central μ_4-O^{2-} ion and four oxygen atoms at the lower rim of TBC[4] with overall distorted square pyramidal geometry. In addition to the central μ_4-O^{2-} ion connecting all four metal centers, each lanthanide ion is coordinated to one oxygen of each TBC[4], a bridging OH^- ion that connects both lanthanides, and coordinating solvent (DMF, CH_3CN, H_2O) molecules, resulting in square antiprismatic geometries.[134] Another 3d-4f mixed cluster has been obtained by reacting bis-calix[4]arene with hydrated copper(II) and terbium(III) nitrates. The cluster consists of $Cu^{II}_4Tb^{III}_5$ core sandwiched between two bis-calix[4]arenes and bridged by hydroxide and nitrate ions. The coordinating solvents (DMF, MeOH, and H_2O) fill the remaining coordination sites of metal ions.[135]

1.2.3 Electrochemistry of calix[4]arene

Although parent calix[4]arene does not contain any redox-active center, the substitution of suitable electrochemically-active groups on the main skeleton leads to several remarkable properties in the system. The resulting calix[4]arenes show anodic or cathodic perturbation in the electrochemical signals in the presence of specific ions.[136] In this context, tetrathiafulvalene modified calix[4]arene has been found to be very responsive for Cu^{2+} and Hg^{2+} ions, due to the oxidation of tetrathiafulvalene to its radical cation and dication in the presence of these ions.[137] Several other calix[4]arenes containing ferrocene, cobaltocenium, and ruthenium bipyridine displayed efficient anion (adipate or hydrogen phosphate) binding ability.[138-141] Similarly, electrochemically reduced *p*-nitrocalix[4]arene has shown remarkable sensitivity towards heavy alkali metal cations (K^+, Rb^+, and Cs^+). The upper cavity of these molecules contains four redox-active nitro groups that undergo reversible four-electron reduction to stable tetraradical-anions in an aprotic solvent. The presence of stable unpaired electron in these species has been monitored by in-situ spectroelectrochemical setup (UV-Vis and ESR).[142,143]

Moreover, the synthesis of calix[4]diquinone-based ligands by electrochemical-oxidation of calix[4]arene have also garnered attention. The process is considered to involve the formation of phenoxylium-cation followed by the attack of residual water in the electrochemical cell resulting in the formation of diquinone **(Scheme 1.10)**. The evaluation of these diquinone ligands as potential sensors displayed a change in their redox behavior in presence of alkali metal ions.[144-147]

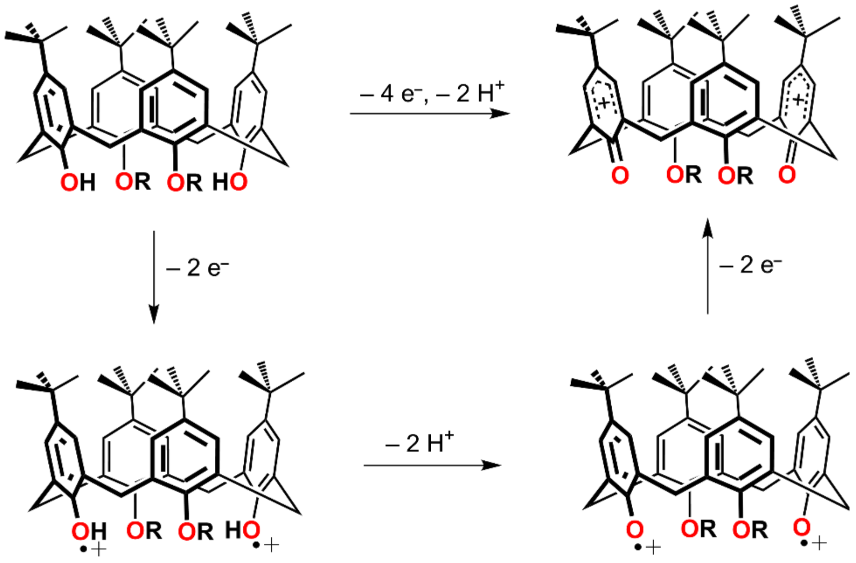

Scheme. 1.10 Electrochemical oxidation of calix[4]arene. (R = *p*-toluenesulfonyl at lower rim).

1.2.4 Applications

The basket-like structure of calixarenes makes them interesting building blocks for supramolecular chemistry. Several functionalities on the main skeleton have been introduced for their use in desired fields such as ion- and molecule-extraction, sensing, catalysis, medicine, and magnetism.[101,148,149]

1.2.4.1 Calix[4]arene as sensors

The construction of calixarene-based devices to sense various chemical and biochemical species in different systems is a topic of considerable interest. As described earlier, calix[4]arene substituted with electrochemically active groups are excellent candidates as redox-dependent ionophores that change the electrochemical response as a result of interaction with various cations or anions. The idea of redox-dependent ionophores can be extended for the molecular switching devices.[136] Besides ion-sensitive electrodes, calix[4]arene have also been tested for ion-selective field-effect transistors (ISFETs), which consist of a film of an ion-sensitive material on the gate electrode and it changes the conductance of the device as a result of a chemical response. In this regard, calix[4]arene-based ISFETs have shown great selectivity for certain cations over others.[150,151]

Calix[4]arenes also find their applications in chromogenic or fluorescent sensors. For example, *p*-sulfonatocalix[4]arene specifically formed a colored complex with Ce(III), therefore, can be used to distinguish that from other rare-earth elements.[152] Anthracene or pyrene modified calix[4]arenes, combining the properties of fluorophore and ionophore, exhibited a fluorescent response upon complexation with alkali (Li^+, Na^+, K^+) and transition metal cations (Cu^{2+}, Ni^{2+}) respectively.[153,154] Similarly, calix[4]arene with imidazole units has shown effective recognition of Cu^{2+} and Zn^{2+} ions. The fluorescent behavior of this system has been manipulated by pH, therefore, could act as a molecular switch.[155]

1.2.4.2 Calix[4]arene-based magnetic material

The polyphenolic nature of calix[4]arene has been successful to isolate clusters with interesting magnetic properties and, some of them behaving as single-molecule magnets (SMM). The first SMM in this family was reported in 2009 and it consists of a butterfly-shaped molecular structure with a mixed-valence tetramanganese core $[Mn^{III}_2Mn^{II}_2(OH)_2]$ sandwiched between two TBC[4] units. In the cluster, the Mn(III)-ions occupy the wing positions while Mn(II) are the body ions of the butterfly core; this structural arrangement of metal ions is reversed to the common manganese-based SMM. Although the complex did not show maxima in frequency-dependent signals above 2K, the SMM behavior was confirmed by the presence of hysteresis loop up to 1.1 K.[127] Structural modification of $[Mn^{III}_2Mn^{II}_2(OH)_2]$ cluster by equatorial coordination through 2,2-bipyridyl ligands indicated a strong influence on the magnetic properties, reaching $U_{\mathrm{eff}} = 29$ K.[156] Besides manganese, the magnetic properties of calixarene-based complexes of other transition metals [Co(II), Ni(II), and Cu(II)] have also been studied.[130,157]

The magnetic properties of heterometallic mixed complexes of calix[4]arene, combining the properties of anisotropic 3d-ions with the large spin-orbit coupling of suitable 4f-ion, have also been described. An important example is $[Mn^{III}_4Ln^{III}_4]$ assembly of calix[4]arene in which the central Ln_4-unit is surrounded by four Mn-calix[4]arene units. The cluster with Gd(III) as lanthanide ion has shown excellent properties as a magnetic refrigerant. The replacement of Gd(III) with Tb(III) and Dy(III) exhibited slow magnetic relaxation with the thermal energy barrier of 3 and 5 K respectively.[158]

The example of calix[4]arene supported polymetallic lanthanide clusters includes a Dy^{III}_6-octahedron sandwiched between two TBC[4] units, presenting an energy barrier of 7.6 K for magnetization reversal.[159] Similarly, *p*-*tert*-butylsulfonylcalix[4]arene produced a disordered Dy^{III}_4-cubane cluster with U_{eff} value of 22.9 K.[160] The seven-coordinated Dy(III) complex of TBC[4] and Kläui′s tripodal ligand represented the first monometallic SMM of calixarene family ($U_{\mathrm{eff}} = 73.7$ K at 900 Oe dc-field).[133] Later on, the structurally analogous complexes of

Dy(III) and Er(III) with *p-tert*-butylthiacalix[4]arene and Kläuiʹs tripodal ligand also exhibited slow magnetic relaxation under the applied field of 1000 Oe.[161]

1.2.4.3 Calix[4]arene in catalysis

Based on the structural resemblance to cyclodextrin, calixarenes are considered as promising building blocks for the development of artificial enzyme mimics to study their mechanism of action. In these enzyme model studies, calix[4]arenes have been widely used in reactions involving hydrolysis of phosphate ester.[162] Naturally occurring metalloenzymes such as DNA-polymerase, nuclease, and phospholipase consist of divalent metals (*e.g.* zinc, iron, or magnesium), which play an important role in the hydrolytic reactions. To mimic the action of these enzymes, calix[4]arene-based artificial systems having upper rim functionalized with mono-, di-, and tri-nuclear zinc(II) have been investigated. These flexible scaffolds displayed excellent catalytic activity under mild conditions, for example, the mononuclear zinc(II)-calix[4]arene has shown the rate acceleration by a factor of six respect to the reference zinc complex.[163] Dinuclear and trinuclear calix[4]arene complexes further improved the catalytic activity, *i.e.* 23000 and 32000 fold in comparison to the reference complex respectively. The rate of these reactions has been monitored by UV-Vis spectroscopy, as the release of *p*-nitrophenol increases the absorbance at 400 nm.[164] Another zinc(II) complex of calix[4]arene displayed efficient activity for methanolysis of esters.[165]

Apart from the investigation as enzyme mimics, bio-recognizable units are added to calixarene skeleton to study the carbohydrate-protein interactions involved in many important biological processes. For example, the compounds prepared by the attachment of carbohydrate on calix[4]arenes, termed as calixsugars, have shown affinity for some charged carbohydrates.[166] Similarly, the electrostatic interactions of some ionic-calixarenes with proteins resulted in a dramatic colorimetric response and change in visible absorbance. This recognition process can be used for diverse medical and diagnostic applications.[167] The non-biomimetic catalytic properties of metallocalixarenes have also been tested for several reactions, such as conversion of nitrogen to nitride,[168] epoxidation of allylic alcohols,[169] and formation of biaryl compounds.[170]

1.2.4.4 Calix[4]arene in medicine

Interaction of calixarenes with various guest compounds has been extended to study their interaction with biological molecules focusing their potential against bacteria, viruses, and cancer cells.[171,172] For example, calix[4]arene 0118, as an anti-angiogenic agent, inhibits tumor cell growth in mice and is further being investigated for clinical trials.[173] Another calix[4]arene containing four platinum centers at the lower rim exhibited anticancer activity against several human cancer cell lines.[174] Similarly, antimicrobial activities of peptido-calix[4]arenes has shown excellent antibacterial profiles against some gram-positive bacterial strains, in comparison to the reference Vancomycin. Further studies to explore the binding mechanism of these complexes with model cell wall have also been performed.[175] The DNA-binding properties of calix[2]arene[2]triazines highlighted their potential as anti-cancer agents. Evaluation of these compounds against human pathogenic bacteria such as *B. cereus*, *S. aureus,* and *E. coli* also exhibited good results.[176] Moreover, *p*-sulfonatocalix[4]arene displayed substantial anti-thrombic and anti-viral activities, such as against HIV and Herpes. Toxicity evaluation of these water-soluble calixarenes indicated no harmful effect up to a dosage of 50 mM.[177]

1.3 Polyoxometalates

Polyoxometalates (POMs) are a diverse family of anionic metal-oxide clusters usually made up of tungsten(VI), molybdenum(VI), vanadium(V), and less commonly niobium(V) and tantalum(V). The empty d-orbitals in these high-valent metals allow them to coordinate to a different number of oxygen ligands forming a range of polyhedra from MO_4 to MO_7. The 3D-framework of POMs arises from the condensation of (MO_x) polyhedra, most commonly octahedra, of these transition metals under acidic conditions.[178]

General representation of condensation of transition metal polyhedra to POMs:

$$x\,[MO_4]^{n-} \quad + \quad y\,H^+ \quad \longrightarrow \quad [M_xO_z]^{m-} \quad + \quad y/2\,H_2O$$

The first synthetic contribution in POMs chemistry was made by Berzelius in 1826 who reported the formation of yellow-colored ammonium phosphomolybdate $(NH_4)_3[PMo_{12}O_{40}]$ by the reaction of ammonium molybdate with an excess of phosphoric acid.[179] However, the structural details of the material remained unknown at that time due to the lack of appropriate analytical techniques. Almost after 100 years, single-crystal X-ray diffraction of dodecatungstophosphoric acid [$H_3PW_{12}O_{40}$] was reported by J. F. Keggin, revealing the structural complexity of POMs.[180,181] Following this discovery of this POM motif, all the structures with general formula [$XM_{12}O_{40}$]$^{m-}$ are termed as Keggin-POMs. Recently a naturally occurring mineral [$AsV_{12}O_{40}$]$^{15-}$ was also named as kegginite.[182]

Transition metals in these clusters are called addenda atoms. The octahedral building blocks in these assemblies are connected by sharing corners, edges, or faces. A rich variety of shapes and sizes can be achieved under various experimental conditions, such as temperature, pH, solvent, and the type of countercations, giving the unrivalled structural diversity to this class of compounds.[183]

The symmetrical assemblies of POMs can be generally classified into two types: Iso-polyoxometalates and hetero-polyoxometalates with general formula [M_yO_z]$^{m-}$ and [$X_nM_yO_z$]$^{m-}$ respectively.[184] The structural assemblies of iso-polyanions such as Lindqvist-type ([M_6O_{19}]$^{2-}$, where M = Mo, W, V) consist of six MO_6 polyhedra with just one type of addenda center exhibiting octahedral symmetry. While the more stable hetero-polyanions contain an additional four- or six-fold coordinated heteroanion XO_n^{m-} in the framework, for examples, *Keggin* {[$XM_{12}O_{40}$]$^{m-}$, M = W, Mo, V; X = P(V), As(V) or Si(IV)}, *Wells-Dawson* {[$X_nM_{18}O_{62}$]$^{m-}$, M = W, Mo, V; X = P(V), Si(IV); n = 1 or 2}, and *Anderson-Evans* {[XM_6O_{24}]$^{m-}$, M = W, Mo, V; X = Mn(III) or Fe(III)}. These hetero-anions play an important role in the structure, charge, and reactivity of these POMs. Some common polyanionic structures are shown in **Fig 1.9**.

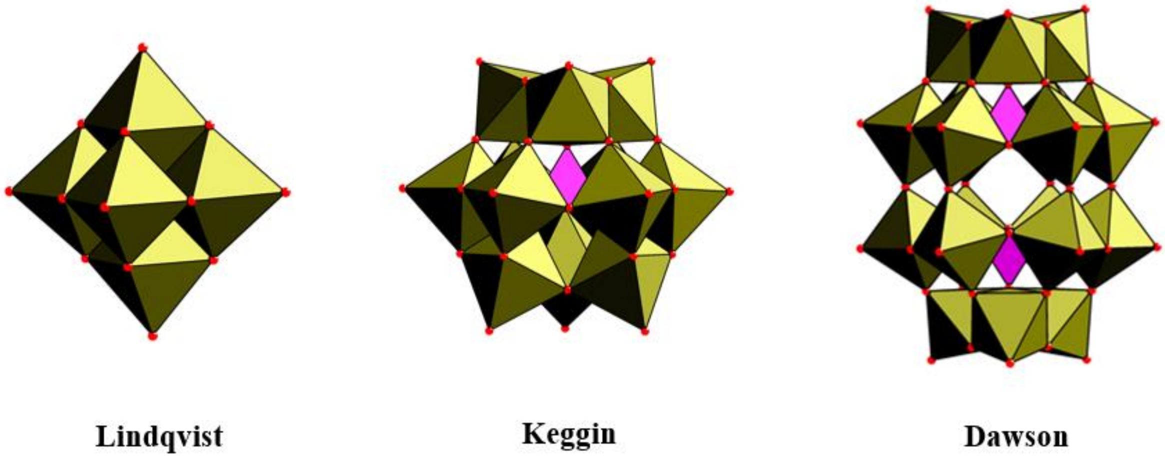
Lindqvist **Keggin** **Dawson**

Fig 1.9 Polyhedral representation of the most common structural families of polyoxometalates.

1.3.1 Tungsten-based Keggin, and lacunary Keggin-derivatives

Among various classes of POMs, tungsten-based Keggin are highly robust, most studied anions, and are composed of a central tetrahedral $[XO_4]^{n-}$ hetero-anion surrounded by twelve WO_6 octahedra **(Fig 1.10)**. In the structure, every three WO_6 octahedra are connected by edge-sharing forming four W_3O_{13} triads, which are interconnected by μ_2-O^{2-} ions and linked to central XO_4^{n-} via four μ_3-O^{2-} ions giving rise to overall tetrahedral (T_d) symmetry. Additionally, each addenda atom is connected to one terminal oxygen through a double bond which limits the growth of these polyanions and forms discrete structures instead of infinite solids. The resulting structure is referred to as α- or plenary-Keggin in which one, two, three, or four W_3O_{13} units can be rotated by 60° resulting in the formation of different isomers. The rotation of one triad of plenary structure produces β-isomer with C_{3v} symmetry. The γ-isomer (C_{2v}-symmetric) and δ-isomer (C_{3v}-symmetric) result from the rotation of the second and third triad respectively. Finally, the rotation of the fourth triad gives ε-isomer with all four equivalent units having T_d-symmetry.[185] The α-isomer exhibits thermal and redox stability in comparison to the rotated isomers in which the increased coulombic repulsion due to shortening of separation between addenda centers lower their stability.[184] However, the type of hetero-anion also affects the stability of different isomers, for example, the β-isomer converts more rapidly into α-isomer in the case of P(V) or As(V) heteroanions than with Si(IV) or Ge(IV).[186,187]

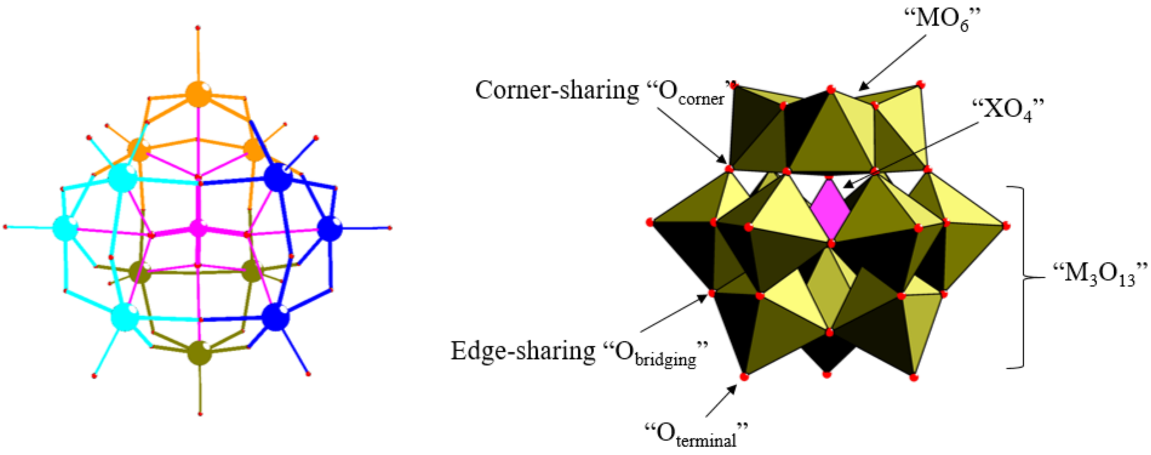

Fig 1.10 (Left) Ball and stick representation of generalized α-Keggin structure with M_3O_{13} units highlighted in blue, dark yellow, turquoise, and orange with the central tetrahedron XO_4 in pink. **(Right)** Polyhedral representation with the details of different types of connectivities.

The redox behavior of the hetero-polyanions depends on the overall charge and nature of metal atoms in the cluster. They act as multielectron oxidants as the high-valent transition metals in these polyanions can accept electrons in empty d-orbitals. The added electrons remain delocalized over the M–O framework without significant geometrical changes.[188] The electrochemical studies on the Keggin structure indicated the addition of two electrons to the cluster under neutral conditions without any decomposition. While in acidified conditions, a further reduction occurred accompanied by protonation to keep the overall molecular charge low.[189]

The structural diversity of Keggin-POMs can be achieved by the loss of one, two, or three [M=O] fragments from the plenary structure resulting in the formation of lacunary or unsaturated structures. The plenary-Keggin anions are usually stable under acidified conditions, but with controlled base hydrolysis, lacunary-Keggin structures are obtained.[184,190] The removal of an octahedral unit from plenary structure places the negative charge on the oxygen of lacunary- or defective-sites, making these polyanions very reactive towards transition metals, main-group, and rare-earth elements. Replacement of one or more addenda atoms also changes the electronic and chemical properties of resultant structures. These lacunary structures are referred to as monolacunary $[XW_{11}O_{39}]^{n-}$, dilacunary $[XW_{10}O_{36}]^{n-}$, or trilacunary $[XW_9O_{34}]^{n-}$ depending on the number of removed polyhedra. Different isomeric (α or β) forms of lacunary-Keggin also exist based on the geometrical arrangement of the oxometallic framework.[191,192] Hydrolysis of the α-Keggin can be generally represented as:

$$[XM_{12}O_{40}]^{p-} + m\,OH^- \longrightarrow [XM_{12-y}O_{40-z}]^{q-} + y\,MO_x + n\,H_2O$$

1.3.2 Monolacunary α-Keggin based phosphotungstate $[PW_{11}O_{39}]^{7-}$

The monolacunary phosphotungstate $[PW_{11}O_{39}]^{7-}$ contains an inner PO_4^{3-} whose oxygen atoms are connected to the eleven tungsten(VI) ions via three μ_3-O^{2-} ions and one μ_2-O^{2-} ion. Similar to the parent Keggin structure, the tungsten centers are linked to each other through μ_2-O^{2-} ions and each tungsten form a double bond to a terminal oxygen atom **(Fig 1.11)**. The defect-site of monolacunary anion offers four highly nucleophilic oxygen atoms for coordination leading to a large diversity of structures.

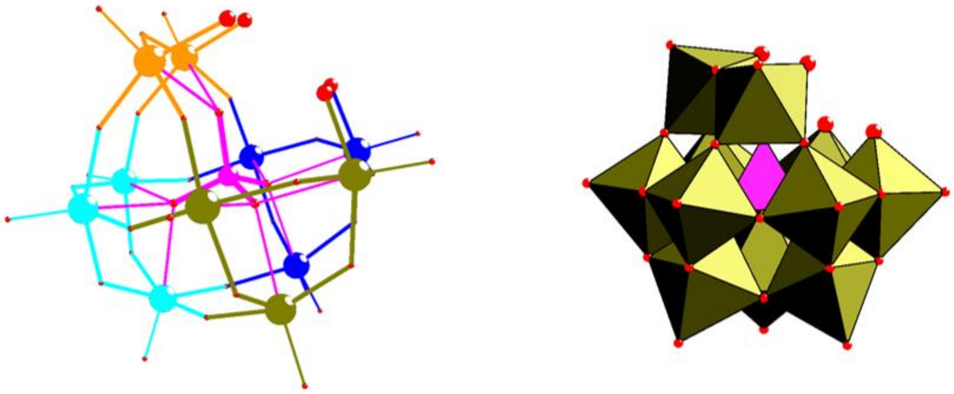

Fig 1.11 (Left) Ball and stick, and **(right)** polyhedral representation of monolacunary-Keggin polyanion $[PW_{11}O_{39}]^{7-}$ with highlighted oxygens at defective-sites.

Although the synthesis of the sodium salt of monolacunary Keggin was reported in 1983,[193] the first crystal structure of this polyanion was not published until 2002.[194] The formation of different isomeric forms of Keggin and lacunary-Keggin derivatives has been investigated by recording the ^{31}P-NMR of freshly prepared aqueous solutions of W(VI) and P(V) with different acidities. The monolacunary $[PW_{11}O_{39}]^{7-}$ appeared in the pH range of 3.5–5. Further consumption of OH^- ions by an increase in alkalinity of solution (pH; 5.5–7.5) converted the $[PW_{11}O_{39}]^{7-}$ to $[PW_9O_{34}]^{9-}$ and finally decomposed to tungstates and phosphates.[195]

After the synthesis and characterization of this lacunary specie, its reactivity towards various heterometals has been widely explored. The reaction of transition metal ions (Cr, Mn, Fe, Co, Cu) with $[PW_{11}O_{39}]^{7-}$ produced an enormous range of structures with the formula $[PMW_{11}O_{39}]^{n-}$.[196-200] Additionally, the polyanion also produced monometallic sandwich-type complexes $[M(\alpha\text{-}PW_{11}O_{39})_2]^{10-}$ with M = Zr(IV) or Hf(IV).[201]

The reactions of $[PW_{11}O_{39}]^{7-}$ with lanthanide salts resulted in 2:2 derivatives. For example, two different types of dinuclear lanthanide clusters $[\{(\alpha\text{-}PW_{11}O_{39}H)Ln^{III}(H_2O)_3\}_2]^{6-}$ (Nd, Gd) and $[\{(\alpha\text{-}PW_{11}O_{39})Ln^{III}(H_2O)(\eta^2,\mu\text{-}1,1)\text{-}CH_3COO\}_2]^{10-}$ (Sm, Eu, Gd, Tb) have been obtained by reacting the polyanion with lanthanide salts at controlled pH. In both types, the monomeric units, consisting of one lanthanide and polyanion, are linked by two Ln–O–W bridges and two η^2,μ-1,1-acetato ligands respectively.[202]

The reaction of trilacunary $[PW_9O_{34}]^{9-}$ with series of lanthanide(III) (La, Pr, Nd, Sm, Eu, Gd, Tb, Dy, Er, Tm, Yb, and Y) salts generated (1:2) sandwich-type enantiomeric $[Ln(\alpha\text{-}PW_{11}O_{39})_2]^{11-}$ compounds. The racemic mixture of these compounds was successfully isolated using a chiral proline molecule as a result of hydrogen bonding interaction between proline and polyanion of the same chirality.[203]

To increase the structural diversity of these polyanions and to obtain materials with unique electronic properties, some hybrid clusters based on $[PW_{11}O_{39}]^{7-}$ have been prepared. For example, in 1978, the reaction of polyanion with $[(\eta^5\text{-}C_5H_5)Ti^{IV}Cl_3]$ produced the first hybrid POT-organometallic complex $[(\eta^5\text{-}C_5H_5)Ti(PW_{11}O_{39})]^{4-}$. In the molecular structure, titanium(IV) occupies the position of lost tungsten(VI), forming a hydrolytically stable hybrid complex.[204] Later on, discrete complexes with the general formula $[M(L)(PW_{11}O_{39})]^{5-}$ were reported by combining the tetrapyrrole ligands (L = porphyrin or phthalocyanine) and monolacunary polyanion. The metal center [Hf(IV) or Zr(IV)] in these complexes couples the electronic properties of both chelating ligands forming a sandwich structure.[205,206] Recently, another family of hybrid complexes with the general formula $[Ln^{III}H(phen)_2(PW_{11}O_{39})]^{3-}$ (Ln = Dy, Er, Gd) has been produced by the reaction of $[PW_{11}O_{39}]^{7-}$ and phenanthroline ligand with lanthanide(III) acetates. The Dy(III) analogue of these hybrid systems exhibited field-induced SMM behavior.[207]

1.3.3 Applications

POMs are multifunctional materials with unique physical and chemical properties. The most promising features of POMs refer to their oxidative and thermal stability, solubility in aqueous and non-aqueous solvents, electron-reservoir, and acidic properties. The combination of these inherent properties along with the huge structural diversity of these clusters attracts wide attention in fields such as catalysis, energy conversion, medicine, and information technology.[208-212]

1.3.3.1 POMs in catalysis

The polyanionic clusters are referred to as electron reservoirs, as under different conditions they can play the role of Lewis bases or Lewis acids. The oxo-groups in the structure of polyanions can donate electrons while the empty d-orbitals on metal atoms can reversibly accept one or two electrons. These fascinating redox properties, resistance toward oxidation, and hydrolytic conditions make them, especially Keggin-POMs, ideal candidates for catalysis of several reactions.[211] For example, the protons on heteropolyacids act as Bronsted acids and help in acid-catalyzed reactions. Based on this, silica-supported $H_3PW_{12}O_{40}$ has shown highly efficient acid catalytic activity in Friedel-Crafts acylation reaction.[213] Similarly, the highly nucleophilic oxygen atoms of lacunary polyoxotungstates (POTs) *e.g.* $[\gamma\text{-}SiW_{10}O_{34}]^{4-}$ has been employed in base-catalyzed reactions.[214] Besides acid or base-catalysis, POMs also catalyze the oxidation of alkenes, alkanes, alcohols, and carbonyl compounds. [215-218]

Irradiation of UV or near-visible light on polyanions can excite the electrons to undergo ligand-to-metal charge-transfer (LMCT). For example, the electron transfer from O^{2-} to W^{6+} in POTs results in the formation of O^{-} and W^{+5} pair, in which the well-separated frontier levels avoid the recombination of holes and electrons.[219,220] These photogenerated species can play role in many reactions due to their strong oxidative and reductive abilities such as degradation of several organic pollutants[221] and recovery of zero-valent transition metals.[222]

The redox properties of polyanions also stimulate their applications in water splitting for the pollution-free production of fuel. In 2008, $[\{Ru^{IV}_4(O_4)(OH)_2(H_2O)_4\}(\gamma\text{-}SiW_{10}O_{36})_2]^{10-}$ cluster was the first breakthrough in POM-catalyzed water oxidation. The cluster accelerated the reaction in presence of $[Ru(bipy)_3]^{2+}$ as a photosensitizer and an oxidant along with $S_2O_8{}^{2-}$ as an electron acceptor to regenerate the oxidant.[223-225] Later on, $[Co^{II}_4(H_2O)_2(PW_9O_{34})_2]^{10-}$ cluster was demonstrated as a stable photocatalyst for O_2 evolution.[226,227] In these reactions, the POT-complex is oxidized by the oxidant and in turn, causes the splitting of water. Besides the photocatalytic oxidation of water, $[\{Ru^{IV}_4(O_4)(OH)_2(H_2O)_4\}(\gamma\text{-}SiW_{10}O_{36})_2]^{10-}$ cluster on multiwalled carbon nanotubes[228] or graphene[229] supported electrodes has been investigated for the electricity-driven water oxidation. These hybrid nanomaterials exhibited excellent performance along with the preservation of structure and electrocatalytic properties after multicycles of oxygen evolution. The reduction of H_2O to H_2 is another source of renewable energy production initiated by a catalyst in the presence of light or electricity. For example, $[Mn^{II}_4(H_2O)_2(VW_9O_{34})_2]^{10-}$ cluster along with $[Ru(bipy)_3]^{2+}$ as photosensitizer and triethanolamine as electron donor catalyzed the water reduction by irradiating the visible light of 455 nm.[230] Another highly durable $\{[Ce^{III}(H_2O)]_2[Ce^{III}(CH_3CN)]_2(\mu_4\text{-}O)(\gamma\text{-}SiW_{10}O_{36})_2\}^{6-}$ cluster has effectively generated H_2 in the presence of alcohols as electron donor and visible light of 400 nm without using any photosensitizer.[231]

POMs have also been employed in oxidative coupling reactions in combination with palladium-based compounds. For example, $\gamma\text{-}SiW_{10}O_{36}$ increased the turnover number of palladium-catalyzed Suzuki-coupling reactions using the hybrid structure of palladium N-heterocyclic carbene-SiW_{10}.[232] Another lacunary Keggin-based palladium nanoparticles Pd_x – $[(PW_{11}O_{39})^{7-}]_y$ catalyzed various C–C and C–N coupling reactions in the aqueous solutions and without any solvent.[233]

1.3.3.2 POMs-based magnetic and electronic materials

Magnetically functionalized POMs have been obtained by coordinating paramagnetic metals to diamagnetic lacunary POMs at specific sites. The first example of POMs-based SMM was a mixed-valence hexameric manganese cluster stabilized by two trilacunary (GeW_9) ligands $[\{\alpha\text{-}GeW_9O_{34}\}_2\{Mn^{III}_4Mn^{II}_2O_4(H_2O)_4\}]^{12-}$, exhibiting an energy barrier of 14.8 K for the reversal of magnetization.[234] Several other manganese-based magnetic molecules have been obtained by reacting $[Mn^{IV}_4Mn^{III}_8O_{12}(CH_3COO)_{16}(H_2O)_4]$ (Mn_{12}) with diamagnetic polyanions. Among them, a heptanuclear manganese-based cluster $[(\alpha\text{-}P_2W_{15}O_{56})Mn^{III}_6Mn^{IV}O_6(H_2O)_6]^{14-}$ with high spin (21/2) ground state has been isolated by reacting Mn_{12} with a trilacunary $[\alpha\text{-}P_2W_{15}O_{56}]^{12-}$. The cluster exhibited out-of-phase frequency-dependent signals below 3 K. However, no maxima in Cole-Cole or χ'' *vs.* T plots have been observed within experimental limits for the determination of U_{eff}.[235] Besides, a series of cobalt(II)-based POT clusters with high symmetries and variable nuclearities have been studied as a model for magnetic exchange interactions. For example, three clusters of $[\{Co_4(OH)_4PO_4\}_4(XW_9O_{34})_4]^{n-}$ with X = P(V), Si(IV), and Ge(IV) presented energy barriers of 26, 24.7, and 25.9 K respectively.[236] Another example of POM-based SMM is the hexanuclear Fe(III)-based cluster $[Fe_4(H_2O)_2(FeW_9O_{34})_2]^{10-}$ containing two trilacunary Keggin-polyanions. The cluster preserved its structure and exhibited magnetic bistability upon grafting to single-walled carbon nanotubes.[237]

Among monometallic POM-clusters, $[Er^{III}(W_5O_{18})_2]^{9-}$ exhibited slow magnetic relaxation with U_{eff} value of 55.2 K.[238] Similarly, strong frequency-dependent ac-signals have been observed in the case of monolacunary Keggin-derivatives $[Ln^{III}(SiW_{11}O_{39})_2]^{13-}$ (Dy, Ho, Er, and Yb).[239] These structures represent the inorganic-analogues of bis-phthalocyanato lanthanide(III) complexes, in which two polyanions encapsulate the lanthanide-ion in a sandwich-type fashion with overall distorted square antiprismatic geometry. Another family of monometallic complexes includes the C_5-symmetric $[Ln^{III}P_5W_{30}O_{110}]^{12-}$ (Tb, Dy, Ho, Er, Tm, and Yb). The clusters with Dy(III) and Ho(III) have shown magnetic hysteresis below 2 K.[240] Moreover, the Gd(III) analogues of $[Ln^{III}(W_5O_{18})_2]^{9-}$ and $[Ln^{III}P_5W_{30}O_{110}]^{12-}$ have shown promise as spin qubits and magnetic refrigerants for achieving ultralow temperature.[241,242] Besides POTs, two families of polyoxomolybdates with rigid square antiprismatic structure have also displayed slow magnetic relaxation. These include organic functionalized $[Ln^{III}\{Mo_5O_{13}(OMe)_4NNC_6H_4\text{-}p\text{-}NO_2\}_2]^{3-}$ (Tb, Dy, Ho, Er, Tm, and Nd) and $[Ln^{III}(\beta\text{-}Mo_8O_{26})_2]^{5-}$ (Tb, Dy, Ho, Er, Tm, and Yb) clusters having very good stability and solubility in organic solvents.[243] The presence of organic groups presents the possibility to incorporate these molecules onto the surfaces for spintronic applications.

POMs-based hybrid materials have been explored as active components for rechargeable batteries, electrodes, and capacitors. For example, a hybrid system of $[PMo_{12}O_{40}]^{3-}$ and single-walled carbon nanotube has been tested as a cathode active material for molecular cluster batteries. The results of the study indicated the fast charging/discharging and good battery capacity of the nanohybrid system due to the high electron storage ability of twelve Mo(VI) centers.[244] Another interesting POMs-based composite material has been developed by the deposition of $H_3PW_{12}O_{40}$ and graphene oxide nanosheets. Irradiation of these films by UV-light converted the insulator graphene oxide to conducting reduced graphene oxide due to the photocatalytic effect of POT. Furthermore, the field-effect transistors devices based on hybrid films have shown good transport properties and tailorable charge carrier mobilities.[245]

POM-based materials also exhibit switchable properties, for example, thin film of Dawson-type $[P_2W_{18}O_{62}]^{6-}$ polyanion and a luminescent $[Ru(bipy)_3]^{2+}$ complex showed electro-switchable fluorescent behavior. In the hybrid film, the electrochemical reduction of polyanion resulted in a color change from yellow to blue along with the quenching of luminescence. This behavior was attributed to the overlap of the absorption band of reduced polyanion with the luminescence band of $[Ru(bipy)_3]^{2+}$ complex. The change in color and luminescence was found to be reversible.[246] Similarly, another Dawson-type $[\beta\text{-}Mo_{18}O_{54}(SO_3)_2]^{4-}$ polyanion displayed a reversible thermoresponsive behavior, *i.e.* pale yellow at 77 K and deep red at 500 K due to the temperature-induced geometrical changes in the structure.[247]

1.3.3.3 POMs in medicine

Well-defined morphology and charges on POMs framework allow them to interact with biomolecules. Several POMs have been thoroughly examined for anti-cancer, anti-bacterial, and anti-viral activities.[248] For example, *in-vivo* and *in-vitro* anti-tumor potential of $[NH_3\textit{i}Pr]_6[Mo_7O_{24}]$ and its photoreduced complex $[Me_3NH]_6[H_2Mo^{V}_{12}O_{28}(OH)_{12}(Mo^{VI}O_3)_4]$ have been tested on a wide range of tumor model cells. The proposed mechanism of their activity is the repeated redox cycles of POMos that inhibit the ATP generation leading to apoptosis of tumor cells.[249,250]

Many Keggin and lacunary-Keggin POTs have been found to enhance the anti-bacterial effectiveness of β-lactam antibiotics against some Gram-positive bacterial strains.[251] In addition, $[Ce(SiW_{11}O_{39})_2]^{13-}$ and $[BGa(H_2O)W_{11}O_{39}]^{6-}$ inhibited the human immunodeficiency virus (HIV-1) at very low concentration. The binding of these polyanions to the host cells of the viruses is attributed to their inhibition activity.[252] Several POTs containing tris-vanadyl $(V^{IV}O)_3$ moiety sandwiched between two $[XW_9O_{33}]^{9-}$ [X = Sb(III), As(III), and Bi(III)] have shown potent activity against acute respiratory syndrome coronaviruses (SARS-CoV).[248] The use of these inorganic drugs against viruses, tumors, and bacterial infections requires further in-vivo examinations.

1.4 References

1. A. V. Braun and J. Tcherniac, *Ber. Dtsch. Chem. Ges.*, 1907, **40**, 2709-2714.
2. A. G. Dandridge, H. A. E. Drescher, and J. Thomas, *Dyes*, **1929**, British Patent, 322, 169.
3. R. Linstead, *J. Chem. Soc. (Resumed),* 1934, 1016-1017.
4. G. Byrne, R. Linstead and A. Lowe, *J. Chem. Soc. (Resumed)*, 1934, 1017-1022.
5. C. Dent, R. Linstead and A. Lowe, *J. Chem. Soc. (Resumed)*, 1934, 1033-1039.
6. H. Tomoda, S. Saito and S. Shiraishi, *Chem. Lett.*, 1983, **12**, 313-316.
7. N. B. McKeown, in *The Porphyrin Handbook: Phthalocyanines: Synthesis*, ed. K.M. Kadish, K.M. Smith and R. Guilard, Elsevier, 2000, vol. 15, 61.
8. B.D. Berezin, *Coordination Compounds of Porphyrin and Phthalocyanine*, Wiley & Sons, New York, 1981.
9. A. M. Schaffer, M. Gouterman and E. R. Davidson, *Theor. Chim. Acta*, 1973, **30**, 9-30.
10. Y. Chen, M. Hanack, W. J. Blau, D. Dini, Y. Liu, Y. Lin and J. Bai, *J. Mater. Sci.*, 2006, **41**, 2169.
11. V. N. Nemykin and E. A. Lukyanets, *Arkivoc*, 2010, **1**, 136-208.
12. E. A. Lukyanets and V. N. Nemykin, *J. Porphyr. Phthalocyanines*, 2010, **14**, 1-40.
13. K. Sakamoto and E. Ohno-Okumura, *Materials*, 2009, **2**, 1127-1179.
14. D. Dini, M. Hanack, in *The Porphyrin Handbook: Phthalocyanines: Properties and Materials*, ed. K.M. Kadish, K.M. Smith and R. Guilard, Elsevier, 2000, vol. 17, 1.
15. A. P. Lever, in *Advances in Inorganic Chemistry and Radiochemistry*, ed. H.J. Emeléus and A.G. Sharpe, Elsevier, 1965, vol. 7, pp. 27-114.
16. S. Chauhan, P. Kumari and S. Agarwal, *Synthesis*, 2007, **2007**, 3713-3721.
17. P. Godlewska, Y. S. Gerasymchuk, L. Tomachynskii, J. Legendziewicz and J. Hanuza, *Struct. Chem*, 2010, **21**, 461-467.
18. N. Ishikawa, *J. Porphyr. Phthalocyanines*, 2001, **5**, 87-101.
19. H. Wang, N. Kobayashi and J. Jiang, *Chem. Eur. J.*, 2012, **18**, 1047-1049.
20. T. Fukuda, T. Biyajima and N. Kobayashi, *J. Amer. Chem. Soc.*, 2010, **132**, 6278-6279.
21. H. Wang, D. Qi, Z. Xie, W. Cao, K. Wang, H. Shang and J. Jiang, *Chem. Commun.*, 2013, **49**, 889-891.

22. M.J. Stillman, T. Nyokong, in *Phthalocyanines: Properties and Applications*, ed. C.C. Leznoff, and A.B.P. Lever, VCH, New York, 1989, vol. 1, ch. 3, 133.
23. M. Gouterman, in *The Porphyrins*, ed. D. Dolphin, Academic Press, 1978, vol. 3.
24. V. E. Pushkarev, L. G. Tomilova and V. N. Nemykin, *Coord. Chem. Rev.*, 2016, **319**, 110-179.
25. Y. Bian, R. Wang, D. Wang, P. Zhu, R. Li, J. Dou, W. Liu, C. F. Choi, H. S. Chan, C. Ma, D. K. P. Ng and J. Jiang, *Helv. Chim. Acta*, 2004, **87**, 2581-2596.
26. M. Arıcı, C. Bozoğlu, A. Erdoğmuş, A. L. Uğur and A. Koca, *Electrochim. Acta*, 2013, **113**, 668-678.
27. P. P. A. Stuzhin, in *Fluorine in Heterocyclic Chemistry*, ed. V. Nenajdenko, Springer, Cham, 2014, vol. 1, pp. 621-681.
28. R. Li, X. Zhang, P. Zhu, D. K. Ng, N. Kobayashi and J. Jiang, *Inorg. Chem.*, 2006, **45**, 2327-2334.
29. H. Tomoda, S. Saito, S. Ogawa and S. Shiraishi, *Chem. Lett.*, 1980, **9**, 1277-1280.
30. K. Stranius, R. Jacobs, E. Maligaspe, H. Lemmetyinen, N. V. Tkachenko, M. E. Zandler and F. D'Souza, *J. Porphyr. Phthalocyanines*, 2010, **14**, 948-961.
31. T. E. Youssef, *Polyhedron*, 2010, **29**, 1776-1783.
32. J. Janczak and R. Kubiak, *Polyhedron*, 2001, **20**, 2901-2909.
33. A. De Cian, M. Moussavi, J. Fischer and R. Weiss, *Inorg. Chem.*, 1985, **24**, 3162-3167.
34. G. Clarisse and M. Riou, *Inorg. Chim. Acta*, 1987, **130**, 139-144.
35. V. Pushkarev, M. Breusova, E. Shulishov and Y. V. Tomilov, *Russ. Chem. Bull.*, 2005, **54**, 2087-2093.
36. V. Nemykin, V. Chernii and S. Volkov, *J. Chem. Soc., Dalton Trans.*, 1998, 2995-3000.
37. A. Iwase and K. Tanaka, *Electrochim. Acta*, 1990, **35**, 1707-1712.
38. V. Pushkarev, A. Ivanov, I. Zhukov, E. Shulishov and Y. V. Tomilov, *Russ. Chem. Bull.*, 2004, **53**, 554-560.
39. J. Jiang, R. C. Liu, T. C. Mak, T. D. Chan and D. K. Ng, *Polyhedron*, 1997, **16**, 515-520.
40. T. V. Dubinina, K. V. Paramonova, S. A. Trashin, N. E. Borisova, L. G. Tomilova and N. S. Zefirov, *Dalton Trans.*, 2014, **43**, 2799-2809.
41. Y. Liu, K. Shigehara, M. Hara and A. Yamada, *J. Amer. Chem. Soc.*, 1991, **113**, 440-443.
42. L.-C. Liu, C.-H. Tai, A. T. Hu and T.-H. Wei, *J. Porphyr. Phthalocyanines*, 2004, **8**, 984-988.
43. N. Ishikawa and Y. Kaizu, *Chem. Phys. Lett.*, 1993, **203**, 472-476.
44. W. Cao, C. Gao, Y.Q. Zhang, D. Qi, T. Liu, K. Wang, C. Duan, S. Gao, and J. Jiang, *Chem. Sci.*, 2015, **6**, 5947-5954.
45. G. Lu, S. Yan, M. Shi, W. Yu, J. Li, W. Zhu, Z. Ou, and K.M. Kadish, *Chem. Commun.*, 2015, **51**, 2411-2413.
46. G. de la Torre, C. G. Claessens and T. Torres, *Chem. Commun.*, 2007, 2000-2015.
47. A. B. Sorokin, *Chem. Rev.*, 2013, **113**, 8152-8191.
48. G. de la Torre, G. Bottari, U. Hahn and T. Torres, in *Functional Phthalocyanine Molecular Materials*, ed. J. Jiang, Springer, Berlin, Heidelberg, 2010, pp. 1-44.
49. D. Hohnholz, S. Steinbrecher and M. Hanack, *J. Mol. Struct.*, 2000, **521**, 231-237.

50. G. Chaidogiannos, F. Petraki, N. Glezos, S. Kennou and S. Nešpůrek, *Appl. Phys. A*, 2009, **96**, 763-767.

51. N. B. Chaure, J. L. Sosa-Sanchez, A. N. Cammidge, M. J. Cook and A. K. Ray, *Org. Electron.*, 2010, **11**, 434-438.

52. Z. Bao, A. J. Lovinger and J. Brown, *J. Amer. Chem. Soc.*, 1998, **120**, 207-208.

53. L. Li, Q. Tang, H. Li, X. Yang, W. Hu, Y. Song, Z. Shuai, W. Xu, Y. Liu and D. Zhu, *Adv. Mater.*, 2007, **19**, 2613-2617.

54. R. Zeis, T. Siegrist and C. Kloc, *Appl. Phys. Lett.*, 2005, **86**, 022103.

55. H. Jiang, J. Ye, P. Hu, F. Wei, K. Du, N. Wang, T. Ba, S. Feng and C. Kloc, *Sci. Rep.*, 2014, **4**, 7573.

56. A. Giraudeau, F.-R. F. Fan and A. J. Bard, *J. Amer. Chem. Soc.*, 1980, **102**, 5137-5142.

57. J. J. Cid, J. H. Yum, S. R. Jang, M. K. Nazeeruddin, E. Martínez-Ferrero, E. Palomares, J. Ko, M. Grätzel and T. Torres, *Angew. Chem. Int. Ed.*, 2007, **46**, 8358-8362.

58. M. Kimura, H. Nomoto, H. Suzuki, T. Ikeuchi, H. Matsuzaki, T. N. Murakami, A. Furube, N. Masaki, M. J. Griffith and S. Mori, *Chem. Eur. J.*, 2013, **19**, 7496-7502.

59. G. de la Torre, P. Vázquez, F. Agulló-López and T. Torres, *J. Mater. Chem.*, 1998, **8**, 1671-1683.

60. J. Perry, K. Mansour, I.-Y. Lee, X.-L. Wu, P. Bedworth, C.-T. Chen, D. Ng, S. Marder, P. Miles and T. Wada, *Science*, 1996, **273**, 1533-1536.

61. J. S. Shirk, R. G. Pong, S. R. Flom, F. J. Bartoli, M. E. Boyle, and A. W. Snow, *J. Eur. Opt. Soc. A*, 1996, **5**, 701.

62. E. A. Kuzmina, T. V. Dubinina, A. V. Zasedatelev, A. V. Baranikov, M. I. Makedonskaya, T. B. Egorova and L. G. Tomilova, *Polyhedron*, 2017, **135**, 41-48.

63. C. M. Allen, W. M. Sharman and J. E. Van Lier, *J. Porphyr. Phthalocyanines*, 2001, **5**, 161-169.

64. N. Brasseur, R. Ouellet, C. La Madeleine and J. Van Lier, *Br. J. Cancer*, 1999, **80**, 1533-1541.

65. E. D. Baron, C. L. Malbasa, D. Santo-Domingo, P. Fu, J. D. Miller, K. K. Hanneman, A. H. Hsia, N. L. Oleinick, V. C. Colussi and K. D. Cooper, *Lasers Surg. Med.*, 2010, **42**, pp.888-895.

66. M. S. Rodríguez-Morgade, M. Planells, T. Torres, P. Ballester and E. Palomares, *J. Mater. Chem.*, 2008, **18**, 176-181.

67. G. J. Simpson, S. W. Hogan, M. Caffio, C. J. Adams, H. Früchtl, T. van Mourik and R. Schaub, *Nano Lett.*, 2014, **14**, 634-639.

68. J. Kügel, M. Leisegang, M. Böhme, A. Krönlein, A. Sixta and M. Bode, *Nano Lett.*, 2017, **17**, 5106-5112.

69. P. R. O. De Montellano, *Cytochrome P450: Structure, Mechanism, and Biochemistry*, Springer Science & Business Media, 2005.

70. N. Morlanés, K. Takanabe and V. Rodionov, *ACS Catal.*, 2016, **6**, 3092-3095.

71. B. Basu, S. Satapathy, A. K. Bhatnagar, *Catal. Rev.*, 1993, **35**, 571-609.

72. J. E. Lyons and P. E. Ellis Jr, *Appl. Catal. A*, 1992, **84**, L1-L6.

73. R. Raja and P. Ratnasamy, *Appl. Catal. A*, 1997, **158**, L7-L15.

74. M. J. Chen, D. E. Fremgen and J. W. Rathke, *J. Porphyr. Phthalocyanines*, 1998, **2**, 473-482.

75. L. M. González and A. Sorokin, *Tetrahedron Lett.*, 2006, **47**, 6465-6468.

76. H. Miyoshi, *Bull. Chem. Soc. Jpn.*, 1974, **47**, 561-565.

77. M. Evangelisti, J. Bartolomé, L. De Jongh and G. Filoti, *Phys. Rev. B*, 2002, **66**, 144410.

78. R. Sessoli, D. Gatteschi, A. Caneschi and M. Novak, *Nature*, 1993, **365**, 141-143.

79. G. Christou, D. Gatteschi, D. N. Hendrickson and R. Sessoli, *MRS Bull.*, 2000, **25**, 66-71.

80. D. N. Woodruff, R. E. P. Winpenny and R. A. Layfield, *Chem. Rev.*, 2013, **113**, 5110-5148.

81. J. Tang and P. Zhang, in *Lanthanide Single Molecule Magnets*, Springer, Heidelberg, 2015, ch. 2, pp. 41-90.

82. N. Ishikawa, M. Sugita, T. Ishikawa, S.-y. Koshihara and Y. Kaizu, *J. Amer. Chem. Soc.*, 2003, **125**, 8694-8695.

83. M. Gonidec, I. Krivokapic, J. Vidal-Gancedo, E. S. Davies, J. McMaster, S. M. Gorun and J. Veciana, *Inorg. Chem.*, 2013, **52**, 4464-4471.

84. C. R. Ganivet, B. Ballesteros, G. de la Torre, J. M. Clemente-Juan, E. Coronado and T. Torres, *Chem. Eur. J.*, 2013, **19**, 1457-1465.

85. Y. Chen, F. Ma, X. Chen, B. Dong, K. Wang, S. Jiang, C. Wang, X. Chen, D. Qi and H. Sun, *Inorg. Chem.*, 2017, **56**, 13889-13896.

86. Y. Chen, F. Ma, X. Chen, Y. Zhang, H. Wang, K. Wang, D. Qi, H.-L. Sun and J. Jiang, *Inorg. Chem.*, 2019, **58**, 2422-2429.

87. K. Wang, F. Ma, D. Qi, X. Chen, Y. Chen, Y.-C. Chen, H.-L. Sun, M.-L. Tong and J. Jiang, *Inorg. Chem. Front.*, 2018, **5**, 939-943.

88. Y. Chen, F. Ma, Y. Zhang, L. Zhao, K. Wang, D. Qi, H.-L. Sun and J. Jiang, *Inorg. Chem. Front.*, 2018.

89. S. Takamatsu and N. Ishikawa, *Polyhedron*, 2007, **26**, 1859-1862.

90. K. Katoh, H. Isshiki, T. Komeda and M. Yamashita, *Chem. Asian J.*, 2012, **7**, 1154-1169.

91. L. Vitali, S. Fabris, A. M. Conte, S. Brink, M. Ruben, S. Baroni and K. Kern, *Nano Lett.*, 2008, **8**, 3364-3368.

92. S. Stepanow, J. Honolka, P. Gambardella, L. Vitali, N. Abdurakhmanova, T.-C. Tseng, S. Rauschenbach, S. L. Tait, V. Sessi and S. Klyatskaya, *J. Amer. Chem. Soc.*, 2010, **132**, 11900-11901.

93. T. Komeda, H. Isshiki, J. Liu, Y.-F. Zhang, N. Lorente, K. Katoh, B. K. Breedlove and M. Yamashita, *Nat. Commun.*, 2011, **2**, 1-7.

94. A. L. Rizzini, C. Krull, T. Balashov, J. Kavich, A. Mugarza, P. S. Miedema, P. K. Thakur, V. Sessi, S. Klyatskaya and M. Ruben, *Phys. Rev. Lett.*, 2011, **107**, 177205.

95. S. Kyatskaya, J. R. n. Galán Mascarós, L. Bogani, F. Hennrich, M. Kappes, W. Wernsdorfer and M. Ruben, *J. Amer. Chem. Soc.*, 2009, **131**, 15143-15151.

96. V. Korolev, T. Lomova, A. Ramazanova, D. Korolev and E. Mozhzhukhina, *Journal of Organometallic Chemistry*, 2016, **819**, 209-215.

97. A. v. Baeyer, *Ber. Dtsch. Chem. Ges.*, 1872, **5**, 280-282.

98. L. H. Baekeland, US Pat., 942 699, 1907.

99. A. Zinke and E. Ziegler, *Ber. Dtsch. Chem. Ges (A and B Series)*, 1944, **77**, 264-272.

100. C. D. Gutsche, B. Dhawan, K. H. No and R. Muthukrishnan, *J. Amer. Chem. Soc.*, 1981, **103**, 3782-3792.

101. C. D. Gutsche, in *Calixarenes Revisited*, 1998, pp. 185-208.

102. M.-Z. Asfari, V. Böhmer, J. Harrowfield and J. Vicens, *Calixarenes 2001*, Springer Science & Business Media, 2007.

103. C. D. Gutsche, in *Calixarenes Revisited*, The Royal Society of Chemistry, 1998, ch.1, pp. 1-9.

104. J. Cornforth, P. D. A. Hart, G. Nicholls, R. Rees and J. Stock, *Br. J. Pharmacol. Chemother.*, 1955, **10**, 73-86.

105. C. D. Gutsche, B. Dhawan, J. A. Levine, K. H. No and L. J. Bauer, *Tetrahedron*, 1983, **39**, 409-426.

106. H. Kämmerer, G. Happel and F. Caesar, *Makromol. Chem.*, 1972, **162**, 179.

107. M. Conner, V. Janout and S. L. Regen, *J. Amer. Chem. Soc.*, 1991, **113**, 9670-9671.

108. J. Scheerder, R. H. Vreekamp, J. F. Engbersen, W. Verboom, J. P. van Duynhoven and D. N. Reinhoudt, *J. Org. Chem.*, 1996, **61**, 3476-3481.

109. C. D. Gutsche, M. Iqbal and D. Stewart, *J. Org. Chem.*, 1986, **51**, 742-745.

110. C. D. Gutsche and M. Iqbal, *Org. Synth.*, 2003, **68**, 234-234.

111. K. Iwamoto, K. Fujimoto, T. Matsuda and S. Shinkai, *Tetrahedron Lett.*, 1990, **31**, 7169-7172.

112. K. Iwamoto, K. Araki and S. Shinkai, *J. Org. Chem.*, 1991, **56**, 4955-4962.

113. A. Casnati, A. Arduini, E. Ghidini, A. Pochini and R. Ungaro, *Tetrahedron*, 1991, **47**, 2221-2228.

114. J. A. Brunink, W. Verboom, J. F. Engbersen, D. N. Reinhoudt and S. Harkema, *Recl. Trav. Chim. Pays-Bas*, 1992, **111**, 511-516.

115. C. D. Gutsche, J. A. Levine and P. d. Sujeeth, *J. Org. Chem.*, 1985, **50**, 5802-5806.

116. J.-D. Van Loon, W. Verboom and D. Reinhoudt, *Org. Prep. Proced. Int*, 1992, **24**, 437-462.

117. P. Linnane, T. D. James and S. Shinkai, *J. Chem. Soc., Chem. Commun.*, 1995, 1997-1998.

118. K.-S. Paek, H.-J. Kim and S.-K. Chang, *Supramol. Chem.*, 1995, **5**, 83-85.

119. C. D. Gutsche and P. F. Pagoria, *J. Org. Chem.*, 1985, **50**, 5795-5802.

120. S. Shinkai, K. Araki, T. Tsubaki, T. Arimura and O. Manabe, *J. Chem. Soc., Perkin Trans. 1*, 1987, 2297-2299.

121. S. W. Man and J.-F. Nicoud, *Tetrahedron Lett.*, 1993, **34**, 8237-8240.

122. P. A. Scully, T. M. Hamilton and J. L. Bennett, *Org. Lett.*, 2001, **3**, 2741-2744.

123. S. Kumar, H. Chawla and R. Varadarajan, *Tetrahedron Lett.*, 2002, **43**, 7073-7075.

124. Y.-L. Lin, T.-S. Yu, W.-Y. Wang and L.-G. Lin, *Tetrahedron*, 2006, **62**, 6082-6089.

125. F. Grynszpan and S. E. Biali, *Chem. Commun.*, 1996, 195-196.

126. C. Aronica, G. Chastanet, E. Zueva, S. A. Borshch, J. M. Clemente-Juan and D. Luneau, *J. Amer. Chem. Soc.*, 2008, **130**, 2365-2371.

127. G. Karotsis, S. J. Teat, W. Wernsdorfer, S. Piligkos, S. J. Dalgarno and E. K. Brechin, *Angew. Chem.*, 2009, **48**, 8285-8288.

128. M. Czakler, C. Artner, C. Maurer and U. Schubert, *Z. Naturforsch. B*, 2014, **69**, 1253-1259.

129. Hosseini, M., Hall, A., Harrowfield, J., Skelton, B. and White, A., *Chem. Commun.*, 1999, **4**, 373-374.

130. T. Kajiwara, T. Kobashi, R. Shinagawa, T. Ito, S. Takaishi, M. Yamashita and N. Iki, *Eur. J. Inorg. Chem.*, 2006, **2006**, 1765-1770.

131. S. Sanz, R. D. McIntosh, C. M. Beavers, S. J. Teat, M. Evangelisti, E. K. Brechin and S. J. Dalgarno, *Chem. Commun.*, 2012, **48**, 1449-1451.

132. J. Gottfriedsen, *Z. Anorg. Allg. Chem*, 2005, **631**, 2928-2930.

133. F. Gao, L. Cui, Y. Song, Y.-Z. Li and J.-L. Zuo, *Inorg. Chem.*, 2014, **53**, 562-567.

134. S. Sanz, K. Ferreira, R. D. McIntosh, S. J. Dalgarno and E. K. Brechin, *Chem. Commun.*, 2011, **47**, 9042-9044.

135. M. Coletta, R. McLellan, S. Sanz, K. J. Gagnon, S. J. Teat, E. K. Brechin and S. J. Dalgarno, *Chem. Eur. J.*, 2017, **23**, 14073-14079.

136. T.D. Chung, *J. Incl. Phenom.*, 1998, **32**, 179-193.

137. B. T. Zhao, X. M. Zhu, Q. M. Peng, Z.N. Yan, F. Le Derf and M. Sallé, *Open Chem.*, 2011, **9**, 1102.

138. M. H. Lee, Q.-Y. Cao, S. K. Kim, J. L. Sessler and J. S. Kim, *J: Org. Chem.*, 2011, **76**, 870-874.

139. A. J. Evans, S. E. Matthews, A. R. Cowley and P. D. Beer, *Dalton Trans.*, 2003, 4644-4650.

140. P. D. Beer, D. Hesek, J. E. Kingston, D. K. Smith, S. E. Stokes and M. G. Drew, *Organometallics*, 1995, **14**, 3288-3295.

141. P. D. Beer, Z. Chen, A. J. Goulden, A. Grieve, D. Hesek, F. Szemes and T. Wear, *Journal of the Chemical Society, Chem. Commun.*, 1994, 1269-1271.

142. A. Liška, P. Vojtíšek and J. Ludvík, *Chem. Commun.*, 2019, **55**, 2817-2820.

143. A. Liška, M. Rosenkranz, J. Klíma, L. Dunsch, P. Lhoták and J. Ludvík, *Electrochim. Acta*, 2014, **140**, 572-578.

144. R. Vataj, A. Louati, C. Jeunesse and D. Matt, *J. Electroanal. Chem.*, 2004, **565**, 295-299.

145. R. Vataj, H. Ridaoui, A. Louati, V. Gabelica, S. Steyer and D. Matt, *J. Electroanal. Chem.*, 2002, **519**, 123-129.

146. R. Vataj, A. Louati, C. Jeunesse and D. Matt, *Electrochem. Commun.*, 2000, **2**, 769-775.

147. M. Gomez-Kaifer, P. A. Reddy, C. D. Gutsche and L. Echegoyen, *J: Amer: Chem. Soc.*, 1994, **116**, 3580-3587.

148. D. Diamond, *J. Incl. Phenom.*, 1994, **19**, 149-166.

149. R. O. Fuller, G. A. Koutsantonis and M. I. Ogden, *Coord. Chem. Rev.*, 2020, **402**, 213066.

150. R. B. Chaabane, M. Gamoudi, G. Guillaud, C. Jouve, R. Lamartine, A. Bouazizi and H. Maaref, *Sens. Actuators B Chem*, 1996, **31**, 41-44.

151. J. A. Brunink, J. G. Bomer, J. F. Engbersen, W. Verboom and D. N. Reinhoudt, *Sens. Actuators B Chem.*, 1993, **15**, 195-198.

152. I. Yoshida, N. Yamamoto, F. Sagara, K. Ueno, D. Ishii and S. Shinkai, *Chem. Lett.*, 1991, **20**, 2105-2108.

153. B. Bodenant, T. Weil, M. Businelli-Pourcel, F. Fages, B. Barbe, I. Pianet and M. Laguerre, *J. Org. Chem.*, 1999, **64**, 7034-7039.

154. C. Pérez-Jiménez, S. J. Harris and D. Diamond, *J. Mater. Chem.*, 1994, **4**, 145-151.

155. Y. D. Cao, Q. Y. Zheng, C. F. Chen and Z.T. Huang, *Tetrahedron Lett.*, 2003, **44**, 4751-4755.

156. S. Aldoshin, I. Antipin, S. Solov’eva, N. Sanina, D. Korchagin, G. Shilov, F. Mushenok, A. Utenyshev and K. Bozhenko, *J. Mol. Struct.*, 2015, **1081**, 217-223.

157. K. Su, F. Jiang, J. Qian, J. Pang, F. Hu, S. M. Bawaked, M. Mokhtar, S. A. Al-Thabaiti and M. Hong, *CrystEngComm*, 2015, **17**, 1750-1753.

158. G. Karotsis, S. Kennedy, S. J. Teat, C. M. Beavers, D. A. Fowler, J. J. Morales, M. Evangelisti, S. J. Dalgarno and E. K. Brechin, *J. Amer. Chem. Soc.*, 2010, **132**, 12983-12990.

159. Y. Bi, G. Xu, W. Liao, S. Du, R. Deng and B. Wang, *Sci. China Chem.*, 2012, **55**, 967-972.

160. C. M. Liu, D. Q. Zhang, X. Hao, D. B. Zhu, *Cryst. Growth Des.*, 2012, **12**, 2948-2954.

161. J. Y. Ge, Z. Chen, H. Y. Wang, H. Wang, P. Wang, X. Duan and D. Huo, *New J. Chem.*, 2018, **42**, 17968-17974.

162. S. Shinkai, Y. Shirahama, T. Tsubaki and O. Manabe, *J. Chem. Soc. Perkin Trans. 1*, 1989, 1859-1860.

163. P. Molenveld, S. Kapsabelis, J. F. Engbersen and D. N. Reinhoudt, *J. Amer. Chem. Soc.*, 1997, **119**, 2948-2949.

164. P. Molenveld, W. M. Stikvoort, H. Kooijman, A. L. Spek, J. F. Engbersen and D. N. Reinhoudt, *J. Org. Chem.*, 1999, **64**, 3896-3906.

165. R. Cacciapaglia, A. Casnati, L. Mandolini, D. N. Reinhoudt, R. Salvio, A. Sartori and R. Ungaro, *J. Org. Chem.*, 2005, **70**, 5398-5402.

166. A. Dondoni, A. Marra, M. C. Scherrmann, A. Casnati, F. Sansone and R. Ungaro, *Chem. Eur. J.*, 1997, **3**, 1774-1782.

167. S. Kolusheva, R. Zadmard, T. Schrader and R. Jelinek, *J. Amer. Chem. Soc.*, 2006, **128**, 13592-13598.

168. A. Zanotti-Gerosa, E. Solari, L. Giannini, C. Floriani, A. Chiesi-Villa and C. Rizzoli, *J. Amer. Chem. Soc.*, 1998, **120**, 437-438.

169. A. Massa, A. D'Ambrosi, A. Proto and A. Scettri, *Tetrahedron Lett.*, 2001, **42**, 1995-1998.

170. L. Monnereau, D. Sémeril, D. Matt and L. Toupet, *Chem. Eur. J.*, 2010, **16**, 9237-9247.

171. S. B. Nimse and T. Kim, *Chem. Soc. Rev.*, 2013, **42**, 366-386.

172. R. V. Rodik, V. I. Boyko and V. I. Kalchenko, *Curr. Med. Chem.*, 2009, **16**, 1630-1655.

173. R. P. Dings, M. C. Miller, I. Nesmelova, L. Astorgues-Xerri, N. Kumar, M. Serova, X. Chen, E. Raymond, T. R. Hoye and K. H. Mayo, *J. Med. Chem.*, 2012, **55**, 5121-5129.

174. F. Nasuhi Pur and K. A. Dilmaghani, *J. Coord. Chem.*, 2014, **67**, 440-448.

175. A. Casnati, M. Fabbi, N. Pelizzi, A. Pochini, F. Sansone, R. Unguro, E. Di Modugno and G. Tarzia, *Bioorg. Med. Chem. Lett.*, 1996, **6**, 2699-2704.

176. K. Rajavelu and P. Rajakumar, *J. Mater. Chem. B*, 2015, **3**, 3340-3350.

177. F. Perret, A. N. Lazar and A. W. Coleman, *Chem. Commun.*, 2006, 2425-2438.

178. M. T. Pope and A. Müller, *Angew. Chem. Int. Ed.*, 1991, **30**, 34-48.

179. J. Berzelius, *Pogg. Ann*, 1826, **6**, 369-371.

180. J. F. Keggin, *Nature*, 1933, **132**, 351-351.

181. J. F. Keggin, *Nature*, 1933, **131**, 908-909.

182. A. R. Kampf, J. M. Hughes, B. P. Nash and J. Marty, *Am. Mineral.*, 2017, **102**, 461-465.

183. J. J. Borrás-Almenar, E. Coronado, A. Müller and M. Pope, *Poly Oxometalate Molecular Science*, Springer Science & Business Media, 2003.

184. M. T. Pope, *Heteropoly and Isopolyoxometalates*: *Inorganic Chemistry Concepts*, Springer-Verlag Berlin Heidelberg, 1983, vol. 8.

185. L. C. Baker and J. S. Figgis, *J. Amer. Chem. Soc.*, 1970, **92**, 3794-3797.

186. I. A. Weinstock, J. J. Cowan, E. M. Barbuzzi, H. Zeng and C. L. Hill, *J. Amer. Chem. Soc.*, 1999, **121**, 4608-4617.

187. D. Laurencin, A. Proust and H. Gérard, *Inorg: Chem.*, 2008, **47**, 7888-7893.

188. M. Sadakane and E. Steckhan, *Chem: Rev:*, 1998, **98**, 219-238.

189. M. T. Pope and G. M. Varga Jr, *Inorg. Chem.*, 1966, **5**, 1249-1254.

190. J. H. Kyle, *Journal of the Chemical Society, Dalton Trans.*, 1983, 2609-2612.

191. S.-T. Zheng and G.-Y. Yang, *Chem. Soc. Rev.*, 2012, **41**, 7623-7646.

192. B. S. Bassil and U. Kortz, *Z. Anorg. Allg. Chem.*, 2010, **636**, 2222-2231.

193. C. Brevard, R. Schimpf, G. Tourne and C. M. Tourne, *J. Amer. Chem. Soc.*, 1983, **105**, 7059-7063.

194. N. Honma, K. Kusaka and T. Ozeki, *Chem. Commun.*, 2002, 2896-2897.

195. S. Himeno, M. Takamoto and T. Ueda, *Bull. Chem. Soc. Jpn.*, 2005, **78**, 1463-1468.

196. J. Li, J. Wang, L. Zhang, X. Sang and W. You, *J. Coord. Chem.*, 2017, **70**, 2950-2957.

197. V. Lahootun, J. Karcher, C. Courillon, F. Launay, K. Mijares, E. Maatta and A. Proust, *Eur. J. Inorg. Chem.*, 2008, **2008**, 4899-4905.

198. A. C. Estrada, I. C. Santos, M. M. Simões, M. G. P. Neves, J. A. Cavaleiro and A. M. Cavaleiro, *Appl. Catal. A*, 2011, **392**, 28-35.

199. L. San Felices, P. Vitoria, J. M. Gutiérrez-Zorrilla, L. Lezama and S. Reinoso, *Inorg. Chem.*, 2006, **45**, 7748-7757.

200. X. Li, Y. Ren, Z. Weng, B. Yue and H. He, *Chem. Commun.*, 2020, **56**, 2324-2327.

201. M. Sokolov, E. Chubarova, E. Peresypkina, A. Virovets and V. Fedin, *Russ. Chem. Bull.*, 2007, **56**, 220-224.

202. S. Zhang, Y. Wang, J. Zhao, P. Ma, J. Wang and J. Niu, *Dalton Trans.*, 2012, **41**, 3764-3772.

203. J. Iijima, H. Naruke and T. Sanji, *RSC Adv.*, 2016, **6**, 91494-91507.

204. R. Ho and W. J. Klemperer, *J. Amer. Chem. Soc.*, 1978, **100**, 6772-6774.

205. A. Falber, B. P. Burton-Pye, I. Radivojevic, L. Todaro, R. Saleh, L. C. Francesconi and C. M. Drain, *Eur. J. Inorg. Chem.*, 2009, **2009**, 2459-2466.

206. I. Radivojevic, K. Ithisuphalap, B. P. Burton-Pye, R. Saleh, L. C. Francesconi and C. M. Drain, *RSC Adv.*, 2013, **3**, 2174-2177.

207. W. Cañón-Mancisidor, M. Zapata-Lizama, P. Hermosilla-Ibáñez, C. Cruz, D. Venegas-Yazigi and G.M. Espallargas, *Chem. Commun.*, 2019, **55**, 14992-14995.

208. N. V. Izarova and P. Kögerler, in *Trends in Polyoxometalates Research*, ed. L. Ruhlmann and D. Schaming, Nova Science Publishers, New York, 2015, ch. 6, pp. 121-149.

209. J. T. Rhule, C. L. Hill, D. A. Judd and R. F. Schinazi, *Chem. Rev.*, 1998, **98**, 327-358.

210. D. L. Long, R. Tsunashima and L. Cronin, 2010, *Angew. Chem. Int. Ed.*, **49**, 1736-1758.

211. S.-S. Wang and G.-Y. Yang, *Chem. Rev.*, 2015, **115**, 4893-4962.

212. K. Y. Monakhov, M. Moors and P. Kögerler, Polyoxometalate Chemistry, in *Adv. Inorg. Chem.*, ed. R. van Eldik and L. Cronin, Academic Press, Elsevier, Amsterdam, 2017, vol. 69, pp. 251-286

213. J. Kaur, K. Griffin, B. Harrison and I. Kozhevnikov, *J. Catal.*, 2002, **208**, 448-455.

214. A. Yoshida, S. Hikichi and N. Mizuno, *J. Organomet. Chem.*, 2007, **692**, 455-459.

215. P. Shringarpure, K. Patel and A. Patel, *J. Clust. Sci.*, 2011, **22**, 587-601.

216. K. Kamata, K. Yonehara, Y. Nakagawa, K. Uehara and N. Mizuno, *Nat. Chem.*, 2010, **2**, 478-483.

217. O. Kholdeeva, M. Vanina, M. Timofeeva, R. Maksimovskaya, T. Trubitsina, M. Melgunov, E. Burgina, J. Mrowiec-Bialon, A. Jarzebski and C. L. Hill, *J. Catal.*, 2004, **226**, 363-371.

218. L. Dermeche, N. Salhi, S. Hocine, R. Thouvenot and C. Rabia, *J. Mol. Catal. A Chem.*, 2012, **356**, 29-35.

219. Y. Guo and C. Hu, *J. Mol. Catal. A Chem.*, 2007, **262**, 136-148.

220. E. Papaconstantinou, *Chem. Soc. Rev.*, 1989, **18**, 1-31.

221. P. Lei, C. Chen, J. Yang, W. Ma, J. Zhao, L. Zang, *Environ. Sci. Technol.*, 2005, **39**, 8466-8474.

222. A. Troupis, A. Hiskia, E. Papaconstantinou, *Environ. Sci. Technol.*, 2002, **36**, 5355-5362.

223. Y. V. Geletii, B. Botar, P. Kögerler, D. A. Hillesheim, D. G. Musaev and C. L. Hill, *Angew. Chem.*, 2008, **47**, 3896-3899.

224. Y. V. Geletii, Z. Huang, Y. Hou, D. G. Musaev, T. Lian and C. L. Hill, *J. Amer. Chem. Soc.*, 2009, **131**, 7522-7523.

225. M. Orlandi, R. Argazzi, A. Sartorel, M. Carraro, G. Scorrano, M. Bonchio and F. Scandola, *Chem. Commun.*, 2010, **46**, 3152-3154.

226. Q. Yin, J. M. Tan, C. Besson, Y. V. Geletii, D. G. Musaev, A. E. Kuznetsov, Z. Luo, K. I. Hardcastle and C. L. Hill, *Science*, 2010, **328**, 342-345.

227. Z. Huang, Z. Luo, Y. V. Geletii, J. W. Vickers, Q. Yin, D. Wu, Y. Hou, Y. Ding, J. Song and D. G. Musaev, *J. Amer. Chem. Soc.*, 2011, **133**, 2068-2071.

228. F. M. Toma, A. Sartorel, M. Iurlo, M. Carraro, P. Parisse, C. Maccato, S. Rapino, B. R. Gonzalez, H. Amenitsch and T. Da Ros, L. Casalis, *Nat. Chem.*, 2010, **2**, 826-831.

229. M. Quintana, A. M. López, S. Rapino, F. M. Toma, M. Iurlo, M. Carraro, A. Sartorel, C. Maccato, X. Ke and C. Bittencourt and T. Da Ros, *ACS Nano*, 2013, **7**, 811-817.

230. H. Lv, J. Song, H. Zhu, Y. V. Geletii, J. Bacsa, C. Zhao, T. Lian, D. G. Musaev and C. L. Hill, *J. Catal.*, 2013, **307**, 48-54.

231. K. Suzuki, F. Tang, Y. Kikukawa, K. Yamaguchi and N. Mizuno, *Chem. Lett.*, 2014, **43**, 1429-1431.

232. S. Berardi, M. Carraro, M. Iglesias, A. Sartorel, G. Scorrano, M. Albrecht and M. Bonchio, *Chem. Eur. J.*, 2010, **16**, 10662-10666.

233. V. Kogan, Z. Aizenshtat, R. Popovitz-Biro and R. Neumann, *Org. Lett.*, 2002, **4**, 3529-3532.

234. C. Ritchie, A. Ferguson, H. Nojiri, H. N. Miras, Y. F. Song, D. L. Long, E. Burkholder, M. Murrie, P. Kögerler, E. K. Brechin and L. Cronin, *Angew. Chem.*, 2008, **47**, 5609-5612.

235. X. Fang, P. Kögerler, M. Speldrich, H. Schilder and M. Luban, *Chem. Commun.*, 2012, **48**, 1218-1220.

236. M. Ibrahim, Y. Lan, B. S. Bassil, Y. Xiang, A. Suchopar, A. K. Powell and U. Kortz, *Angew. Chem. Int. Ed.*, 2011, **50**, 4708-4711.

237. A. Giusti, G. Charron, S. Mazerat, J. D. Compain, P. Mialane, A. Dolbecq, E. Rivière, W. Wernsdorfer, R. Ngo Biboum and B. Keita, and L. Nadjo, *Angew. Chem. Int. Ed.*, 2009, **48**, 4949-4952.

238. M. A. AlDamen, J. M. Clemente-Juan, E. Coronado, C. Martí-Gastaldo and A. Gaita-Ariño, *J. Amer. Chem. Soc.*, 2008, **130**, 8874-8875.

239. M. A. AlDamen, S. Cardona-Serra, J. M. Clemente-Juan, E. Coronado, A. Gaita-Arino, C. Marti-Gastaldo, F. Luis and O. Montero, *Inorg. Chem.*, 2009, **48**, 3467-3479.

240. S. Cardona-Serra, J. Clemente-Juan, E. Coronado, A. Gaita-Ariño, A. Camón, M. Evangelisti, F. Luis, M. J. Martínez-Pérez and J. Sesé, *J. Amer. Chem. Soc.*, 2012, **134**, 14982-14990.

241. M. J. Martínez-Pérez, O. Montero, M. Evangelisti, F. Luis, J. Sesé, S. Cardona-Serra and E. Coronado, *Adv. Mater.*, 2012, **24**, 4301-4305.

242. M. Martínez-Pérez, S. Cardona-Serra, C. Schlegel, F. Moro, P. Alonso, H. Prima-García, J. Clemente-Juan, M. Evangelisti, A. Gaita-Ariño and J. Sesé and J. Van. Slageren, *Phys. Rev. Lett.*, 2012, **108**, 247213.

243. J. J. Baldoví, Y. Duan, C. Bustos, S. Cardona-Serra, P. Gouzerh, R. Villanneau, G. Gontard, J. M. Clemente-Juan, A. Gaita-Ariño, C. Giménez-Saiz, A. Proust and E. Coronado, *Dalton Trans.*, 2016, **45**, 16653-16660.

244. N. Kawasaki, H. Wang, R. Nakanishi, S. Hamanaka, R. Kitaura, H. Shinohara, T. Yokoyama, H. Yoshikawa and K. Awaga, *Angew. Chem.*, 2011, **50**, 3471-3474.

245. H. Li, S. Pang, S. Wu, X. Feng, K. Müllen and C. Bubeck, *J. Amer. Chem. Soc.*, 2011, **133**, 9423-9429.

246. B. Wang, L.-H. Bi and L.-X. Wu, *J. Mater. Chem.*, 2011, **21**, 69-71.

247. R. Tsunashima, D.-L. Long, T. Endo, S.-i. Noro, T. Akutagawa, T. Nakamura, R. Q. Cabrera, P. F. McMillan, P. Kögerler and L. Cronin, *Phys. Chem. Chem. Phys.*, 2011, **13**, 7295-7297.

248. T. Yamase, *J. Mater. Chem.*, 2005, **15**, 4773-4782.

249. S. Mitsui, A. Ogata, H. Yanagie, H. Kasano, T. Hisa, T. Yamase, M. Eriguchi, *Biomed. Pharmacother.*, 2006, **60**, 353-358.

250. A. Ogata, H. Yanagie, E. Ishikawa, Y. Morishita, S. Mitsui, A. Yamashita, K. Hasumi, S. Takamoto, T. Yamase and M. Eriguchi, *Br. J. Cancer*, 2008, **98**, 399-409.

251. T. Yamase, N. Fukuda, Y. Tajima, *Biol. Pharm. Bull.*, 1996, **19**, 459-465.

252. N. Yamamoto, D. Schols, E. De Clercq, Z. Debyser, R. Pauwels, J. Balzarini, H. Nakashima, M. Baba, M. Hosoya and R. Snoeck, *Mol. Pharmacol.*, 1992, **42**, 1109-1117.

Chapter 2.

Hybrid double-decker lanthanide(III) complexes based on phthalocyanine and polyoxotungstate

2.1 Introduction

The interdisciplinary field of single-molecule magnets (SMMs) finds potential applications in high data storage density, quantum computation, electronic sensors, and molecular spintronics.[1-4] The bistable magnetic states in these SMMs could store the information of about 30 terabits per square centimeter. This represents the storage of up to 10^4 more information than current conventional magnets, whose spin contribution comes from the collective behavior of metal centers instead of single molecules.[5] The bistability arises due to the presence of an energy barrier to the magnetization reversal, generally represented as $U_{\mathrm{eff}} = DS^2$ for integer and $D(S^2 - ¼)$ for half-integer spins. The initial approach to enhance this energy barrier focused on producing polymetallic 3d-complexes with a high spin ground state (S), arising from the magnetic exchange of the metal centers.[6] However, since the report of the magnetic properties of $NBu_4[Tb(Pc)_2]$ in 2003, the focus has been progressively shifting towards the study of monometallic Ln-based complexes due to the higher energy barrier and blocking temperature originating from a single-metal ion.[7-9] In addition to the magnetic anisotropy of the free ion, experimental and theoretical studies revealed the clear influence of ligand-field on the anisotropy barrier, as the low lying spin-orbit multiplets of 4f-ion are affected by subtle changes in the coordination environment.[10] So far, the strategic molecular design based on the electron density of 4f-ion proved to be successful in producing SMMs with high anisotropy barrier, especially the complexes comprising of Tb(III) or Dy(III) sandwiched between phthalocyanine or cyclopentadienyl ligands having D_{4d} or D_{5h} molecular symmetries.[11]

Phthalocyanine (Pc) is an efficient ligand to study the structure-property relationship due to the ease of derivatization of the ring that results in modification of the ligand-field. In this regard, besides the peripheral substitution in sandwich-type $[Ln(Pc)_2]$ complexes, which significantly enhanced the anisotropy barrier,[12-15] few reports also described the replacement of one phthalocyanine ring by other aromatic ligands to reinforce the properties of two different units in double-decker complexes. For example, coordination of porphyrin or Schiff base ligands with lanthanide(III) phthalocyanine exhibited out-of-phase ac signals similar to

$[Ln(Pc)_2]$ complexes.[16,19] The coordination environment of tetrapyrrole ligand has also been modified by replacing nitrogen of pyrrole with oxygen or sulfur atoms. These furan and thiophene modified complexes showed substantial enhancement of the anisotropy barrier than the parent complex due to different charge distribution on the ligand.[20]

Polyoxometalates (POMs), anionic metal-oxo clusters (M usually Mo, W, V, Nb and Ta in their highest oxidation state), interact with organic molecules forming a range of hybrid materials with unique electronic properties. There are plenty of reports on donor-acceptor molecules formed by electrostatic interactions of anionic-POM and porphyrin or phthalocyanine units exhibiting efficient photocatalytic or photovoltaic response.[21] However, there are just four molecules constituted by POM, Pc, and metal ion through a metal-ligand bond, and these examples utilized lacunary POMs due to the high reactivity of oxygen atoms present at the defect site of polyanions. The first two molecules include the discrete hybrid structures containing a monolacunary phosphotungstate $[PW_{11}O_{39}]^{7-}$ and a phthalocyanine with diamagnetic Hf(IV) and Zr(IV) ions. The central metal atom in these sandwiched complexes couples the light-absorbing and electronic properties of the tetrapyrrole ligand with the unique properties of the polyoxotungstate (POT) unit.[24,25] Recently, two hybrid materials containing one and two units of a late lanthanide (Yb^{III})-phthalocyanine coordinated to the lacunary polyoxovanadate $[HV_{12}O_{32}(Cl)]^{4-}$ have been reported. The two-dimensional self-assembled monolayers of these hybrid materials on gold surface displayed electrical conductivity, however, no SMM behavior was observed for these systems.[26]

This chapter describes the synthesis, spectroscopic characterization, and magnetic studies of a new family of lanthanide double-decker complexes with the general formula $[Ln^{III}(H_{16}Pc)(PW_{11}O_{39})]^{6-}$, representing the first example of these scaffolds combined through Tb(III) and Dy(III) ions. The choice of ligands was driven due to the excellent coordination abilities and reported magnetic properties with lanthanide metal ions. Furthermore, the β-protons of Pc-ring were replaced with electron-donating (di-*iso*-propylphenoxy) and electron-withdrawing (fluorine) groups to form derivatized hybrid complexes. These groups are supposed to change the electron density around the lanthanide center due to different donating ability of derivatized Pc-ligand, which in turn affects the electronic and magnetic properties of the hybrid complexes.

2.2 Results and discussion

A general structural representation of hybrid complexes $(NBu_4)_4H_2[Dy^{III}(H_{16}Pc)(PW_{11}O_{39})]$ **[2],** $(NBu_4)_4H_2[Tb^{III}(H_{16}Pc)(PW_{11}O_{39})]$ **[3],** $(NBu_4)_6[Dy^{III}(i\mathrm{Pr}_2Pc)(PW_{11}O_{39})]$ **[4],** $(NBu_4)_6[Tb^{III}(i\mathrm{Pr}_2Pc)(PW_{11}O_{39})]$ **[5],** $(NBu_4)_6[Dy^{III}(F_8Pc)(PW_{11}O_{39})]$ **[6],** and $(NBu_4)_6[Tb^{III}(F_8Pc)(PW_{11}O_{39})]$ **[7]** is shown in **Fig 2.1**. These compounds were characterized by single-crystal XRD, elemental analysis, infrared spectroscopy, electrospray ionization mass spectrometry, thermogravimetric analysis, UV-Vis spectroscopy, and cyclic voltammetry. The initial synthesis of $(NBu_4)_4H_2[Y^{III}(H_{16}Pc)(PW_{11}O_{39})]$ **[1]** permitted a fast screening of the synthetic conditions (reactants stoichiometry, solvent selection, heating regime, use of base and countercation addition) by NMR before synthesizing complexes **[2–7]**. The magnetic properties of complexes **[2–7]** were studied using SQUID magnetometry.

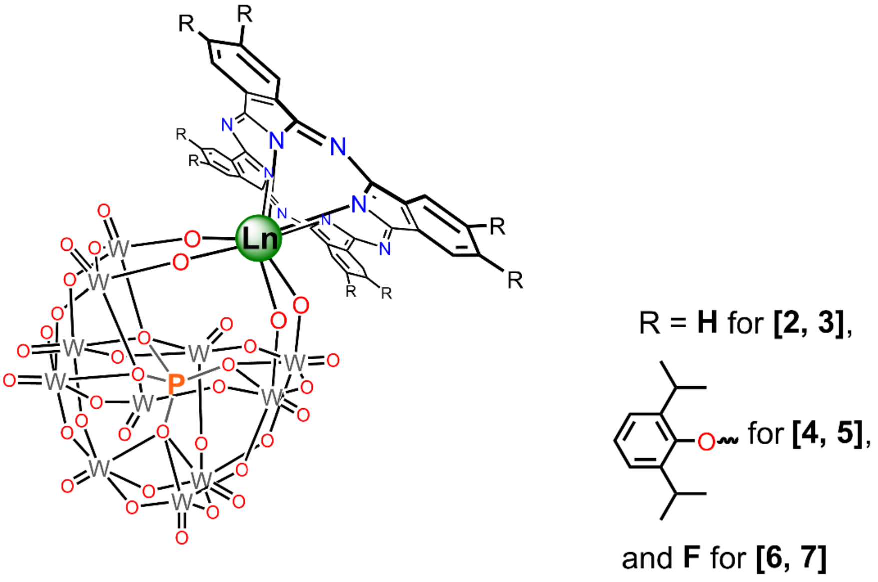

Fig 2.1 Structural representation of the main skeleton of complexes **[2–7]**, along with the nature of R-groups on the periphery of the Pc-ring.

Synthetic procedure

Tetra-*n*-butylammonium (TBA) salt of monolacunary phosphotungstate $(NBu_4)_4H_3[PW_{11}O_{39}]$ was synthesized as described in the literature.[27,28] Lanthanide(III) single-decker of unsubstituted phthalocyanine $[Ln^{III}(H_{16}Pc)(OAc)]$ and octa(2,6-di-*iso*-propylphenoxy) phthalocyanine $[Ln^{III}(i\mathrm{Pr}_2Pc)(OAc)]$ were obtained using the similar procedure reported for the synthesis of single-decker compounds.[29] The newly synthesized, lanthanide(III) single-decker of octafluorinated phthalocyanine were isolated in three steps

(Scheme 2.1). In the first step, a magnesium complex of octafluorinated phthalocyanine [$Mg^{II}F_8Pc$] was synthesized by heating a 4:1 mixture of 4,5-difluorophthalonitrile (previously synthesized as described in the literature[30]) and magnesium(II) acetate in a vacuum-sealed tube at 270 °C. In the second step, the demetallation of [$Mg^{II}F_8Pc$] with concentrated sulfuric acid produced free-base octafluorinated phthalocyanine [F_8Pc]. The final step involved the synthesis of lanthanide(III) single-decker of octafluorinated phthalocyanine [$Ln^{III}(F_8Pc)(OAc)(DBU)$] by reacting [$F_8Pc$] with lanthanide(III) acetate in presence of 1,8-diazabicyclo[5.4.0]undec-7-ene (DBU) in refluxing *o*-dichlorobenzene (*o*-DCB) followed by chromatographic purification. DBU, as a base, hinders the formation of sandwiched complexes of phthalocyanine by binding to the lanthanide center.[31] The use of any nucleophilic base or solvents like hexanol or octanol was avoided, as the fluorine atoms, being electron-deficient, are susceptible to nucleophilic substitution.[32,33]

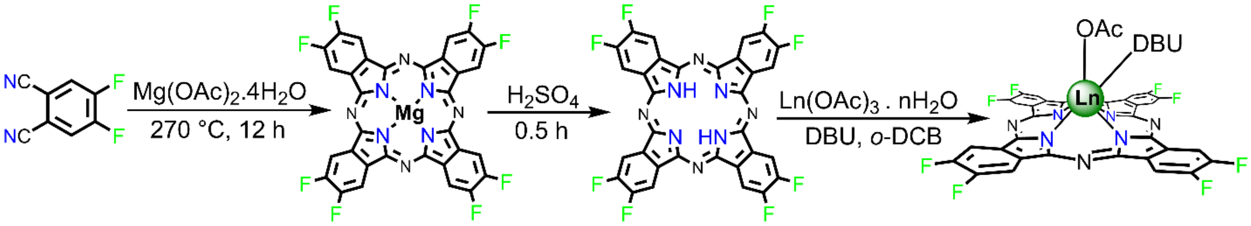

Scheme 2.1 Synthetic approach to lanthanide(III) single-decker of octafluorinated phthalocyanine.

It should be noted that the derivatization of Pc-ring with fluorine groups at these positions and its further coordination with Dy(III) or Tb(III) centers has never been reported so far. There is just a single report describing lanthanide(III) double-decker phthalocyanine substituted with perfluoro-*iso*-propyl groups at β- and fluorine at α-positions on the Pc-ring (Ln = Tb, Lu).[13] This is perhaps due to the difficulty of getting pure products in good yield and limited solubility of free-base fluorinated phthalocyanine.

All hybrid complexes [$Ln^{III}(Pc)(PW_{11}O_{39})]^{6-}$ **[2–7]** were isolated by heating the respective single-decker phthalocyanine [$Ln^{III}(Pc)(OAc)$], $(NBu_4)_4H_3[PW_{11}O_{39}]$, tetra-*n*-butylammonium bromide (NBu_4Br), and triethylamine (NEt_3) in a solvent mixture of CH_2Cl_2:CH_3CN:CH_3OH overnight at 50 °C. The resulting reaction mixture was filtered and evaporated to dryness under reduced pressure. The product was dissolved in a minimum amount of dichloromethane and, precipitation with pentane yielded a green solid. After filtration, the solid was further purified by column chromatography.

NMR spectroscopy

The diamagnetic yttrium compound **[1]** was initially synthesized to develop the synthetic strategy towards the construction of the more challenging hybrid complexes $[Ln^{III}(Pc)(PW_{11}O_{39})]^{6-}$, Ln = Tb and Dy **[2–7]**, as it permits to monitor easily the purity of the sample by NMR in comparison to paramagnetic Tb- and Dy-based complexes, which hamper any possible characterization by NMR. In this regard, the use of ^{1}H- and ^{31}P-NMR and comparison to the starting materials ($[Y^{III}(H_{16}Pc)(OAc)]$ and $(NBu_4)_4H_3[PW_{11}O_{39}]$ ascertained the purity of the crude before further purification by chromatographic column.

The most characteristic signals in ^{1}H-NMR of complex **[1]** are the presence of two broad singlets observed in the aromatic region 9.61–9.20 and 8.34–8.05 ppm, corresponding to the non-peripheral (α) and peripheral (β) protons of Pc-ring respectively **(Fig 2.3)**.The broadening of Pc-aromatic signals and observation of a "hump" on both signals indicate that coordination of $[Y^{III}(H_{16}Pc)(OAc)]$ to $[PW_{11}O_{39}]^{7-}$ results in the tilting of Pc-ring to one side, creating the two halves of the complex. The shift of Pc-protons in the hybrid complex depends upon their proximity to POT unit. Therefore, in comparison to $[Y^{III}(H_{16}Pc)(OAc)]$ (**Fig 2.2**), the protons at the alpha position are shifted from 9.41 ppm to 9.50 ppm upon coordination to $[PW_{11}O_{39}]^{7-}$, while the chemical shift of H^{β} remains almost unchanged as they are farther away from POT unit than H^{α}. The integration of signals between 0.9 ppm to 3 ppm confirms the presence of four TBA countercations. The results of elemental analyses also confirm the presence of four TBA and two protons as countercations in **[1]**.

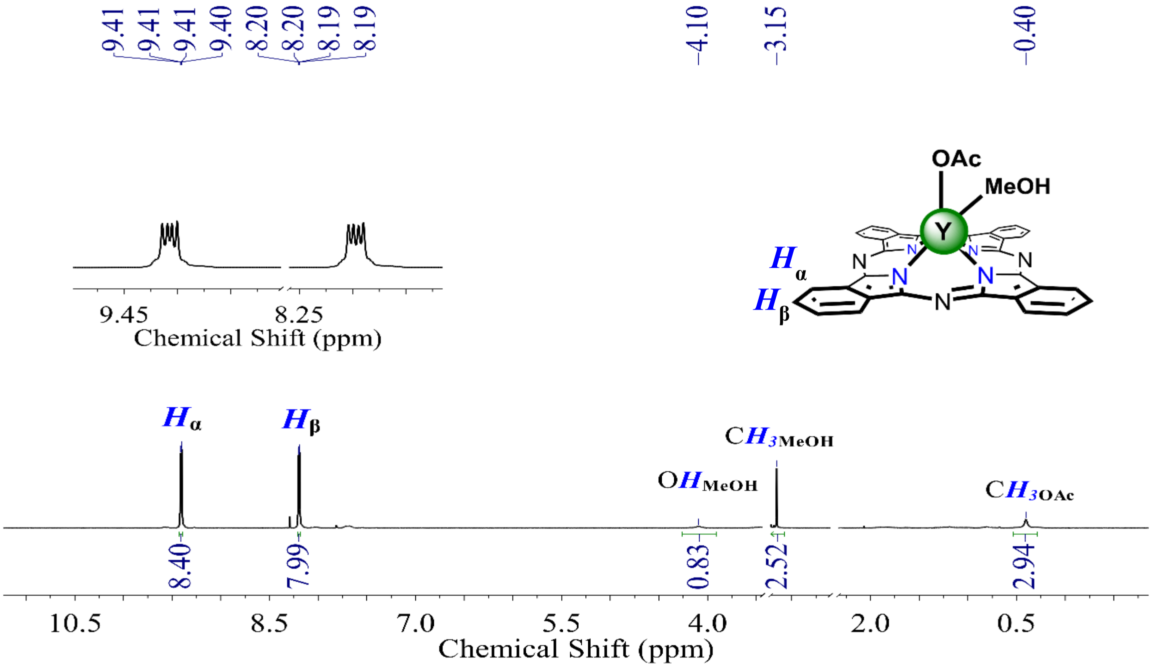

Fig 2.2 ^{1}H-NMR spectrum of [$Y^{III}(H_{16}Pc)(OAc)$]. The signals corresponding to residual solvents ($(CD_3)_2SO$ and water) have been removed for clarity.

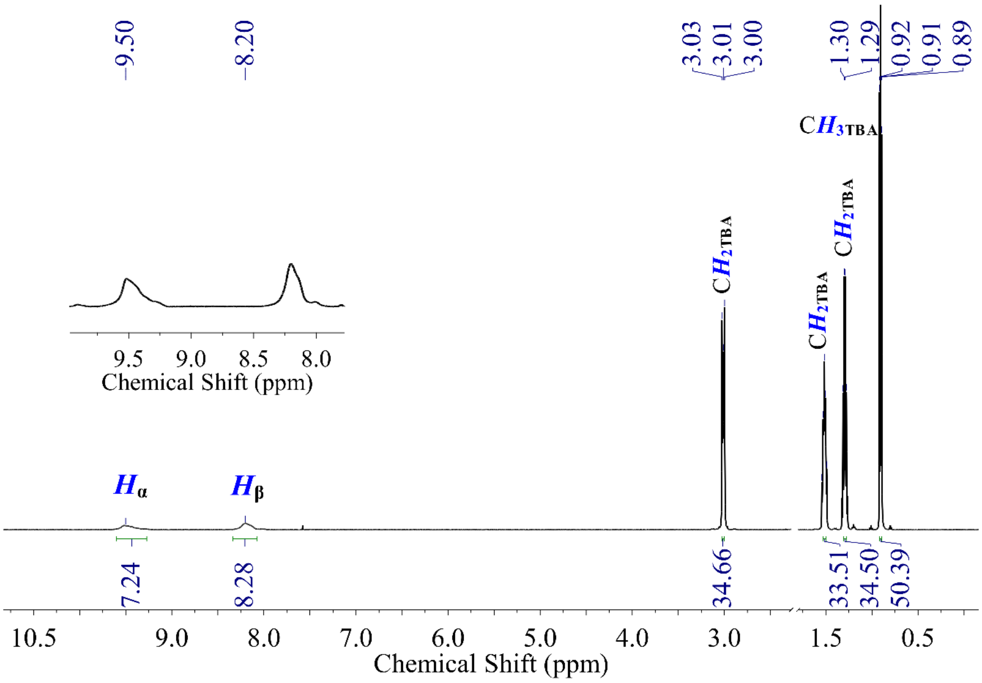

Fig 2.3 ^{1}H-NMR spectrum of complex **[1]**. The signals corresponding to residual solvents (CD_3CN and water) have been removed for clarity. TBA stands for tetra-*n*-butylammonium.

The presence of the inner phosphate group in $[PW_{11}O_{39}]^{7-}$ facilitates the characterization of the complex by ^{31}P-NMR and, to detect the possible impurities derived from the POT substrate.

In complex **[1]**, a shift in ^{31}P-NMR signal from –13.24 ppm to –14.64 ppm is observed upon coordination of $[PW_{11}O_{39}]^{7-}$ unit to $[Y(H_{16}Pc)]$ as shown in **Fig 2.4**.

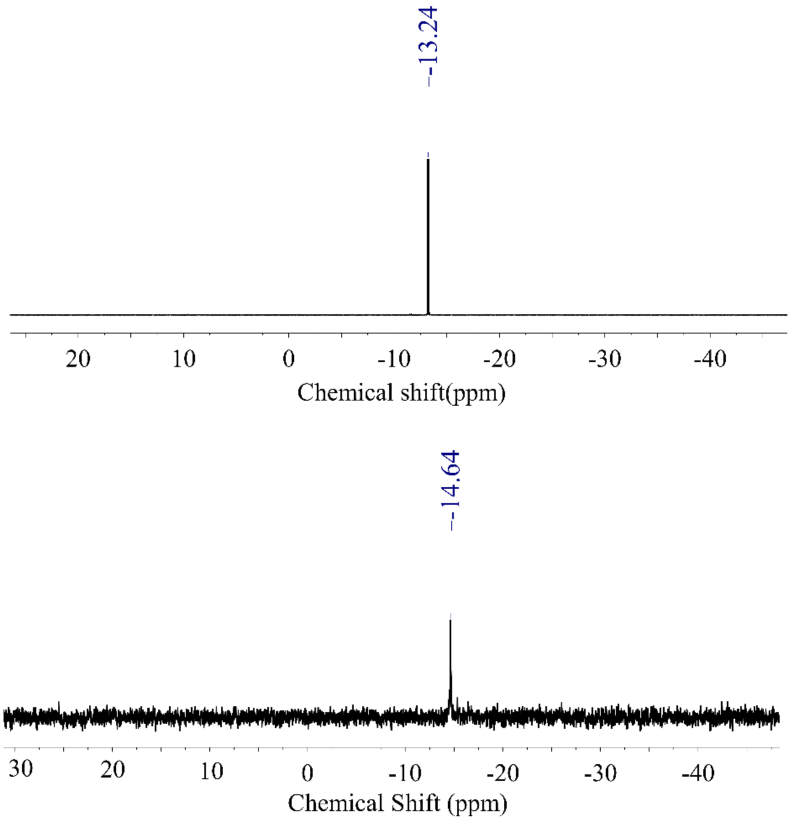

Fig 2.4 ^{31}P-NMR spectrum of **(top)** $(NBu_4)_4H_3[PW_{11}O_{39}]$ and **(bottom)** complex **[1]** in CD_3CN.

The ^{19}F-NMR spectra were recorded for the compounds containing fluorine substituents on the periphery of Pc-ring as it is a sensitive nucleus and provides a good tool to study the purity of the compounds. The spectrum of free-base $[F_8Pc]$ shows a triplet at –128.30 ppm which is slightly shifted to the signal of starting material 4,5-difluorophthalonitrile, appearing at –125.7 ppm **(Fig 2.5)**. The presence of a triplet for the fluorine atoms is due to similar coupling constants $^{3}J_{F\text{–}F}$ and $^{3}J_{H\text{–}F}$. The presence of a hump feature in the spectrum is not obvious; it could be attributed to a background signal.

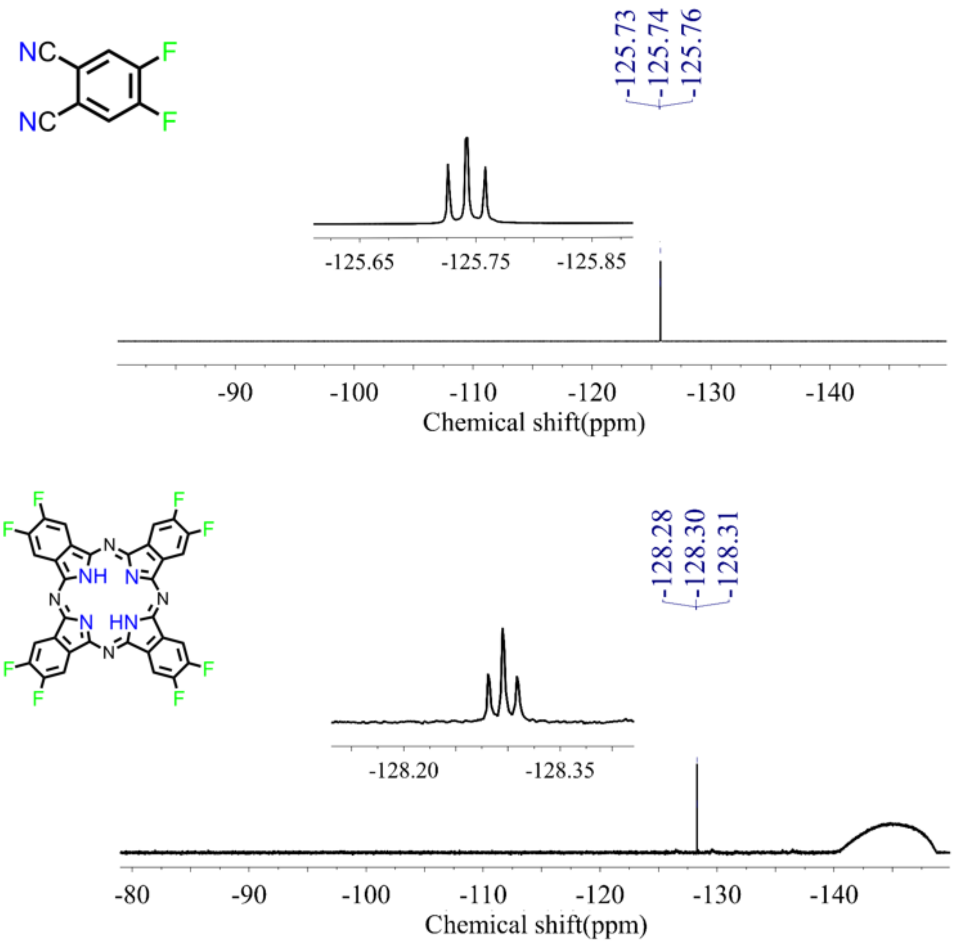

Fig 2.5 ^{19}F-NMR spectra of **(top)** 4,5-difluorophthalonitrile and **(bottom)** free-base F$_8$Pc in (CD$_3$)$_2$SO.

^{19}F-NMR spectra of Dy(III) and Tb(III) octafluorinated single-decker complexes exhibit two broad singlets for the peripheral fluorine between –140 to –160 ppm as shown in **Fig 2.6**. The two different chemical shifts of peripheral fluorine atoms in comparison to the free-base F$_8$Pc can be related to the different environment produced by the coordination of the metal ion to two different ligands (acetate and DBU molecule) in the complexes.

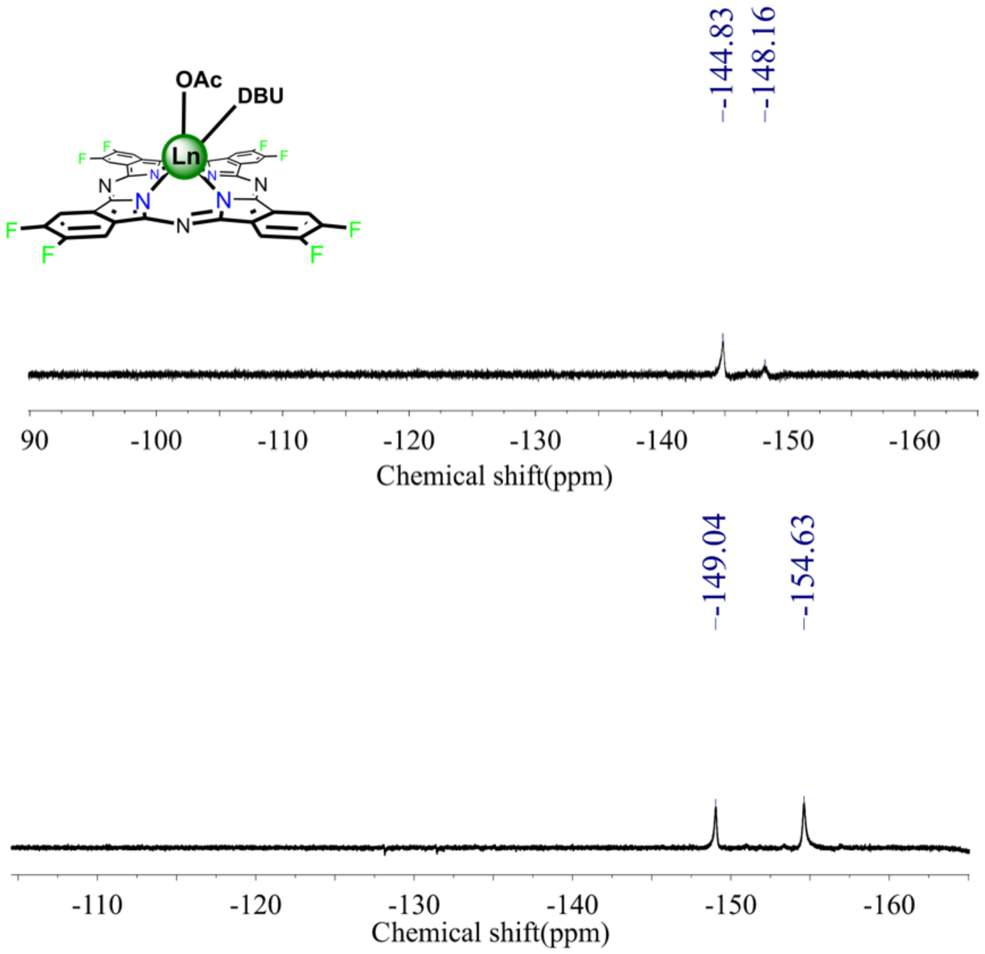

Fig 2.6 ^{19}F-NMR spectra of single-decker **(top)** [Dy^{III}(F$_8$Pc)(OAc)(DBU)] and **(bottom)** [Tb^{III}(F$_8$Pc)(OAc)(DBU)] in $(CD_3)_2SO$.

The ^{1}H-, ^{31}P-, and ^{19}F-NMR spectra of hybrid complexes containing Dy(III) and Tb(III) display no signals related to the complexes, even on scanning over a large chemical shift window, due to the fast relaxation rates induced by the paramagnetic lanthanide centers. However, further characterization by elemental analysis, ESI-MS, IR, UV-Vis, CV, and SQUID magnetometry corroborated the purity of the hybrid complexes **[2–7]**.

Crystal structures

Different solvents, countercations, and crystallization conditions were tried to get single crystals of all synthesized complexes. However, crystals suitable for X-ray diffraction were obtained just for complex **[1]** and **[3]**. The data were collected, solved and refined by Dr. Gary. S. Nichol (School of Chemistry, The University of Edinburgh, UK).

Single green plate-shaped crystals of the complex **[1]** with the formula $(NBu_4)_4H_2[Y^{III}(H_{16}Pc)(PW_{11}O_{39})]$ were isolated by slow evaporation of a dichloromethane solution at room temperature. X-ray quality crystals of complex **[3]** were obtained by cation exchange using triethylammonium cations. Slow evaporation of a dichloromethane solution produced blue-green plate-shaped crystals of $(NBu_4)_2(NHEt_3)_2H_2[Tb^{III}(H_{16}Pc)(PW_{11}O_{39})]$. Both complexes crystallized in the monoclinic system. The space group is $P2_1/c$ for **[1]** and $C2/m$ for **[3]**.

In the crystal structure of complex **[3] (Fig 2.7)**, Tb(III) ion is bonded to the four nitrogen atoms of Pc-ring and four oxygen atoms at the defect site of $[PW_{11}O_{39}]^{7-}$ unit, in a coordination sphere of slightly distorted square antiprism. The Pc- and POT-units are rotated by a twist angle (φ) of 44.44° and 46.08° to their eclipsed positions. The Tb–N distances (2.452, 2.465, and 2.467 Å) are almost similar to that in $[Tb(Pc)_2]^-$ complex (average 2.435 Å).[34] In the molecular structure, $[PW_{11}O_{39}]^{7-}$ unit contains an inner PO_4^{3-} (P–O: 1.478–1.547 Å), whose oxygen atoms are connected to the eleven tungsten(VI) ions via three μ_3-O and one μ_2-O_P sites (W–O: 2.390–2.498 Å). On the periphery, the tungsten(VI) ions are linked by μ_2-O^{2-} ions (W–O: 1.792–2.077 Å), and the remaining coordination sites are capped by oxo groups (W–O: 1.684–1.704 Å). The bond lengths of Tb–O vary between 2.361 and 2.389 Å, which are close to those reported for $[Tb^{III}(\alpha\text{-}PW_{11}O_{39})_2]^{11-}$ (average 2.38 Å).[35] The angle between coordinating N_4 and O_4 plane is 5.73°, indicating the tilting of Pc-ring towards $[PW_{11}O_{39}]^{7-}$ on one side, breaking the symmetry of the complex. This effect is also observed in the ^{1}H-NMR spectrum of complex **[1]** by the presence of broad singlets featuring a hump. The structural core and connectivity around Y(III) in complex **[1]** is similar to **[3]**, hence the same interpretation can be applied. The crystallographic parameters, selected bond lengths, and bond angles for both complexes are given in **Table 2.1** and **2.2** respectively.

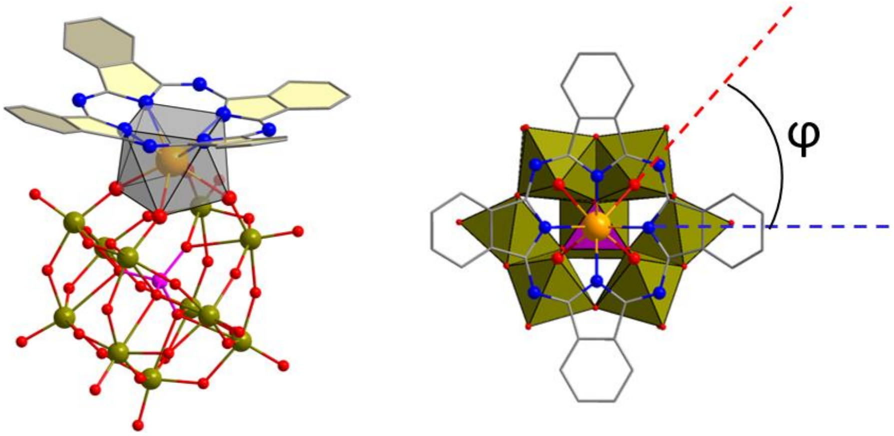

Fig 2.7 Molecular structure of $[Tb^{III}(H_{16}Pc)(PW_{11}O_{39})]^{6-}$ anion in **[3]** **(left)** ball and stick style with distorted square-antiprismatic TbO_4N_4 coordination polyhedron highlighted in transparent grey and **(right)** top view highlighting the POT in a polyhedral model and twist angle representation as the rotation of coordination squares from their eclipsed position. Color code: Tb(III) = orange, W = dark yellow, P = pink, O = red, N = blue, C = grey. Hydrogen atoms are omitted for clarity. Benzene and pyrrole units of the Pc-ring are shown in transparent yellow to better illustrate the bent Pc geometry.

The molecular packing in crystals of complex **[1]** and **[3]** is shown in **Fig 2.8**. In the complexes, both units (Pc and POT) are arranged face to face due to π-π interactions between the Pc-rings of adjacent molecules whereas, the interactions between two adjacent layers of molecules are mediated by countercations. The shortest Y···Y distance is 10.569 Å, while Tb···Tb is 12.259 Å, which is large enough to avoid the intermolecular magnetic interactions according to the previous observations.[19,20]

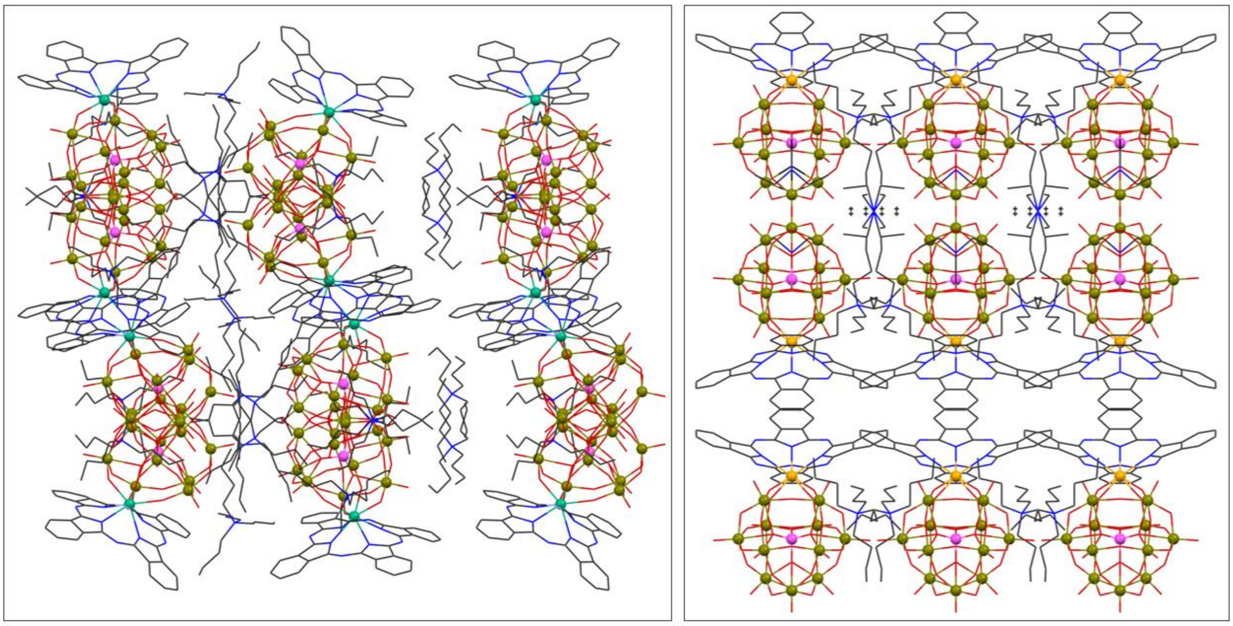

Fig 2.8 Molecular packing of **(left)** complex **[1]** viewed along the c-axis and **(right)** complex **[3]** viewed along the a-axis. Color code: Y(III) = cyan, Tb(III) = orange, W = dark yellow, P = pink, O = red, N = blue, C = black. Hydrogen atoms are omitted for clarity.

Refinement special details

Complex **[1]** contains two molecules per asymmetric unit. The countercations were modeled using the fragment database of Olex2. Seven out of eight TBA countercations were identified as discrete atoms. The eighth TBA and 3.5 molecules of dichloromethane per asymmetric unit were handled using the solvent masking procedure in Olex2. In addition to $(NBu_4)^+$ cations, the complex contains two protons as countercations (four per asymmetric unit) as indicated by elemental analysis and other characterization methods. Two of these protons are included as N–bound H atoms in phthalocyanine core, due to the presence of likely N–H···O hydrogen bonds evidenced by the short N···O distance. The position of the other two protons could not be assigned even by hydrogen bond interaction deduction and so are not included in the model. However, they are included in the total chemical formula. For complex **[3]**, one triethylammonium $(Et_3NH)^+$ countercation was located on the symmetry element. The ethyl groups of a second highly disordered $(Et_3NH)^+$ were modeled with occupancies linked using SUMP in ShelXL in such a way that the total number of carbon and hydrogen sum up correctly. The two protons as countercations could not be located in any chemically reasonable location and so are not included in the model. However, the two protons and six dichloromethane molecules, which are handled with solvent masking, are included in the total chemical formula. The shape of the Pc-ring was controlled by geometric restraints and constraints.

Table 2.1 Crystallographic details for **[1]** and **[3]**.

$[Ln^{III}(H_{16}Pc)(PW_{11}O_{39})]^{6-}$	**1**	**3**
Formula	$C_{195.5}H_{331}N_{24}O_{78}P_2W_{22}Y_2Cl_7$	$C_{82}Cl_{12}H_{134}N_{12}O_{39}PTbW_{11}$
Formula Weight	8798.43	4549.64
Color	Green	Blue
Shape	Plate	Plate
Size/mm^3	0.04×0.04×0.02	0.05×0.02×0.02
T/K	100.0	100.15
Crystal System	Monoclinic	Monoclinic
Space Group	$P2_1/c$	$C2/m$
μ//mm^{-1}	9.036	9.767
a/Å	29.676(4)	22.5917(14)
b/Å	30.709(4)	21.7413(12)

c/Å	29.725(4)	26.2648(15)
α/°	90	90
β/°	91.830(2)	95.3550(10)
γ/°	90	90
V/Å^3	27074(5)	12844.3(13)
Z	4	4
Z'	1	0.5
Wavelength/Å	0.6889	0.6889
Radiation type	Synchrotron	Synchrotron
θ_{min}/°	0.665	1.263
θ_{max}/°	20.222	20.294
Measured Reflections	213327	53920
Unique Reflections	28548	7102
Reflections with $I > 2\sigma(I)$	18075	5609
R_{int}	0.1538	0.0833
Parameters	2727	585
Restraints	4697	931
Largest Peak	2.249	1.798
Deepest Hole	–1.590	–0.814
GooF	1.028	1.110
wR_2 (all data)	0.2344	0.1507
wR_2	0.2095	0.1470
R_1 (all data)	0.1264	0.0595
R_1	0.0869	0.0509
CCDC number	1993274	1993275

Table 2.2 Selected bond lengths and angles in **[1]** and **[3]**.

Bond type	**1** **Bond length (Å)**	**3** **Bond length (Å)**
P–μ_3–O	1.50 (2) – 1.56 (2)	1.531 (10) – 1.547 (13)
P–μ_2–O	1.53 (2)	1.478 (13)
W–μ_3–O (W–O–P)	2.38 (2) – 2.50 (2)	2.406 (10) – 2.498 (10)
W–μ_2–O (W–O–P)	2.345 (19) – 2.38 (2)	2.390 (9)
W–μ_2–O (W–O–W)	1.81 (2) – 2.09 (2)	1.792 (10) – 2.077 (9)
W=O_t	1.63 (2) – 1.75 (2)	1.684 (11) – 1.704 (15)
Ln–O	2.283 (19) – 2.37 (2)	2.361(10) – 2.389 (10)
Ln–N	2.44 (3) – 2.47 (3)	2.452(16) – 2.467 (16)
Ln–mean N_4 plane	1.44	1.42
Ln–mean O_4 plane	1.20	1.23

Mass spectrometry

All hybrid complexes were characterized by ESI-MS, as the energy of MALDI-MS was large enough to break the complexes. **Fig 2.9** shows the spectra of complexes **[1–3]** in negative-ion mode. The peaks are corresponding to triple and double negatively charged species formed by the fragmentation and loss of different countercations from the main skeleton, where M stands for $[Ln^{III}(H_{16}Pc)(PW_{11}O_{39})]^{6-}$.

In complex **[1]**, the peak at *m/z* = 1174.5303 corresponds to $[M + 1NBu_4 + 2H]^{3-}$, which appears due to the loss of three TBA countercations from the molecule with the formula $(NBu_4)_4H_2[Y^{III}(H_{16}Pc)(PW_{11}O_{39})]$ as indicated by elemental analysis. The complex **[2]** and **[3]** also show the triple negatively charged highest intensity peak at 1198.873 and 1197.872 respectively, with the same fragmentation as in complex **[1]**, *i.e.* due to the loss of three TBA from the molecule. The other highlighted peak at 1093.7730 in the spectrum of **[1]** belongs to $[M + 3H]^{3-}$, *i.e.*, due to the loss of four TBA and uptake of one proton. Similarly, the peak at 1278.9644 in **[2]**, and 1917.9511 in **[3]** are related to $[M + 2NBu_4 + 1H]^{3-}$ and $[M + 2NBu_4 + 2H]^{2-}$ respectively. The experimental and calculated isotopic distributions of the observed peaks are perfectly matching with the deviation of ~0.0005 *m/z* as shown in the inset of **Fig 2.9**. For the sake of comparison, the relative intensity of experimental isotopic pattern is adjusted to 50 %.

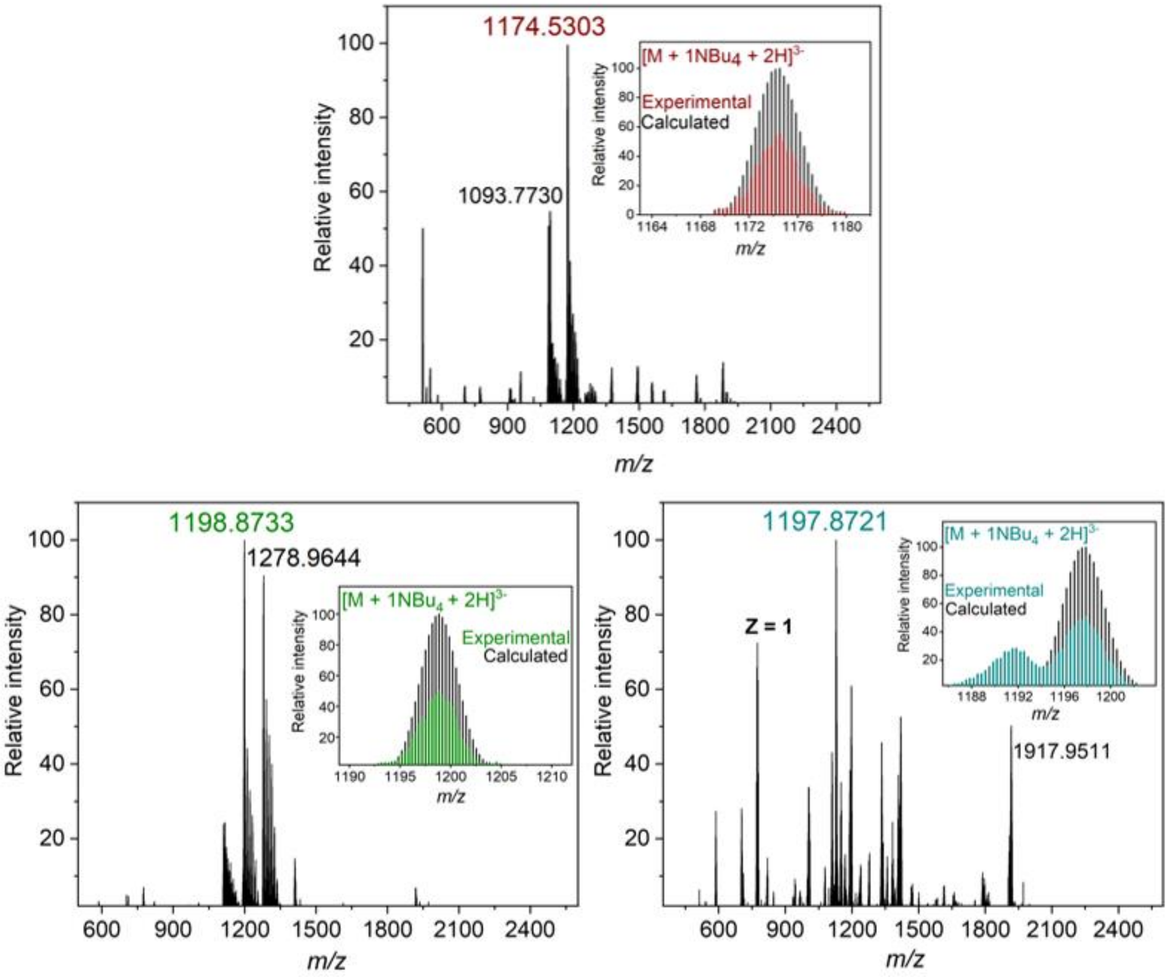

Fig 2.9 ESI-MS spectra of **(top)** complex **[1]**, **(bottom left)** complex **[2]**, and **(bottom right)** complex **[3]**. The insets show the comparison of experimental (adjusted to 50 %) and calculated isotopic pattern of the highest intensity peak.

The ESI-MS of complex **[4]** and **[5]** in the negative-ion mode also show the characteristic peaks corresponding to triple negatively charged species resulting from the loss of different countercations from complexes with the formula $(NBu_4)_6[Ln^{III}(iPr_2Pc)(PW_{11}O_{39})]$ deduced from all characterization data. The peaks at m/z = 1588.1017 and 1587.1026 in the spectrum of **[4]** and **[5]** respectively, correspond to $[M + 3H]^{3-}$, which results from the loss of six TBA and uptake of three protons during the ionization process. M in the figure stands for $[Ln^{III}(iPr_2Pc)(PW_{11}O_{39})]^{6-}$. The other highlighted peaks at m/z = 1668.5262 and 1667.5277 are related to the $[M + 1NBu_4 + 2H]^{3-}$, and are the result of the loss of five TBA and uptake of two protons by the respective molecules. The isotopic distribution of the experimentally observed and calculated peaks perfectly matches, with the deviation less than ~0.001 *m/z* as shown in the inset of **Fig 2.10**.

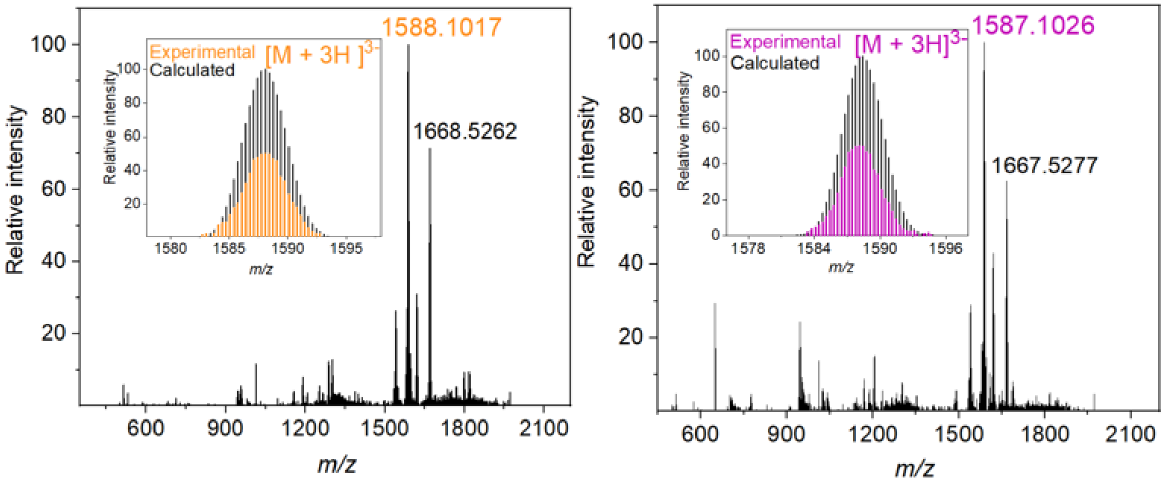

Fig 2.10 ESI-MS spectra of **(left)** complex **[4]** and **(right)** complex **[5]**. The inset shows the comparison of experimental (adjusted to 50 %) and calculated isotopic pattern of the highest intensity peak.

The MALDI-MS of octafluorinated magnesium phthalocyanine in positive-ion mode displays the main peak at *m/z* = 680.057 corresponding to $[M - 1e]^+$, where M = $Mg^{II}F_8Pc$. The spectrum of free-base $[F_8Pc]$ also shows one expected molecular ion peak related to $[F_8Pc - 1H]^-$ in negative-ion mode. ESI-MS of $[Ln^{III}(F_8Pc)(OAc)(DBU)]$ with Tb and Dy in negative-ion mode show $[M - DBU + OAc]^-$ as a main fragment, where $M = [Ln^{III}(F_8Pc)(OAc)(DBU)]$. A small peak corresponding to the sandwiched-complex $[Ln^{III}(F_8Pc)_2]$ is also observed, likely to be the result of the ionization process rather than an impurity in the sample. The experimental and calculated isotopic distribution of the observed peaks perfectly matches as shown in the inset of **Fig 2.11**.

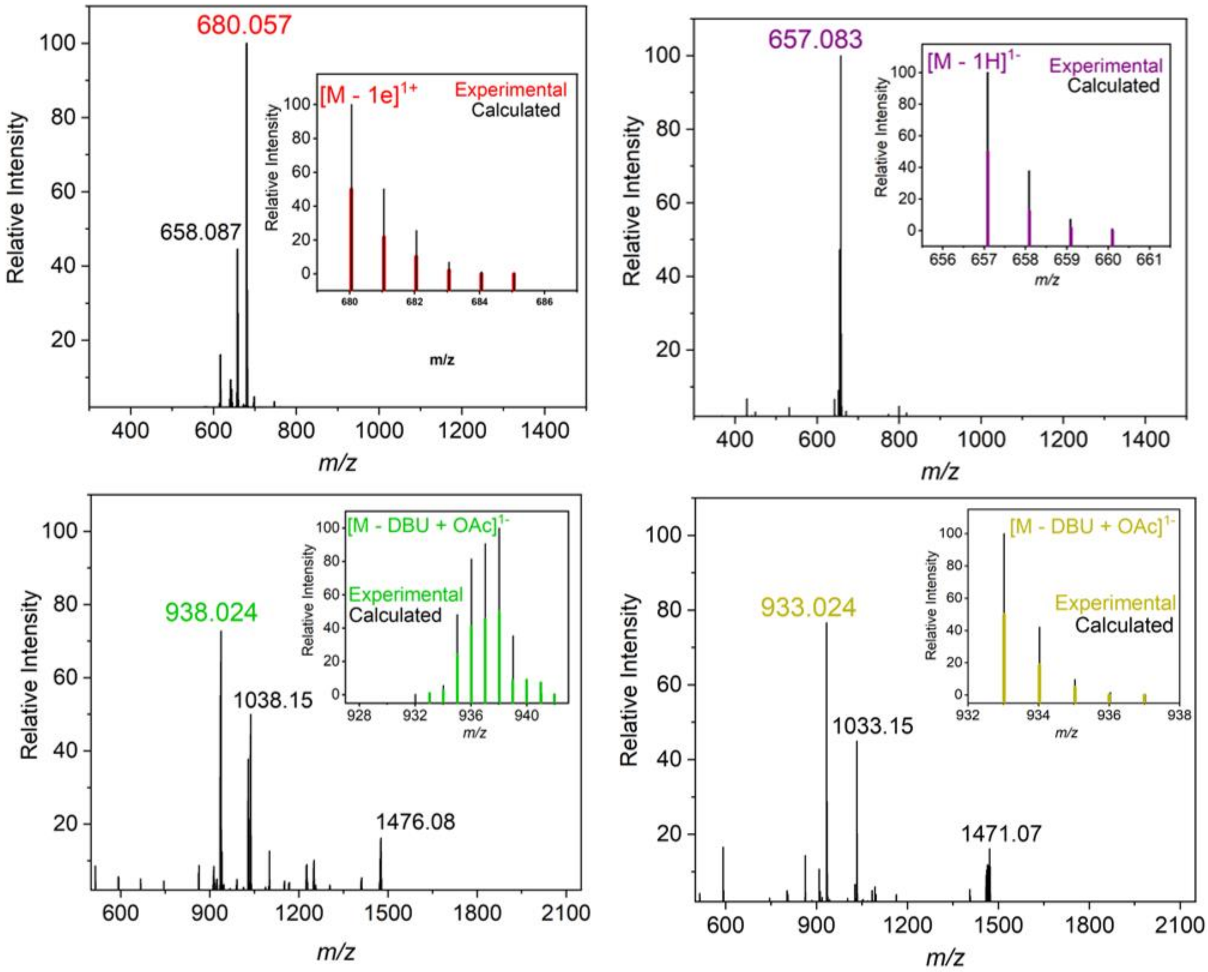

Fig 2.11 MALDI-MS spectra of **(top left)** [$Mg^{II}F_8Pc$] and **(top right)** [F_8Pc]. ESI-MS spectra of **(bottom left)** [$Dy^{III}(F_8Pc)(OAc)(DBU)$ and **(bottom right)** [$Tb^{III}(F_8Pc)(OAc)(DBU)$]. The inset shows the comparison of experimental (adjusted to 50 %) and calculated isotopic pattern of highest intensity peak.

The ESI-MS spectra of **[6]** and **[7]** display the triple negatively charged species resulting from the fragmentation of hybrid complexes with the formula $(NBu_4)_6[Ln^{III}(F_8Pc)(PW_{11}O_{39})]$ as indicated by all characterization data. In the spectrum of complex **[6]**, the peak at $m/z = 1327.2712$ corresponds to $[M + 2NBu_4 + 1H]^{3-}$, where M stands for $[Ln^{III}(F_8Pc)(PW_{11}O_{39})]^{6-}$. This peak arises from the loss of four TBA and the uptake of one proton. Similarly, the highest intensity peak at 1245.5109 in the spectrum of complex **[7]** results from the loss of five TBA and uptake of two protons. The isotopic distribution of experimental peaks deviates from the calculated pattern by less than 0.003 *m/z* as shown in the inset of **Fig 2.12**.

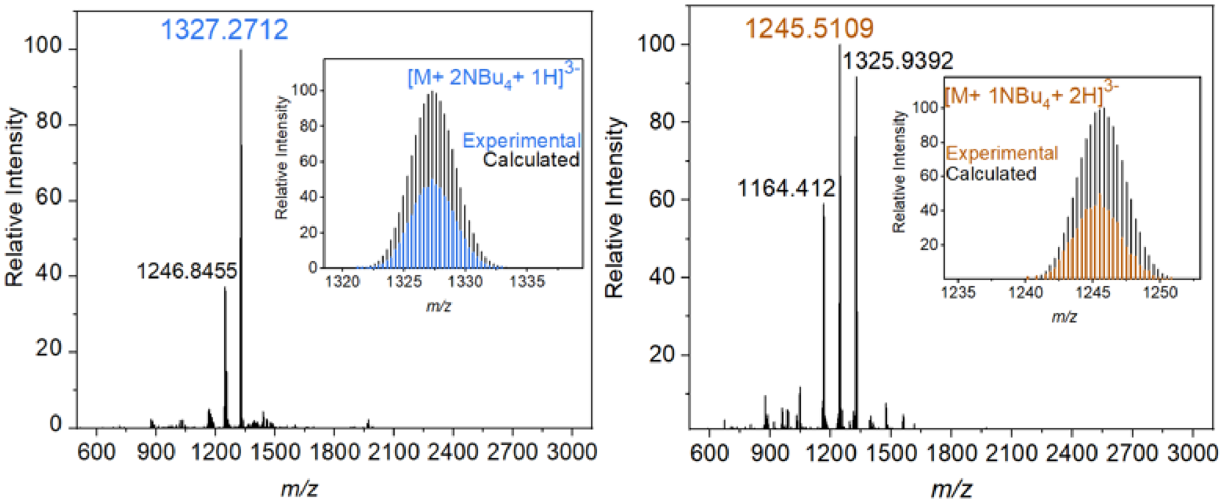

Fig 2.12 ESI-MS spectra of **(left)** complex **[6]** and **(right)** complex **[7]**. The inset shows the comparison of experimental (adjusted to 50 %) and calculated isotopic pattern of the highest intensity peak.

Infrared spectroscopy

Complexes of Pc exhibit three characteristic features in IR spectra: out-of-plane C–H bending vibrations at ~730 cm^{-1}, in-plane C–H bending vibrations and isoindole breathing between 1000–1300 cm^{-1}, isoindole and benzene stretching between 1300–1650 cm^{-1}.[36] On the other hand, W–O and P–O vibrations in $[PW_{11}O_{39}]^{7-}$ appear in the region of 750–950 cm^{-1} and 1050–1100 cm^{-1} respectively.[37]

The FT-IR spectra of complexes **[1–3]** display the peaks stemming from the vibrations in $H_{16}Pc$, $[PW_{11}O_{39}]^{7-}$, and countercations. **Fig 2.13** shows the comparison of FT-IR spectra of hybrid complexes **[1–3]** and starting materials. The spectrum of $[Y^{III}(H_{16}Pc)(OAc)]$ single-decker complex is shown as the analogous complexes (with Dy and Tb) show similar vibrations. The spectra of **[1–3]** are very similar and the small shift amongst them is due to the coordination of “$H_{16}Pc$” and “$PW_{11}O_{39}$” to the different metal centers. The bands of C–H stretching vibrations are observed between 2960–2853 cm^{-1}. The spectra contain the peaks for υ(C–C), υ(C–N), δ(CH_3), and δ(CH_2) in the fingerprint region in 1600–1150 cm^{-1} range. Similar to the spectrum of $[PW_{11}O_{39}]^{7-}$, two characteristic peaks at ~1100 and 1056 cm^{-1} are attributed to P–O stretching vibrations. The signal at ~952 cm^{-1} corresponds to terminal W=O vibrations and the peaks related to (W–O$_{\text{corner}}$–W) and (W–O$_{\text{bridging}}$–W) appear at ~888 cm^{-1} and 800 cm^{-1} respectively. However, a strong C–H out-of-plane bending vibration of Pc-ring at ~730 cm^{-1} dominates a medium intensity band of (W–O$_{\text{bridging}}$–W), which appears at 750 cm^{-1} in the spectrum of $[PW_{11}O_{39}]^{7-}$.

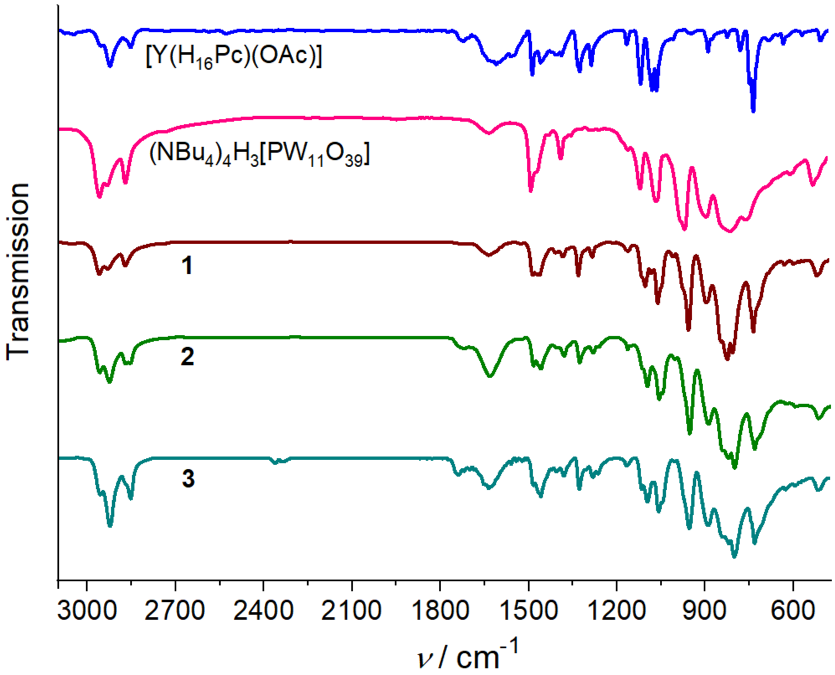

Fig 2.13 FT-IR spectra of complexes **[1–3]** and the starting materials $(NBu_4)_4H_3[PW_{11}O_{39}]$ and $[Y^{III}(H_{16}Pc)(OAc)]$ as a representative single-decker complex.

FT-IR spectra of **[4]** and **[5]** are similar and display the vibration arising from *i*Pr_2Pc, $[PW_{11}O_{39}]^{7-}$, and countercations. The comparative study of vibrations coming from **[4]**, **[5]**, and starting materials is shown in **Fig 2.15**. The hybrid complexes display a slight shift in the peaks as compare to the starting single-decker of phthalocyanine and POT units. The spectra of **[4]** and **[5]** display C–H stretching vibrations between 2960–2857 cm^{-1}. Signals between 1650 cm^{-1} and 1300 cm^{-1} are originating from pyrrole stretching [C–C and C–N] of *i*Pr_2Pc-ring, methyl, and methylene bending vibrations of TBA cations. As compare to unsubstituted analogues, the spectra of **[4]** and **[5]** exhibit more intense C–H stretching (~2960–2857 cm^{-1}) and CH_3 bending (~1390 cm^{-1}) vibrations due to di-*iso*-propylphenoxy groups on the periphery of Pc-ring. The vibrations corresponding to C–O–C stretch of the *i*Pr_2Pc fragment appear at ~1185 and 1265 cm^{-1}. Similar to complexes **[1–3]**, the peaks between 1000 and 1100 cm^{-1} are attributed to P–O vibrations of the POT fragment. The set of vibrations related to $(W{=}O_{terminal})$, $(W{-}O_{corner}{-}W)$, and $(W{-}O_{bridging}{-}W)$ appear at ~954 cm^{-1}, ~885 cm^{-1}, and ~820–745 cm^{-1} respectively. The peak at ~723 cm^{-1} is due to the out-of-plane C–H bending of *i*Pr_2Pc-ring.

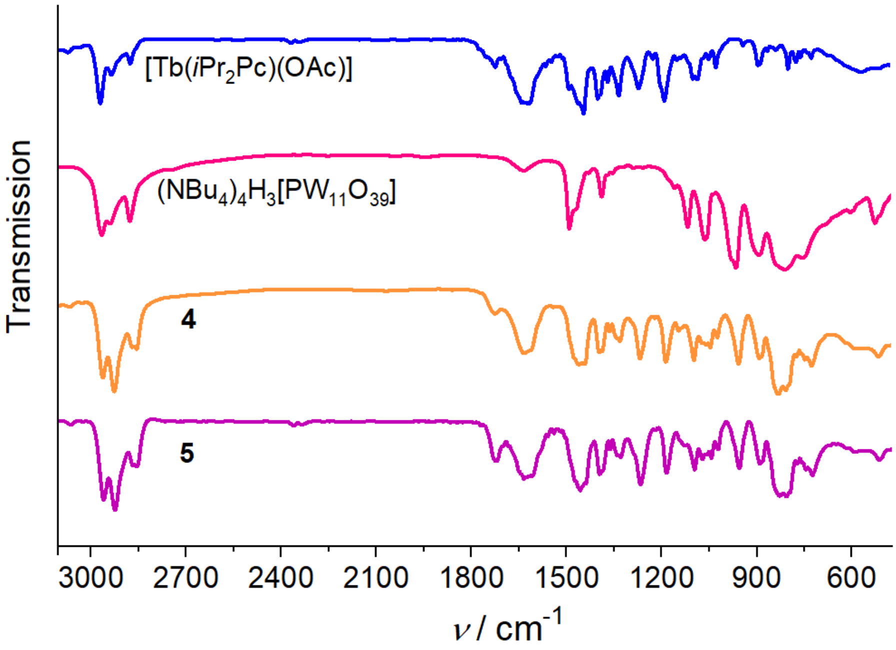

Fig 2.14 FT-IR spectra of complex **[4]**, **[5]**, and the starting materials $(NBu_4)_4H_3[PW_{11}O_{39}]$ and $[Tb^{III}(iPr_2Pc)(OAc)]$ as a representative single-decker complex.

The FT-IR spectrum of $[F_8Pc]$ exhibits a characteristic band arising from N–H bending vibrations of free-base phthalocyanine at 1009 cm^{-1} in addition to the bands of Pc-core between ~700–1000 cm^{-1} **(Fig 2.15)**. The peaks of C–H and N–H stretching vibrations are overlapped by a huge band at ~3000–3600 cm^{-1}, generated by the O–H stretch signal as the sample was washed with water in the synthetic process. This presence of water is observable by FT-IR even after having placed under reduced pressure overnight. In addition to the isoindole stretching between 1630 and 1300 cm^{-1}, the spectra show C–F stretching vibrations at ~1175 and ~1280 cm^{-1}, as observed in fluorinated aromatic compounds.[38] The absence of C≡N stretching around 2250 cm^{-1} indicates the complete conversion of starting 4,5-difluorophthalonitrile. Furthermore, the N–H bending vibration of free-base phthalocyanine disappears on the coordination of F_8Pc to lanthanide(III) center. Similar to F_8Pc, the spectra of $[Ln^{III}(F_8Pc)(OAc)(DBU)]$ exhibit all the vibrations in the range of 1620–1320 cm^{-1} corresponding to [C–C and C–N] stretching of benzene and isoindole ring. The peak at ~1073 cm^{-1} could be attributed to υ(C–O) vibrations of acetate ligand.

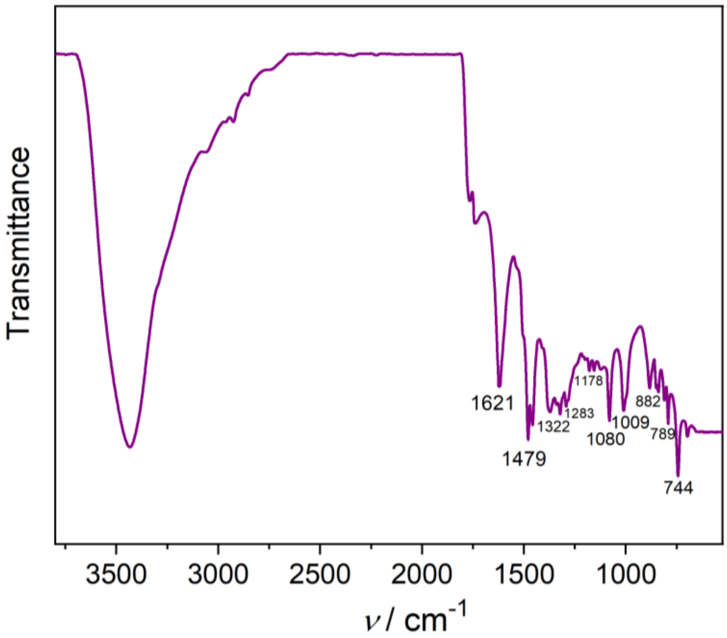

Fig 2.15 FT-IR spectrum of free-base fluorinated phthalocyanine.

The hybrid complexes **[6]** and **[7]** display C–H stretching vibrations between 2960–2870 cm^{-1}. Similar to the octafluorinated single-decker reactants, the signals between 1620 and 1100 cm^{-1} are derived from benzene and isoindole stretching of F_8Pc-ring. Additionally, the spectra show signals corresponding to CH_3 and CH_2 bending vibrations of TBA cations at ~1380 and ~1465 cm^{-1} respectively. The bands for P–O vibrations appear between ~1050 and 1100 cm^{-1}. Both complexes exhibit (W=O$_{terminal}$), (W–O$_{corner}$–W), and (W–O$_{bridging}$–W) vibrations at 953 cm^{-1}, ~890 cm^{-1}, and 810–745 cm^{-1} respectively. A weak band at ~720 cm^{-1} is assigned to (C–H) out-of-plane bending of F_8Pc-ring. All of these peaks show a shift of ~1–10 cm^{-1} from the starting single-decker of phthalocyanine and $[PW_{11}O_{39}]^{7-}$. A comparison of the FT-IR spectra of **[6]**, **[7]**, and starting materials is shown in **Fig 2.16**.

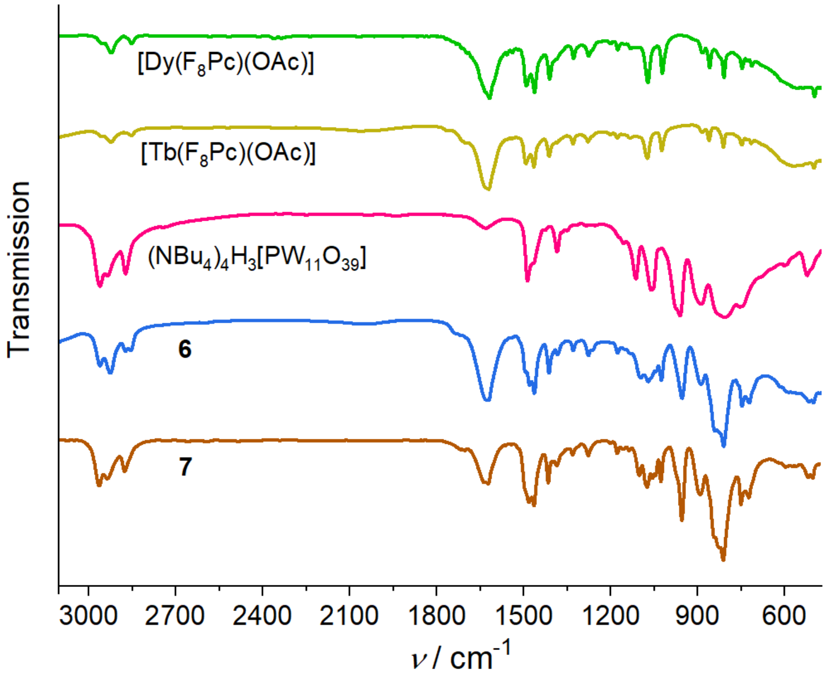

Fig 2.16 FT-IR spectra of complex **[6]**, **[7]**, and the starting materials $(NBu_4)_4H_3[PW_{11}O_{39}]$ and $[Ln^{III}(F_8Pc)(OAc)]$ (Ln = Tb and Dy).

Thermogravimetric analysis

The thermal stability of hybrid complexes was determined by thermogravimetric analysis within the range of 25–850 °C under N_2 atmosphere. The loss of mass recorded for complexes **1**–**3** are similar in the range of 25–600 °C **(Fig 2.17)**. Upon heating, the mass remains almost unchanged until 200 °C, wherefrom there is a substantial loss of ~22 % at 400 °C, and subsequently ~28 % at 600 °C. From this temperature, there is a sudden drop reaching a minimum value of 61 % **[1]**, 44 % **[2]**, and 25 % for **[3]** at 850 °C. These results show that the three compounds remain intact up to ~200 °C; after that the first step of weight loss, observed between 200–400 °C, corresponds to the loss of four TBA cations (calculated 22.8 %, found 22.7 % for **1**), (calculated 22.38 %, found 22.9 % for **2**), and (calculated 22.4 %, found 22.2 % for **3**). Further increase in temperature results in the decomposition of compounds, observed in the last drop occurring between 500–850 °C.

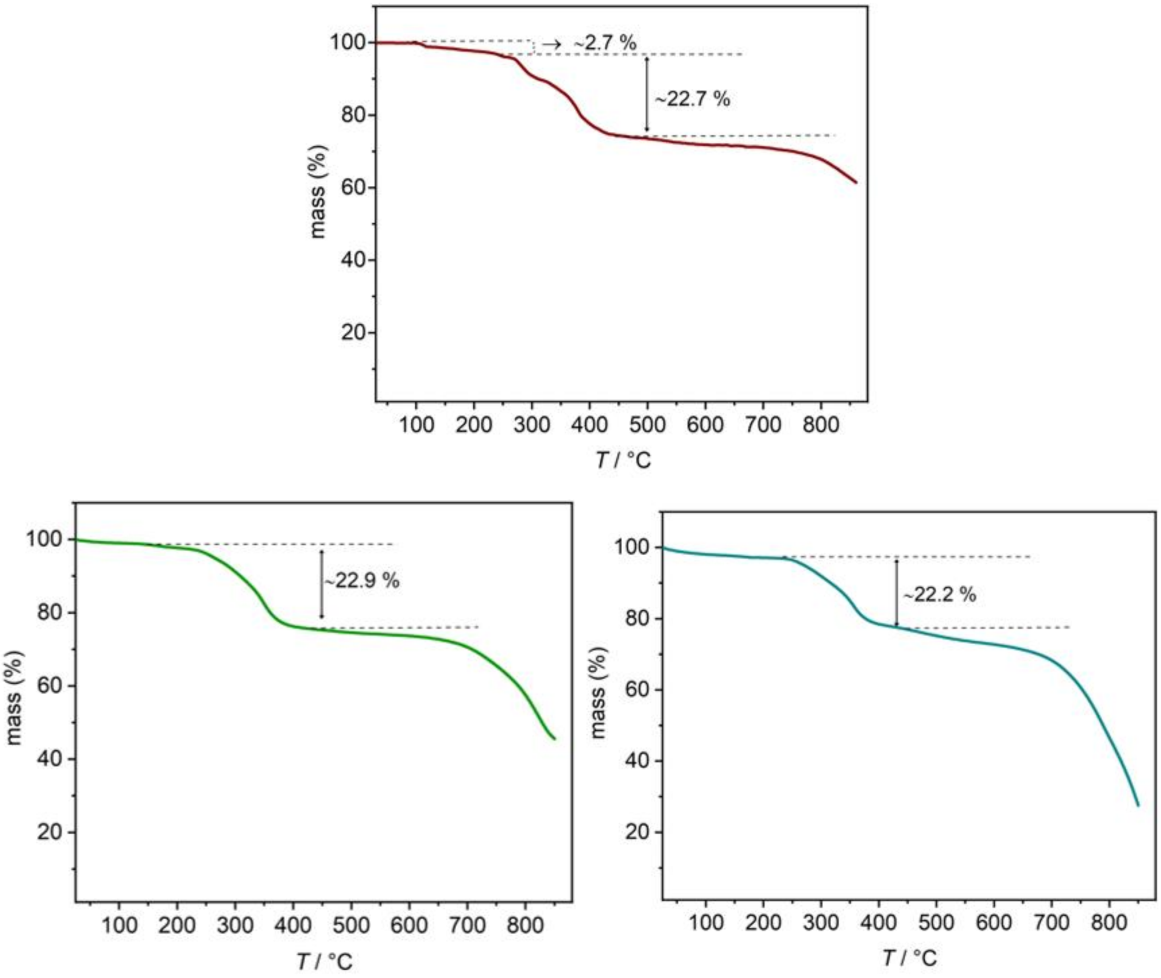

Fig 2.17 TGA curves of complexes **[1–3]** in the range of 25–850 °C.

To compare the thermal stability of hybrid complexes with different substituents on Pc-ring, TGA analysis of complex **[4]** and **[6]** was performed. The curve of **[4]** shows the stability up to ~210 °C, after that a number of overlapping steps appear between 210–600 °C as shown in **Fig 2.18**. As the curve indicates, the mass drops to a value of ~75.1 % at 430 °C, and further heating reduces the mass to ~59.7 % at 550 °C. After that, the last step shows the mass falling to ~45 % at 850 °C. The *% mass* loss between 200–420 °C is matching to the loss of TBA cations (calculated for six $C_{16}H_{36}N$: 23.3 %, found ~24.9 % for **4**). The next step that reaches a temperature of ~550 °C, corresponds to a mass loss of ~40.3 % and could be related to the partial decomposition of di-*iso*-propylphenoxy units of the Pc-ring (calculated for six $C_{16}H_{36}N$ and eight $C_{12}H_{17}O$: 44 %). Above 550 °C, the double-decker skeleton starts to decompose.

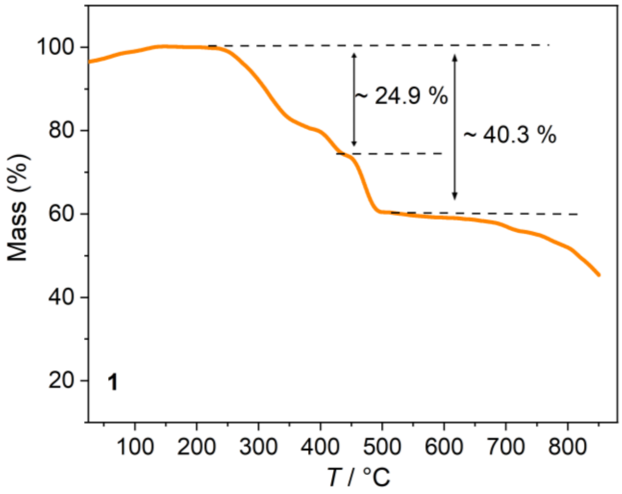

Fig 2.18 TGA curve of complex **[4]** in the range of 25–850 °C.

The TGA curve of complex **[6]** is shown in **Fig 2.19**. The mass remains almost unchanged up to ~180 °C, wherefrom it starts to descend steeply to a value of 68.9 % at ~390 °C. On further increasing the temperature, the percentage of mass continues to decrease gradually until 850 °C, reaching a minimum value of 46 %. From the result, the first step between 180–400 °C could be attributed to the loss of TBA cations (calculated for six $C_{16}H_{36}N$: 29.4 %, found ~31.1 % for **6**) similar to **[1–4]**. Increase in temperature above ~400 °C leads to the decomposition of the main skeleton of double-decker complex, observed between 400–850 °C. Hence, the TGA analyses indicate the thermal stability of hybrid complexes up to ~200 °C.

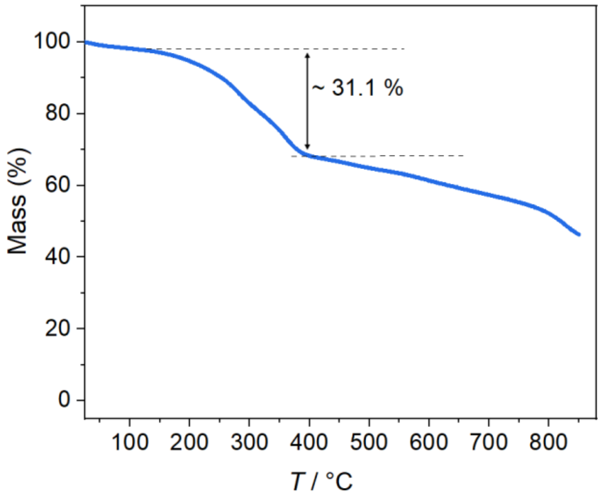

Fig 2.19 TGA curve of complex **[6]** in the range of 25–850 °C.

UV-Vis absorption spectroscopy

The 18-π electronic structure of the Pc-ligand shows an intense Q-band in the visible region and a weaker Soret-band in UV-region. These bands are the result of π-π* electronic transitions.[39] The spectra of complexes **[1–3]** also display a typical Soret-band at ~352 nm and, Q-bands at ~692 and ~710 nm. However, both bands exhibit a significant bathochromic shift in comparison to the lanthanide(III) single-decker phthalocyanine, in which the Soret-band appears at ~340 nm and the Q-band at ~672 nm. This red shift can be attributed to the donation of electron density from $[PW_{11}O_{39}]^{7-}$ that results in the shifting of spectra towards higher wavelengths. Another difference in the spectra of hybrid complexes is the splitting of Q-band due to lowered molecular symmetry as observed in heteroleptic bis(phthalocyanato) lanthanide(III) complexes.[40,41] Besides Pc-based absorption bands, complexes **[1–3]** display another band at ~260 nm, stemming from O→W charge transfer transition in POT unit. **Fig 2.20** shows the comparison of the spectra of $[Y^{III}(H_{16}Pc)(OAc)]$, $[PW_{11}O_{39}]^{7-}$ and complex **[1]**.

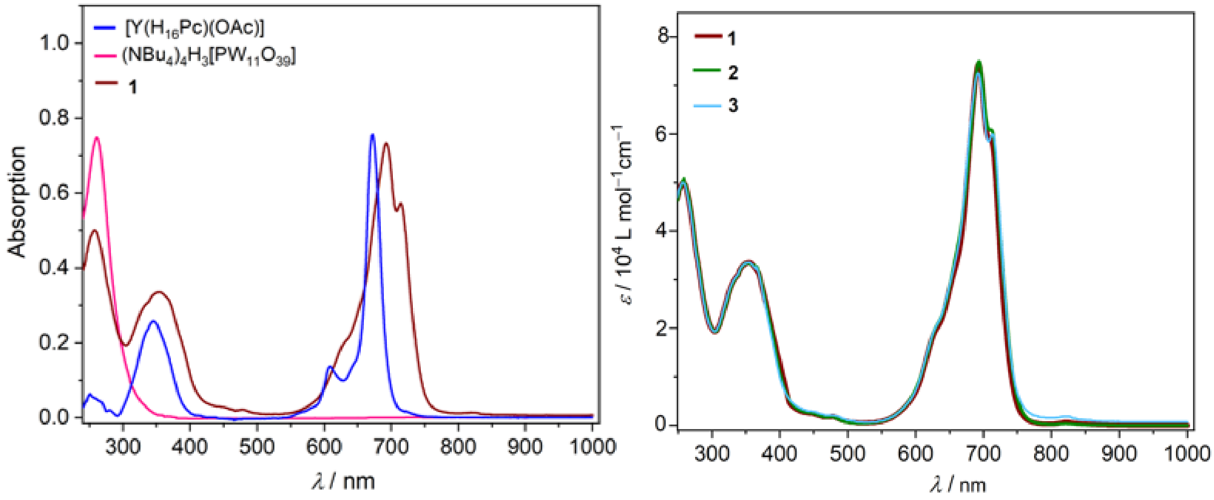

Fig 2.20 (Left) UV-Vis spectra of complex **[1]** (in DCM), $[Y^{III}(H_{16}Pc)(OAc)]$ (in DCM), and $(NBu_4)_4H_3[PW_{11}O_{39}]$ (in acetonitrile). **(Right)** Molar extinction graphs for **[1–3]** (in DCM).

The electronic absorption spectra of complex **[4]** and **[5]** exhibit similar features as for **[1–3]**, *i.e.* a Soret-band at ~370 nm and, Q-bands at ~696 and ~727 nm. Both of these bands show a ~10–20 nm bathochromic shift in comparison to the starting lanthanide(III) single-decker phthalocyanine $[Ln^{III}(iPr_2Pc)(OAc)]$ displaying a Soret-band at ~360 and Q-band at ~679 nm as shown in **Fig 2.21** (left). By comparing to the starting materials, a strong band at ~251 nm in the spectra of **[4]** and **[5]** could be the overlap of transitions in Pc- and POT-units. The Soret and Q-bands of **[4]** and **[5]** are also red shifted than unsubstituted analogues **[1–3]**, which is consistent with the previous observations in lanthanide(III) phthalocyanine complexes substituted with electron-donating groups.[42]

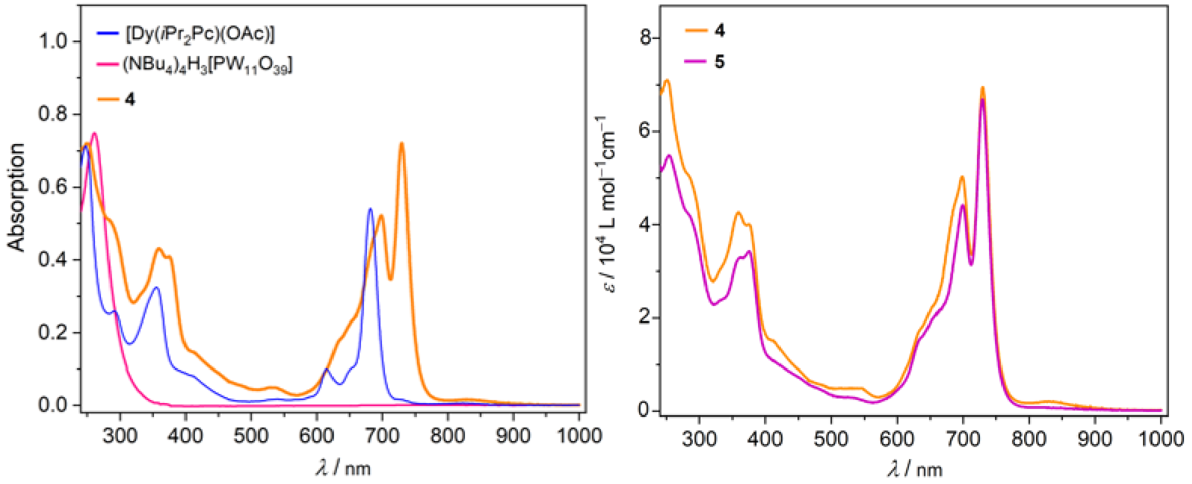

Fig 2.21 (Left) UV-Vis spectra of complex **[4]** (in DCM), [Dy^{III}($i$$Pr_2$Pc)(OAc)] (in DCM), and $(NBu_4)_4H_3[PW_{11}O_{39}]$ (in acetonitrile). **(Right)** Molar extinction graphs for **[4]** and **[5]** (in DCM).

The quantitative spectral properties of [$Mg^{II}F_8Pc$] and [F_8Pc] were not determined due to their poor solubility. The spectrum of [$Mg^{II}F_8Pc$] displays a Soret-band at 337 nm and a Q-band at 660 nm. The ligand [F_8Pc] shows a Soret-band at 320 nm and a broad Q-band located between ~540–720 nm. Coordination of the lanthanide(III) center to the [F_8Pc] unit shifts the Soret- and Q-bands to ~342 and ~663 nm respectively **(Fig 2.22)**. The electronic absorption spectra of **[6]** and **[7]** are almost identical to those of [Ln^{III}(F_8Pc)(OAc)(DBU)], with a shift of ~2 nm, *i.e.* the Soret-band at ~339 nm and Q-band at ~661 nm. This is in contrast to the unsubstituted or di-*iso*-propylphenoxy substituted analogues, in which the coordination of $[PW_{11}O_{39}]^{7-}$ unit to single-decker of the corresponding Pc-ring induced a red shift of ~10–20 nm. The spectra of **[6]** and **[7]** also show the absorption band at ~260 nm that could be the overlap of transitions in Pc- and POT-units.

The absorption bands of all fluorinated complexes exhibit a significant blue shift in comparison to the unsubstituted analogues, indicating the stabilization of HOMO due to the electron-withdrawing inductive effect of fluorine atoms as found in [$Cu^{\beta}F_8Pc$] and [$Zn^{\beta}F_8Pc$].[43,44] The effect of the electronic nature of substituents on the spectra of hybrid complexes, taking as a reference the Dy-based complexes, is shown in **Fig 2.23**.

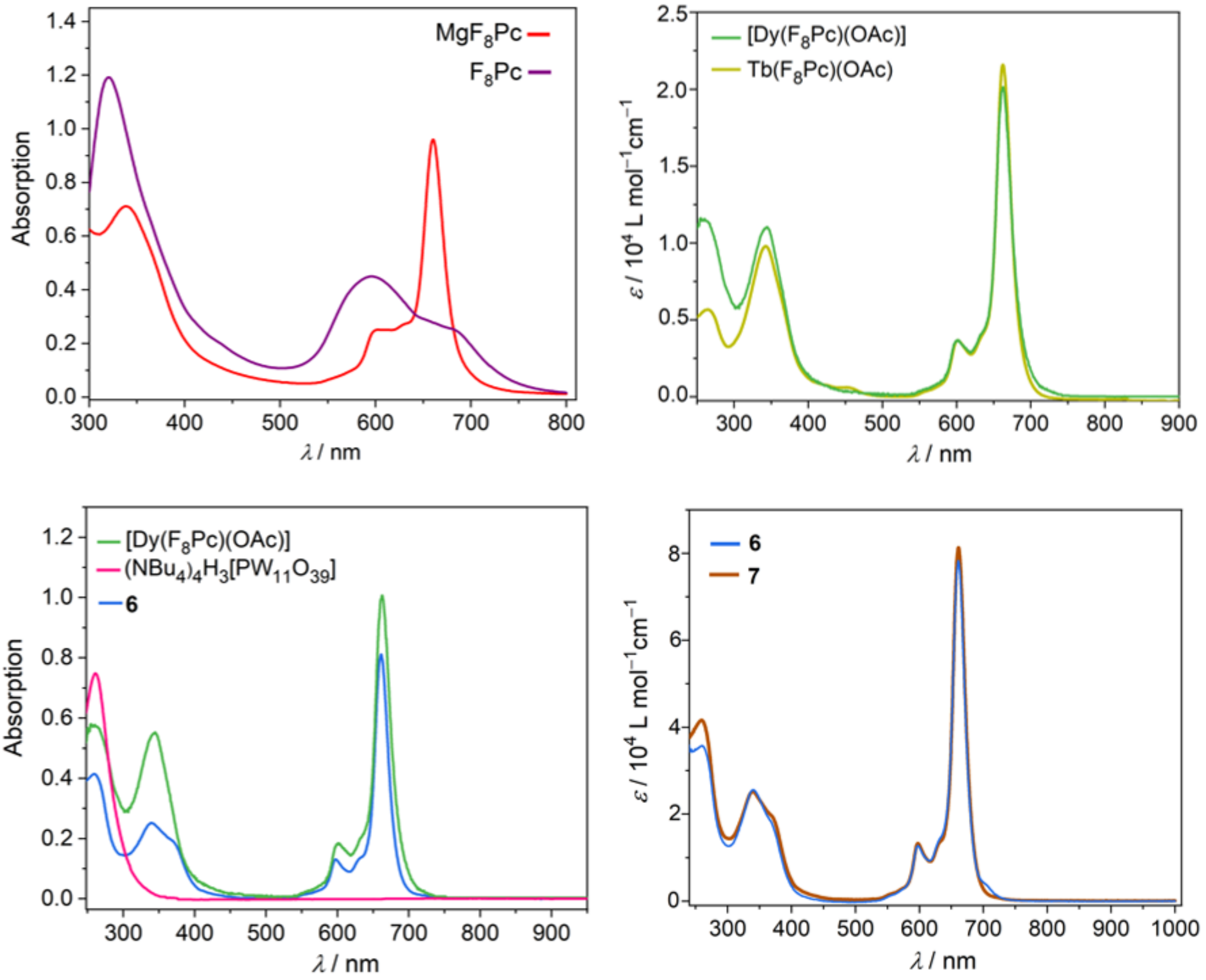

Fig 2.22 UV-Vis spectra of **(top left)** $[\mathrm{Mg^{II}F_8Pc}]$ and $[\mathrm{F_8Pc}]$ in DMSO and **(top right)** molar extinction graphs for $[\mathrm{Ln^{III}(F_8Pc)(OAc)(DBU)}]$, Ln = Tb and Dy (in DCM). **(Bottom left)** Comparison of the UV-Vis spectra of starting materials and complex **[6]**. **(Bottom right)** Molar extinction graphs for **[6]** and **[7]** (in DCM).

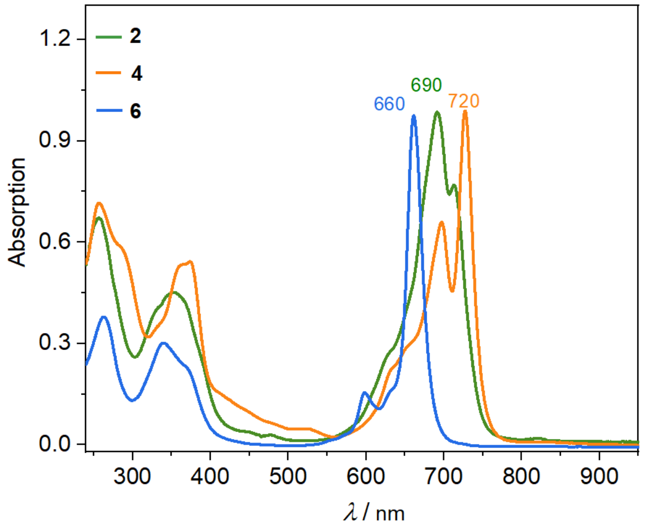

Fig 2.23 Comparison of UV-Vis spectra of complex **[2]**, **[4]**, and **[6]**.

Electrochemical properties

The redox properties of all hybrid complexes were studied by recording the cyclic voltammograms in CH_2Cl_2 solution using 0.1 M tetra-*n*-butylammonium hexafluorophosphate (NBu_4PF_6) as an electrolyte at a scan rate of 100 mV/s. The voltammograms of hybrid complexes containing the same substituents on the periphery of Pc-ring exhibit similar redox processes with slight shifts of potentials, therefore the peaks for Dy-analogues are described in detail. The oxidation and reduction peak potentials for **[1–7]** are given in **Table 2.3**.

The voltammogram of complex **[2]** displays superimposed oxidation waves labeled as Oxi_1 at ~ +0.15 V, Oxi_2 at ~ +0.46 V, and well-defined reduction waves labeled as Red_2 ~ –1.4 V and Red_3 ~ –1.8 V. In addition to these processes, some less marked peaks with E_{pa} ~ –1.3 V, ~ –1.6 V are also observed. The oxidation peak with E_{pa} ~ –0.19 V is related to the broad reduction wave at ~ –0.65 V (Red_1) and it does not appear upon scanning the window between –0.4 V to +0.9 V as shown in the insets in **Fig 2.24**. The complexes of phthalocyanine show multiple redox waves based on the addition or removal of electrons to or from the Pc-ring.[45] However, to find out the origin of redox waves in hybrid complexes, CV of $(NBu_4)_4H_3[PW_{11}O_{39}]$ was recorded, which displayed five quasi-reversible processes corresponding to the W^{VI}/W^{V} redox couples between –0.5 V to –2.51 V as shown in **Fig 2.25**. Therefore, in complexes **[1–3]**, the waves between ~ 0 to ~ +1 V could be assigned to the redox reactions on Pc-ring, while the peaks appearing between ~ 0 to –2 V are likely to be an overlap of redox processes on $H_{16}Pc$ and $[PW_{11}O_{39}]^{7-}$ units. The shapes and position of redox waves remain unchanged upon narrowing down the sweeping window to only positive or negative potential.

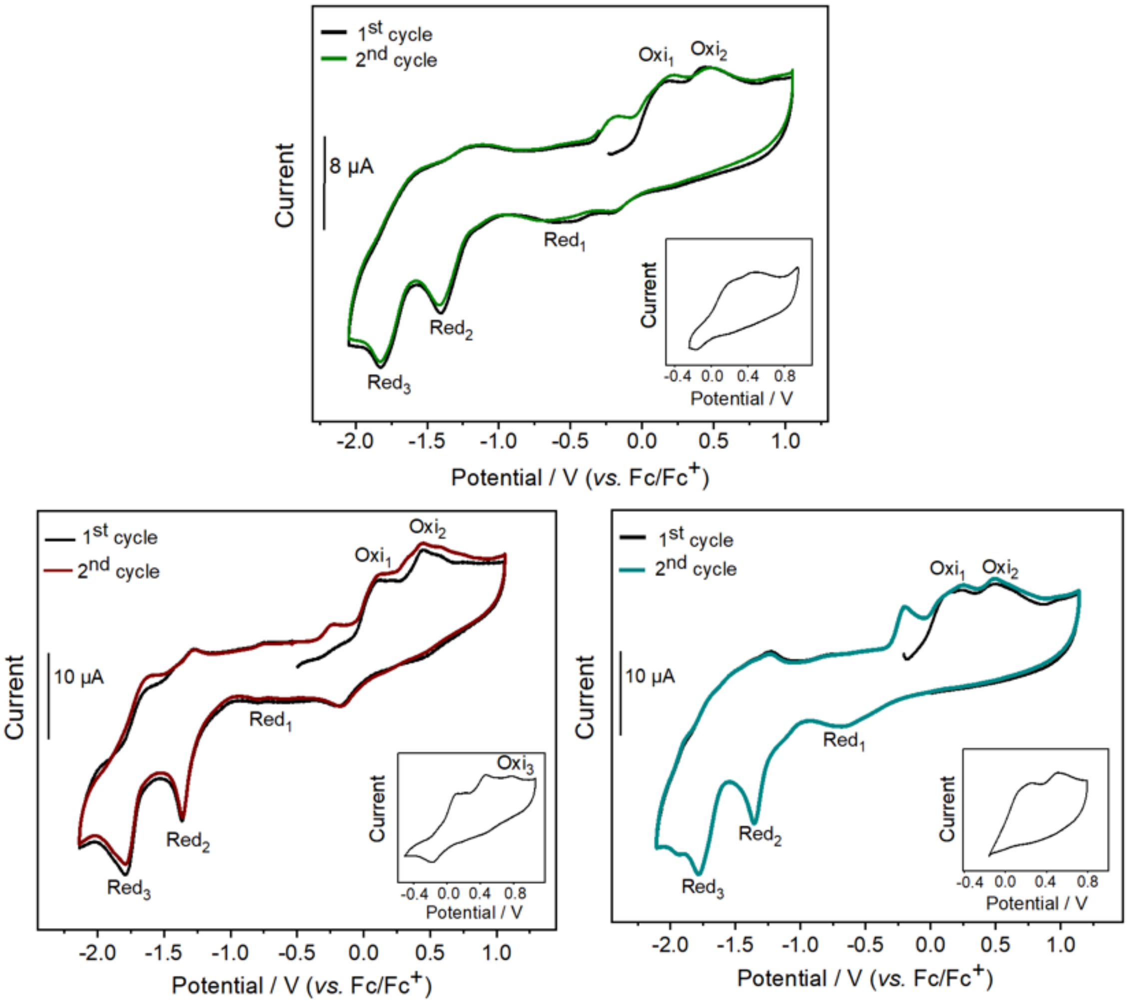

Fig 2.24 Cyclic voltammograms of **(top)** 0.33 mM solution of complex **[2]**, **(bottom left)** 0.5 mM solution of **[1]**, and **(bottom right)** 0.5 mM solution of **[3]** with 0.1 M NBu_4PF_6 in dichloromethane. The insets show the voltammograms in a scan window between –0.4 to +0.85 V.

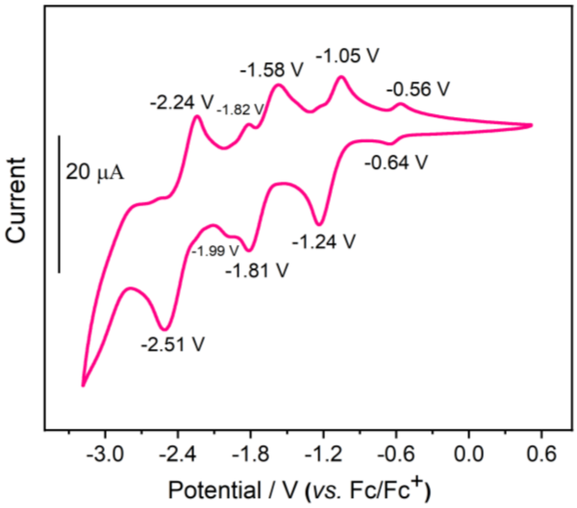

Fig 2.25 Cyclic voltammogram of 1 mM solution of $(NBu_4)_4H_3[PW_{11}O_{39}]$ with 0.1 M NBu_4PF_6 in CH_3CN at 100 mV/s.

The redox behavior of **[4]** and **[5]** is very similar to the unsubstituted analogues *i.e.* the oxidation waves with E_{pa} ~ –0.05 V (Oxi_1), ~ +0.27 V (Oxi_2), ~ +0.49 V (Oxi_3), and the reduction waves with E_{pc} ~ –0.7 V (Red_1), ~ –1.17 V (Red_2), –1.63 V (Red_3), and ~ –2.03 V (Red_4). Akin to **[1–3]**, the redox processes between ~ –0.1 to ~ +0.6 V could be associated with the redox processes on iPr_2Pc-ring, whereas the waves between ~ –0.1 to ~ –2 V can be the overlap of redox reactions on iPr_2Pc and $[PW_{11}O_{39}]^{7-}$ units. As expected, the oxidation potentials of these complexes are more negative in comparison to **[1–3]**, due to the electron-rich di-*iso*-propylphenoxy groups on Pc-ring which make the oxidation processes in complexes **[4–5]** easier. This shifting of redox waves is similar to the reported $[Ln(Pc)_2]$ complexes containing electron-donating groups on the periphery of Pc-ring.[42,46]

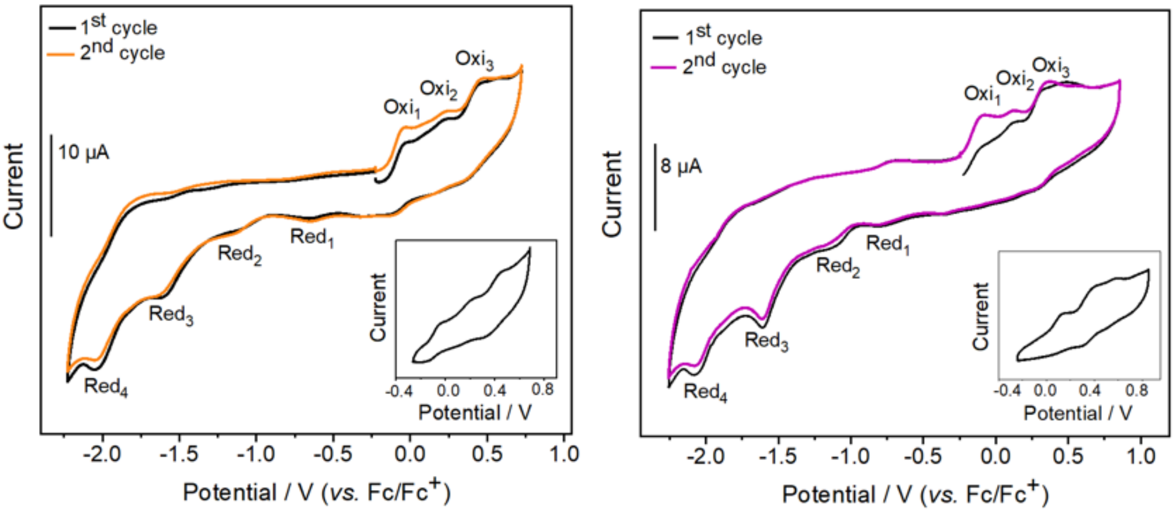

Fig 2.26 Cyclic voltammograms of **(left)** 0.4 mM solution of complex **[4]** and **(right)** 0.3 mM solution of complex **[5]** with 0.1 M NBu_4PF_6 in dichloromethane. The insets show the voltammogram in a scan window between –0.3 to +0.8 V.

Cyclic voltammetry of octafluorinated magnesium phthalocyanine and free-base F_8Pc was not recorded due to their poor solubility. The CV of single-decker complexes $[Ln^{III}(F_8Pc)(OAc)(DBU)]$ was recorded in dimethyl sulfoxide using (0.1 M) NBu_4PF_6 as an electrolyte at a scan rate of 100 mV/s **(Fig 2.27)**.

The voltammograms of both complexes show two reversible one-electron processes with $E_{1/2}$ ~ +0.39 V and ~ –1.24 V. Besides the reversible waves, one oxidation wave with E_{pa} ~ +0.3 V and three reduction waves with E_{pc} ~ –1.63 V, ~ –1.95 V, and ~ –2.41 V are observed. Compared to the double-decker $[Ln(Pc)_2]^{\bullet}$ complexes, having quite low first reduction potential, single-decker [Ln(Pc)(X)] complexes tend to reduce at more negative potential as observed here. The difference between first oxidation and first reduction potential ($\Delta E_{1/2}$) of these complexes is ~0.98 V, which is less than the separation (*i.e.* 1.5 V) demonstrated for lutetium single-decker phthalocyanine complexes bearing dimethoxyphenylthio groups on the periphery of Pc-ring.[42] However, the reports describing the redox behavior of [Ln(Pc)(X)] complexes are very scarce, therefore the influence of fluorine atoms on the shifting of redox potential and $\Delta E_{1/2}$ of these complexes cannot be compared. The compounds exhibit identical processes upon narrowing down the sweeping window to only positive or negative potential.

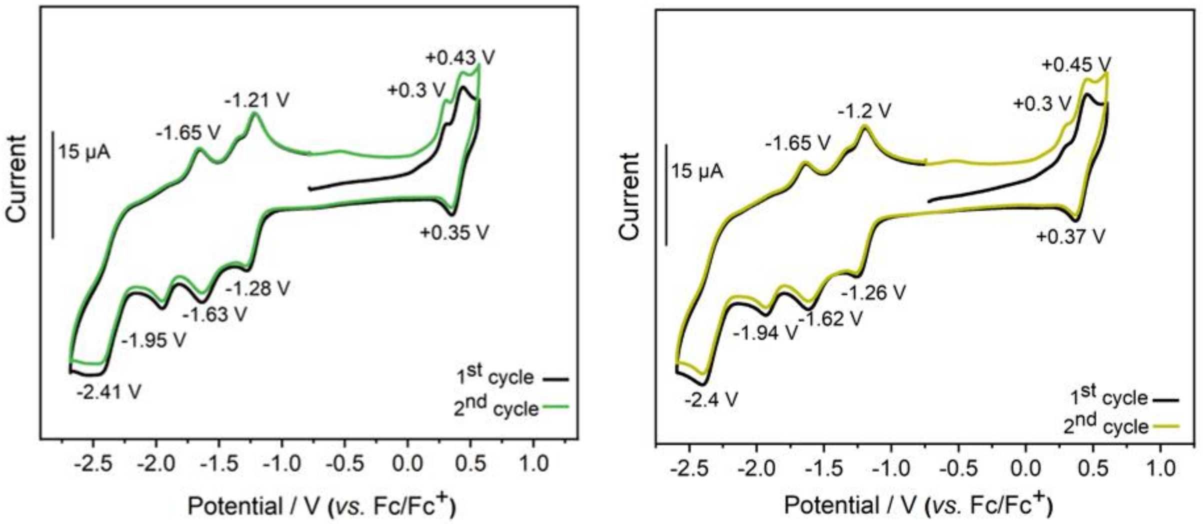

Fig 2.27 Cyclic voltammograms of 1 mM solution of **(left)** $[Dy^{III}(F_8Pc)(OAc)(DBU)]$ and **(right)** $[Tb^{III}(F_8Pc)(OAc)(DBU)]$, with 0.1 M NBu_4PF_6 in dimethyl sulfoxide.

The cyclic voltammograms of **[6]** and **[7]** in CH_2Cl_2 solution are similar to the other hybrid complexes **[1–5]**. The voltammogram of complex **[6]** displays two quasi-reversible oxidation waves labeled as Oxi_1 ~ +0.22 V, Oxi_2 +0.54 V, and four reduction waves labeled as Red_1 ~ –0.63 V, Red_2 ~ –1.1 V, Red_3 ~ –1.59 V, and Red_4 ~ –1.97 V. The first oxidation peak at ~ –0.05 V is related to the reduction wave at ~ –0.63 V and it disappears upon scanning the window between –0.2 V to +0.9 V as shown in the insets in **Fig 2.28**.

Similar to complexes **[1–5]**, the oxidation waves at positive potentials (between 0 to +0.9 V) could be associated with the redox reactions on F_8Pc-ring, whereas the rest of waves appearing in the negative potential window (0 to –2.1 V) could be overlapped processes from F_8Pc and tungsten redox couple of $[PW_{11}O_{39}]^{7-}$. Additionally, the inductive effect of fluorine atoms on the periphery of Pc-ring has slightly shifted the redox potential of complexes towards positive potentials in comparison to $[Ln^{III}(H_{16}Pc)(PW_{11}O_{39})]^{6-}$. This anodic shift is in agreement with the blue shift of Q-band in the electronic absorption spectra of these complexes. The shapes and position of redox waves remain unchanged upon narrowing down the sweeping window to only positive or negative potential.

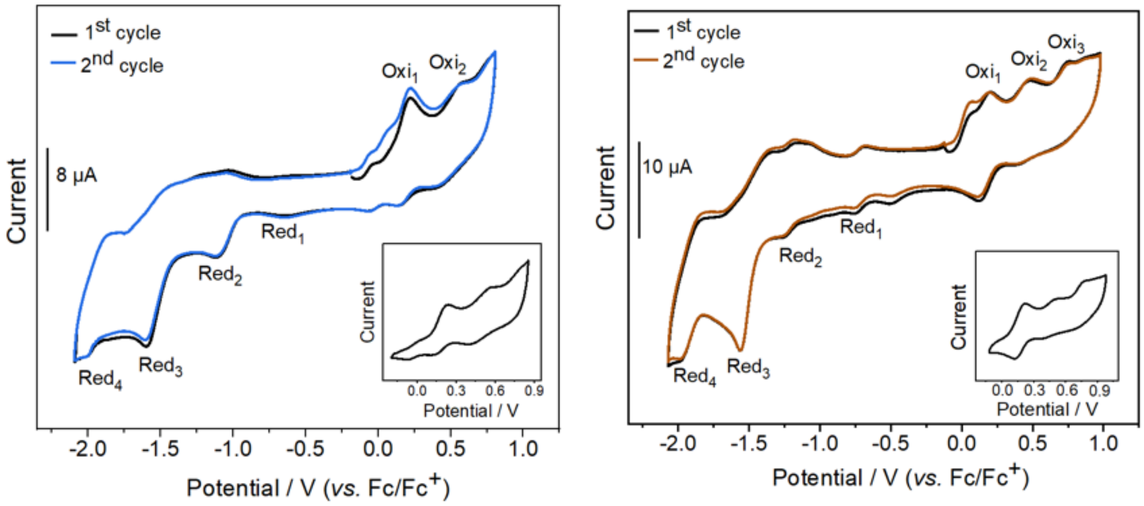

Fig 2.28 Cyclic voltammograms of **(left)** 0.3 mM solution of **[6]** and **(right)** 0.4 mM solution of **[7]** with 0.1 M NBu_4PF_6 in dichloromethane. The insets show the voltammogram in a scan window between –0.2 to +0.9 V.

Table 2.3 Electrochemical data of **[1–7]** referenced *vs.* $[Cp_2Fe]/[Cp_2Fe]^+$.

Complex	**Oxi$_3$**	**Oxi$_2$**	**Oxi$_1$**	**Red$_1$**	**Red$_2$**	**Red$_3$**	**Red$_4$**
1	+0.75	+0.45	+0.15	–0.66	–1.37	–1.79	-
2	-	+0.46	+0.15	–0.65	–1.4	–1.8	-
3	-	+0.48	+0.14	–0.67	–1.36	–1.78	-
4	+0.49	+0.27	–0.05	–0.7	–1.17	–1.63	–2.03
5	+0.55	+0.34	+0.1	–0.8	–1.14	–1.61	–2.1
6	-	+0.54	+0.22	–0.63	–1.1	–1.59	–1.97
7	+0.76	+0.5	+0.21	–0.76	–1.21	–1.56	–1.98

Magnetic properties

In case of lanthanides, the source of angular momentum is not just the total spin, but also the large unquenched orbital momentum. Therefore, the electronic structure is described by multiplets of spin-orbit coupled term symbol $^{2S+1}L_J$. These multiplets are usually separated by large energy values and the magnetic properties are mostly determined by ground state multiplet. The interaction of ligand-field removes the degeneracy of $^{2S+1}L_J$ multiplet, producing an energy barrier to the opposite reorientation of *mj* states. Contrary to 3d-ions, the spin-orbit coupling energy is much larger than ligand-field splitting. Therefore, the strength of interactions determining the energy level structure is as follows: electron-electron interaction>spin-orbit coupling>ligand-field.[47]

As an example, **Fig 2.29** shows the energy levels of the electronic structure of Dy(III) ion with $4f^9$ configuration (L = 5 and S = 5/2). Electron-electron repulsion in Dy(III) ion gives rise to the ground state sextuplet ^6H, which is well separated from the second term ^6F. The spin-orbit coupling further splits these terms into multiplets with different *J*-values, producing $^6H_{15/2}$ ground state in this case. According to 2*J*+1 formula, the magnetic microstates of ground state $^6H_{15/2}$ are: *mj* = ±15/2, ±13/2, ±11/2, ±9/2, ±7/2, ±5/2, ±3/2, ±1/2. The degeneracy of these *mj* states is influenced by ligand-field, however, the energies of this splitting differ depending on the interaction of Dy(III) electrons and surrounding ligands. Therefore, in the case of lanthanides, the effect of ligand-field is small but still an important factor in producing SMMs with different heights of the anisotropy barrier.[10]

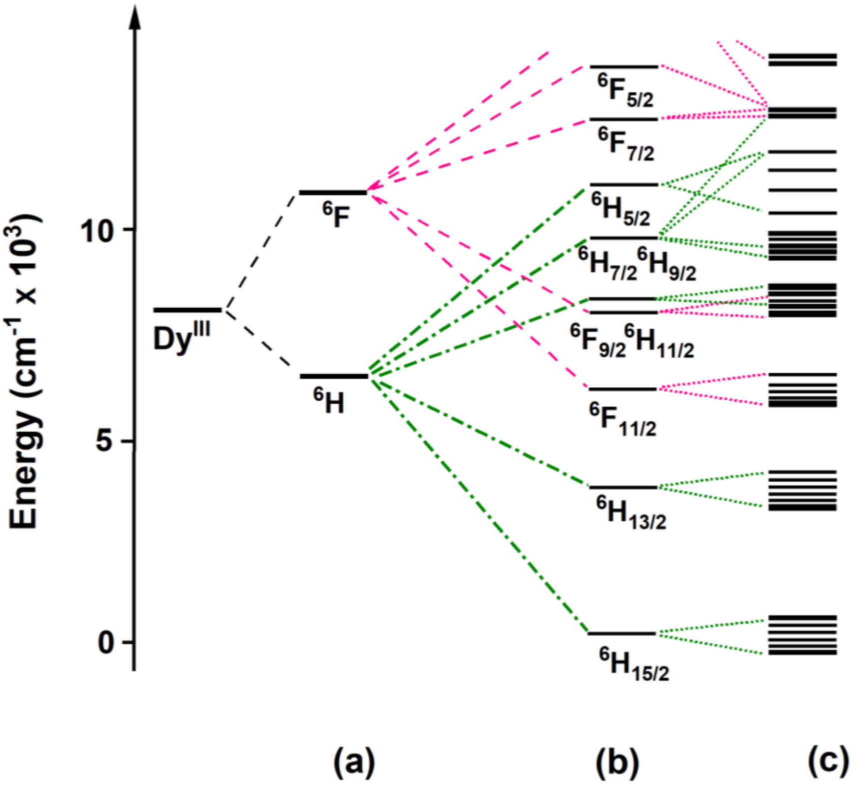

Fig 2.29 Energy scale of the electronic structure of a free dysprosium(III) ion with **(a)** electron-electron interaction **(b)** spin-orbit coupling and **(c)** ligand-field interaction.

To investigate the static magnetic susceptibility of complexes, direct current magnetic measurements were performed between 2–300 K under an applied field of 0.1 T. Analysis of the magnetic data was done by Dr. rer. nat. Dr. -Ing. Jan van Leusen (Institute of Inorganic chemistry, RWTH Aachen University). The curves of $\chi_m T$ product *vs*. temperature for **[2]** and **[3]** are shown in **Fig 2.30** (left). The room temperature values of $\chi_{\mathrm{m}}T$ are 13.26 **[2]** and 11.84 **[3]** cm^3 K mol^{-1}, in good agreement with theoretical value of (13.0–14.05 cm^3 K mol^{-1}) and (11.76–12.01 cm^3 K mol^{-1}) for an isolated Dy(III) ion [$^6H_{15/2}$, L = 5, S = 5/2, g = 4/3] and Tb(III) ion [$^7F_6$, L = 3, S = 3, g = 3/2] respectively.[48] On lowering the temperature down to 90 K, the values of $\chi_{\mathrm{m}}T$ slowly decrease to 12.63 **[2]** and 11.24 cm^3 K mol^{-1} **[3]** and then drop to the minimum value of 9.10 and 9.31 cm^3 K mol^{-1} for **[2]** and **[3]** respectively. This behavior can be attributed to the thermal depopulation of energy states of split ground terms $^6H_{15/2}$ for Dy(III) and $^7F_6$ for Tb(III).

Additionally, the field dependence of molar magnetization for both complexes was obtained at 2 K in the range of 0–5 T **(Fig 2.30**, right**)**. Above 1 T, a sharp increase in M_{m} *vs*. B curve is observed, followed by a slight increase reaching the value of 5.1 **[2]** and 4.8 **[3]** $N_A \mu_B$ at 5 T.

This value is almost half of the saturation value of single Dy(III) (10 $N_A \mu_B$) and Tb(III) (9 N_A μ_B) center, as expected for the powder samples of magnetically anisotropic centers.

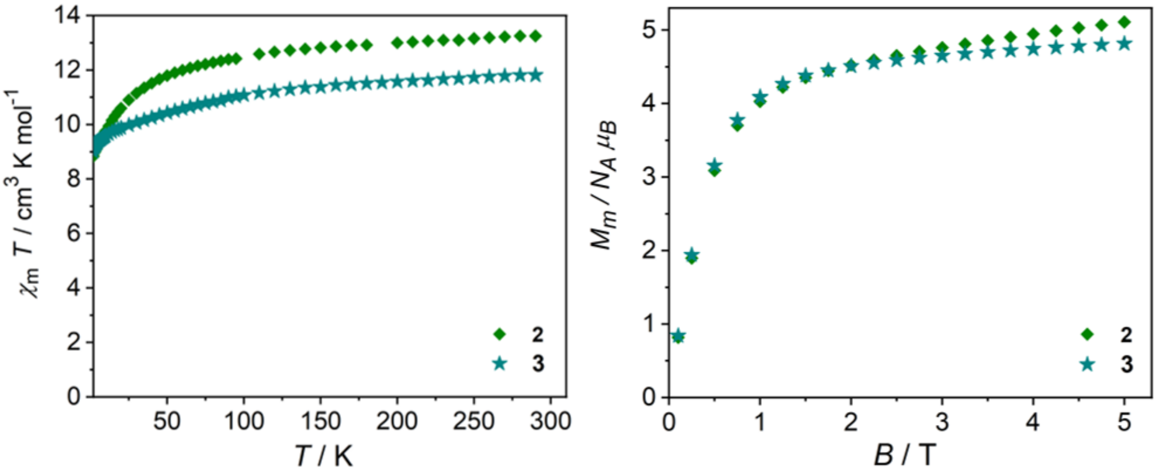

Fig 2.30 Dc-data for **[2]** and **[3]**: **(left)** $\chi_m T$ *vs.* T at 0.1 T; because of the loss of lattice solvent during the treatment of the sample, leading to uncertainty in the molar mass, the $\chi_m T$ for **[3]** at 290 K was scaled to 11.84 cm^3 K mol^{-1}, **(right)** M_m *vs.* B at 2 K.

To investigate the slow magnetic relaxation behavior, alternating current magnetic measurements were performed on both complexes in 3.5 Oe ac-field in the range of 3–938 Hz. Complex **[2]** shows the tails of out-of-phase ac susceptibility signals in a zero static bias field due to fast relaxation associated with quantum tunneling of magnetization (QTM) **(Fig 2.31)**. However, well-resolved maxima in the signals are observed at 500 Oe static bias field, indicating the SMM behavior of the complex with slow magnetic relaxation **(Fig 2.32)**. The ac-data were analyzed according to generalized Debye expression[49] at each temperature and the relaxation time τ, extracted from the Cole-Cole and (χ_m', χ_m'') *vs.* f plots **(Fig 2.33)**. This resulted in the distribution parameter $\alpha = 0.383 \pm 0.052$ suggesting multiple relaxation pathways. Therefore, the data in Arrhenius plot was analyzed considering Orbach, Raman, and direct relaxation processes according to the formula, $\tau^{-1} = \tau_0^{-1}\exp(-U_{\mathrm{eff}}/k_B T) + CT^n + A_K T$ (k_B Boltzmann's constant). The best fitting results in an effective energy barrier U_{eff} = 33.7±1.5 cm^{-1} and $\tau_0 = 1.08 \pm 0.31 \times 10^{-7}$ s for the Orbach process, a constant $C = 0.41 \pm 0.08$ s^{-1}K^{-n} and an exponent $n = 4.9 \pm 0.2$ for the Raman process, and a constant $A_K = 8.9 \pm 0.6$ s^{-1}K^{-1} at 500 Oe static bias field for the direct process. The Orbach process parameters are in common range of Dy(III) SMMs,[8] while the parameters for Raman and direct process are within the expected range for the systems with closely spaced Kramers levels ($n = 5$).[50]

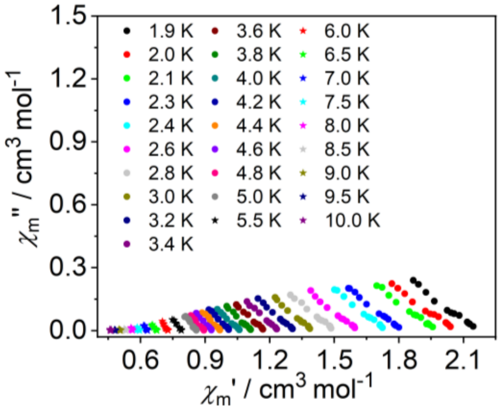

Fig 2.31 Cole-Cole plot of the molar magnetic ac susceptibility of **[2]** at zero static bias field.

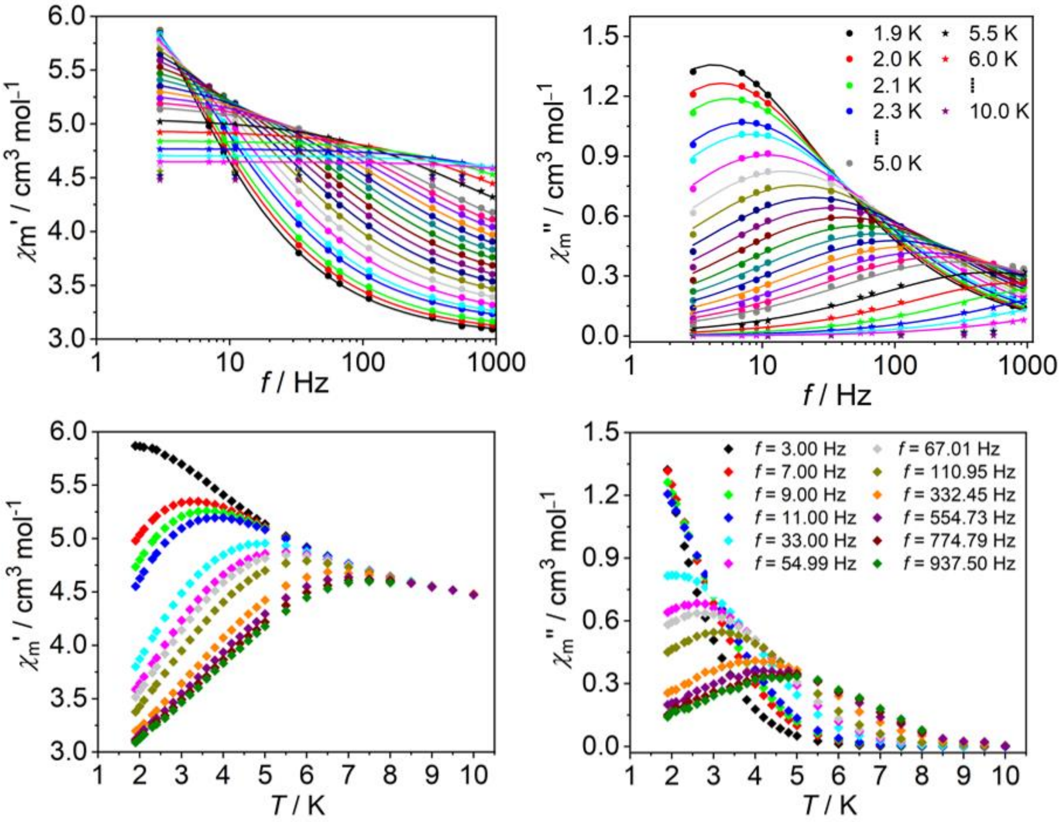

Fig 2.32 Molar magnetic ac susceptibility components of **[2]** in a static bias field of 500 Oe: **(top left)** in-phase (χ_m') molar magnetic susceptibility *vs.* frequency, **(top right)** out-of-phase (χ_m'') molar magnetic susceptibility *vs.* frequency, **(bottom left)** in-phase molar magnetic susceptibility (χ_m') *vs.* temperature, and **(bottom right)** out-of-phase molar magnetic susceptibility (χ_m'') *vs.* temperature.

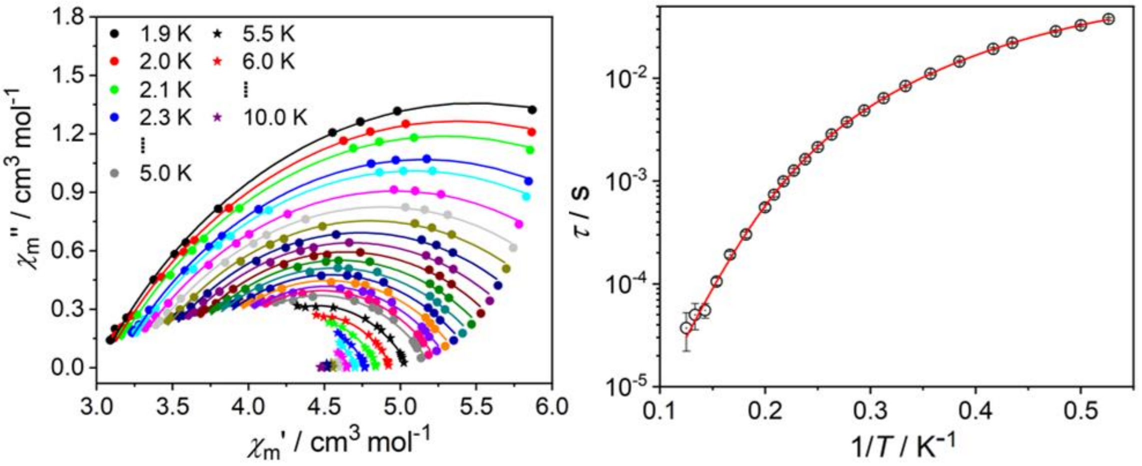

Fig 2.33 Magnetic ac-data for **[2]**: **(left)** Cole-Cole plot in the range 1.9–10.0 K at a static bias field of 500 Oe (symbols: data, lines: fits to a generalized Debye expression) and **(right)** Arrhenius plot of relaxation time τ *vs.* T^{-1} ($1.9\ \mathrm{K} \leq T \leq 8.0\ \mathrm{K}$), the red line shows a combined fit to Orbach, Raman, and direct relaxation processes.

As with complex **[2]**, **[3]** needs an induced dc magnetic field in order to overcome relaxation processes related to quantum tunneling of magnetization (QTM). Weak out-of-phase signals are observed at static bias field between 100–1000 Oe, however, the curvatures in Cole-Cole plot are not pronounced for the fitting of data as shown in **Fig 2.34**.

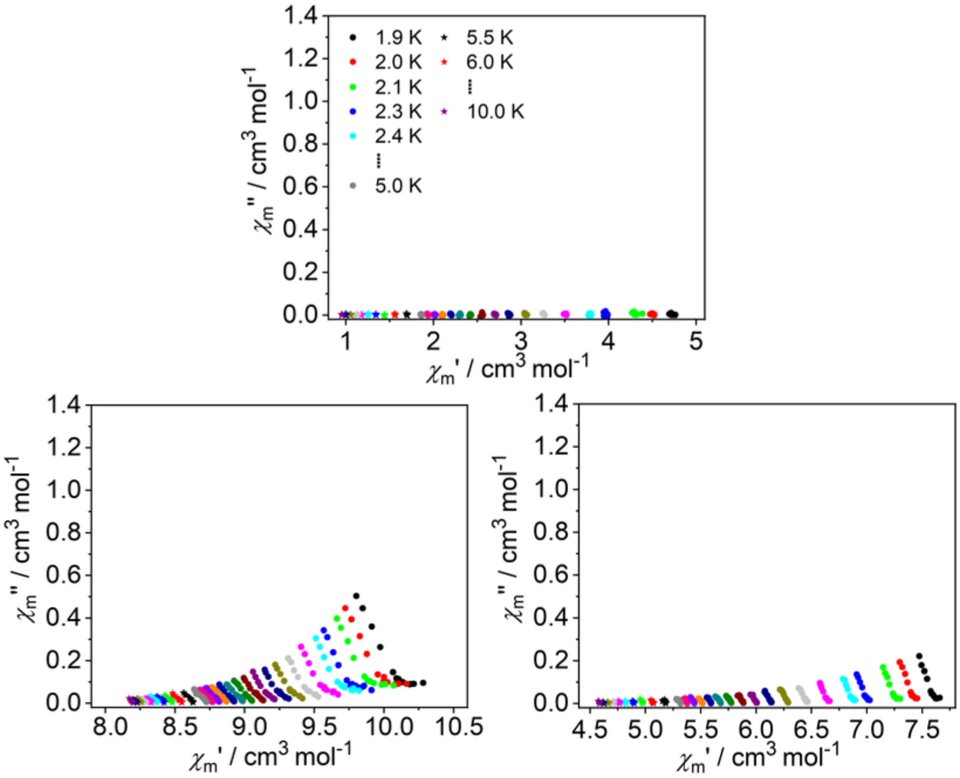

Fig 2.34 Cole-Cole plots of the molar magnetic ac susceptibility of **[3]**: **(top)** at zero static bias field, **(bottom left)** at a static bias field of 500 Oe, and **(bottom right)** at a static bias field of 1000 Oe.

Direct current magnetic measurements ($\chi_m T$ *vs.* T and M_m *vs.* B plots) for complexes **[4]** and **[5]** are shown in **Fig 2.35**. The room temperature $\chi_m T$ value for **[4]** is 13.76 cm^3 K mol^{-1} and for **[5]** is 11.88 cm^3 K mol^{-1}, which are in the expected ranges for an isolated Dy(III) and Tb(III) ion.[48] On lowering the temperature, the values of $\chi_m T$ steadily decrease to 12.96 **[4]** and 10.27 cm^3 K mol^{-1} **[5]** at 90 K and then drop to the minimum value of 9.86 and 9.58 cm^3 K mol^{-1} for **[4]** and **[5]** respectively. This behavior is due to the thermal depopulation of energy states of split ground terms $^6H_{15/2}$ for Dy(III) and $^7F_6$ for Tb(III).

The molar magnetization M_m at 2.0 K **(Fig 2.35**, right**)** show a linear increase with the applied field up to about 0.5 T, and then steadily increases from 1 to 5 T reaching the value of 5.4 $N_A \mu_B$ **[4]** and 4.8 $N_A \mu_B$ **[5]** at 5 T. The values are around half of the saturation value for a single Dy(III) (10 $N_A \mu_B$) and Tb(III) (9 $N_A \mu_B$) center, indicating the magnetic anisotropy of Dy(III) and Tb(III) ions.

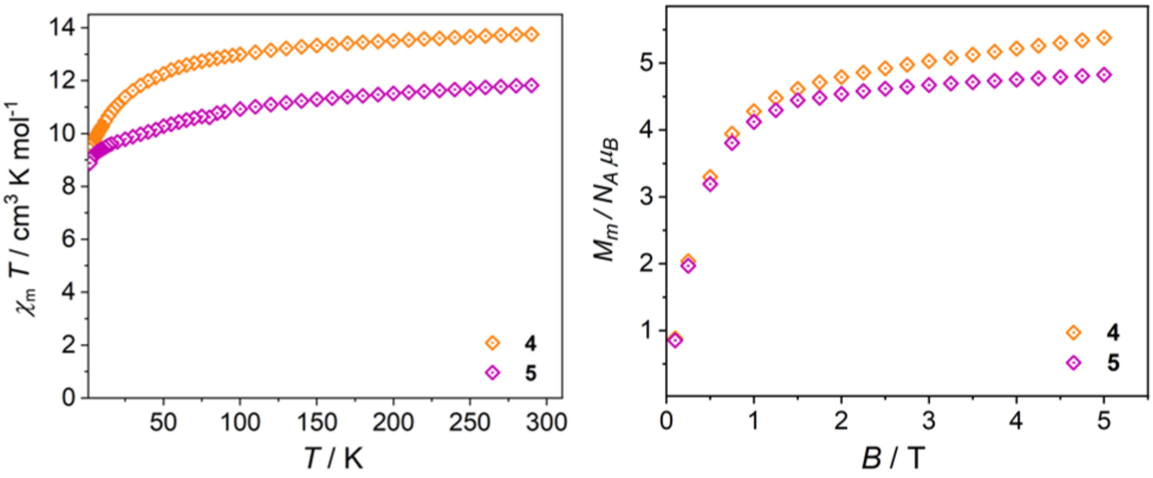

Fig 2.35 Dc-data for **[4]** and **[5]**: **(left)** $\chi_m T$ *vs.* T at 0.1 T and **(right)** M_m *vs.* B at 2 K.

Alternating current magnetic measurements on complexes **[4]** and **[5]** were performed in 3.5 Oe ac-field in the range of 3–938 Hz. Similar to **[2]**, complex **[4]** shows the tails of out-of-phase ac susceptibility signals in a zero static bias field **(Fig 2.36)** and pronounced curvature in the signals at 500 Oe bias field, indicating the SMM behavior of the complex **(Fig 2.37)**. The data were analyzed according to generalized Debye expression[49] by simultaneously fitting (χ_m' and χ_m'') *vs.* f plots between 1.9 and 8.5 K. The resulting relaxation times τ are plotted against $1/T$, which resulted in the value of "α" between 0.25 and 0.50 with a mean value of 0.43±0.08. Therefore, the data in Arrhenius plot was analyzed considering Orbach and a direct relaxation process according to the formula, $\tau^{-1} = \tau_0^{-1}\exp(-U_{eff}/k_B T) + A_K T$. The least-squares fit gives an attempt time $\tau_0 = 2.87 \pm 0.42 \times 10^{-6}$ s, an effective barrier $U_{eff} = 17.9 \pm 0.5$ cm^{-1} for the Orbach relaxation process, and the constant $A_K = 76.1 \pm 0.7\ s^{-1}K^{-1}$ for the direct process relaxation process.

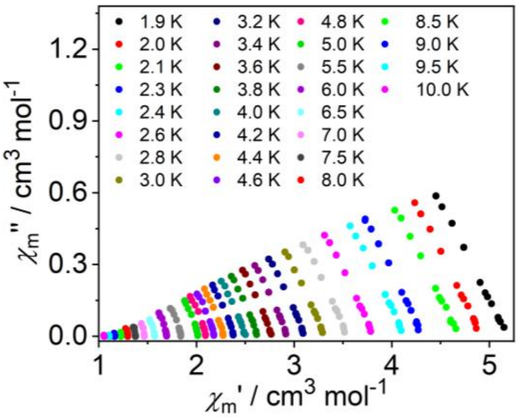

Fig 2.36 Cole-Cole plot of the molar magnetic ac susceptibility of **[4]** at zero static bias field.

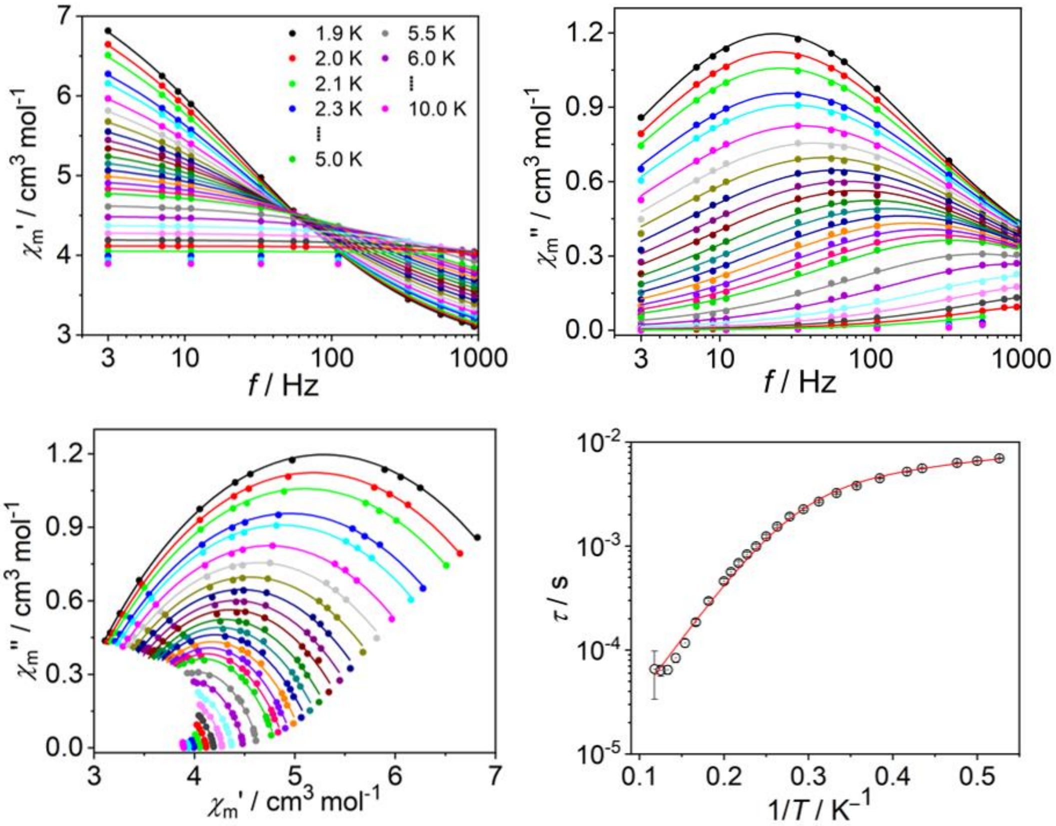

Fig 2.37 Molar magnetic ac susceptibility components of **[4]** in a static bias field of 500 Oe: **(top left)** in-phase (χ_m') molar magnetic susceptibility *vs.* frequency, **(top right)** out-of-phase (χ_m'') molar magnetic susceptibility *vs.* frequency, **(bottom left)** Cole-Cole plot of χ_m'' *vs.* χ_m', and **(bottom right)** Arrhenius plot of relaxation time τ *vs.* $1/T$.

Complex **[5]** also needs an induced dc-field to quench the relaxation process related to quantum tunneling of magnetization. However, even at the bias field of 800 Oe, the ac-data indicates at least two overlapping regimes of temperature and frequency-dependent slow relaxation processes. This manifests, e.g., in the almost constant behavior of χ_m'' at lower frequencies. Besides that, there are also some artifacts at higher frequencies at temperatures above 3–4 K. Thus, ac-data was analyzed (at 800 Oe static bias field) up to 3.0 K, which can be meaningfully analyzed within the range of the experimental set-up in terms of a generalized Debye expression[49]. This resulted in the relaxation times with a distribution $\alpha = 0.19 \pm 0.04$ with values between 0.16 and 0.24. The rather large error margins emphasize that the following analysis results have to be taken with extreme care. In particular, two different solutions can be found with similar fit qualities: assuming an Orbach or a Raman process besides a direct relaxation process yields the curves shown in **Fig 2.38** (bottom right) as red solid and blue dashed line, respectively. The first model is described by $\tau^{-1} = \tau_0^{-1}\exp(-U_{\mathrm{eff}}/k_{\mathrm{B}}T) + A_{\mathrm{nK}}T$, while the latter is by $\tau^{-1} = CT^n + A_{\mathrm{nK}}T$. The corresponding parameters of the least-squares fit are the attempt time $\tau_0 = (2.8 \pm 4.7) \times 10^{-8}$ s, the effective energy barrier $U_{\mathrm{eff}} = (13.8 \pm 3.2)$ cm^{-1} and the direct process constant $A_{\mathrm{nK}} = (8475 \pm 633)$ s^{-1}K^{-1}. The parameters employing Raman and direct relaxation processes are the constant $C = (21.2 \pm 39.1)$ s^{-1}K^{-n} and the exponent $n = 7.1 \pm 1.8$ for the Raman relaxation process, and $A_{\mathrm{nK}} = (7930 \pm 965)$ s^{-1}K^{-1} for the direct relaxation process.

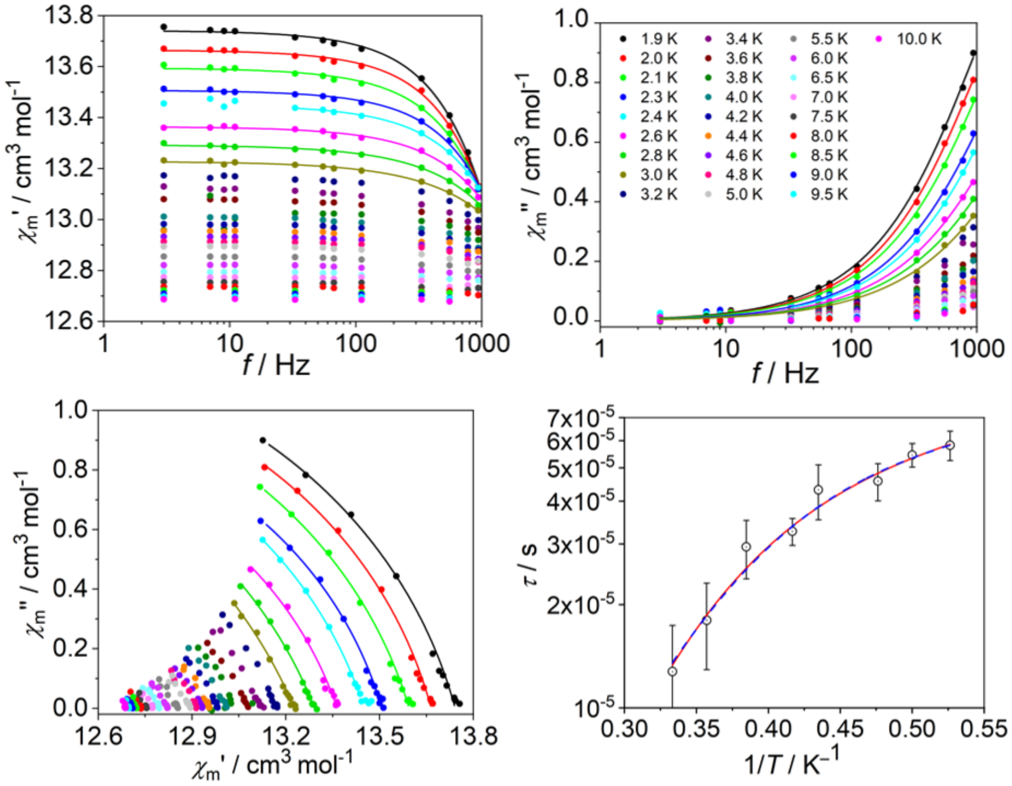

Fig 2.38 Molar magnetic ac susceptibility components of **[5]** at 500 Oe: **(top left)** in-phase (χ_m') molar magnetic susceptibility *vs.* frequency, **(top right)** out-of-phase (χ_m'') molar magnetic susceptibility *vs.* frequency, **(bottom left)** Cole-Cole plot of χ_m'' *vs.* χ_m', and **(bottom right)** Arrhenius plot of relaxation

time τ *vs.* $1/T$ (red solid line: fit to Raman and direct relaxation process, blue dashed line: fit to Orbach and direct relaxation process).

Direct current magnetic measurements (χ_mT vs. T and M_m vs. B plots) for complexes **[6]** and **[7]** are shown in **Fig 2.39**. At room temperature, the values of χ_mT (13.67 **[6]** and 11.99 **[7]** cm^3 K mol^{-1}) are consistent with the expected range for an isolated Dy(III) and Tb(III) ion.[48] Upon cooling, the χ_mT values of both complexes slowly decrease until about 100 K and then drop to the minimum value of 9.47 and 9.75 cm^3 K mol^{-1} for **[6]** and **[7]** respectively. This behavior can be attributed to the thermal depopulation of excited energy states of respective ground terms, which are splitted due to electron-electron repulsion, spin-orbit coupling, and ligand-field.

The molar magnetization M_m at 2.0 K and 5 T **(Fig 2.39**, right**)** show the value of 5.2 $N_A\mu_B$ for **[6]** and 4.7 $N_A\mu_B$ for **[7]**. These are less than the saturation value for Dy(III) (10 $N_A\mu_B$) and Tb(III) (9 $N_A\mu_B$), as expected for the powder samples of highly anisotropic lanthanide centers.

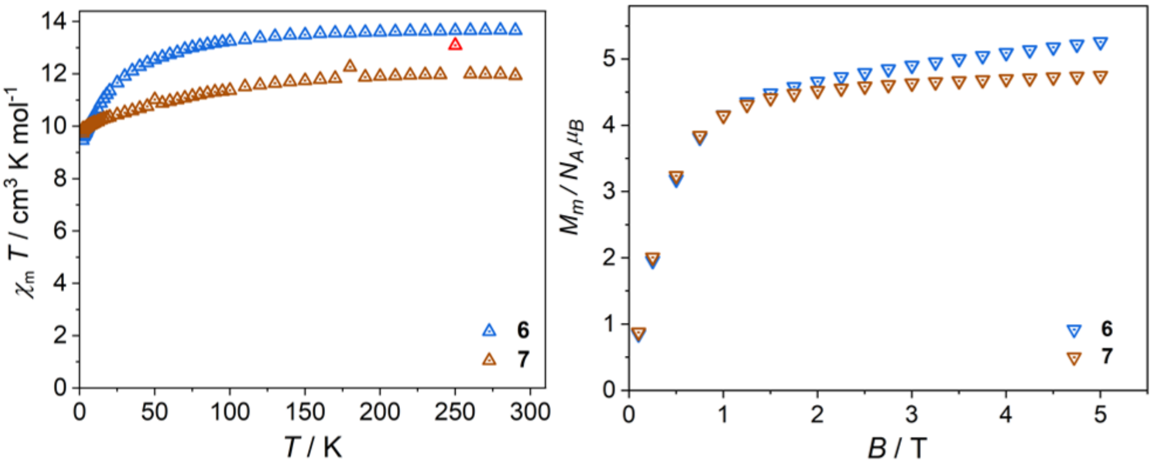

Fig 2.39 Dc-data for **[6]** and **[7]**: **(left)** χ_mT *vs.* T at 0.1 T, **(right)** M_m *vs.* B at 2 K.

Alternating current magnetic measurements on complexes **[6]** and **[7]** were also performed with and without static applied bias fields. Similar to analogous **[2]** and **[4]**, complex **[6]** shows the pronounced curvature in the signals at 500 static Oe bias field **(Fig 2.40)**. According to generalized Debye expression[49], the fitting of ac susceptibilities between 1.9 and 9.0 K extracted the relaxation times τ, which are plotted against the inverse of temperature $1/T$. The mean value of distribution parameter α is 0.40±0.09 with values between 0.16 and 0.47, which indicates the multiple relaxation pathways. Hence, considering a Raman and a direct relaxation processes adequately described the data, according to the formula $\tau^{-1} = CT^n + A_KT$. The least-squares fit yields the constant $C = (0.15\pm0.02)\ s^{-1}K^{-n}$ and the exponent $n = 5.8\pm0.1$ for the

Raman relaxation process, and A_K = (7.08±0.39) $s^{-1}K^{-1}$ for the direct relaxation process (at 500 Oe static bias field). Since Dy^{III} centers are Kramers systems, a Raman exponent of about six indicates an optical acoustic Raman process, i.e. optical and acoustic phonons are involved in the spin transition process.[50]

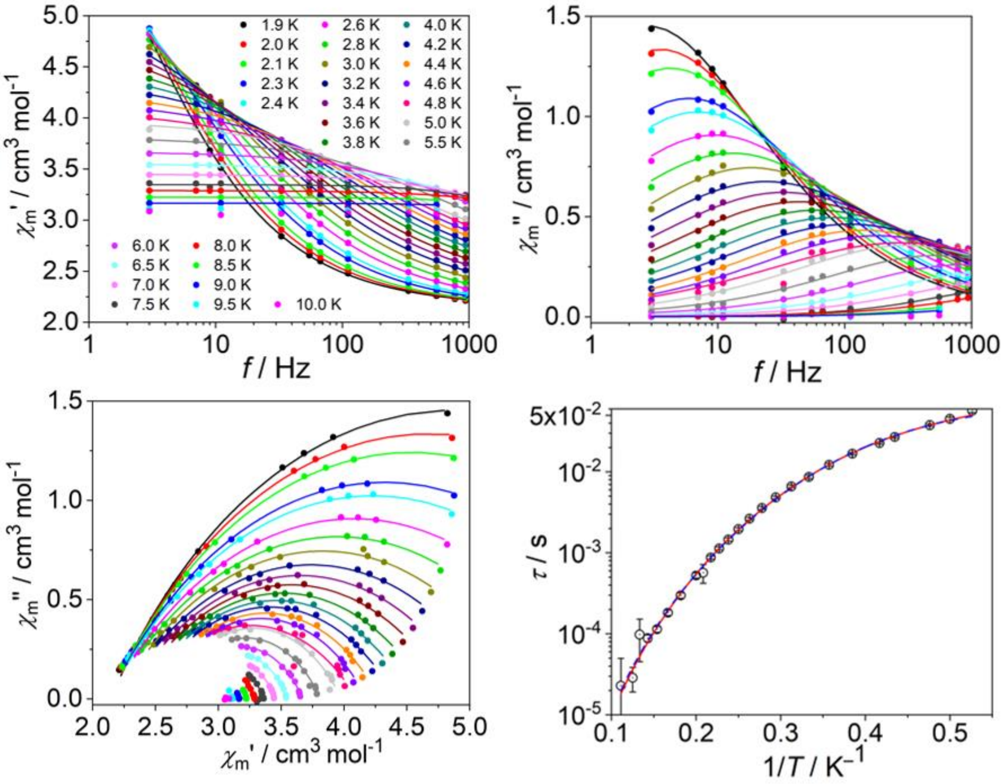

Fig 2.40 Molar magnetic ac susceptibility components of **[6]** at 500 Oe: **(top left)** in-phase (χ_m') molar magnetic susceptibility *vs.* frequency, **(top right)** out-of-phase (χ_m'') molar magnetic susceptibility *vs.* frequency, **(bottom left)** Cole-Cole plot of χ_m'' *vs.* χ_m', and **(bottom right)** Arrhenius plot of relaxation time τ *vs.* $1/T$.

Similar to complex **[5]**, the ac-data of **[7]** also indicates at least two overlapping regimes of temperature and frequency dependent slow relaxation processes. The data was analyzed up to 3.8 K resulting in the relaxation times **(Fig 2.41**, bottom right**)** with a distribution α = 0.12±0.03 (range 0.09–0.16), which are best described by a Raman and a direct relaxation process, i.e. $\tau^{-1} = CT^n + A_{nK}T$. The least-squares fit parameters are C = (255±197) $s^{-1}K^{-n}$, n = 4.2±0.7 and A_{nK} = (3214±835) $s^{-1}K^{-1}$. The data, thus, seem to prefer an optical acoustic Raman process[50] (similar to **5**) due to the exponent of about four and Tb^{III} centers being non-Kramers systems, although the results are rather vague considering the error margins and found values.

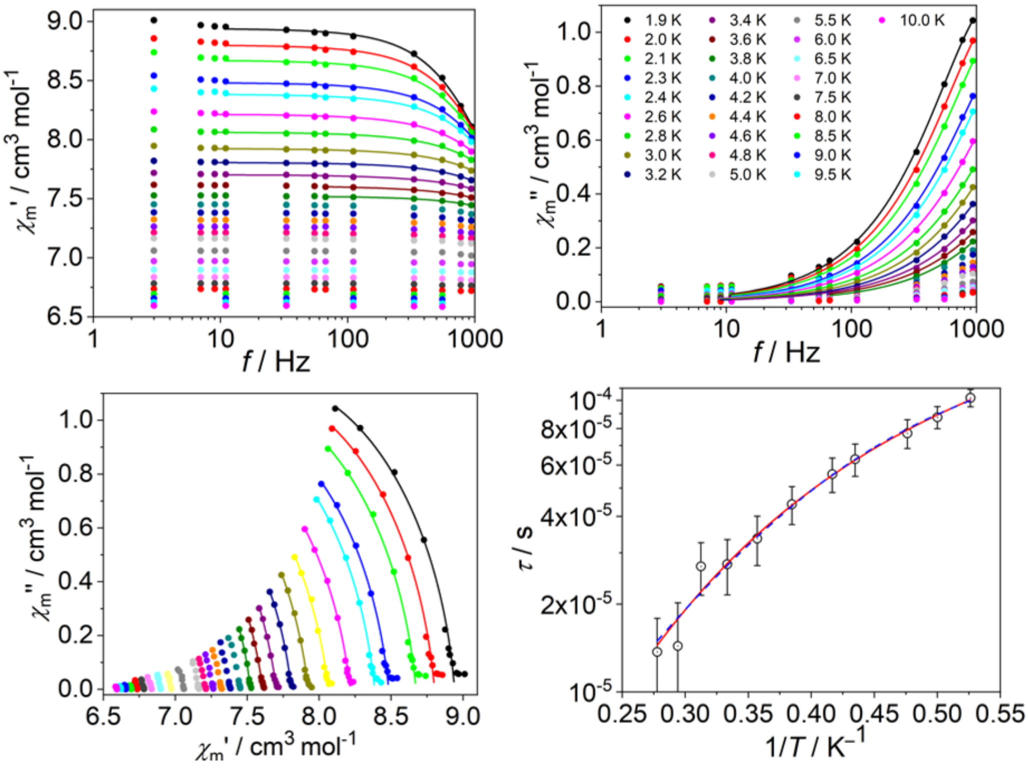

Fig 2.41 Molar magnetic ac susceptibility components of **[7]** at 800 Oe: **(top left)** χ_m' *vs.* *f*, **(top right)** in-phase (χ_m') molar magnetic susceptibility *vs.* frequency, **(top right)** out-of-phase (χ_m'') molar magnetic susceptibility *vs.* frequency, **(bottom left)** Cole-Cole plot of χ_m'' *vs.* χ_m', and **(bottom right)** Arrhenius plot of relaxation time τ *vs.* $1/T$.

Comparing these results to the homoleptic double-decker complexes, *i.e.* $[Dy^{III}(H_{16}Pc)_2]^-$ and $[Dy^{III}(PW_{11}O_{39})_2]^{11-}$ displaying slow magnetic relaxation (U_{eff} = 28 and 38.2 cm^{-1} and τ_0 = 6.25 × 10^{-6} and 9.6× 10^{-12} s respectively)[7,51], the U_{eff} value of **[2]** is the average of both complexes. However, in contrast to $[Dy^{III}(PW_{11}O_{39})_2]^{11-}$, it shows well-resolved maxima in ac-measurements at much smaller dc-field (500 Oe *vs.* 3000 Oe). Furthermore, the results of three Dy(III) analogues **[2]**, **[4]**, and **[6]**, indicate that changing the electron density on Pc-ring does not affect the strength of the applied dc-field. However, the electron-donation due to di-*iso*-propylphenoxy groups in **[4]** suppresses the Raman relaxation process, and slightly changes the parameters of the Orbach (~ 2/3×U_{eff}, 30×τ_0 with respect to the unsubstituted analogue **[2]**) and increases the relaxation through a direct relaxation process (~ 8×A_K). Whereas, a decrease in electron-density in **[6]** due to peripheral fluorine atoms suppresses the Orbach relaxation process, marginally changes the parameters of the direct relaxation process, and prefers a different Raman relaxation process including optical and acoustic phonons ($n \approx 6$ instead of 5) and a slightly larger amplitude C (in relation to the exponent about a factor of 3–4).

The behavior of Tb(III) analogues is significantly different from $[Tb^{III}(H_{16}Pc)_2]^-$ complex, which exhibits a high energy barrier (U_{eff} = 230 cm^{-1}) to magnetic relaxation.[7] There are various factors to rationalize the results, including the ligand-field around lanthanide center, as the coordination of anionic POT changes the electron density around the lanthanide and provides a different ligand-field. Additionally, in the case of lanthanide sandwiched-complexes, an ideal D_{4d} symmetry has been crucial for getting high values of the energy barrier for magnetic relaxation. As indicated by the crystal structure of complex **[3]**, Pc- and POT-units are deviating from coplanarity with a value of 5.73°, indicating distorted square antiprism. These distortions may contribute to the fast relaxation observed in the complexes. However, the difficulty in getting the crystal structure of derivatized complexes hampers the magnetostructural correlation.

2.3 Conclusions

In summary, a new family of monometallic double-decker complexes **[1–7]** with the general formula $[Ln^{III}(Pc)(PW_{11}O_{39})]^{6-}$ was synthesized by reacting tetra-*n*-butylammonium salt of monolacunary phosphotungstate and lanthanide(III) single-decker of phthalocyanine in the presence of triethylamine as a base. The complexes were characterized by NMR, EA, ESI-MS, IR, TGA, UV-Vis, and CV. The crystal structures of $[Ln^{III}(H_{16}Pc)(PW_{11}O_{39})]^{6-}$ (Ln = Tb and Y) showed the octacoordination around the metal center with a slightly distorted square antiprismatic geometry. The possibility to derivatize the periphery of Pc-ring allowed to study the influence of the electronic nature of substituents on the properties of hybrid complexes. In **[4–7]**, the periphery of Pc-ring was substituted with electron-donating (2,6-di-*iso*-propylphenoxy) and electron-withdrawing (fluorine) groups. This derivatization caused the obvious shifting of frontier orbitals as demonstrated by UV-Vis absorption spectra and redox potentials of complexes. Alternating current magnetic measurements revealed the SMM behavior with pronounced ac-signals of dysprosium analogues; each favoring different relaxation processes due to the different electron density on Pc-ring. The results of thermogravimetric analyses indicated the thermal stability of complexes up to ~200 °C.

The presence of phthalocyanine, a highly suitable molecule for surface deposition due to its quasiplanar conjugated aromatic structure, and polyoxotungstate, which is expected to provide magnetic isolation,[52] presents a possibility to explore the potential applications of hybrid complexes in the field of molecular electronics, spintronics, or spin qubits. Furthermore, the observation of slow magnetic relaxation in dysprosium analogues certainly attracts further interest for the fabrication of hybrid complexes with other lacunary POMs to study their magnetic response.

2.4 Experimental

2.4.1 Materials and instrumentation

The reagents were used as received from commercial suppliers. High-grade solvents were obtained from an SPS 800 (MBraun) solvent purification system. The reactions were performed under an inert atmosphere using Schlenk techniques. Tetra-*n*-butylammonium hexafluorophosphate (NBu_4PF_6), used as an electrolyte for cyclic voltammetry measurements, was recrystallized in dichloromethane.

NMR experiments were performed on a Bruker Advance 600 MHz spectrometer equipped with a CryoProbe Prodigy operating at 600.15 MHz for ^{1}H-NMR, 242.95 MHz for ^{31}P-NMR, and 564.6 MHz for ^{19}F-NMR. Matrix-assisted laser desorption ionization mass spectra (MALDI-MS) were recorded on a MALDI LTQ-Orbitrap XL^{TM} instrument with a hybrid linear ion trap (LTQ) and an Orbitrap analyzer. Electrospray ionization mass spectra (ESI-MS) were obtained using hybrid mass spectrometer LTQ-FT Ultra^{TM} with a linear ion trap and FT-ICR mass spectrometer. The Fourier-transform infrared spectra (FT-IR) were collected on a Bruker Vertex 70 spectrometer using KBr pellets of compounds. Wavenumbers (ν) are given in cm^{-1}; intensities are labelled as s = strong, m = medium, w = weak. CHN-content was measured by combustion analysis using VarioelCube Elementar and ICS-3000 Thermo Fisher was used for quantification of fluorine. Elemental analyses, NMR, and ESI-MS were performed by the Central Institute for Engineering, Electronics, and Analytics (ZEA-3) Forschungszentrum Jülich, Germany. Thermogravimetric analyses (TGA) were carried out on NETZSCH TG 209F1 Libra under N_2 (20 mL/min) and a heating rate of 5 K/min. The electronic absorption spectra were collected using Shimadzu UV-3600 plus spectrophotometer with 1-cm quartz glass cuvettes. Cyclic voltammetry experiments were recorded on a Biologic SP-150 potentiostat using EC-Lab software V.11.12. The three-electrode cell consisted of a glassy carbon working electrode with a diameter of 3.0 mm and two Pt wires. The solutions were purged with argon before recording the voltammograms. Plotted data were corrected for ohmic drop (PEIS method) and referenced *vs.* $[Cp_2Fe]/[Cp_2Fe]^+$. Single crystal X-ray diffraction data were collected using the I-19 beamline of Diamond Light Source, Southampton (UK). Crystals were mounted on a MITIGEN holder in Paratone oil. The crystal was kept at a steady

$T = 100.0$ K during data collection. The structures were solved with the ShelXT solution[53] program using dual methods and by using Olex2[54] as the graphical interface. The models were refined with ShelXL 2018/3[55] using full-matrix least-squares minimization on F^2. Magnetic measurements were recorded using Quantum Design MPMS-5XL SQUID magnetometer for direct current (dc) and alternating current (ac) measurements. Powder and microcrystalline samples were compacted and immobilized into cylindrical PTFE sample holders. Experimental dc-data were recorded at 0.1 T and 1.0 T in the temperature range 2–290 K and at 2.0 K in the field range 0–5 T. Experimental ac-data were collected at various static bias fields between 0 and 1000 Oe in the temperature range 1.9–50 K and frequency range 3–937 Hz using an amplitude of $B_{ac} = 3.5$ Oe.

2.4.2 Synthesis of $(NBu_4)_4H_2[Y^{III}(H_{16}Pc)(PW_{11}O_{39})]$ (1)

A completely soluble solution of $(NBu_4)_4H_3[PW_{11}O_{39}]$ (0.36 g, 0.1 mmol), NBu_4Br (64.4 mg, 0.2 mmol) and NEt_3 (0.2 mL, 1.5 mmol) in 10 mL acetonitrile was dropwise added to a flask containing $[Y^{III}(H_{16}Pc)(OAc)]$ (66 mg, 0.1 mmol) in 20 mL mixture of dichloromethane/methanol (1:1). The resulting solution was heated overnight at 50 °C under argon. The green reaction mixture was filtered and evaporated under reduced pressure. The product was precipitated by the addition of pentane into the dichloromethane solution and further purified by silica column chromatography using the eluent mixture of dichloromethane/acetone (1:1). Yield (89 mg, 21 %). **^{1}H-NMR** (600 MHz, CD_3CN): δ 9.52 (bs, 8H, H–α), 8.21 (bs, 8H, *H*–β), 3.03–3.00 (m, 45H, CH_{2TBA}), 1.54–1.49 (m, 45H, CH_{2TBA}), 1.31–1.28 (m, 45H, CH_{2TBA}), 0.92–0.89 (t, 67H, CH_{3TBA}) ppm. **^{31}P-NMR** (243 MHz, CD_3CN): δ –14.64 ppm. **Elemental analysis** (%) calculated for $C_{96}H_{162}N_{12}O_{39}PW_{11}Y$: C 27.13, H 3.84, N 3.95. Found: C 27.42, H 4.07, N 4.01. **ESI-HRMS** *m/z*: found 1093.7730 $[M + 3H]^{3-}$ (55 %), calculated for $[C_{32}H_{19}N_8O_{39}PW_{11}Y]^{3-}$ 1093.7733; found 1174.5303 $[M + NBu_4 + 2H]^{3-}$ (100 % relative abundance), calculated for $[C_{48}H_{54}N_9O_{39}PW_{11}Y]^{3-}$ 1174.5311. M stands for $[Y^{III}(H_{16}Pc)(PW_{11}O_{39})]^{6-}$. **IR** (KBr, cm^{-1}): 2959 (m), 2930 (w), 2871 (m), 1630 (m), 1483(m), 1459 (m), 1379 (w), 1327 (m), 1280 (w), 1158 (w), 1101 (m), 1057 (m), 952 (s), 890 (m), 802 (s), 732 (m), 515 (w). **UV-Vis** {CH_2Cl_2, λ / nm and ε / 10^4 M^{-1} cm^{-1} (in parentheses)}: 258 (5.0), 351 (3.3), 692.5 (7.49), 710 (5.8).

2.4.3 Synthesis of $(NBu_4)_4H_2[Dy^{III}(H_{16}Pc)(PW_{11}O_{39})]$ (2)

The Dy-analogue was synthesized following the same procedure as described for $(NBu_4)_4H_2[Y^{III}(H_{16}Pc)(PW_{11}O_{39})]$, except that $[Dy^{III}(H_{16}Pc)(OAc)]$ (73 mg, 0.1 mmol) was used instead of $[Y^{III}(H_{16}Pc)(OAc)]$. Yield (81 mg, 18 %). **Elemental analysis** (%) calculated for $C_{96}H_{162}N_{12}O_{39}PW_{11}Dy$: C 26.67, H 3.78, N 3.89. Found: C 26.90, H 3.86, N 3.64. **ESI-HRMS** *m/z*: found 1198.8733 $[M + NBu_4 + 2H]^{3-}$ (100 % relative abundance), calculated for $[C_{48}H_{54}N_9O_{39}PW_{11}Dy]^{3-}$ 1198.8732; found 1278.9644 $[M + 2NBu_4 + 1H]^{3-}$ (90 %), calculated for $[C_{64}H_{89}N_{10}O_{39}PW_{11}Dy]^{3-}$ 1278.9649. $M = [Dy^{III}(H_{16}Pc)(PW_{11}O_{39})]^{6-}$. **IR** (KBr, cm^{-1}): 2959 (w), 2925 (m), 2856 (w), 1632 (m), 1483(m), 1458 (m), 1379 (w), 1326 (m), 1280 (w), 1164 (w), 1096 (m), 1056 (m), 953 (s), 886 (m), 800 (s), 730 (m), 514 (w). **UV-Vis** {CH_2Cl_2, λ / nm and ε / 10^4 M^{-1} cm^{-1} (in parentheses)}: 259 (5.1), 352.5 (3.4), 693 (7.45), 711 (6.0).

2.4.4 Synthesis of $(NBu_4)_4H_2[Tb^{III}(H_{16}Pc)(PW_{11}O_{39})]$ (3)

The Tb-analogue was synthesized following the same procedure as described for $(NBu_4)_4H_2[Y^{III}(H_{16}Pc)(PW_{11}O_{39})]$, except that $[Tb^{III}(H_{16}Pc)(OAc)]$ (73 mg, 0.1 mmol) was used instead of $[Y^{III}(H_{16}Pc)(OAc)]$. Yield (85 mg, 19 %). **Elemental analysis** (%) calculated for $C_{96}H_{162}N_{12}O_{39}PW_{11}Tb$: C 26.69, H 3.78, N 3.89. Found: C 26.70, H 3.84, N 3.68. **ESI-HRMS** *m/z*: found 1197.8721 $[M + NBu_4 + 2H]^{3-}$ (100 % relative abundance), calculated for $[C_{48}H_{54}N_9O_{39}PW_{11}Tb]^{3-}$ 1197.8726; found 1917.9501 $[M + 2NBu_4 + 2H]^{2-}$ (50 %), calculated for $[C_{64}H_{90}N_{10}O_{39}PW_{11}Tb]^{2-}$ 1917.9511. $M = [Tb^{III}(H_{16}Pc)(PW_{11}O_{39})]^{6-}$. **IR** (KBr, cm^{-1}): 2959 (w), 2923 (s), 2853 (m), 1633 (m), 1483(m), 1457 (m), 1379 (w), 1326 (m), 1280 (w), 1164 (w), 1094 (m), 1056 (m), 952 (s), 888 (m), 799 (s), 730 (m), 514 (w). **UV-Vis** {CH_2Cl_2, λ / nm and ε / 10^4 M^{-1} cm^{-1} (in parentheses)}: 258.5 (4.9), 350 (3.5), 692 (7.26), 713 (5.98).

2.4.5 Synthesis of $(NBu_4)_6[Dy^{III}(i\mathrm{Pr}_2Pc)(PW_{11}O_{39})]$ (4)

A completely soluble solution of $(NBu_4)_4H_3[PW_{11}O_{39}]$ (0.36 g, 0.1 mmol), NBu_4Br (64.4 mg, 0.2 mmol) and NEt_3 (0.2 mL, 1.5 mmol) in 10 mL acetonitrile was dropwise added to a flask containing $[Dy^{III}(i\mathrm{Pr}_2Pc)(OAc)]$ (0.21 g, 0.1 mmol) in 20 mL of dichloromethane/methanol (1:1). The resulting solution was heated overnight at 50 °C under argon. The green reaction mixture was filtered and evaporated under reduced pressure. The product was precipitated by the addition of pentane into the dichloromethane solution and further purified by silica column chromatography using an eluent mixture of dichloromethane/acetone (1:1). Yield (144 mg, 24 %). **Elemental analysis** (%) calculated for $C_{224}H_{360}N_{14}O_{47}PW_{11}Dy$: C 43.27, H 5.84, N 3.15. Found: C 43.6, H 5.96, N 2.97. **ESI-HRMS** *m/z*: found 1588.1017 $[M + 3H]^{3-}$ (100 % relative abundance), calculated for $[C_{128}H_{147}N_8O_{47}PW_{11}Dy]^{3-}$ 1588.1015; found 1668.5262 $[M + 1NBu_4 + 2H]^{3-}$ (64 %), calculated for $[C_{144}H_{182}N_9O_{47}PW_{11}Dy]^{3-}$ 1668.5272. $M = [Dy^{III}(iPr_2Pc)(PW_{11}O_{39})]^{6-}$. **IR** (KBr, cm^{-1}): 2960 (m), 2923 (s), 2857 (w), 1630 (m), 1458 (m), 1440(m), 1396 (m), 1329 (w), 1267 (m), 1185 (m), 1095 (m), 1041(w), 954 (m), 885 (m), 820 (s), 745(w), 723 (w), 515 (w). **UV-Vis** {CH_2Cl_2, λ / nm and ε / 10^4 M^{-1} cm^{-1} (in parentheses)}: 251 (7.1), 359 (4.2), 375 (4.0), 698 (5.0), 729.5 (6.95).

2.4.6 Synthesis of $(NBu_4)_6[Tb^{III}(iPr_2Pc)(PW_{11}O_{39})]$ (5)

The Tb-analogue was synthesized following the same procedure as described for $(NBu_4)_6[Dy^{III}(iPr_2Pc)(PW_{11})]$, except that $[Tb^{III}(iPr_2Pc)(OAc)]$ (0.21 g, 0.1 mmol) was used instead of $[Dy^{III}(iPr_2Pc)(OAc)]$. Yield (139 mg, 23 %). **Elemental analysis** (%) calculated for $C_{224}H_{360}N_{14}O_{47}PW_{11}Tb$: C 43.3, H 5.84, N 3.16. Found: C 43.62, H 5.96, N 2.98. **ESI-HRMS** *m/z*: found 1587.1026 $[M + 3H]^{3-}$ (100 % relative abundance), calculated for $[C_{128}H_{147}N_8O_{47}PW_{11}Tb]^{3-}$ 1587.1008; found 1667.5277 $[M + 1NBu_4 + 2H]^{3-}$ (57 %), calculated for $[C_{144}H_{182}N_9O_{47}PW_{11}Tb]^{3-}$ 1667.5266. $M = [Tb^{III}(iPr_2Pc)(PW_{11}O_{39})]^{6-}$. **IR** (KBr, cm^{-1}): 2960 (m), 2923 (s), 2857 (w), 1632 (m), 1458 (m), 1440 (m), 1393 (m), 1329 (w), 1265 (m), 1184 (m), 1096 (m), 1042(s), 954 (m), 885 (m), 829 (s), 745(w), 723 (w), 515 (w). **UV-Vis** {CH_2Cl_2, λ / nm and ε / 10^4 M^{-1} cm^{-1} (in parentheses)}: 253 (5.5), 361 (3.3), 376 (3.4), 699 (4.4), 729 (6.7).

2.4.7 Synthesis of $[Mg^{II}F_8Pc]$

A well grinded mixture of 4,5-difluorophthalonitrile (0.5 g, 3 mmol) and $Mg(OAc)_2.4H_2O$ (0.16 g, 0.76 mmol) was pressed into pellets. The pellets were placed in an evacuated glass tube, which was sealed under vacuum and heated overnight at 270 °C. At this temperature, 4,5-difluorophthalonitrile cyclotetramerized to magnesium(II) phthalocyanine as a result of two-electron transfer from magnesium to Pc-ring. The reaction also produced a small amount of free-base octafluorinated phthalocyanine. Upon cooling, the crude mixture was washed with methanol and water. Yield (0.47 g, 92 %). **MALDI-MS** *m/z*: found 680.057 $[M - 1e]^+$ (100 % relative abundance), calculated for $[C_{32}H_8F_8N_8Mg]^+$ 680.058; found 658.087 $[M - Mg + 2H - 1e]^+$ (44 % relative abundance), calculated for $[C_{32}H_{10}F_8N_8]^+$ 658.089. M stands for [$Mg^{II}F_8Pc$]. **IR** (KBr, cm^{-1}): 1619 (m), 1479 (m), 1374 (w), 1321 (w), 1283 (w), 1178 (w), 1078 (m), 1009 (m), 882 (w), 744 (m). **UV-Vis** {DMSO, λ / nm}: 337, 601, 660.

2.4.8 Synthesis of [F_8Pc]

The magnesium complex (0.5 g, 0.73 mmol) was dissolved in 25 mL of concentrate sulfuric acid. The mixture was stirred for about half an hour at room temperature followed by the addition of ice-cold water. A blue-colored precipitate was filtered and, washed with water and methanol. Yield (0.32 g, 66 %). **MALDI-MS** *m/z*: found 657.085 [M – 1H]$^-$ (100 % relative abundance), calculated for [$C_{32}H_{10}F_8N_8$]$^-$ 657.083. M = [F_8Pc]. **^{19}F-NMR** (565 MHz, $(CD_3)_2SO$: δ –128.30 ppm (t, J = 7.7 Hz, 8F). **IR** (KBr, cm^{-1}): 1621 (m), 1479 (m), 1374 (w), 1321 (w), 1283 (w), 1178 (w), 1080 (m), 1009 (m), 882 (w), 789 (w), 744 (m). **UV-Vis** {DMSO, λ / nm}: 320, 594, 680.

2.4.9 Synthesis of [$Dy^{III}(F_8Pc)(OAc)(DBU)$]

A mixture of F_8Pc (0.25 g, 0.37 mmol) and dysprosium(III) acetate hydrate (0.23 g, 0.56 mmol) along with DBU (0.28 mL, 1.9 mmol) was heated at 180 °C in 7 mL of *o*-DCB for 2 hours under argon. Upon cooling to room temperature, pentane was added to the reaction mixture and the resulting precipitate was filtered. The blue product was purified by repeated silica column chromatography using chloroform/methanol as an eluent (95:5). Yield (22 mg, 5.8 %). **MALDI-MS** *m/z*: found 938.024, [M – DBU + OAc]$^-$ (74 % relative abundance), calculated for [$C_{36}H_{14}F_8N_8O_4Dy$]$^-$ 938.031; found 1038.153 [M + Li + 2e]$^-$ (49 %), calculated for [$C_{43}H_{27}F_8N_{10}O_2DyLi$]$^-$ 1038.164; found 1476.080 [M – OAc – DBU + F_8Pc]$^-$ (15 %), calculated for [$C_{64}H_{16}F_{16}N_{16}Dy$]$^-$ 1476.079. M = [$Dy^{III}(F_8Pc)(OAc)(DBU)$]. **^{19}F-NMR** (565 MHz, $(CD_3)_2SO$: δ –144. 83 (bs, 4F), δ –148. 16 (bs, 4F) ppm. **IR** (KBr, cm^{-1}): 2924 (w), 2853 (w), 1621 (s), 1492 (m), 1465 (m), 1412 (m), 1330 (w), 1276 (w), 1177 (w), 1073 (m), 1023 (w), 860 (w), 811 (m), 747 (w), 715 (w). **UV-Vis** {CH_2Cl_2, λ / nm and ε / 10^4 M^{-1} cm^{-1} (in parentheses)}: 260 (1.1), 342 (1.1), 602 (3.6), 663 (2.0).

2.4.10 Synthesis of [$Tb^{III}(F_8Pc)(OAc)(DBU)$]

The Tb-analogue was synthesized following the same procedure as described for [$Dy^{III}(F_8Pc)(OAc)(DBU)$], except that terbium(III) acetate hydrate (0.23 g, 0.56 mmol) was used instead of [$Dy(OAc)_3.nH_2O$]. Yield (21 mg, 5.3 %). **MALDI-MS** *m/z*: found 933.024

[M – DBU + OAc]$^{1–}$ (77 % relative abundance), calculated for [$C_{36}H_{14}F_8N_8O_4Tb$]$^{–}$ 933.026; found 1033.151 [M + Li + 2e]$^{–}$ (44 %), calculated for [$C_{43}H_{27}F_8N_{10}O_2TbLi$]$^{–}$ 1033.160; found 1471.074 [M – OAc – DBU + F_8Pc]$^{–}$ (16 %), calculated for [$C_{64}H_{16}F_{16}N_{16}Tb$]$^{–}$ 1471.074. M = [Tb^{III}(F_8Pc)(OAc)(DBU)]. **^{19}F-NMR** (565 MHz, $(CD_3)_2SO$: δ –149. 04 (bs, 4F), δ –154. 63 (bs, 4F) ppm. **IR** (KBr, cm$^{–1}$): 2923 (w), 2852 (w), 1621 (s), 1492 (m), 1463 (m), 1412 (m), 1382 (w), 1329 (w), 1276 (w), 1175 (w), 1073 (m), 1021 (m), 859 (w), 810 (m), 747 (w), 714 (w). **UV-Vis** {CH_2Cl_2, λ / nm and ε / 10^4 M$^{–1}$ cm$^{–1}$ (in parentheses)}: 263 (0.57), 343 (0.98), 601 (3.6), 662 (2.1).

2.4.11 Synthesis of $(NBu_4)_6$[Dy^{III}(F_8Pc)($PW_{11}O_{39}$)] (6)

A completely soluble solution of $(NBu_4)_4H_3[PW_{11}O_{39}]$ (0.36 g, 0.1 mmol), NBu_4Br (64.4 mg, 0.2 mmol) and NEt_3 (0.2 mL, 1.5 mmol) in 10 mL acetonitrile was dropwise added to a flask containing [Dy^{III}(F_8Pc)(OAc)(DBU)] (104 mg, 0.1 mmol) in a 20 mL mixture of dichloromethane/methanol (1:1). The resulting solution was heated overnight at 50 °C under argon. The green reaction mixture was filtered and evaporated under reduced pressure. The product was precipitated by the addition of pentane into the dichloromethane solution and, further purified by silica column chromatography using an eluent mixture of dichloromethane/acetone (1:1). Yield (82 mg, 16 %). **Elemental analysis** (%) calculated for $C_{128}H_{224}F_8N_{14}O_{39}PW_{11}Dy$: C 31.05, H 4.56, N 3.96, F 3.07. Found: C 30.76, H 4.37, N 3.83, F 3.15. **ESI-HRMS** *m/z*: found 1327.2712 [M + 2NBu_4 + 1H]$^{3–}$ (100 % relative abundance), calculated for [$C_{64}H_{81}F_8N_{10}O_{39}PW_{11}Dy$]$^{3–}$ 1327.2738; found 1246.8455 [M + 1NBu_4 + 2H]$^{3–}$ (37 %), calculated for [$C_{48}H_{46}F_8N_9O_{39}PW_{11}Dy$]$^{3–}$ 1246.8481. M = [Dy^{III}(F_8Pc)($PW_{11}O_{39}$)]$^{6–}$. **IR** (KBr, cm$^{–1}$): 2961 (w), 2925 (w), 2872 (w), 1620 (m), 1480 (m), 1463 (m), 1412 (m), 1382 (w), 1329 (w), 1276 (w), 1176 (w), 1070 (w), 1025 (w), 953 (m), 890 (w), 810 (s), 747 (w), 721 (w), 516 (w). **UV-Vis** {CH_2Cl_2, λ / nm and ε / 10^4 M$^{–1}$ cm$^{–1}$ (in parentheses)}: 260 (3.5), 339 (2.5), 597.5 (1.2), 661 (7.26).

2.4.12 Synthesis of $(NBu_4)_6[Tb^{III}(F_8Pc)(PW_{11}O_{39})]$ (7)

The Tb-analogue was synthesized following the same procedure as described for $(NBu_4)_6[Dy^{III}(F_8Pc)(PW_{11}O_{39})]$, except that $[Tb^{III}(F_8Pc)(OAc)(DBU)]$ (103 mg, 0.1 mmol) was used instead of $[Dy^{III}(F_8Pc)(OAc)]$. Yield (91 mg, 18 %). **Elemental analysis** (%) calculated for $C_{128}H_{224}F_8N_{14}O_{39}PW_{11}Tb$: C 31.07, H 4.56, N 3.96, F 3.07. Found: C 30.79, H 4.37, N 3.81, F 3.14. **ESI-HRMS** *m/z*: found 1245.5109 $[M + 1NBu_4 + 2H]^{3-}$ (100 % relative abundance), calculated for $[C_{48}H_{46}F_8N_9O_{39}PW_{11}Tb]^{3-}$ 1245.5134; found 1325.9392 $[M + 2NBu_4 + 1H]^{3-}$ (91 %), calculated for $[C_{64}H_{81}F_8N_{10}O_{39}PW_{11}Tb]^{3-}$ 1325.9391. M = $[Tb^{III}(F_8Pc)(PW_{11}O_{39})]^{6-}$. **IR** (KBr, cm^{-1}): 2960 (w), 2923 (m), 2870 (w), 1621 (m), 1480 (m), 1462 (m), 1412 (w), 1382 (w), 1328 (w), 1273 (w), 1175 (w), 1072 (w), 1023 (w), 952 (m), 892 (w), 809 (s), 746 (w), 720 (w), 516 (w). **UV-Vis** {CH_2Cl_2, λ / nm and ε / 10^4 M^{-1} cm^{-1} (in parentheses)}: 260 (3.9), 340 (2.3), 597 (1.2), 661 (7.26).

2.5 References

1. G. Christou, D. Gatteschi, D. N. Hendrickson and R. Sessoli, *MRS Bull.*, 2000, **25**, 66-71.
2. L. Bogani and W. Wernsdorfer, *Nat. Mater.*, 2008, **7**, 179.
3. M. Urdampilleta, N.-V. Nguyen, J.-P. Cleuziou, S. Klyatskaya, M. Ruben and W. Wernsdorfer, *Int. J. Mol. Sci.*, 2011, **12**, 6656-6667.
4. A. Gaita-Ariño, F. Luis, S. Hill and E. Coronado, *Nat. Chem.*, 2019, **11**, 301-309.
5. S. Yanlin and Z. Daoben, *High density data storage: Principle, Technology, and Materials*, World Scientific, 2009.
6. D. Gatteschi, R. Sessoli and J. Villain, *Molecular nanomagnets*, Oxford University Press on Demand, 2006.
7. N. Ishikawa, M. Sugita, T. Ishikawa, S.-Y. Koshihara and Y. Kaizu, *J. Amer. Chem. Soc.*, 2003, **125**, 8694-8695.
8. D. N. Woodruff, R. E. P. Winpenny and R. A. Layfield, *Chem. Rev.*, 2013, **113**, 5110-5148.
9. J. Tang and P. Zhang, in *Lanthanide Single Molecule Magnets*, Springer, Heidelberg, 2015, ch. 2, pp. 41-90.
10. J. D. Rinehart and J. R. Long, *Chem. Sci.*, 2011, **2**, 2078-2085.
11. J.-L. Liu, Y.-C. Chen and M.-L. Tong, *Chem. Soc. Rev.*, 2018, **47**, 2431-2453.
12. C. R. Ganivet, B. Ballesteros, G. de la Torre, J. M. Clemente-Juan, E. Coronado and T. Torres, *Chem. Eur. J.*, 2013, **19**, 1457-1465.
13. M. Gonidec, I. Krivokapic, J. Vidal-Gancedo, E. S. Davies, J. McMaster, S. M. Gorun and J. Veciana, *Inorg. Chem.*, 2013, **52**, 4464-4471.
14. Y. Chen, F. Ma, X. Chen, B. Dong, K. Wang, S. Jiang, C. Wang, X. Chen, D. Qi and H. Sun, *Inorg. Chem.*, 2017, **56**, 13889-13896.

15. Y. Chen, F. Ma, X. Chen, Y. Zhang, H. Wang, K. Wang, D. Qi, H.-L. Sun and J. Jiang, *Inorg. Chem.*, 2019, **58**, 2422-2429.

16. F. Gao, X. Feng, L. Yang and X. Chen, *Dalton Trans.*, 2016, **45**, 7476-7482.

17. H. Wang, K. Wang, J. Tao and J. Jiang, *Chem. Commun.*, 2012, **48**, 2973-2975.

18. H. Wang, W. Cao, T. Liu, C. Duan and J. Jiang, *Chem. Eur. J.*, 2013, **19**, 2266-2270.

19. W. Cao, Y. Zhang, H. Wang, K. Wang and J. Jiang, *RSC Adv.*, 2015, **5**, 17732-17737.

20. W. Cao, C. Gao, Y.-Q. Zhang, D. Qi, T. Liu, K. Wang, C. Duan, S. Gao and J. Jiang, *Chem. Sci.*, 2015, **6**, 5947-5954.

21. C. Costa-Coquelard, S. Sorgues and L. Ruhlmann, *J. Phys. Chem. A.*, 2010, **114**, 6394-6400.

22. Y. Yang, L. Xu, F. Li, X. Du and Z. Sun, *J. Mat. Chem.*, 2010, **20**, 10835-10840.

23. L. Xu, E. Wang, Z. Li, D. G. Kurth, X. Du, H. Zhang and C. Qin, *New. J. Chem.*, 2002, **26**, 782-786.

24. I. Radivojevic, K. Ithisuphalap, B. P. Burton-Pye, R. Saleh, L. C. Francesconi and C. M. Drain, *RSC Adv.*, 2013, **3**, 2174-2177.

25. A. Falber, B. P. Burton-Pye, I. Radivojevic, L. Todaro, R. Saleh, L. C. Francesconi and C. M. Drain, *Eur. J. Inorg. Chem.,* 2009, **2009**, 2459-2466.

26. R. Pütt, X. Qiu, P. Kozłowski, H. Gildenast, O. Linnenberg, S. Zahn, R. Chiechi and K. Monakhov, *Chem. Commun.*, 2019, **55**, 13554.

27. R. Contant, *Can. J. Chem.*, 1987, **65**, 568-573.

28. E. Radkov and R. H. Beer, *Polyhedron*, 1995, **14**, 2139-2143.

29. V. Pushkarev, M. Breusova, E. Shulishov and Y. V. Tomilov, *Russ. Chem. Bull.*, 2005, **54**, 2087-2093.

30. Z. Iqbal, A. Lyubimtsev and M. Hanack, *Synlett*, 2008, **2008**, 2287-2290.

31. Y. G. Gorbunova, L. Lapkina, A. Martynov, I. Biryukova and A. Y. Tsivadze, *Russ. J. Coord. Chem.*, 2004, **30**, 245-251.

32. E. Morkved, H. Ossletten and H. Kjosen, *Acta Chem. Scand.*, 1999, **53**, 1117-1121.

33. M. Hamdoush, S. S. Ivanova, O. I. Koifman, M. Kos’kina, G. L. Pakhomov and P. A. Stuzhin, *Inorg. Chim. Acta.*, 2016, **444**, 81-86.

34. C. Loosli, S.-X. Liu, A. Neels, G. Labat and S. Decurtins, *Z. Kristallogr. NCS.,* 2006, **221**, 135-141.

35. J. Iijima, H. Naruke and T. Sanji, *RSC Adv.*, 2016, **6**, 91494-91507.

36. J. Jiang, M. Bao, L. Rintoul and D. P. Arnold, *Coord. Chem. Rev.*, 2006, **250**, 424-448.

37. D. Rocchiccioli, R. Thouvenot, *J. Chem. Res.*, 1977, (S) 46, (M) 0549-0571

38. G. Socrates, *J. Amer. Chem. Soc.*, 1995, **117**, 1671-1671.

39. M.J. Stillman, T. Nyokong, in *Phthalocyanines: properties and applications*, ed. C.C. Leznoff, and A.B.P. Lever, VCH, New York, 1989, vol. 1, ch. 3, 133.

40. Y. Bian, R. Wang, D. Wang, P. Zhu, R. Li, J. Dou, W. Liu, C. F. Choi, H. S. Chan, C. Ma, D. K. P. Ng and J. Jiang, *Helv. Chim. Acta.*, 2004, **87**, 2581-2596.

41. M. M. Ayhan, A. Singh, E. Jeanneau, V. Ahsen, J. Zyss, I. Ledoux-Rak, A. G. Gürek, C. Hirel, Y. Bretonnière and C. Andraud, *Inorg. Chem.*, 2014, **53**, 4359-4370.

42. M. Arıcı, C. Bozoğlu, A. Erdoğmuş, A. L. Uğur and A. Koca, *Electrochim. Acta.*, 2013, **113**, 668-678.

43. P. A. Stuzhin, in *Fluorine in Heterocyclic Chemistry*, ed. V. Nenajdenko, Springer, Cham, 2014, vol. 1, pp. 621-681.

44. H. Brinkmann, C. Kelting, S. Makarov, O. Tsaryova, G. Schnurpfeil, D. Wöhrle and D. Schlettwein, *Phys. Status Solidi (A)*, 2008, **205**, 409-420.

45. A. Koca, *In Electrochemistry of N4 Macrocyclic Metal Complexes*, ed. J. H., Zagal, and F. Bedioui, Springer, Cham, 2nd edn, 2016, vol. 2, ch. 4, pp. 135-200.

46. P. Zhu, F. Lu, N. Pan, Dennis P. Arnold, S. Zhang and J. Jiang, *Eur. J. Inorg. Chem.*, 2004, **2004**, 510-517.

47. L. Sorace and D. Gatteschi, in *Lanthanides and Actinides in Molecular Magnetism*, ed. R.A. Layfield and M. Murugesu, Wiley-VCH, 2015, ch. 1, pp. 1-26.

48. H. Lueken and B. Magnetochemie, Teubner, Stuttgart, 1999.

49. K. S. Cole and R. H. Cole, *J. Chem. Phys.*, 1941, **9**, 341-351.

50. K. N. Shrivastava, *Phys. Status Solidi (B)*, 1983, **117**, 437-458.

51. P. Ma, F. Hu, Y. Huo, D. Zhang, C. Zhang, J. Niu and J. Wang, *Cryst. Growth Des.*, 2017, **17**, 1947-1956.

52. J. M. Clemente-Juan, E. Coronado and A. Gaita-Ariño, *Chem. Soc. Rev.*, 2012, **41**, 7464-7478.

53. G. M. Sheldrick, *Acta. Crystallogr. A.*, 2015, **71**, 3-8.

54. O. V. Dolomanov, L. J. Bourhis, R. J. Gildea, J. A. Howard and H. Puschmann, *J. Appl. Crystallogr.*, 2009, **42**, 339-341.

55. G. M. Sheldrick, *Acta Crystallogr. C*, 2015, **71**, 3-8.

Chapter 3.

Hybrid double-decker cerium(IV) complex based on calix[4]arene and polyoxotungstate

3.1 Introduction

The oxidant nature of tetravalent ($4f^0$) cerium, unique among other lanthanides, finds potential applications in synthetic organic chemistry,[1-3] heterogeneous catalysis,[4-6] and renewable energy.[7] Nonetheless, the coordination chemistry of Ce(IV) has seen less development due to the high reduction potential of Ce(IV/III) couple, making the control and stabilization of tetravalent state quite challenging. The nature of the ligand field plays a fundamental role in stabilizing the cerium metal ion as evidenced by the large window range of Ce(IV/III) redox potential, *e.g.* +1.63 V *vs* SCE for $Ce(ClO_4)_3$ in aqueous conditions and – 1.49 V *vs* SCE for Ce(2-^{t}BuNO-py)$_4$ in dichloromethane (^{t}BuNO-py = *N*-*tert*-butyl-*N*-2-pyridylnitroxide).[8,9]

Oxygen donor electron-rich ligands, like polyoxotungstates (POTs), have shown to effectively stabilize the $4f^0$ configuration by providing an adequate coordination environment and charge.[10] These inorganic building blocks present thermal stability, redox properties, and highly modular structure representing ideal ligands for complexation with lanthanide metal ions. However, the coordination chemistry of POT with cerium is very scarce, these include some reports in which the redox potential of Ce(IV/III) have been found between +0.86 to +0.28 V.[11-13]

Complexes with calixarene ligands are important in the field of crystal engineering and supramolecular chemistry. The cone conformation of *p*-*tert*-butylcalix[4]arene (TBC[4]) has been used to form complexes with several transition and lanthanide metal ions. Regarding the cerium ion, most of complexes are based on trivalent cerium, such as [Ce^{III}(H$_2$O)$_5$(*p*-sulfonatocalix[4]arene + H$^+$)] and [Ce^{III}(LH$_{-2}$)(MeOH)$_2$A]HA (L = *p*-*tert*-butyl-25,27-bis(diethylcarbamoylmethoxy)-26,28-dihydroxycalix[4]arene, HA = picric acid).[14,15] The examples of tetravalent cerium include just three monomeric structures produced by reacting different analogues of [Ce(acac)$_4$] with [*p*-*tert*-butylcalix[4](OMe)$_2$(OH)$_2$].[16,17] The evaluation of oxidation state of cerium in these complexes by XPS indicated a mixed-valence state (between 3.6 and 3.65), suggesting a partial delocalization of the ligand π-electron density to the 4f-orbitals.[18] This behavior is not unique to calixarene-based ligands, as the oxidation state of cerium in $[Ce(COT)_2]$ (COT = cyclooctatetraenyl) through evaluation of the magnetic properties and X-ray absorption near-edge spectroscopy (XANES), also indicated a trivalent oxidation state in the complex despite starting with cerium(IV).[19,20] Similarly, X-ray photoelectron spectroscopy (XPS) analysis of cerium in double-decker tetrapyrrole complexes $[Ce(L)_2]$ (L = porphyrin, phthalocyanine, and naphthalocyanine) revealed a mixed-valent state ranging between +3 to +4, depending on the electronic nature of the coordinated ligand.[21]

This chapter describes the first hybrid structure containing a Ce(IV) ion sandwiched between a $(TBC[4](OMe)_2O_2)$ and a monolacunary phosphotungstate $[PW_{11}O_{39}]^{7-}$. To date, the construction of such lanthanide-based hybrid complexes composed of calixarene and polyoxometalate moieties remains unexplored. Hence, this constitutes a milestone towards the future development of similar systems with different Ln(III) ions and lacunary POMs. The complete structural characterization and detailed electrochemical behavior of the hybrid complex is presented. To compare the electrochemical properties of Ce(IV) complex, an analogous complex with the redox-inactive zirconium(IV) center was synthesized. Keeping in view the mixed-valence state of cerium in its complexes, the oxidation state of the cerium complex was evaluated by XPS and SQUID magnetometry.

3.2 Results and discussion

The proposed molecular structure of $[M^{IV}(TBC[4](OMe)_2O_2)(PW_{11}O_{39})]^{5-}$ (M = Ce(IV) in complex **[8]** and Zr(IV) in complex **[9]**), is shown in **Fig 3.1**. Both complexes were identified by multinuclear NMR, elemental analysis, electrospray ionization mass spectrometry, infrared spectroscopy, UV-Vis spectroscopy, and cyclic voltammetry. The complex **[8]** was additionally characterized by 2D NMR experiments (COSY, HSQC, and HMBC), thermogravimetric analysis, X-ray photoelectron spectroscopy, and SQUID magnetometry. Thin polygonal purple plates of complex **[8]** were obtained by vapor diffusion of diisopropyl ether to acetonitrile solution of the product. However, several attempts to obtain a single-crystal X-ray structure determination failed due to the lack of resolution and twinning of the crystals. Nonetheless, the two possible molecular structures due to the pinched conformation of the ligand are highlighted in **Fig 3.1**.

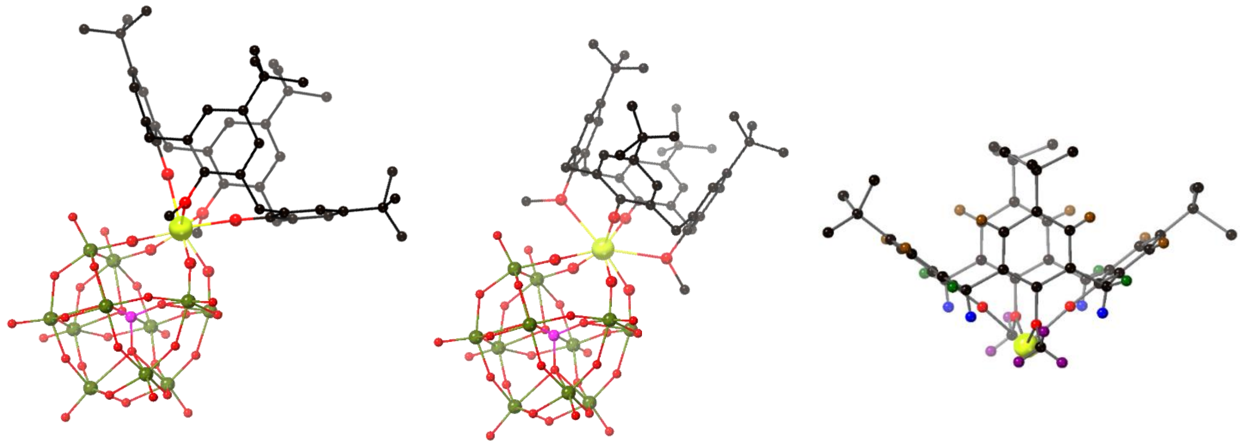

Fig 3.1 (Left and **center)** The proposed molecular structure of $[M^{IV}(TBC[4](OMe)_2O_2)(PW_{11}O_{39})]^{5-}$, showing two possible modes of coordination between "$[M^{IV}(TBC[4](OMe)_2O_2)]$" and "$PW_{11}O_{39}$". Color code: M = yellow, O = red, W = green, P = pink, and C = black. H-atoms omitted for clarity. **(Right)** Representation of the different hydrogen atoms in the "$[M^{IV}(TBC[4](OMe)_2O_2)]$" unit observable by ^{1}H NMR. Hydrogen-atoms color code: *H*-aromatics = brown, *H*-CH_3O = dark magenta, *H*-CH_2exo = green and *H*-CH_2endo = blue. Hydrogen atoms of *tert*-butyl groups are omitted for clarity.

Synthetic procedure

$[TBC[4](OMe)_2(OH)_2]$,[22] $[Ce^{IV}(TBC[4](OMe)_2O_2)(acac)_2]$,[16] and $(NBu_4)_4H_3[PW_{11}O_{39}]$[23,24] were synthesized as described in the literature. Hybrid complex **[8]** was obtained by refluxing an acetonitrile solution of $[Ce^{IV}(TBC[4](OMe)_2O_2)(acac)_2]$, $(NBu_4)_4H_3[PW_{11}O_{39}]$, and NBu_4Br for 3 h under argon. The resulting solution was evaporated to dryness under reduced pressure and washed with dichloromethane. Crystallization from acetonitrile/diisopropyl ether yielded purple thin polygonal plates. Attempts to obtain the paramagnetic derivate by using Ce(III) salts, under similar reaction conditions, failed; in all the cases the oxidation to Ce(IV) complex was observed characterized by its intense purple color.

To synthesize $(NBu_4)_5[Zr^{IV}(TBC[4](OMe)_2O_2)(PW_{11}O_{39})]$ **[9]**, the first step involved the preparation of $[Zr^{IV}(TBC[4](OMe)_2O_2)(acac)_2]$, which was done using the procedure reported for the cerium(IV) analogue. However, attempts to coordinate the POT using the same procedure as for **[8]** was unsuccessful and resulted in decoordination of the starting material in to $[TBC[4](OMe)_2(OH)_2]$ due to the presence of acidic protons on $(NBu_4)_4H_3[PW_{11}O_{39}]$. Therefore, the complex **[9]** was synthesized by adding the solution of tetra-*n*-butylammonium hydroxide (NBu_4OH) to $(NBu_4)_4H_3[PW_{11}O_{39}]$ in acetonitrile. The resulting solution was slowly transferred to a flask containing $[Zr^{IV}(TBC[4](OMe)_2O_2)(acac)_2]$ in acetonitrile and refluxed overnight under argon. The mother liquor was filtered and evaporated under reduced pressure. Dissolving the crude in dichloromethane and, precipitation and washing with diethyl ether produced light yellow powder of complex **[9]**.

NMR spectroscopy

Complex **[8]** was characterized by ^{1}H-, ^{13}C-, and ^{31}P-NMR. To confirm the formation and purity of hybrid complex, the spectra of starting materials $[Ce^{IV}(TBC[4](OMe)_2O_2)(acac)_2]$ and $[PW_{11}O_{39}]^{7-}$ were also recorded.

The ^{1}H-NMR spectrum of $[Ce^{IV}(TBC[4](OMe)_2O_2)(acac)_2]$ displays two singlets in the aromatic region **(Fig 3.2, a)** corresponding to the aromatic protons of two unsubstituted phenolic rings “A” and two methylated phenolic rings “B”. The coordination of monolacunary $[PW_{11}O_{39}]^{7-}$ to $[Ce^{IV}(TBC[4](OMe)_2O_2)]$ results in the tilting of TBC[4] to one side, hence breaking the equivalency of opposed phenolic pairs. This tilting and shielding effects created by the proximity of the POT unit is indicated by the splitting from two signals of aromatic protons, featured in $[Ce^{IV}(TBC[4](OMe)_2O_2)(acac)_2]$, to four signals in complex **[8]**, highlighted as A1 (7.11), A2 (7.08), B1 (7.04), and B2 (7.01) ppm **(Fig 3.2)**. Upon coordination, the *endo*-protons of the methylene bridges show a large shift from one signal at 5.43 ppm to two signals at 5.43 and 4.93 ppm, whereas, the signal of *exo*-protons at 3.21 ppm display a slight shift, appearing close to each other at 3.26 and 3.19 ppm in complex **[8]**. Protons of methoxy groups are slightly shifted from 4.62 ppm towards lower chemical shift value at 4.52 ppm. The signals related to the *tert*-butyl groups remain almost unchanged due to the large distance from POT unit. The integration of signals between 0.9 ppm to 3 ppm confirms the presence of four tetra-*n*-butylammonium (TBA) countercations. The result of elemental analysis of complex **[8]** also indicates the presence of four TBA and one proton as countercations.

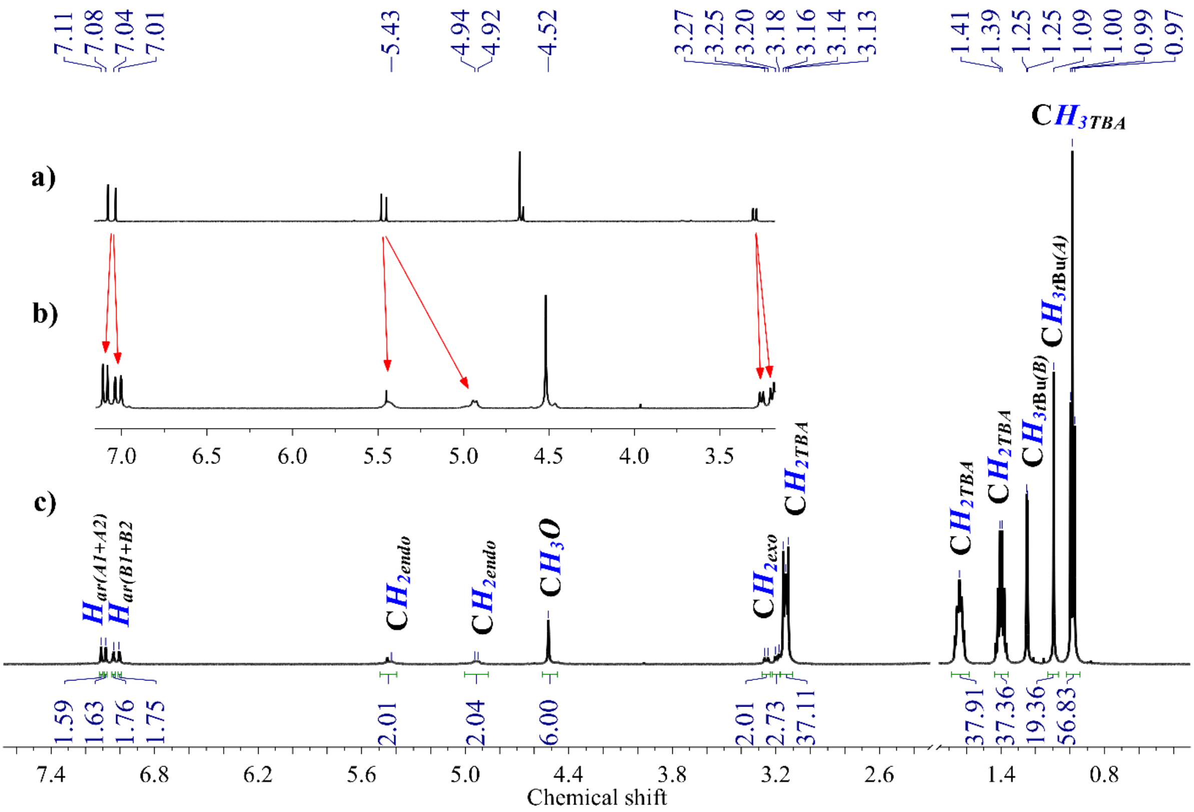

Fig 3.2 ^{1}H-NMR spectrum in CD_3CN; **a)** Zoomed spectrum of [Ce^{IV}(TBC[4](OMe)$_2$O$_2$)(acac)$_2$] between 3–7 ppm; **b)** Zoomed spectrum of complex **[8]**; **c)** Full spectrum of complex **[8]**. The signals corresponding to residual solvents (CD_3CN and water) have been removed for clarity.

The ^{1}H-^{1}H-COSY spectrum of complex **[8]** displays the intense cross peaks related to the protons of CH_3 and CH_2 groups of TBA countercations **(Fig 3.3)**. However, the most important signals in the spectrum are the cross peaks of $CH_{2endo/exo}$ protons originating from the same methylene bridges. As presented in the zoomed spectrum in **Fig 3.4**, the protons of CH_{2exo} at 3.19 ppm are coupled to the CH_{2endo} at 5.43 ppm. Similarly, CH_{2exo} at 3.26 ppm and CH_{2endo} at 4.93 ppm belong to the same methylene bridges.

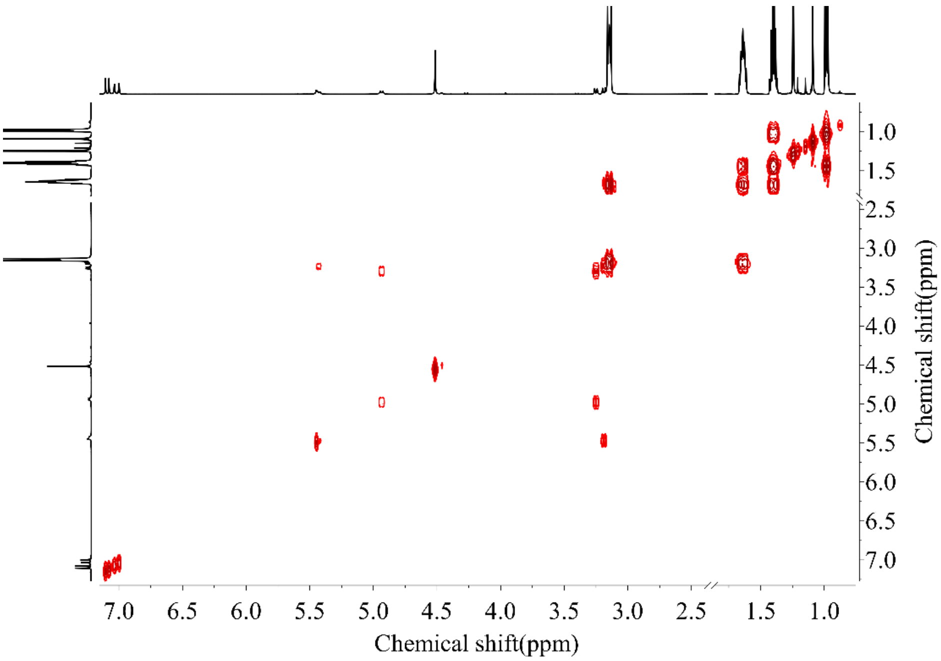

Fig 3.3 COSY spectrum of complex **[8]** in CD_3CN. The signals corresponding to residual solvents (CD_3CN and water) have been removed for clarity.

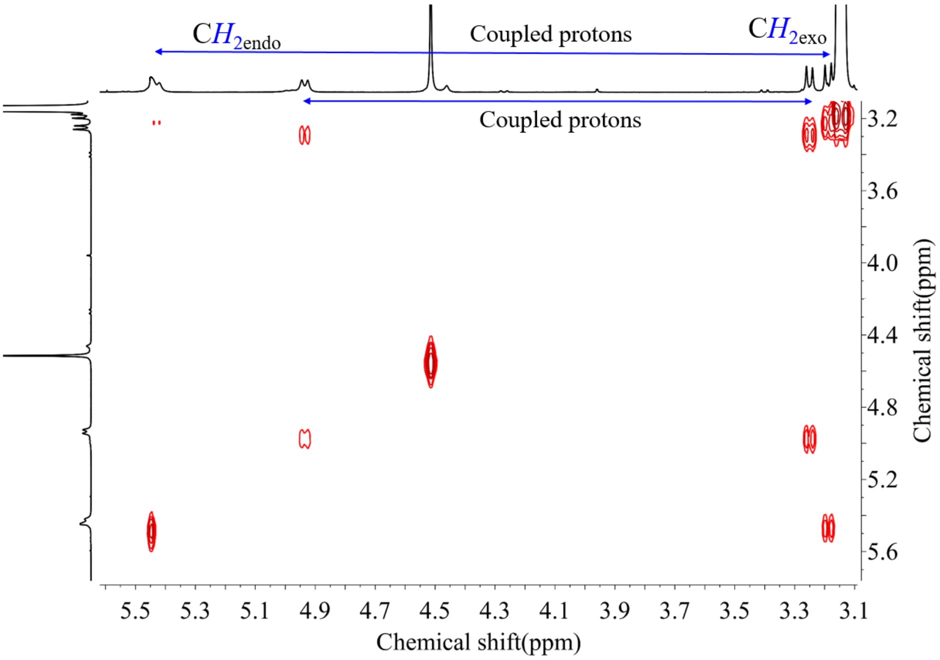

Fig 3.4 Partial COSY spectrum of complex **[8]** in CD_3CN, highlighting the coupling between CH_2*endo*/*exo* protons.

To get the detailed structural information, the ^{13}C-NMR spectrum of complex **[8]** was recorded. However, for the complete assignments of signals to particular carbon, ^{1}H-^{13}C 2D-NMR experiments were required.

The zoomed ^{13}C-NMR spectra with the assignment of signals are depicted in **Fig 3.5** and **3.6**. The most intense signals are related to the carbons of TBA cations and the methyl of *tert*-butyl groups on TBC[4] unit. The four carbons of methylene bridges (CH_{2calix}) appear close to each other at 32.46 and 32.52 ppm. The carbons of methoxy groups of TBC[4] display a distinguishable signal at 68.97 ppm.

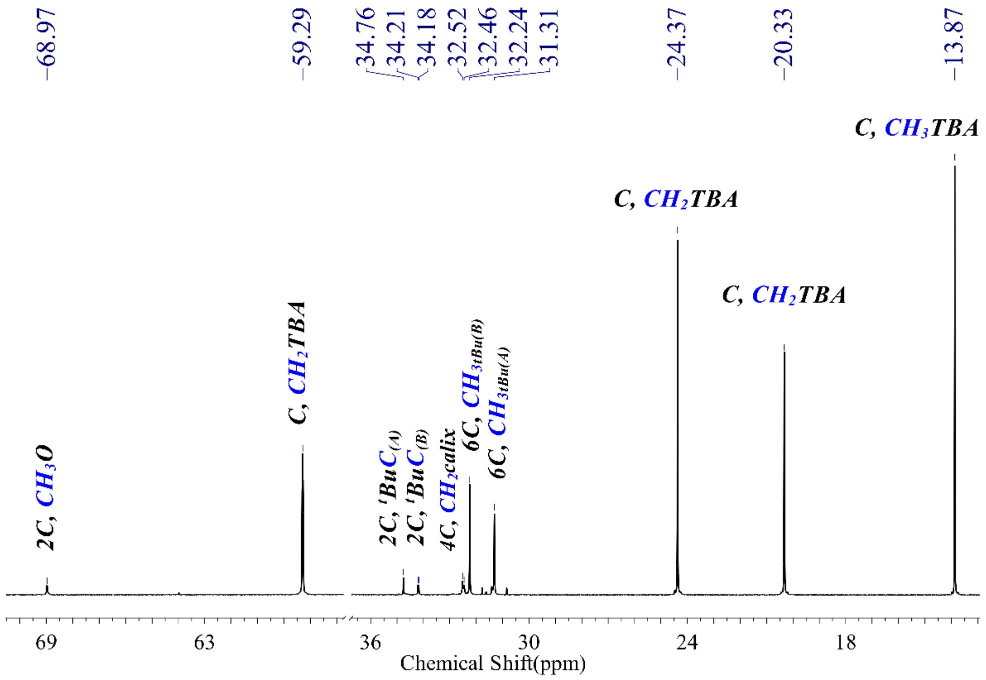

Fig 3.5 Partial ^{13}C-NMR spectrum of complex **[8]** between 10–70 ppm in CD_3CN. TBA stands for tetra-*n*-butylammonium.

The tertiary carbons of the phenolic units ($C_{ar}H_{(A+B)}$) exhibit four signals between 124.11 to 126.74 ppm. Further downfield, the signals corresponding to the quaternary carbons bound to the methylene bridges of TBC[4] ($C_{ar}CH_{2(A+B)}$) appear between 132.12 to 134.67 ppm. The quaternary carbons that bind with the *tert*-butyl groups ($C_{ar}{}^{t}Bu$) on “B and A” rings are observed at 142.45 and 148.18 ppm respectively. The most downfield signals are related to the O-bonded quaternary carbons, appearing at 155.80 ($C_{ar}OMeCe$) and 169.79/170.52 ppm ($C_{ar}OCe$).

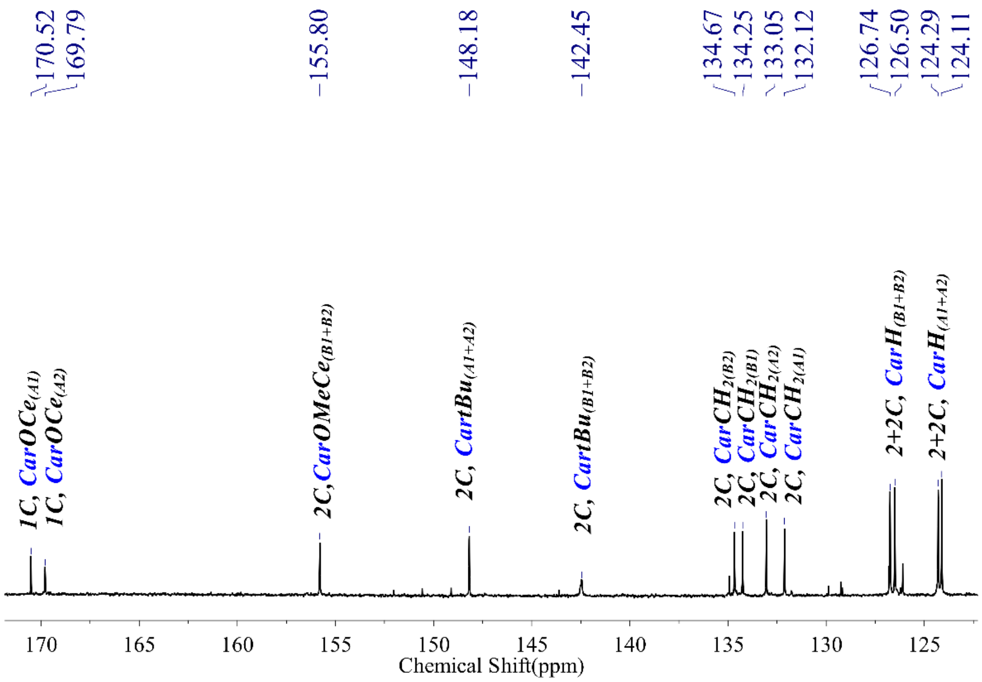

Fig 3.6 Partial ^{13}C-NMR spectrum of complex **[8]**, highlighting the aromatic region.

As mentioned above, the assignment of ^{13}C-NMR signals containing protons was confirmed by ^{1}H-^{13}C-HSQC spectroscopy. The cross peaks between 0–3 ppm along the ^{1}H-axis and 10–32 ppm along ^{13}C-axis can be related to the signal of CH_3 and CH_2 groups of TBA cations and CH_3 of *tert*-butyl groups in TBC[4] **(Fig 3.7)**.

Further downfield, the protons of methylene bridges ($C\mathit{H}_{2exo/endo}$ at 3.19, 3.26, 4.93, and 5.43 ppm) show the coupling to the carbons of methylene bridges ($\mathit{C}H_{2calix}$ at 32.46 and 32.52 ppm) as presented in zoomed spectrum in **Fig 3.8**.

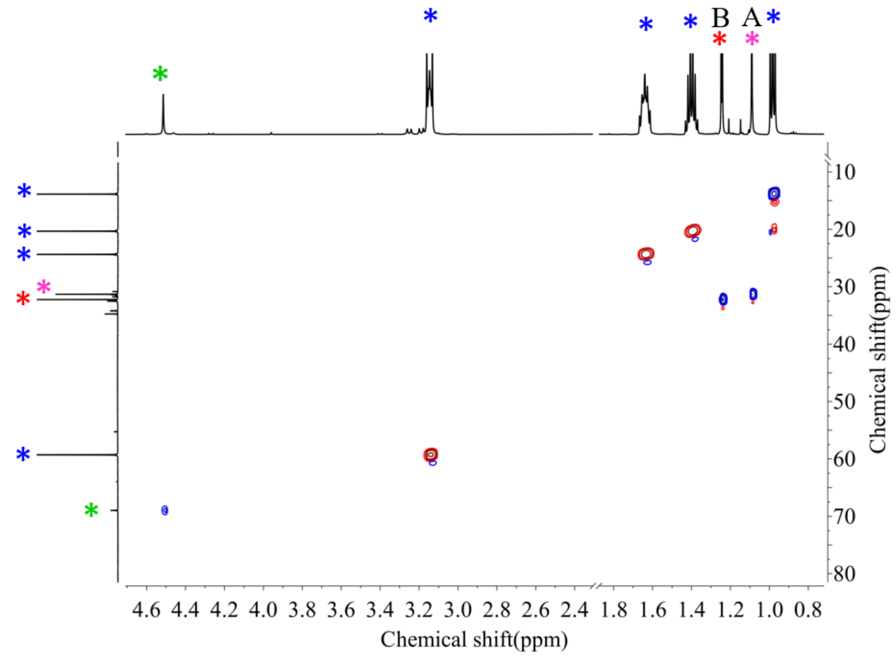

Fig 3.7 Partial HSQC spectrum of complex **[8]** in CD_3CN. Highlighting the coupling between *C–H–*(TBA) blue color, *C–H–*(CH_3O) green color, *C–H–*(^{t}Bu$_{(A)}$) pink color, and *C–H–*(^{t}Bu$_{(B)}$) red color.

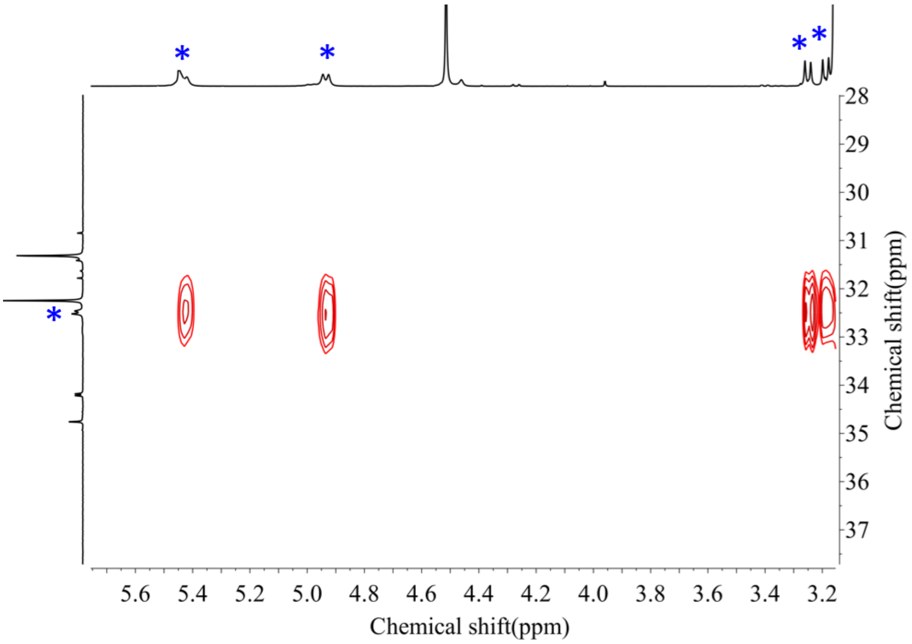

Fig 3.8 Partial HSQC spectrum of complex **[8]** in CD_3CN. Highlighting the coupling between *C–H–*($CH_{2exo/endo}$) blue color.

The signals of aromatic protons between 7.11 to 7.01 ppm exhibit $^1J_{H\text{–}C}$ cross peaks between 124.17 to 126.80 ppm along ^{13}C-axis, indicating that the pattern "A1A2B1B2" (from downfield to upfield) in ^{1}H-NMR is shifted to "B1B2A1A2" in ^{13}C-NMR. As highlighted in different colors in **Fig 3.9**, the most downfield signal of aromatic proton of rings "A" (phenoxide units) at 7.11 and 7.08 ppm are coupled to the carbon at 124.29 and 124.11 ppm respectively.

Whereas, the protons of rings “B” (methoxybenzene units) at 7.04 and 7.01 ppm are attached to the carbons appearing downfield at 126.74 and 126.50 ppm respectively.

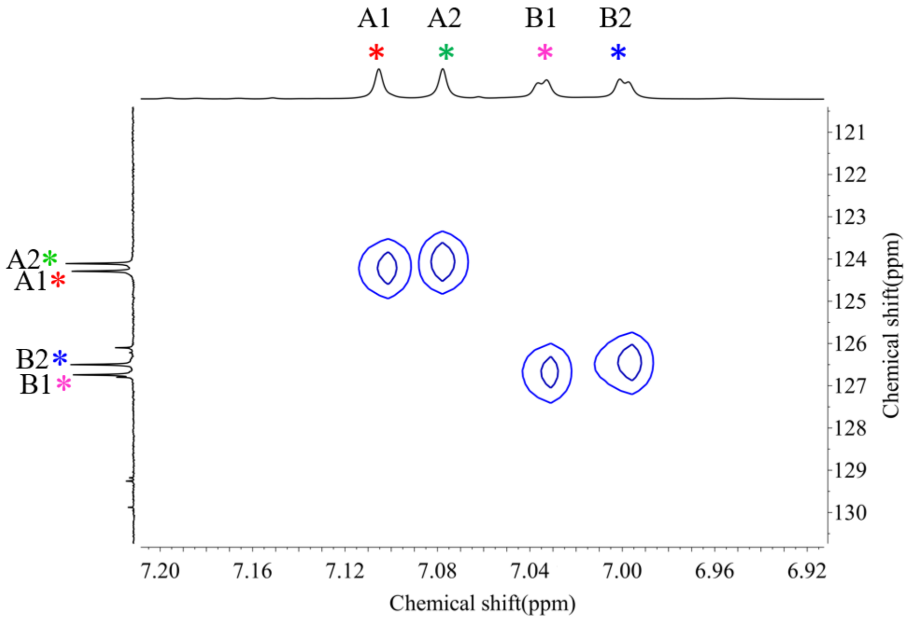

Fig 3.9 Partial HSQC spectrum of complex **[8]** in CD_3CN. Highlighting the coupling between *C–H*–(aromatic rings: A1, A2, B1, and B2). Color code: A1 red, A2 green, B1 pink, and B2 blue color.

^{1}H-^{13}C-HMBC spectroscopy was required for the assignment of quaternary carbons. The resonance of the aliphatic quaternary carbons of the four *tert*-butyl groups (at 34.72 and 34.18/34.21 ppm) were identified by $^2J_{C–H}$ cross peaks with the CH_3 protons of the *tert*-butyl groups (at 1.09 and 1.25 ppm) as pictured in **Fig 3.10**.

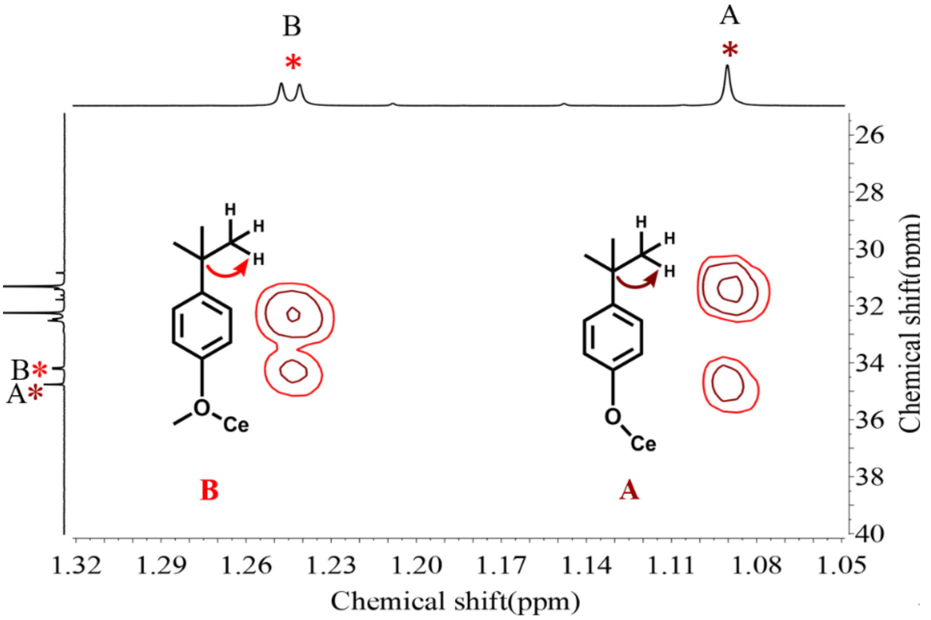

Fig 3.10 Partial HMBC spectrum of complex **[8]** in CD_3CN. Highlighting the *C–H* coupling between C^tBu and CH_3-^{t}Bu from aromatic units A and B. Color code: A brown and B red color.

The quaternary aromatic carbons at 169.85 and 170.58 ppm show $^{3}J_{C\text{–}H}$ to the aromatic protons at 7.11 and 7.08 ppm. Whereas the carbons appearing at 155.86 ppm display $^{3}J_{C\text{–}H}$ to the aromatic protons at 7.04 and 7.01 ppm as well as $^{3}J_{C\text{–}H}$ to the protons of methoxy groups at 4.52 ppm **(Fig 3.11)**. These couplings endorse the assignments of signals related to "A and B" rings in the ^{13}C-NMR spectrum and show that ^{13}C nuclei in the "A" rings are more affected by the shielding effect stemming from the electrons of the POT unit, as indicated by the splitting in A1 and A2 signals.

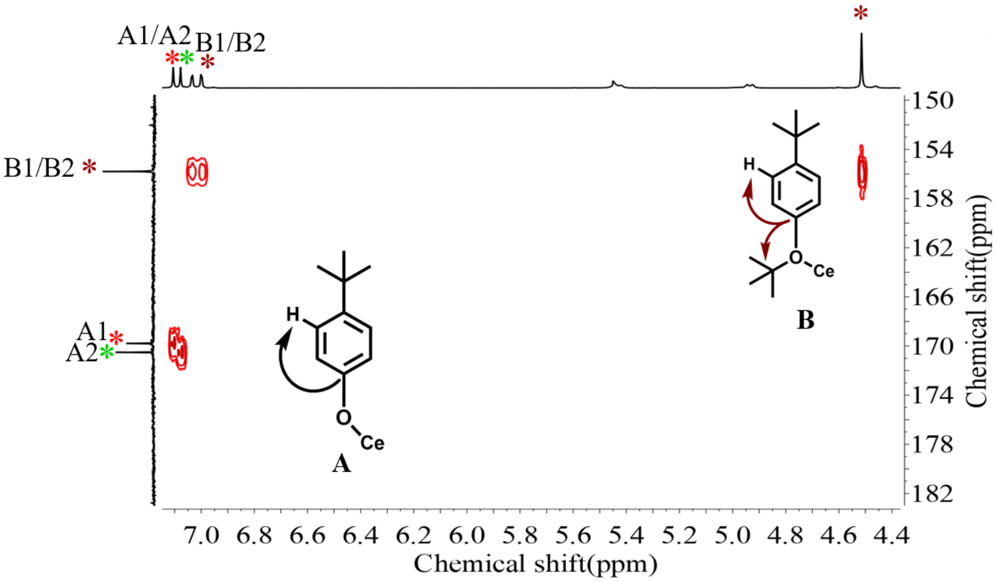

Fig 3.11 Partial HMBC spectrum of complex **[8]** in CD_3CN. Highlighting the three bonds *C–H* coupling in aromatic units A and B. Color code: A1 red, A2 green, B1 and B2 brown color.

HMBC experiments can determine the proximity between CH_2 protons and aromatic units "A and B". **Fig 3.12** shows the correlation of CH_{2exo} protons with previously identified tertiary carbons ($C_{ar}H_{(A1, A2, B1, B2)}$) (see **Fig. 3.9**) and quaternary carbons C_{ar}OMeCe/C_{ar}OCe (see **Fig. 3.11**). The lack of cross peaks of CH_{2exo} at 3.26 ppm with A2 indicates that these two protons are not bonded to this unit; at the same time, CH_{2exo} protons at 3.19 ppm show no link with the A1 unit. This information helps to further name the quaternary carbons attached to the methylene bridges ($C_{ar}CH_{2(A1, A2, B1, B2)}$) at 132.12, 133.05, 134.25, and 134.67 ppm through $^{2}J_{C\text{–}H}$ to the CH_{2exo}.

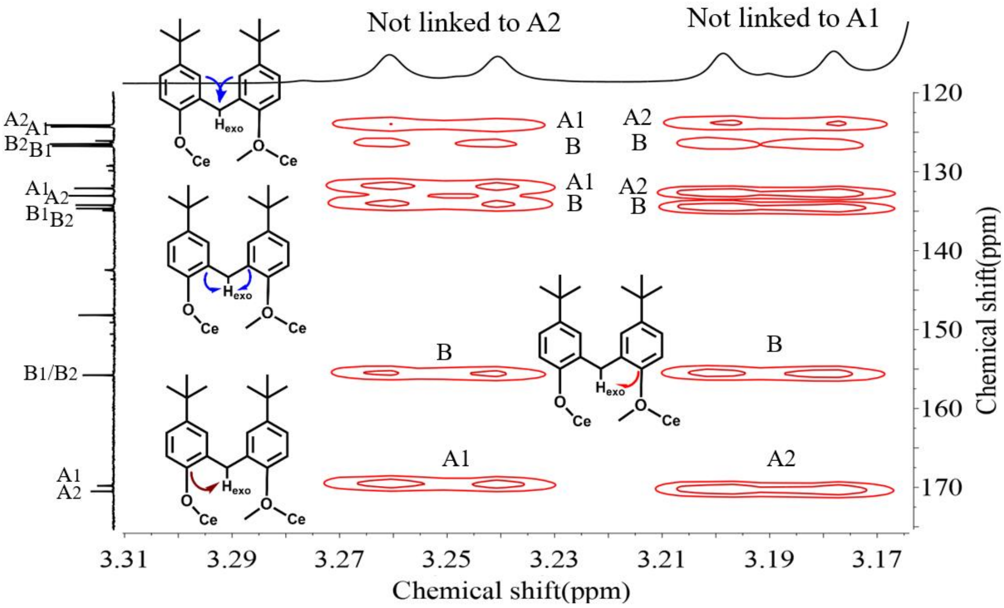

Fig 3.12 Partial HMBC spectrum of complex **[8]** in CD_3CN. Highlighting the *C–H* coupling between aromatic carbons and CH_{2exo}.

COSY experiments showed in **Fig. 3.4** correlates CH_{2exo} protons at 3.26 ppm to CH_{2endo} protons at 4.93 ppm. The partial HMBC spectrum in **Fig 3.13** depicts the $^{2}J_{C\text{–}H}$ between $C_{ar}CH_{2(A1,\ B1,\ B2)}$ and CH_{2endo} protons at 4.93 ppm, not showing any correlation to the A2 unit and, therefore, supporting the previous assignment (**Fig. 3.11**).

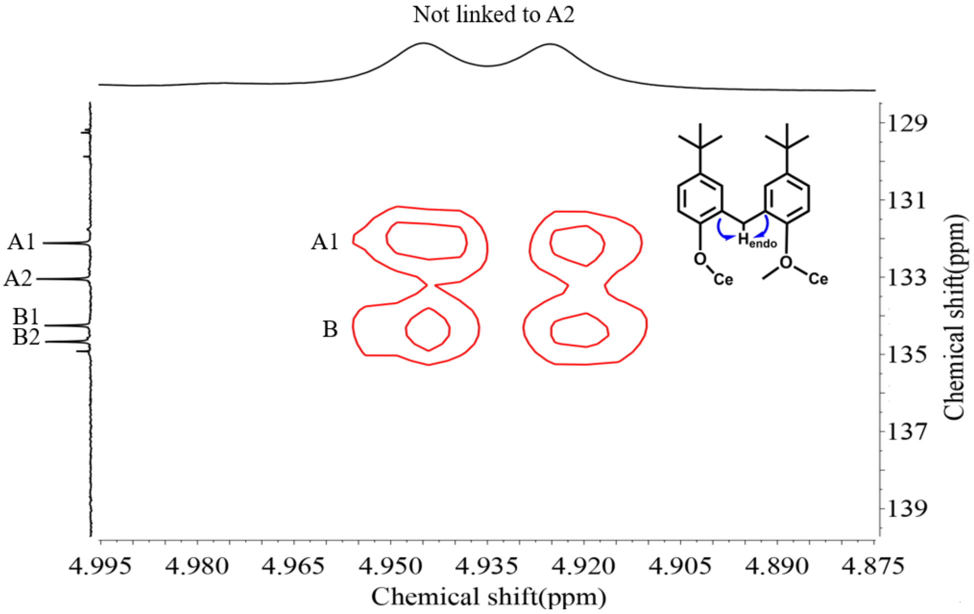

Fig 3.13 Partial HMBC spectrum of complex **[8]** in CD_3CN. Highlighting the *C–H* coupling between $C_{ar}CH_2$ with CH_{2endo}.

The coordination of $[PW_{11}O_{39}]^{7-}$ to $[Ce^{IV}(TBC[4](OMe)_2O_2)]$ creates a shielding effect that is best manifested in the large shift of the CH_{2endo} protons to 4.93 ppm. As the above experiments revealed that these protons are linked to the aromatic ring A1, therefore, from the two proposed molecular structures shown in **Fig. 3.1**, the possible structure of the molecule is depicted in **Fig 3.14**, with the POT unit closer to ring A1.

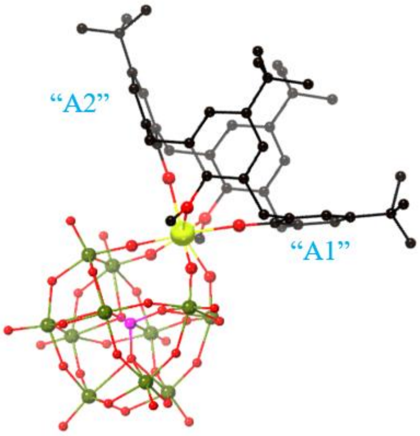

Fig 3.14 Molecular structure of complex **[8]** based on NMR experiments.

The ^{31}P-NMR spectrum of complex **[8]** is presented in **Fig 3.15**. The spectrum displays an intense signal at –12.94 ppm with a slight shift to the signal of uncoordinated $[PW_{11}O_{39}]^{7-}$ (appearing at –13.24 ppm) in acetonitrile. Another peak at –15.33 ppm is related to the plenary structure $PW_{12}O_{40}$; however, it is very small in comparison to the signal of complex **[8]**.

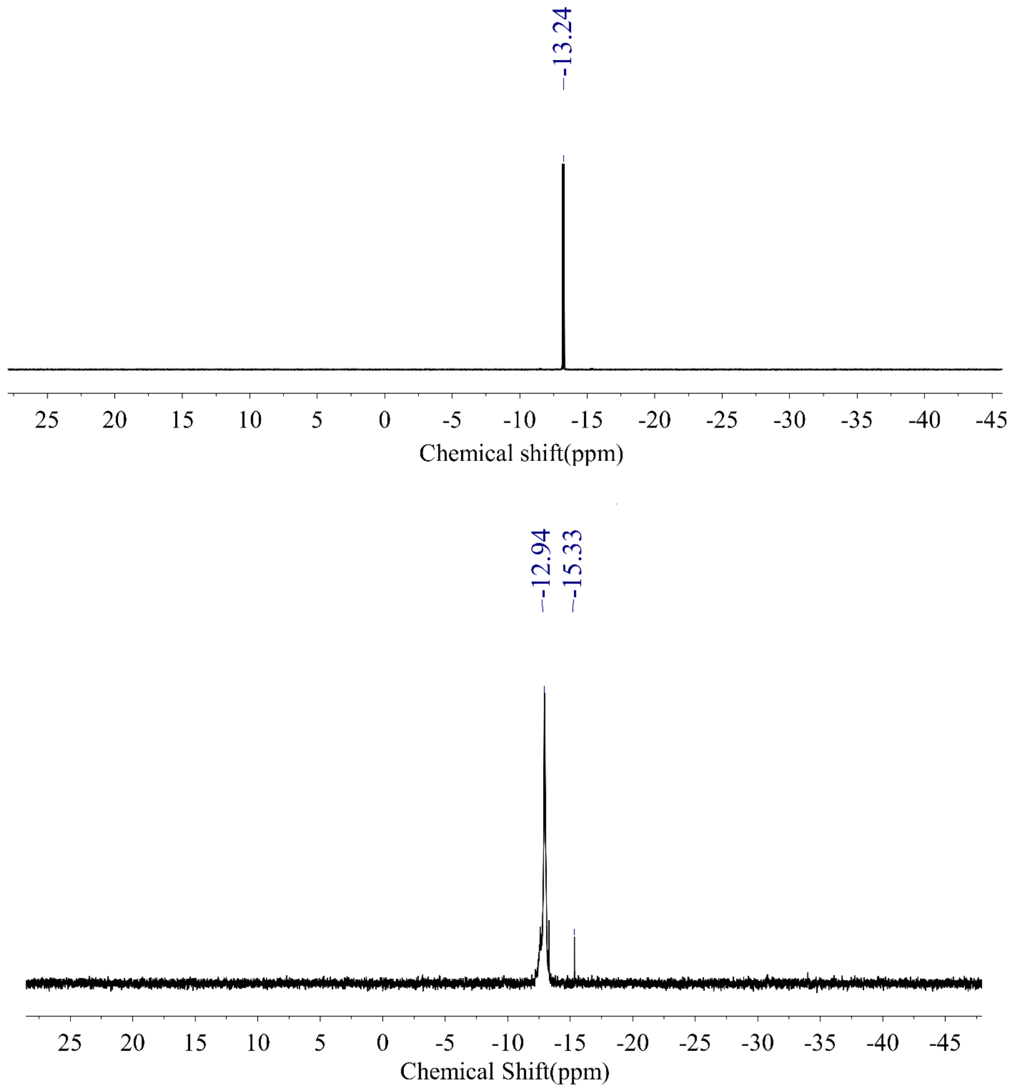

Fig 3.15 ^{31}P-NMR spectrum of **(top)** $(NBu_4)_4H_3[PW_{11}O_{39}]$ and **(bottom)** complex **[8]** in CD_3CN.

The ^{1}H-^{13}C-NMR spectra of complex **[9]** exhibit similar signals as **[8]**, with a little difference in the chemical shifts; hence, no 2D-experiments were recorded.

The comparison of ^{1}H-NMR spectrum of complex **[9]** and $[Zr^{IV}(TBC[4](OMe)_2O_2)(acac)_2]$ is shown in **Fig 3.16**. The aromatic protons ($H_{ar(A+B)}$) of complex **[9]** show four signals between 6.87 to 7.00 ppm in comparison to the two signals in starting $[Zr^{IV}(TBC[4](OMe)_2O_2)(acac)_2]$. Upon coordination to $[PW_{11}O_{39}]^{7-}$, the signals of *endo* protons (CH_{2endo}) show a large shift from 4.38 ppm to two signals at 4.98/5.35 ppm. Similar to complex **[8]**, the *exo* protons of methylene bridges (CH_{2exo}) show a small shift from 3.13 ppm to two signals at 2.99/3.05 ppm in complex **[9]**. The signals corresponding to the protons of methoxy groups (OCH_3) as well as *tert*-butyl units ($CH_{3t\mathrm{Bu}}$) also display small shifts to the starting material. The protons of TBA countercations appear between 0.9 ppm to 3 ppm. The integration of signals is higher than five

TBA due to the difficulty of removing the excess of NBu_4 from the complex. However, the rest of signals in ^{1}H-, ^{13}C-, and ^{31}P-NMR, and ESI-MS confirm the formation of complex.

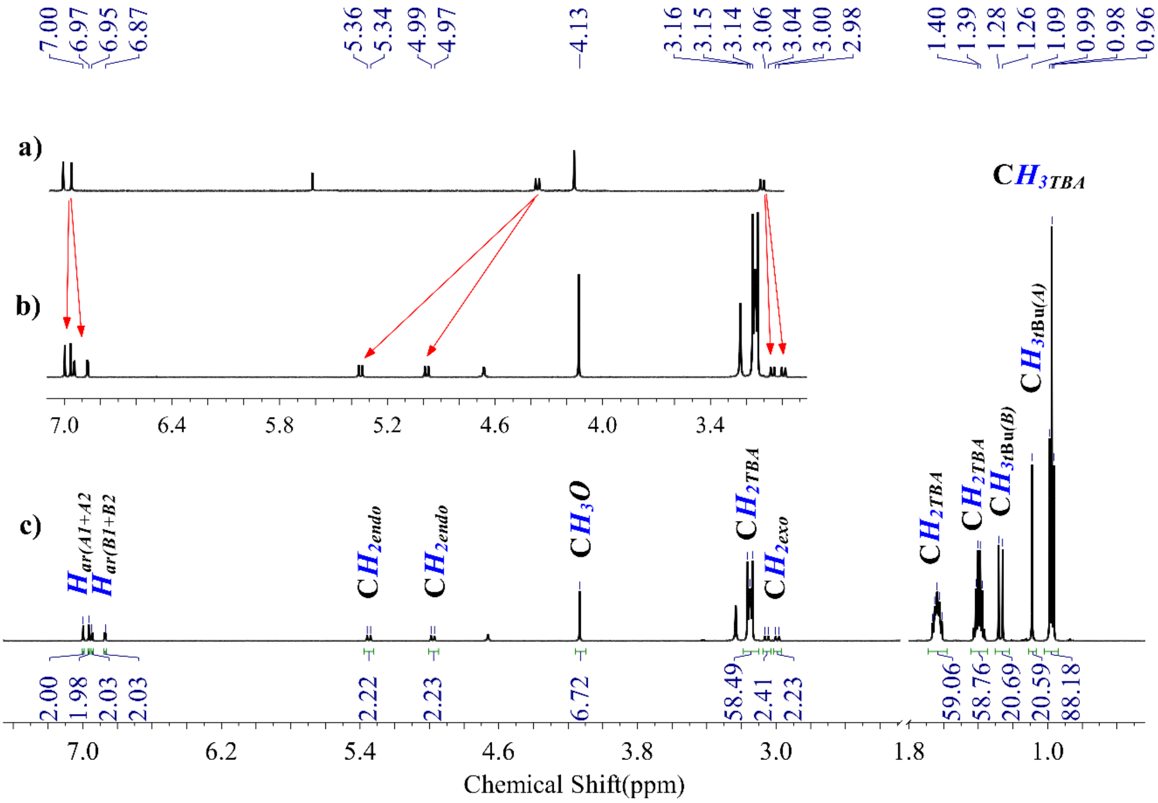

Fig 3.16 ^{1}H-NMR spectrum in CD_3CN; **a)** Zoomed spectrum of $[Zr^{IV}(TBC[4](OMe)_2O_2)(acac)_2]$ between 3–7 ppm; **b)** Zoomed spectrum of complex **[9]**; **c)** Full spectrum of complex **[9]**. The signals corresponding to residual solvents (CD_3CN and water) have been removed for clarity.

The ^{13}C-NMR spectrum of complex **[9]** is shown in **Fig 3.17** and **3.18**. The most intense signals at 13.90, 20.33, 24.42, and 59.26 ppm correspond to CH_3 and CH_2 carbons of TBA cations. The CH_3 of *tert*-butyl groups appear at 31.53 and 32.09/32.14 ppm. The signals at 34.13 and 34.66 ppm are related to the carbons of methylene bridges (CH_{2calix}) and aliphatic quaternary carbons of *tert*-butyl groups (^{t}BuC). The two carbons of the OCH_3 groups in TBC[4] appear at 67.96 ppm.

Similar to complex **[8]**, the tertiary carbons of phenolic rings containing proton ($C_{ar}H$) display four signals between 125.35 to 125.54 ppm. The signals between 129.79 to 134.96 ppm are assigned to the quaternary carbons attached to the methylene bridges ($C_{ar}CH_2$). The signals of quaternary carbons bound to the *tert*-butyl groups ($C_{ar}{}^{t}Bu$) appear at 138.68/138.91 and 146.94 ppm. The most downfield signals at 156.23 and 161.46/161.56 ppm are attributed to the O-bonded quaternary carbons ($C_{ar}OMeZr$+$C_{ar}OZr$).

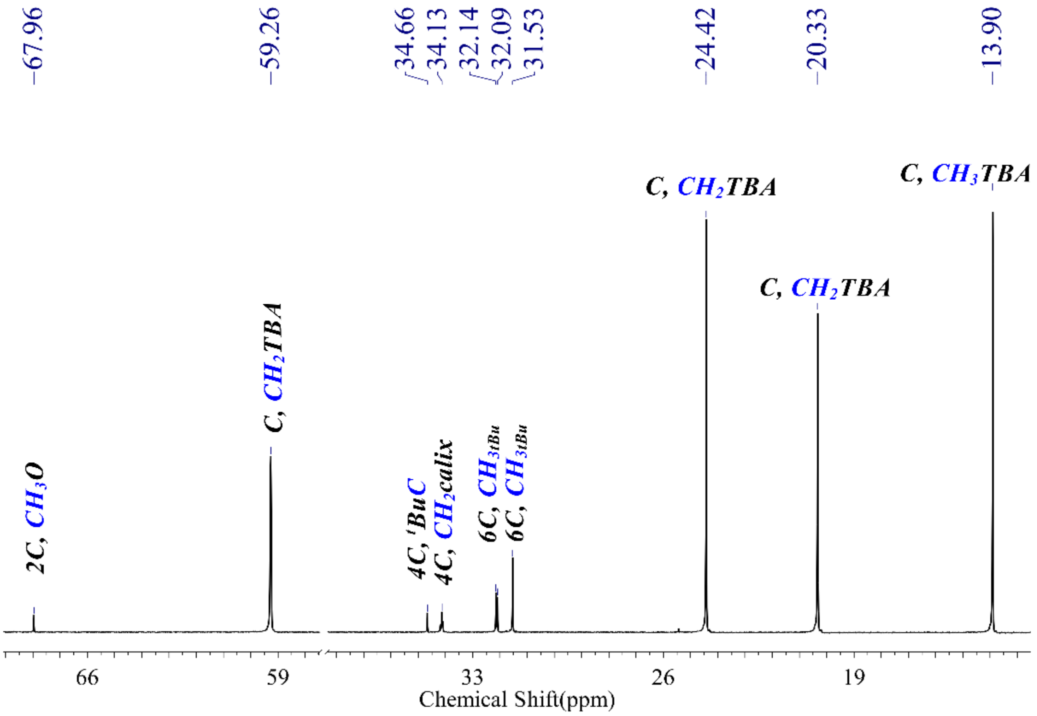

Fig 3.17 Partial ^{13}C-NMR spectrum of complex **[9]** between 10–70 ppm.

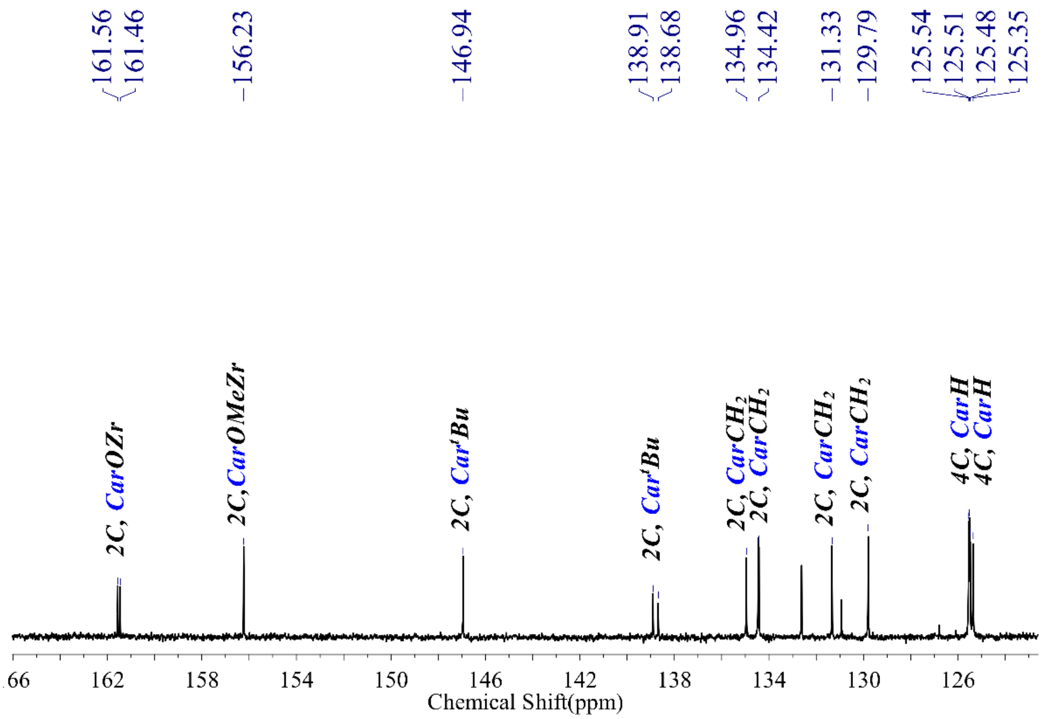

Fig 3.18 ^{13}C-NMR spectrum of complex **[9]**, highlighting the aromatic region.

^{31}P-NMR spectrum of complex **[9]** also display an intense signal at –14.60 ppm as compare to the signal of uncoordinated $[PW_{11}O_{39}]^{7-}$ at –13.24 ppm in acetonitrile, indicating the coordination of the [Zr^{IV}(TBC[4]$(OMe)_2O_2$)$(acac)_2$] unit to the POT, and absence of possible impurity coming from the POT.

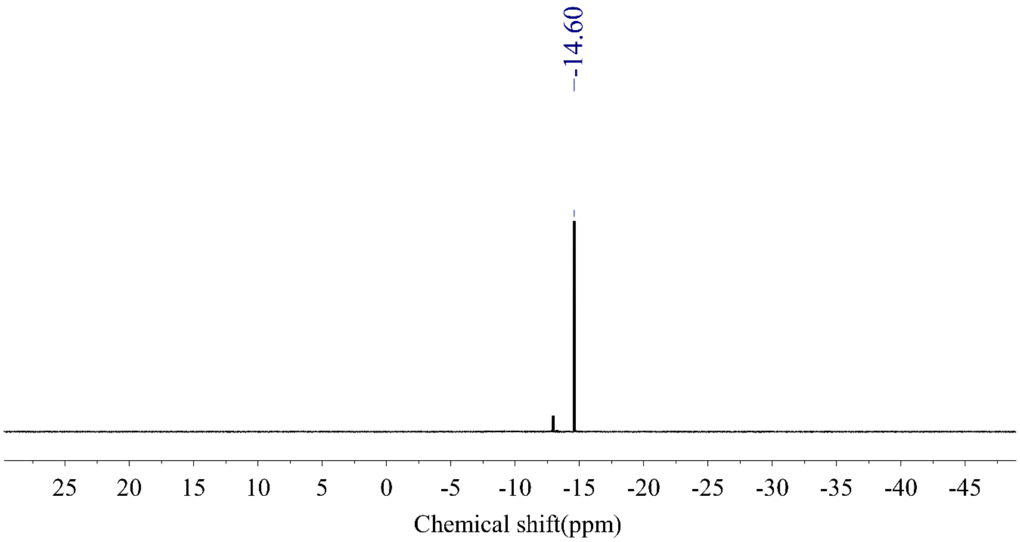

Fig 3.19 ^{31}P-NMR spectrum of complex **[9]** in CD_3CN.

Mass spectrometry

Both complexes were characterized by ESI-MS in negative-ion mode **(Fig 3.20)**. The triple and double negatively charged species correspond to the fragmentation and loss of different countercations from the main skeleton, where M stands for [Ce^{IV}(TBC[4]$(OMe)_2O_2$)$(PW_{11}O_{39})$]$^{5-}$ in **[8]** and in [Zr^{IV}(TBC[4]$(OMe)_2O_2$)$(PW_{11}O_{39})$]$^{5-}$ in **[9]**.

In the spectrum of complex **[8]**, $(NBu_4)_4H$[Ce^{IV}(TBC[4]$(OMe)_2O_2$)$(PW_{11}O_{39})$], the peak at $m/z = 1989.0713$ corresponds to $[M + 2NBu_4 + 1H]^{2-}$, which appears due to the loss of two TBA from the complex. Similarly, another peak at $m/z = 1868.4333$ is matching with $[M + 1NBu_4 + 2H]^{2-}$, *i.e.* due to the loss of three TBA and uptake of one proton. The spectrum of complex **[9]**, $(NBu_4)_5$[Zr^{IV}(TBC[4]$(OMe)_2O_2$)$(PW_{11}O_{39})$], displays the highest intensity peak at 2085.2001 corresponding to $[M + 3NBu_4]^{2-}$. The peak appears due to the loss of two TBA cations from the complex. The other peak at 1309.3722 is related to $[M + 2NBu_4]^{3-}$, and arises from the loss of three TBA cations.

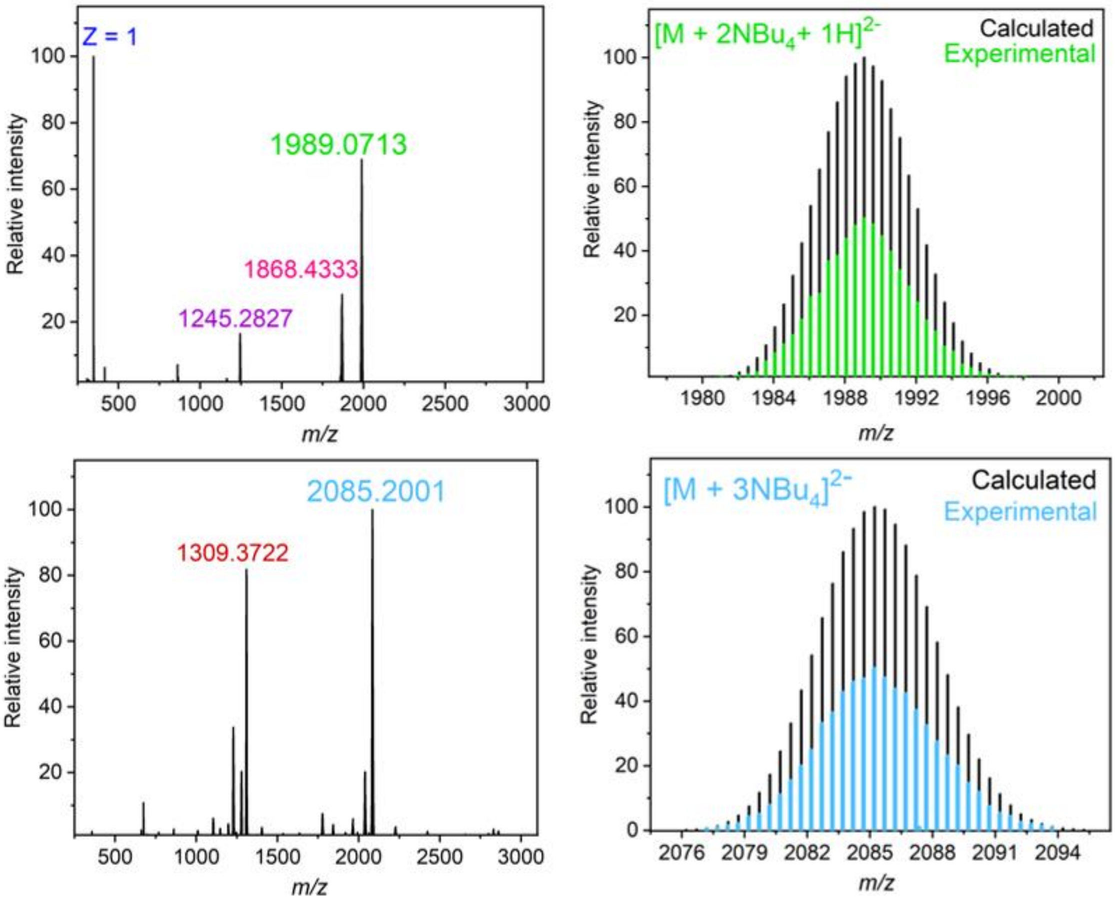

Fig 3.20 ESI-MS spectrum of complex **[8]** **(top left)** between *m/z* = 250–3000 and **(top right)** comparison of experimental and calculated isotopic pattern of the peak at *m/z* = 1989.0713 $[C_{78}H_{131}O_{43}N_2PW_{11}Ce]^{2-}$. ESI-MS spectrum of complex **[9]** **(bottom left)** between 250–3000 *m/z* and **(bottom right)** comparison of experimental and calculated isotopic pattern of the peak at *m/z* = 2085.2001 $[C_{94}H_{166}O_{43}N_3PW_{11}Zr]^{2-}$. Experimental and theoretical relative abundance in the isotopic distributions have been adjusted to 50% and 100% respectively for the purpose of comparison.

FT-IR spectroscopy

FT-IR spectrum of TBC[4] and TBA exhibit typical ν(C–H), $\delta_{as}(CH_3)$, $\delta_s(CH_3)$, and $\delta(CH_2)$ vibrations. Besides, phenoxide and methoxybenzene units in the TBC[4] contribute with ν(C–O) and ν(arC–C) vibrations.[25] The characteristic bands in $[PW_{11}O_{39}]^{7-}$ fragment feature ν(W–O) and ν(P–O) vibrations.[26]

The spectra of complex **[8]** and **[9]** display the vibrations arising from $(TBC[4](OMe)_2O_2)$, $[PW_{11}O_{39}]^{7-}$, and TBA cations. A comparison of the FT-IR spectrum of starting materials, complex **[8]**, and **[9]** is presented in **Fig 3.21**. Both complexes display medium to intense peaks between ~2960–2870 cm^{-1} corresponding to C–H stretching vibrations; intense overlapping bands at ~1480 cm^{-1} related to aromatic C–C stretching vibrations, CH_2 and asymmetrical CH_3 bending vibrations; and symmetrical CH_3 bending vibrations at ~1380 cm^{-1}. The band at

~1210 cm^{-1} can be attributed to the C–O stretching vibrations in the TBC[4]. Similar to uncoordinated $[PW_{11}O_{39}]^{7-}$, the spectra of both complexes exhibit P–O stretches between 1100 and 1050 cm^{-1}. The set of vibrations at ~950, ~880, and 800–700 cm^{-1} can be assigned to (W=O$_{terminal}$), (W–O$_{corner}$–W), and (W–O$_{bridging}$–W) respectively.

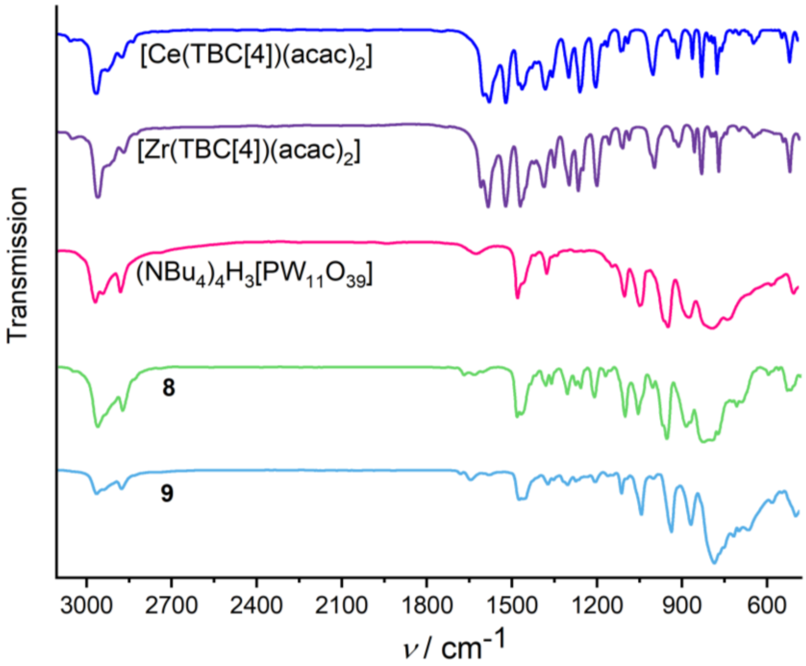

Fig 3.21 FT-IR spectra of complex **[8]**, **[9]**, and the starting materials $[Ce^{IV}(TBC[4](OMe)_2O_2)(acac)_2]$, $[Zr^{IV}(TBC[4](OMe)_2O_2)(acac)_2]$, and $(NBu_4)_4H_3[PW_{11}O_{39}]$.

Thermogravimetric analysis

The thermal stability of complex **[8]** was determined by thermogravimetric analysis within the range of 25–850 °C under N_2 atmosphere **(Fig 3.22)**. Upon heating, the complex remains unchanged up to 220 °C, thereafter two overlapped steps appear with initial mass loss of ~21.8 % at 350 °C, and then it continues to increase up to ~35.89 % at 450 °C. Above this temperature, the percentage of mass decreases very slowly up to 850 °C.

The result indicates the thermal stability of complex until ~220 °C, followed by a gradual decomposition. The first step of weight loss, observed between 220–350 °C, corresponds to the loss of TBA cations (calculated for four $C_{16}H_{36}N$: 21.69 %, found 21.8 %). The next step, that reaches the temperature of ~450 °C with a mass loss of ~35.89 %, represents the decomposition of the complex and closely matches to the loss of $(TBC[4](OMe)_2O_2)$ unit (calculated for four $C_{16}H_{36}N$ and one $C_{46}H_{58}O_4$: 36.8 %). The mass loss at higher temperature could be related to the decomposition of the POT unit.

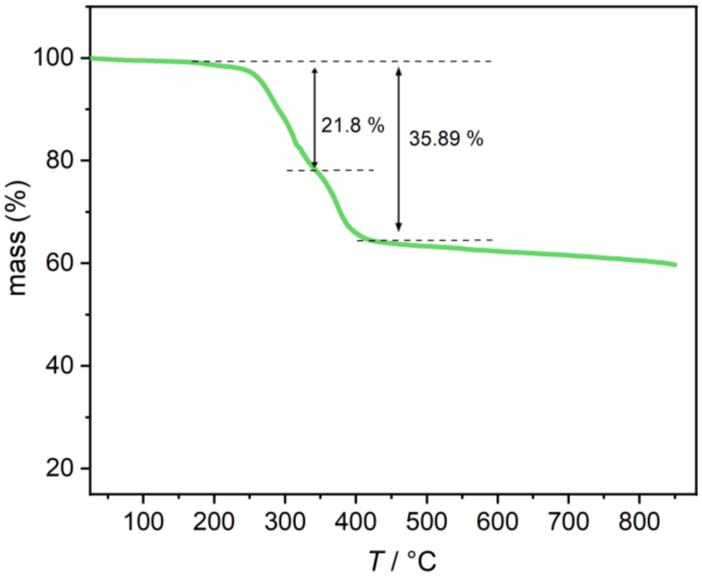

Fig 3.22 TGA curve of complex **[8]** in the range of 25–850 °C.

UV-Vis spectroscopy

A characteristic feature of cerium(IV) compounds is the appearance of a broad band in UV-visible region due to ligand-to-metal charge transfer transitions which give an intense color to the compounds.[27,28] The UV-Vis spectrum of calixarene exhibits two peaks in UV-region at around 280 and 290 nm attributed to (π-π*) transition centered on the phenyl rings.[25]

As expected, the UV-Vis absorption spectrum of complex **[8]** displays a broad peak at ~560 nm, attributed to the transition from π-orbitals of the ligand to vacant Ce-4f orbitals. Additionally, the spectrum exhibits intense peaks at 254 nm and a shoulder at ~298 nm corresponding to charge transfer bands of O→W in the $[PW_{11}O_{39}]^{7-}$ fragment and of calixarene-centered origin respectively. The spectrum of complex **[9]** also shows similar peaks as in **[8]**, except for the absence of band in the visible region. The spectrum displays an intense peak related to $[PW_{11}O_{39}]^{7-}$ at ~255 nm and a shoulder originating from TBC[4] at ~300 nm. The comparison of UV-Vis spectra of complex **[8]**, **[9]**, and starting materials is shown in **Fig 3.23**.

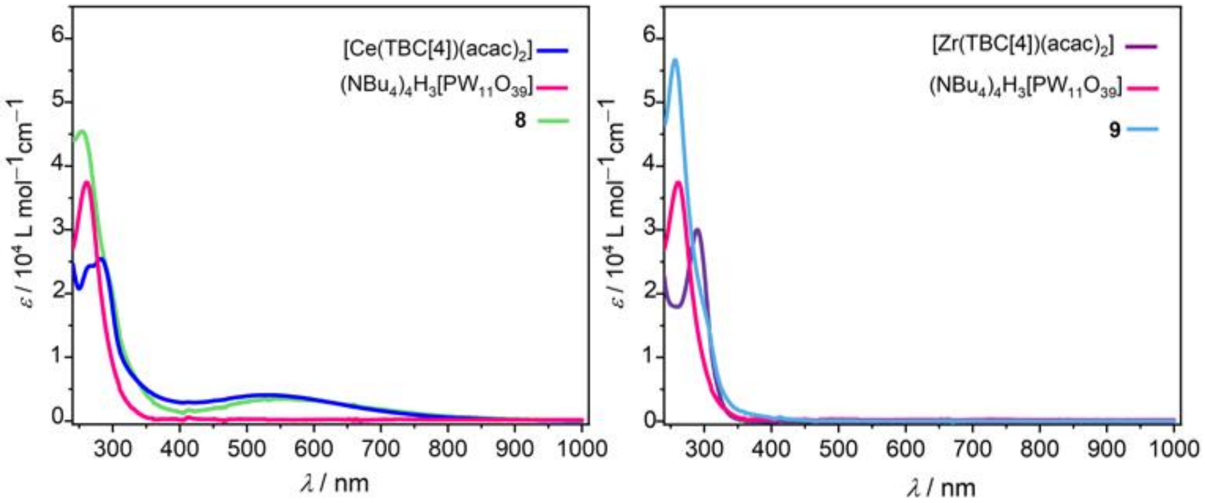

Fig 3.23 UV-Vis spectra of acetonitrile solutions of **(left)** complex **[8]** and the starting materials [Ce^{IV}(TBC[4](OMe)$_2$O$_2$)(acac)$_2$] and (NBu$_4$)$_4$H$_3$[PW$_{11}$O$_{39}$] and **(right)** complex **[9]** and the starting materials [Zr^{IV}(TBC[4](OMe)$_2$O$_2$)(acac)$_2$] and (NBu$_4$)$_4$H$_3$[PW$_{11}$O$_{39}$].

Electrochemical properties

The redox behavior of complex **[8]** was studied by recording the cyclic voltammograms in acetonitrile solution using 0.1 M tetra-*n*-butylammonium hexafluorophosphate (NBu$_4$PF$_6$) as an electrolyte. To assign the origin of peaks in hybrid complexes, CV of starting materials was also recorded in acetonitrile. As shown in **Fig 3.24**, (bottom left), [TBC[4](OMe)$_2$(OH)$_2$] exhibits an intense irreversible wave at +0.93 V, which changes to two quasi-reversible waves at $E_{1/2}$ = +0.48 and +0.74 V in [Ce^{IV}(TBC[4](OMe)$_2$O$_2$)(acac)$_2$] **(Fig 3.24**, bottom right**).** In addition to the TBC[4] centered peaks, there is a reversible peak at $E_{1/2}$ = –0.75 V, which can be attributed to the Ce(IV/III) redox couple, as it is in the expected range of Ce(IV/III) redox potential in the complexes with oxygen donor ligands.[13]

Cyclic voltammogram of [PW$_{11}$O$_{39}$]$^{7-}$ exhibits five quasi-reversible processes corresponding to the reduction and reoxidation of W(VI) centers with $E_{1/2}$ values of –0.6, –1.14, –1.69, –1.91, and –2.37 V as shown in **Fig 3.24** (top).

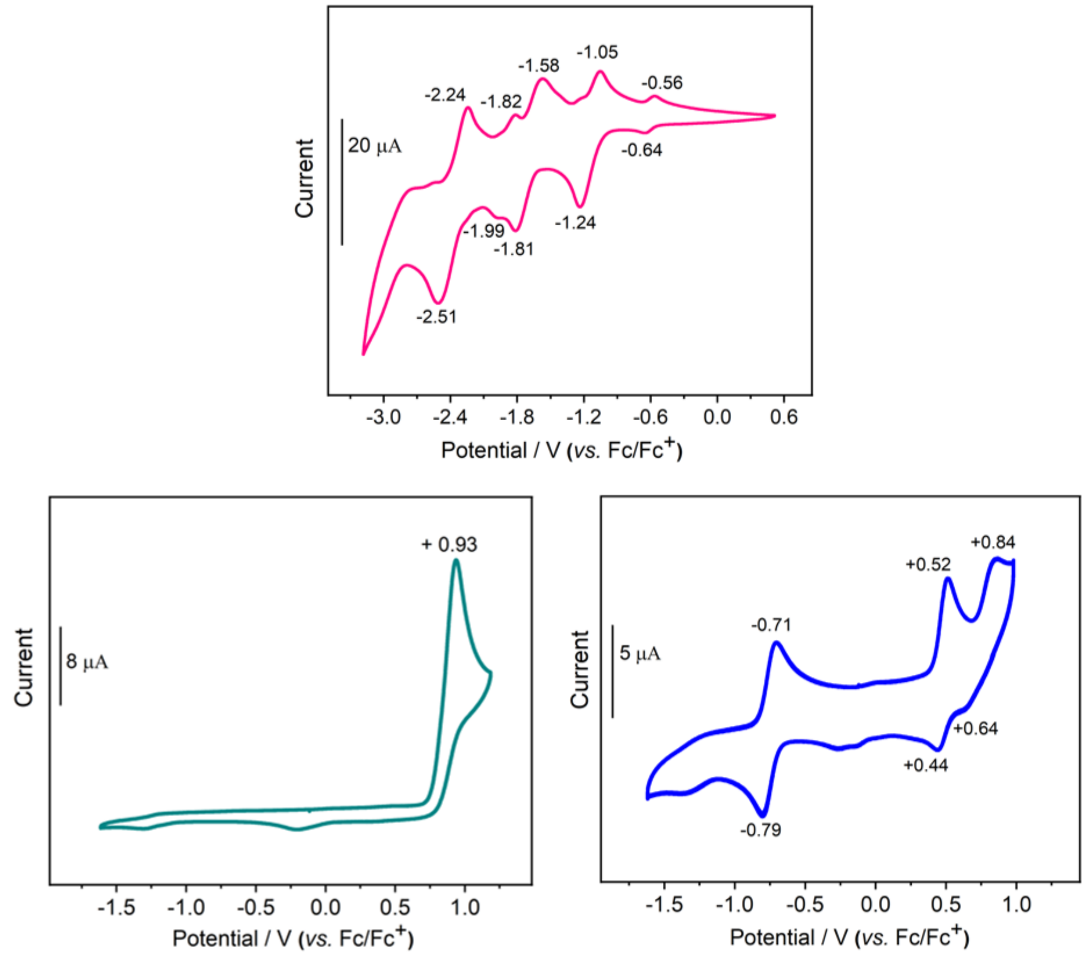

Fig 3.24 Cyclic voltammogram of **(top)** 1 mM solution of $NBu_4H_3[PW_{11}O_{39}]$, **(bottom** left) 1 mM solution of $[TBC[4](OMe)_2(OH)_2]$ and **(bottom right)** 0.5 mM solution of $[Ce^{IV}(TBC[4](OMe)_2O_2)(acac)_2]$ with 0.1 M NBu_4PF_6 in acetonitrile.

The cyclic voltammogram of complex **[8]** is shown in **Fig 3.25** (left). The complex displays two reversible redox processes at $E_{1/2}$ = +0.33 V (i_{pa}/i_{pc} = 1.2, ΔE = 68 mV) and +0.57 V (i_{pa}/i_{pc} = 1.1, ΔE = 83 mV), and a set of quasi-reversible peaks with $E_{1/2}$ value of –0.66, –1.21, –1.57, –1.92, and –2.34 V.

The reversibility of both redox waves at positive potential was confirmed by recording the cyclic voltammograms between –0.1 V to +0.9 V at different scan rates **(Fig 3.25**, right**)**. The relationship between peak currents and the square root of the scan rate for both processes is depicted in **Fig 3.26**. The graphs show linearity indicating that both redox waves follow the Randles-Sevcik equation, as expected for freely diffusing species.

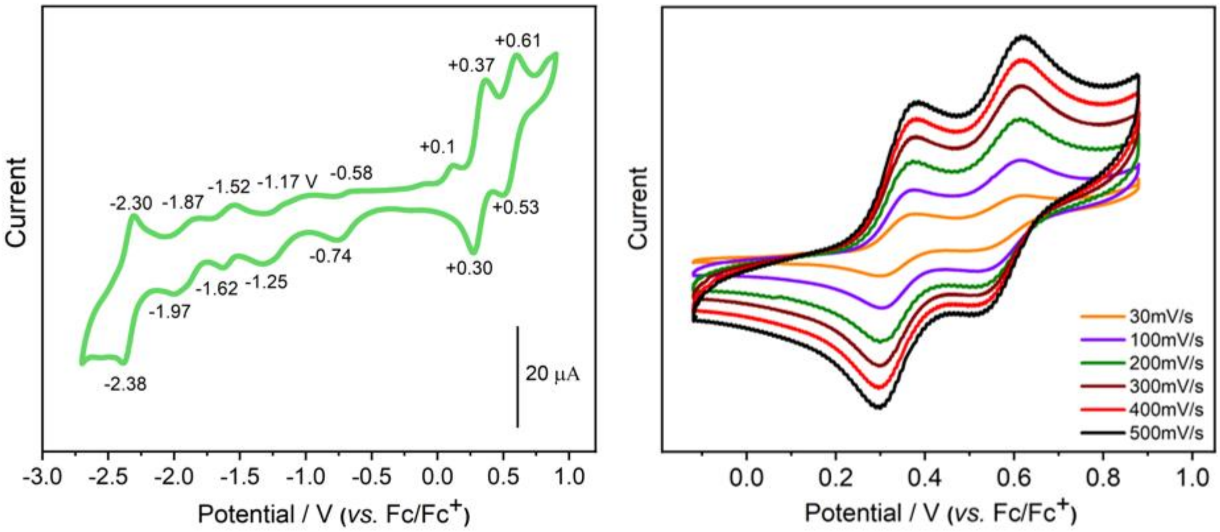

Fig 3.25 Cyclic voltammogram of 1 mM solution of complex **[8]** with 0.1 M NBu_4PF_6 in acetonitrile **(left)** in a scan window from –2.7 V to +0.9 V, **(right)** at different scan rates between –0.1 V to +0.9 V.

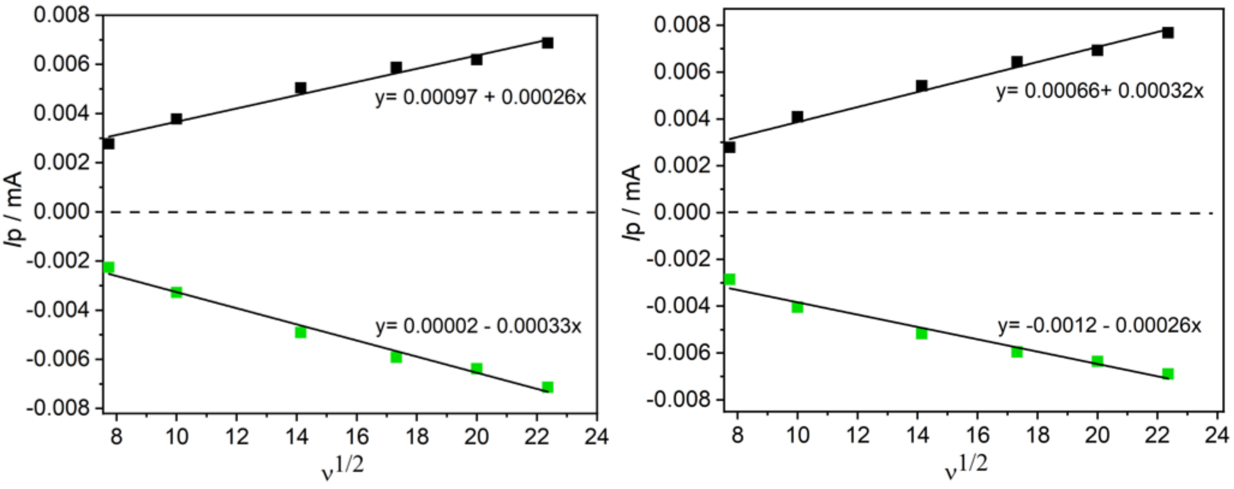

Fig 3.26 Plot of peak currents *versus* $\nu^{1/2}$ at different scan rates of 0.5 mM of **[8]** with 0.1 M NBu_4PF_6 in acetonitrile at **(left)** $E_{1/2}$ = +0.33 V, **(right)** $E_{1/2}$ = +0.57 V, and linear fit indicating that the redox couples are diffusion-controlled in agreement with Randles-Sevcik equation.

Comparing to the CV of starting materials, the peaks at positive potentials ($E_{1/2}$ = +0.33 and +0.57 V) in complex **[8]** can be attributed to the calixarene ligand origin. These redox waves exhibit reversible behavior and shift to lower positive potential values than $[Ce^{IV}(TBC[4](OMe)_2O_2)(acac)_2]$. Another difference is the change of reversible Ce(IV/III) redox couple to a quasi-reversible peak with E_{pc} = –0.74 V and E_{pa} = –0.58 V in complex **[8]**. A small peak with E_{pa} = +0.1 V could be related to the re-oxidation of some specie formed during the reduction process, and it disappears on scanning the window to just positive potentials. The rest of the peaks in the negative potential window are originated from POT unit with slight shifts of potential in comparison to uncoordinated $[PW_{11}O_{39}]^{7-}$. Solution analysis of **[8]** by cyclic voltammetry, ^{1}H-NMR, and UV-vis spectroscopy over a period of seven days showed no significant changes, indicating the stability of the complex.

The two reversible redox pair at positive potentials in **[8]** could be possibly connected with the formation of “phenoxy radical” and further oxidation to “phenoxylium cation”. The electrochemical generation of radical specie and the following cation is reported for calix[4]arene-based free ligands, exhibiting irreversible electron loss.[29,30] To date, the synthetic approach towards redox-active calixarenes is based on the introduction of electrochemically active groups, like ferrocene,[31] TTF,[32] quinone[33], cobaltocenium[34], ruthenium bipyridine[35] at the upper or lower rim. The electrochemical behavior of these molecules is mainly located on these redox-responsive groups, although the structural effects also play an important role. Complex **[8]** is the first example in which TBC[4] shows redox-active behavior without the necessity of introducing redox-active groups; this property seems to be triggered by the coordination to the Ce(IV) metal ion. Each redox wave in complex **[8]** is assumed to involve an overlapped two-electron process on two opposite phenolic units as shown in **Scheme 3.1**. In-situ generation and identification of the phenoxy radical specie by EPR spectroscopy (in progress) and, the structure determination (*e.g.* NMR, MS, X-ray) of the electrochemically generated cationic unit would support the viability of the proposed process in **Scheme 3.1**. The peak separation “ΔE” for both redox waves is between 70–80 mV, which is larger than the ideal 59 mV for two equivalent, non-interacting redox units. This observation of larger “ΔE” suggests some communication between electrochemically generated species.[31,32]

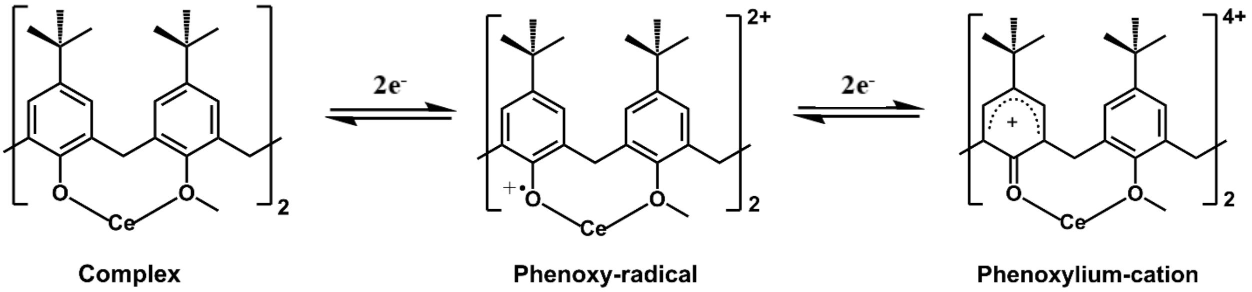

Scheme 3.1 Proposed redox reactions on the TBC[4] unit of **[8]** producing phenoxy-radical and phenoxylium species.

To investigate the effect of redox-active cerium on electrochemical properties of complex **[8]**, CV of $[Zr^{IV}(TBC[4](OMe)_2O_2)(acac)_2]$ and complex **[9]** was recorded in acetonitrile with NBu_4PF_6 as an electrolyte. As expected, the voltammogram of

[$Zr^{IV}(TBC[4](OMe)_2O_2)(acac)_2$] displays only two redox processes arising from TBC[4] unit, with $E_{1/2}$ value of +0.44 and +0.79 V **(Fig 3.27)**.

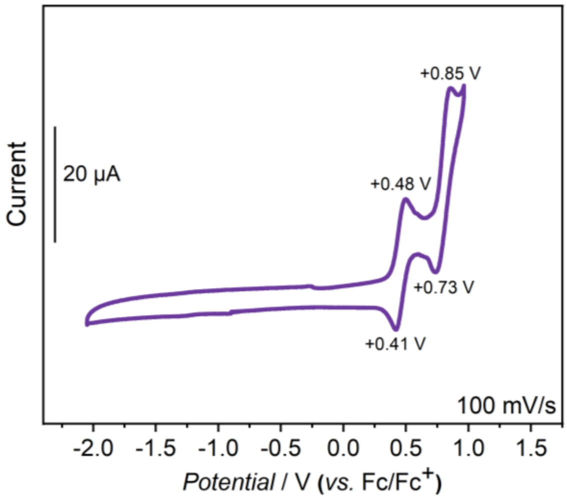

Fig 3.27 Cyclic voltammogram of 1 mM solution of [$Zr^{IV}(TBC[4](OMe)_2O_2)(acac)_2$] with 0.1 M NBu_4PF_6 in acetonitrile.

The complex **[9]** exhibits two quasi-reversible redox waves at positive potentials with $E_{1/2}$ = +0.19 V (i_{pa}/i_{pc} = 1.2, ΔE = 78 mV) and +0.52 V (i_{pa}/i_{pc} = 1.6, ΔE = 76 mV), and four quasi-reversible at negative potentials with $E_{1/2}$ value of –1.47, –1.89, –2.26 V, and –2.49 V. Additionally, an irreversible peak at –2.79 V is observed. Narrowing down the sweeping window to only positive or negative potential exhibited the same redox waves as shown in **Fig 3.28** (left). In comparison to complex **[8]**, all redox processes are shifted towards negative potential and the peak around –0.7 V, assigned to Ce(IV/III) redox couple, is absent in complex **[9]**. This finding confirms that the redox-active behavior in complex **[8]** at positive potentials has its origin in the TBC[4] scaffold; this conduct it is not unique to the cerium metal ion, but seems to be general for lanthanide and transition metal atoms like zirconium. The waves at the negative potential in complex **[9]** are assigned to the redox reactions on the POT unit, however, these peaks are negatively shifted in comparison to uncoordinated $[PW_{11}O_{39}]^{7-}$ and complex **[8]**, indicating the redox stability of POT unit upon coordination to redox-inactive Zr(IV).

The dependence of peak currents on scan rates was analyzed by recording the voltammograms between –0.3 V to +0.85 V at different scan rates **(Fig 3.28**, right**)**. Plots of peak currents *vs.* square root of the scan rates for both redox waves show linearity, indicating the diffusion-controlled processes as presented in **Fig 3.29**.

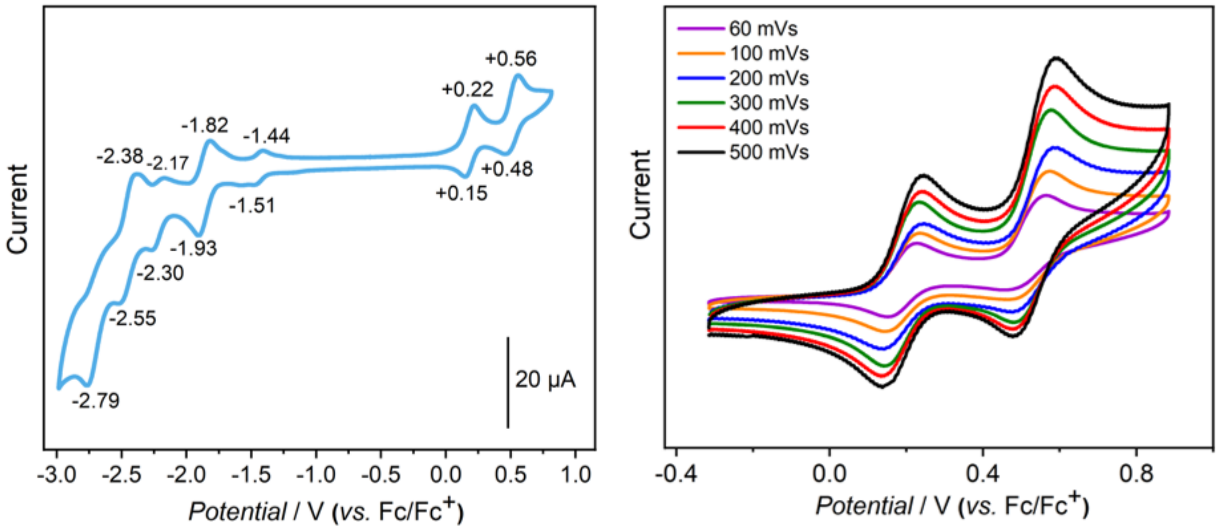

Fig 3.28 Cyclic voltammogram of 1 mM solution of complex **[9]** with 0.1 M NBu_4PF_6 in acetonitrile **(left)** scan window –3.0 V to +0.85 V **(right)** at different scan rates between –0.3 V to +0.85 V.

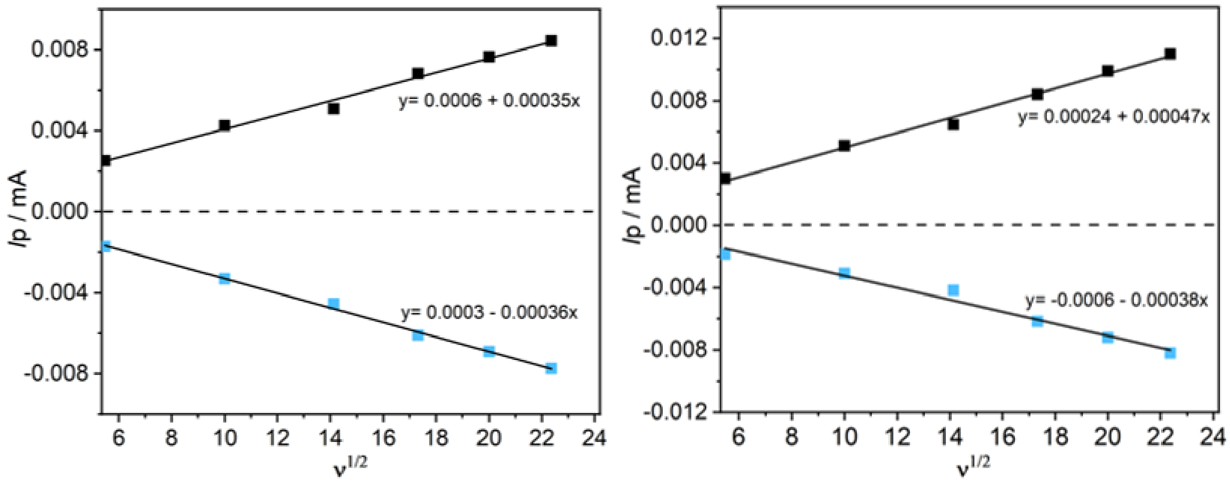

Fig 3.29 Plot of peak currents *versus* $\nu^{1/2}$ at different scan rates of 1 mM of complex **[9]** with 0.1 M NBu_4PF_6 in acetonitrile at **(left)** $E_{1/2}$ = +0.19 V, **(right)** $E_{1/2}$ = +0.52 V, and linear fit.

The presence of reversible curves in the cyclic voltammograms of complex **[8]** and **[9]** indicate the stability of different redox states and hence, it could be a potential candidate for the electrochemically controlled molecular switch. The key requirements for such applications are the long-term stability of different states and the persistence of properties upon surface deposition. Further investigations will focus on the identification, isolation, and stability of these species as potential candidates for molecular switches.

X-ray photoelectron spectroscopy

In order to investigate the oxidation state of cerium in complex **[8]**, Ce-3d core-level photoelectron spectra were recorded. The inspiration for this analysis was the mixed-valence oxidation states in previously reported cerium complexes as indicated by XPS or XANES. The spectra were recorded and analyzed by Muhammad Younas (Central Institute for Engineering, Electronics, and Analytics (ZEA-3) Forschungszentrum Jülich). The Ce-3d core-level XPS of complex **[8]** are shown in **Fig 3.30**. The X-rays induced reduction of cerium in complex **[8]** was also monitored by recording the spectra after different exposure time to the radiations. However, to avoid the reduction due to ultrahigh vacuum, the analysis was done in the near ambient pressure (NAP) cell under 1 mbar pressure of argon.

Cerium exhibits a very complicated 3d-spectrum consisted of two multiplets v and u, corresponding to the spin-orbit split $3d_{5/2}$ and $3d_{3/2}$ core holes, respectively. The multiplets appear because of the hybridization with ligand orbitals and variable occupancy of the valence Ce-4f orbitals creating several final states ($4f^0$, $4f^1$, $4f^2$), which are manifested in the spectrum as a multi-peak envelope. Therefore, a total of ten peaks appear in the case of mixed-valence cerium compounds. The peak components v^o, u^o, v', and u' originate from Ce(III), and are the result of final state of Ce: $3d^9$ $4f^2$ O $2p^5$ and Ce $3d^9$ $4f^1$ O $2p^6$. Whereas, the peak components v, u, v'', and u'' indicate Ce(IV), and are related to the final state of Ce: $3d^9$ $4f^2$ O $2p^4$ and Ce $3d^9$ $4f^1$ O $2p^5$. The peak v''' and the satellite peak u''' are associated with the final state of Ce: $3d^9$ $4f^0$ O $2p^6$ and are characteristics of Ce(IV), as no $4f^0$ state is involved in Ce(III).[18,36]

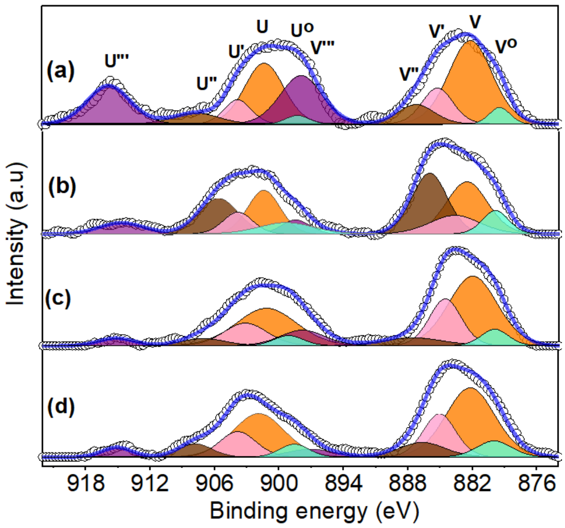

Fig 3.30 Ce-3d XPS collected at different X-rays exposure time of **(a)** 1 h **(b)** 4 h **(c)** 7 h, and **(d)** 10 h. Black circles represent the experimental data of complex **[8]** and the blue overlaps indicate the least-square fits of individual peak components highlighted in different colors.

The initial spectrum in **Fig 3.30** reveals the existence of both oxidation states of Ce(IV/III) in complex **[8]**, with Ce(IV) being the predominant state. However, upon increasing the exposure time of X-rays (spectra from **a** to **d**), the characteristic satellite peak of tetravalent cerium (u''') at the highest binding energy (~ 916 eV) started to fade away, indicating the reduction of cerium(IV) induced by X-rays. Another noticeable difference is the shifting of the peaks towards the lower binding energy as a function of the X-rays exposure time, exhibiting the dynamical response of the oxidation state to the X-rays irradiation. The atomic ratios of Ce(III) and Ce(IV) in the complex were estimated at different X-rays exposure time from the area of the associated peaks compared to the area of Ce-3d region. The information is summarized in **Table 3.1**. The oxidation state of cerium was noted between 3.83 and 3.69 over the X-rays irradiation time. Upon extrapolating to zero exposure, the oxidation state of cerium for the freshly synthesized complex can be roughly assigned between 3.81 and 3.85.

Table 3.1 Percentage composition and average oxidation state of cerium in **[8]** at different exposure of X-rays.

X-rays exposure time (h)	$Ce^{(III)}$ (at.%)	$Ce^{(IV)}$ (at.%)	Avg. Ce oxidation states
1[a]	17.57	82.43	3.83
4	24.11	75.99	3.76
7	27.95	72.05	3.72
10	30.68	69.32	3.69

[a] 1 hour acquisition time for each spectrum.

In comparison to the reported oxidation state of starting material $[Ce^{IV}(TBC[4](OMe)_2O_2)(acac)_2]$,[18] the complex **[8]** shows higher content of Ce(IV), *i.e.* 3.61 *vs.* 3.83 respectively. The difference could be attributed to a poorer electron donation from ligands towards the Ce-4f orbitals in **[8]**.

Magnetic properties

To compare the content of Ce(III) in the complex as indicated by XPS, direct current (dc) magnetic susceptibility measurements were performed on **[8]** between 2–300 K under an applied field of 0.1 T. The curve of $\chi_m T$ *vs* temperature is shown in **Fig 3.31** (left). At room temperature, the complex shows the $\chi_m T$ value of 0.03 cm^3 K mol^{-1}. In comparison to the expected range (0.66–0.78 cm^3 K mol^{-1}) for an isolated Ce(III) center [$^2F_{5/2}$, L = 3, S = 1/2, g = 6/7],[37] this yields a contribution of 3.8–4.5 % of Ce(III) in complex **[8]**.

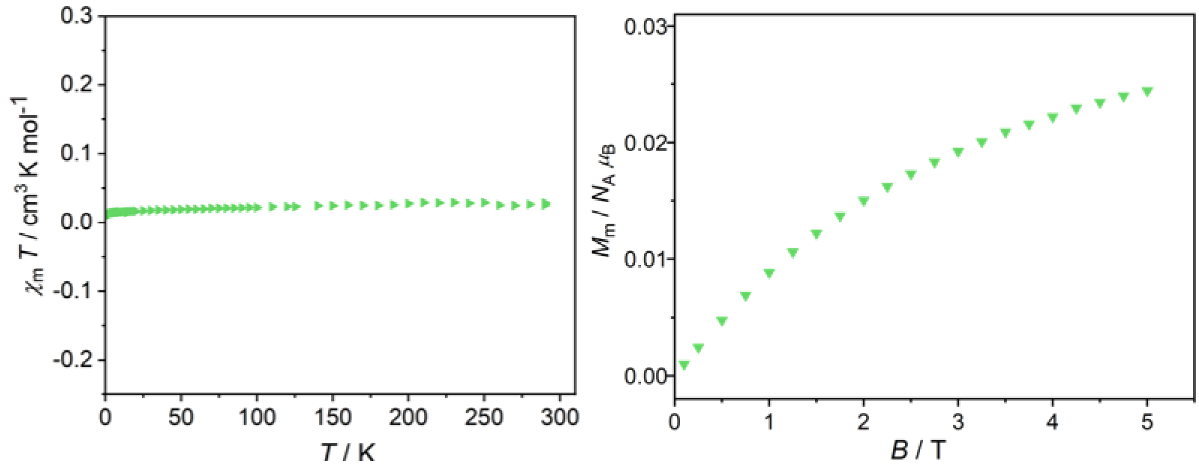

Fig 3.31 Dc-data: **(left)** $\chi_m T$ vs. T at 0.1 T and **(right)** M_m vs. B at 2.0 K for complex **[8].**

The data of molar magnetization M_m vs. B at 2.0 K is also in agreement with $\chi_m T$ value at room temperature **(Fig 3.31**, right**)**. At 5 T the magnetization is about 0.024 $N_A\,\mu_B$, far away from the saturation value of 1.07 $N_A\,\mu_B$ for an isolated Ce(III). Considering half of this saturation value, which is mostly obtained in the case of lanthanides, the percentage of Ce(III) in complex **[8]** can be estimated about 3–4 %.

The result obtained by the SQUID measurements is surprising, considering that XPS analysis showed the presence of Ce(III) in the sample between 15–19 %. Although it is difficult to ascertain which technique is more accurate, X-rays induced reduction of cerium has been reported[27] and also observed here upon long exposure to radiations. Hence, the high percentage demonstrated by XPS could be due to the reduction of cerium by X-rays, as the first spectrum was also obtained after the continuous exposure to the X-rays for a period of 1 h.

3.3 Conclusions

The first hybrid structures **[8]** and **[9]** containing a single-metal ion sandwiched between a calixarene and a polyoxometalate scaffolds were synthesized and characterized by NMR, EA, ESI-MS, IR, TGA, UV-Vis, and CV. XPS and SQUID magnetometry were used to evaluate the percentage of Ce(III) in complex **[8]**; the lack of consistency highlights the need to use different techniques to assess the oxidation state on such complexes, although the result yielded by SQUID magnetometry seems to be more reliable. The complexes exhibited interesting electrochemical behavior with two reversible redox waves at positive potentials which, according to the previous reports, could be related to the formation of phenoxy radical/phenoxylium cation on the TBC[4] unit. The presence of distinct states, which are easily interchanged by electrochemical means, is an object of investigations for developing molecular switch electroactive materials[38-40] with potential applications in molecular electronics[41-43] and ultra-high density storage devices.[44,45] Moreover, the novel structure based on Ce(IV) also provides a pathway for the development of complexes involving other paramagnetic lanthanide metal ions, calixarenes and lacunary POMs, with possibly important intrinsic magnetic properties.

3.4 Experimental

3.4.1 Materials and instrumentation

The reagents were used as received from commercial suppliers. High-grade solvents were obtained from an SPS 800 (MBraun) solvent purification system.

NMR experiments were performed on a Bruker Advance 600 MHz spectrometer equipped with a CryoProbe Prodigy operating at 600.15 MHz for ^{1}H-NMR, 150.92 MHz for ^{13}C-NMR, and 242.95 MHz for ^{31}P-NMR. Electrospray ionization mass spectra (ESI-MS) were obtained using hybrid mass spectrometer LTQ-FT Ultra^{TM} with a linear ion trap and FT-ICR mass spectrometer. CHN-content was measured by combustion analysis using VarioelCube Elementar. Elemental analyses, NMR, and ESI-MS were performed by the Central Institute for Engineering, Electronics, and Analytics (ZEA-3) Forschungszentrum Jülich, Germany. The Fourier-transform infrared spectra (FT-IR) were collected on a Bruker Vertex 70 spectrometer using KBr pellets of compounds. Wavenumbers (ν) are given in cm^{-1}; intensities are labelled as s = strong, m = medium, w = weak. Thermogravimetric analysis (TGA) was carried out on NETZSCH TG 209F1 Libra under N_2 (20 mL/min) and a heating rate of 5 K/min. The electronic absorption spectra were collected using Shimadzu UV-3600 plus spectrophotometer with 1-cm quartz glass cuvettes. Cyclic voltammetry experiments were recorded on a Biologic SP-150 potentiostat using EC-Lab software V.11.12. The three-electrode cell consisted of a glassy carbon working electrode with a diameter of 3.0 mm and two Pt wires. The solutions were purged with argon during the experiments. Plotted data were corrected for ohmic drop (PEIS method) and referenced *vs.* $[Cp_2Fe]/[Cp_2Fe]^+$. X-ray photoelectron spectra were recorded on Specs Near Ambient Pressure-XPS System, using a monochromated Al Kα (1486.6 eV) source. A small amount of sample was pressed into an indium foil without any further pretreatment before analysis. Dedicated software CasaXPS 2.3.22 was used for peak fitting. The spectra were calibrated at C-1s peak position of binding energy 284.8 eV for static charging correction as an internal reference. The peak position, peak area, and FWHM were allowed to optimize. The distance between the spin-orbit doublets (18.6 eV) was fixed as suggested in the XPS database (https://xpssimplified.com/elements/cerium.php). Magnetic measurements were recorded using Quantum Design MPMS-5XL SQUID magnetometer. The sample was compacted and immobilized into cylindrical PTFE sample holder. Experimental dc-data were recorded at 0.1 T and 1.0 T in the temperature range 2–290 K and at 2.0 K in the field range 0–5 T.

3.4.2 Synthesis of $(NBu_4)_4H[Ce^{IV}(TBC[4](OMe)_2O_2)(PW_{11}O_{39})]$ [8]

A completely soluble solution of $(NBu_4)_4H_3[PW_{11}O_{39}]$ (0.1 mmol, 365 mg) and NBu_4Br (0.1 mmol, 32 mg) in 50 mL of dry CH_3CN was slowly added to a flask containing $[Ce^{IV}(TBC[4](OMe)_2O_2)(acac)_2]$ (0.1 mmol, 101 mg) in 50 mL CH_3CN. The solution was refluxed for 3 h at 90 °C under argon. Evaporation of the mother liquor and washing with DCM produced a purple solid. Yield (190 mg, 42 %). **Elemental analysis** (%) calculated for $C_{110}H_{203}O_{43}N_4PW_{11}Ce$: C 29.60, H 4.58, N 1.26. Found: C 29.50, H 4.59, N 1.25. **^{1}H-NMR** (600 MHz, CD_3CN): δ 7.11 (s, 2H, $H_{ar(A1)}$), 7.08 (s, 2H, $H_{ar(A2)}$), 7.04 (d, 2H, $H_{ar(B1)}$), 7.00 (d, 2H, $H_{ar(B2)}$), 5.43 (bs, 2H, CH_{2endo}), 4.92 (d, J = 11.7 Hz, 2H, CH_{2endo}), 4.52 (s, 6H, CH_3O), 3.26 (d, J = 12.1 Hz, 2H, CH_{2exo}), 3.19 (d, J = 12.4 Hz, CH_{2exo}, 2H), 3.16–3.13 (m, 40H, CH_{2TBA}), 1.67–1.61 (m, 40H, CH_{2TBA}), 1.43–1.37 (m, 40H, CH_{2TBA}), 1.24 (d, 18H, $CH_{3tBu(B)}$), 1.09 (s, 18H, $CH_{3tBu(A)}$), 0.98 (t, J = 7.3 Hz, 60H, CH_{3TBA}) ppm. **^{13}C-NMR** (151 MHz, CD_3CN): δ 170.52 (1C, Ar-$C_{ar}OCe_{(A2)}$), 169.79 (1C, $C_{ar}OCe_{(A1)}$), 155.80 (2C, $C_{ar}OMeCe_{(B1+B2)}$), 148.18 (2C, $C_{ar}{}^tBu_{(A1+A2)}$), 142.45 (2C, $C_{ar}{}^tBu_{(B1+B2)}$), 134.67 (2C, $C_{ar}CH_{2(B2)}$), 134.25 (2C, $C_{ar}CH_{2(B1)}$), 133.05 (2C, $C_{ar}CH_{2(A2)}$), 132.12 (2C, $C_{ar}CH_{2(A1)}$), 126.74 (2C, $C_{ar}H_{(B1)}$), 126.50 (2C, $C_{ar}H_{(B2)}$), 124.29 (2C, $C_{ar}H_{(A1)}$), 124.11 (2C, $C_{ar}H_{(A2)}$), 68.97 (2C, CH_3O), 59.29 (20C, CH_{2TBA}), 34.76 (2C, $^tBuC_{(A)}$), 34.21 (1C, $^tBuC_{(B)}$), 34.18 (1C, $^tBuC_{(B)}$), 32.52 (2C, CH_{2calix}), 32.64 (2C, CH_{2calix}), 32.24 (6C, $CH_{3tBu(B)}$), 31.31 (6C, $CH_{3tBu(A)}$), 24.37 (20C, CH_{2TBA}), 20.33 (20C, CH_{2TBA}), 13.87 (20C, CH_{3TBA}) ppm. **^{31}P-NMR** (243 MHz, CD_3CN): δ –12.94 ppm. **ESI-HRMS** *m/z*: found 1989.0713 $[M + 2NBu_4 + 1H]^{2-}$ (70 % relative abundance), calculated for $[C_{78}H_{131}O_{43}N_2PW_{11}Ce]^{2-}$ 1989.0792; found 1868.4333 $[M + 1NBu_4 + 2H]^{2-}$ (29 %), calculated for $[C_{62}H_{96}O_{43}NPW_{11}Ce]^{2-}$ 1868.4407; found 1245.2827 $[M + 1NBu_4 + 1H]^{3-}$ (18 %), calculated for $[C_{62}H_{95}O_{43}NPW_{11}Ce]^{3-}$ 1245.2914. M stands for

$[Ce^{IV}(TBC[4](OMe)_2O_2)(PW_{11}O_{39})]^{5-}$. **IR** (KBr, cm^{-1}): 2961 (s), 2873 (s), 1481 (s), 1460 (s), 1380 (w), 1305 (w), 1259 (w), 1209 (w), 1101 (m), 1055 (m), 954 (s), 885 (s), 823 (s), 708 (m), 529 (w). **UV-Vis** {CH_3CN, λ / nm and ε / 10^4 M^{-1} cm^{-1} (in parentheses)}: 254 (4.5), ~298 (2.1), 560 (0.35).

3.4.3 Synthesis of $[Zr^{IV}(TBC[4](OMe)_2O_2)(acac)_2]$

A solution of $Zr(acac)_4$ (1 mmol, 0.48 g) and $[TBC[4](OMe)_2(OH)_2]$ (1 mmol, 0.67 g) in 20 mL toluene was heated at 120 °C for 2 h and left overnight on stirring at room temperature. The reaction mixture was evaporated at reduced pressure and product was recrystallized with DCM. Yield (0.98 g, 69 %). **Elemental analysis** (%) calculated for $C_{56}H_{72}O_8Zr$: C 69.74, H 7.52. Found: C 69.80, H 7.54. **^{1}H-NMR** (600 MHz, CD_3CN): δ 7.03 (s, 4H, H_{ar}), 6.99 (s, 4H, H_{ar}), 5.64 (s, 2H, CH_{acac}), 4.38 (d, J = 11.87 Hz, 4H, CH_{2endo}), 4.18 (s, 6H, CH_3O), 3.13 (d, J = 11.9 Hz, 4H, CH_{2exo}), 2.10 (s, 12H, CH_{3acac}), 1.25 (s, 18H, $CH_{3tBu(B)}$), 1.08 (s, 18H, $CH_{3tBu(A)}$) ppm. **^{13}C-NMR** (151 MHz, CD_2Cl_2): δ 189.58 (4C, C=O_{acac}), 159.62 (2C, C_{ar}OZr), 154.30 (2C, C_{ar}OMeZr), 147.58 (2C, $C_{ar}{}^t$Bu), 140.03 (2C, $C_{ar}{}^t$Bu), 132.80 (4C, $C_{ar}CH_2$), 130.36 (4C, $C_{ar}CH_2$), 125.90 (4C, C_{ar}H), 125.50 (4C, C_{ar}H), 102.51 (2C, CH_{acac}), 66.32 (2C, CH_3O), 34.48 (2C, ^{t}BuC), 33.92 (2C, ^{t}BuC), 33.50 (4C, CH_{2calix}), 31.86 (6C, CH_{3tBu}), 31.53 (6C, CH_{3tBu}), 26.42 (4C, CH_{3acac}) ppm. **ESI-HRMS** *m/z*: found 985.4167 $[M + Na]^+$ (100 % relative abundance), calculated for $[C_{56}H_{72}O_8NaZr]^+$ 985.4166; found 962.4272 $[M - 1e]^+$ (30 %), calculated for $[C_{56}H_{72}O_8Zr]^+$ 962.4269. M stands for $[Zr^{IV}(TBC[4](OMe)_2O_2)(acac)_2]$. **IR** (KBr, cm^{-1}): 2959 (s), 2868 (s), 1591 (s), 1530 (s), 1478 (s), 1396 (m), 1308 (m), 1275 (m), 1210 (m), 1122 (w), 1009 (m), 922 (w), 845 (m), 784 (m), 536 (m). **UV-Vis** {CH_3CN, λ / nm and ε / 10^4 M^{-1} cm^{-1} (in parentheses)}: 289 (3.0).

3.4.4 Synthesis of $(NBu_4)_5[Zr^{IV}(TBC[4](OMe)_2O_2)(PW_{11}O_{39})_2]$ [9]

A solution of $(NBu_4)_4H_3[PW_{11}O_{39}]$ (0.1 mmol, 365 mg) and NBu_4OH (40 wt.% in methanol; 0.2 mmol, 0.14 mL) in 30 mL of dry CH_3CN was slowly added to a flask containing $[Zr^{IV}(TBC[4](OMe)_2O_2)(acac)_2]$ (0.1 mmol, 96 mg) in 30 mL CH_3CN. The solution was refluxed overnight at 90 °C under argon. The reaction mixture was filtered and evaporated under reduced pressure. The product was redissolved in dichloromethane and precipitated by the addition of diethyl ether. Washing the precipitates with diethyl ether gave the complex **[9]** with a little excess of NBu_4 as indicated by NMR. **^{1}H-NMR** (600 MHz, CD_3CN): δ 7.00 (s, 2H, $H_{ar(A1)}$), 6.96 (s, 2H, $H_{ar(A2)}$), 6.94 (d, 2H, $H_{ar(B1)}$), 6.87 (d, 2H, $H_{ar(B2)}$), 5.35 (d, J = 11.9

Hz, 2H, CH_{2endo}), 4.98 (d, J = 11.7 Hz, 2H, CH_{2endo}), 4. 13 (s, 6H, CH_3O), 3.16–3.14 (m, 75H, CH_{2TBA}), 3.05 (d, J = 11.9 Hz, 2H, CH_{2exo}), 2.99 (d, J = 12.1 Hz, CH_{2exo}, 2H), 1.67–1.62 (m, 79H, CH_{2TBA}), 1.43–1.38 (m, 79H, CH_{2TBA}), 1.27 (d, 18H, C$H_{3tBu(B)}$), 1.09 (s, 18H, C$H_{3tBu(A)}$), 0.98 (t, J = 7.3 Hz, 117H, CH_{3TBA}) ppm. **^{13}C-NMR** (151 MHz, CD$_3$CN): δ 161.56 (1C, C_{ar}OZr), 161.46 (1C, C_{ar}OZr), 156.23 (2C, C_{ar}OMeZr), 146.94 (2C, $C_{ar}{}^t$Bu), 138.91 (1C, $C_{ar}{}^t$Bu), 138.68 (1C, $C_{ar}{}^t$Bu), 134.96 (2C, C_{ar}CH$_2$), 134.42 (2C, C_{ar}CH$_2$), 131.33 (2C, C_{ar}CH$_2$), 129.79 (C_{ar}CH$_2$), 125.54 (2C, C_{ar}H), 125.51 (2C, C_{ar}H), 125.48 (2C, C_{ar}H), 125.35 (2C, C_{ar}H), 67.96 (2C, CH$_3$O), 59.26 (C, CH$_{2TBA}$), 34.66 (4C, ^{t}BuC), 34.18 (4C, CH$_{2calix}$), 32.14 (3C, CH$_{3tBu}$), 32.09 (3C, CH$_{3tBu}$), 31.53 (6C, CH$_{3tBu}$), 24.42 (C, CH$_{2TBA}$), 20.33 (C, CH$_{2TBA}$), 13.90 (C, CH$_{3TBA}$) ppm. **^{31}P-NMR** (243 MHz, CD$_3$CN): δ –14.60 ppm. **ESI-HRMS** *m/z*: found 2085.2001 [M + 3NBu$_4$]$^{2-}$ (100 % relative abundance), calculated for [C$_{94}$H$_{166}$O$_{43}$N$_3$PW$_{11}$Zr]$^{2-}$ 2085.2176; found 1309.3722 [M + 2NBu$_4$]$^{3-}$ (82 %), calculated for [C$_{78}$H$_{130}$O$_{43}$N$_2$PW$_{11}$Zr]$^{3-}$ 1309.3837. M stands for [Zr^{IV}(TBC[4](OMe)$_2$O$_2$)(PW$_{11}$O$_{39}$)]$^{5-}$. **IR** (KBr, cm^{-1}): 2959 (m), 2872 (m), 1480 (m), 1461 (m), 1378 (w), 1309 (w), 1280 (w), 1212 (w), 1120 (m), 1050 (m), 946 (s), 880 (s), 800 (s), 728 (m), 515 (w). **UV-Vis** {CH$_3$CN, λ / nm and ε / 10^4 M^{-1} cm^{-1} (in parentheses)}: 255 (5.6), 300 (1.6).

3.5 References

1. V. Sridharan and J. C. Menéndez, *Chem. Rev.*, 2010, **110**, 3805-3849.
2. V. Nair and A. Deepthi, *Chem. Rev.*, 2007, **107**, 1862-1891.
3. V. Nair, L. Balagopal, R. Rajan and J. Mathew, *Acc. Chem. Res.*, 2004, **37**, 21-30.
4. C. T. Campbell and C. H. Peden, *Science*, 2005, **309**, 713-714.
5. A. Trovarelli, C. de Leitenburg, M. Boaro and G. Dolcetti, *Catal. Today*, 1999, **50**, 353-367.
6. S. Park, J. M. Vohs and R. J. Gorte, *Nature*, 2000, **404**, 265-267.
7. W. C. Chueh, C. Falter, M. Abbott, D. Scipio, P. Furler, S. M. Haile and A. Steinfeld, *Science*, 2010, **330**, 1797-1801.
8. J. A. Bogart, A. J. Lewis, S. A. Medling, N. A. Piro, P. J. Carroll, C. H. Booth and E. J. Schelter, *Inorg. Chem.*, 2013, **52**, 11600-11607.
9. G. F. Smith and C. A. Getz, *Ind. Eng. Chem. Anal. Ed.*, 1938, **10**, 191-195.
10. Y.-M. So and W.-H. Leung, *Coord. Chem. Rev.*, 2017, **340**, 172-197.
11. N. Haraguchi, Y. Okaue, T. Isobe and Y. Matsuda, *Inorg. Chem.*, 1994, **33**, 1015-1020.
12. M. Antonio, C. Williams and L. Francesconi, *J. Chem. Soc., Dalton Trans.*, 1999, 3825-3830.
13. N. A. Piro, J. R. Robinson, P. J. Walsh and E. J. Schelter, *Coord. Chem. Rev.*, 2014, **260**, 21-36.

14. J. L. Atwood, L. J. Barbour, S. Dalgarno, C. L. Raston and H. R. Webb, *J. Chem. Soc., Dalton Trans.*, 2002, 4351-4356.

15. P. Beer, M. Drew, A. Grieve and M. Ogden, *J. Chem. Soc., Dalton Trans.*, 1995, 3455-3466.

16. Gottfriedsen and J. Gottfriedsen, *Z. Anorg. Allg. Chem.*, 2005, **631**, 2928-2930.

17. J. Gottfriedsen, R. Hagner, M. Spoida and Y. Suchorski, *Eur. J. Inorg. Chem.*, 2007, **2007**, 2288-2295.

18. Y. Suchorski, J. Gottfriedsen, R. Wrobel, B. Strzelczyk and H. Weiss, *Solid State Phenom.*, 2007, **128**, 115-120.

19. N. M. Edelstein, P. Allen, J. Bucher, D. Shuh, C. Sofield, N. Kaltsoyannis, G. Maunder, M. Russo and A. Sella, *J. Amer. Chem. Soc.*, 1996, **118**, 13115-13116.

20. C. H. Booth, M. D. Walter, M. Daniel, W. W. Lukens and R. A. Andersen, *Phys. Rev. Lett.*, 2005, **95**, 267202.

21. Y. Bian, J. Jiang, Y. Tao, M. T. Choi, R. Li, A. C. Ng, P. Zhu, N. Pan, X. Sun and D. P. Arnold, *J. Amer. Chem. Soc.*, 2003, **125**, 12257-12267.

22. A. Casnati, A. Arduini, E. Ghidini, A. Pochini and R. Ungaro, *Tetrahedron*, 1991, **47**, 2221-2228.

23. R. Contant, *Can. J. Chem.*, 1987, **65**, 568-573.

24. E. Radkov and R. H. Beer, *Polyhedron*, 1995, **14**, 2139-2143.

25. C. D. Gutsche, in *Calixarenes Revisited*, The Royal Society of Chemistry, 1998, ch. 3, pp. 32-40.

26. D. Rocchiccioli, R. Thouvenot, *J. Chem. Res.*, 1977, (S) 46, (M) 0549-0571.

27. B. D. Mahoney, N. A. Piro, P. J. Carroll and E. J. Schelter, *Inorg. Chem.*, 2013, **52**, 5970-5977.

28. U. J. Williams, D. Schneider, W. L. Dorfner, C. Maichle-Mössmer, P. J. Carroll, R. Anwander and E. J. Schelter, *Dalton Trans.*, 2014, **43**, 16197-16206.

29. R. Vataj, A. Louati, C. Jeunesse and D. Matt, *Electrochem. Commun.*, 2000, **2**, 769-775.

30. R. Vataj, A. Louati, C. Jeunesse and D. Matt, *J. Electroanal. Chem.*, 2004, **565**, 295-299.

31. E. Métay, M. C. Duclos, S. Pellet-Rostaing, M. Lemaire, R. Kannappan, C. Bucher, E. Saint-Aman and C. Chaix, *Tetrahedron*, 2009, **65**, 672-676.

32. M. H. Düker, R. Gómez, C. M. V. Velde and V. A. Azov, *Tetrahedron Lett.*, 2011, **52**, 2881-2884.

33. M. Gomez-Kaifer, P. A. Reddy, C. D. Gutsche and L. Echegoyen, *J. Amer. Chem. Soc.*, 1994, **116**, 3580-3587.

34. P. D. Beer, M. G. Drew, D. Hesek and K. C. Nam, *Chem. Commun.*, 1997, 107-108.

35. P. D. Beer, Z. Chen, A. J. Goulden, A. Grieve, D. Hesek, F. Szemes and T. Wear, *Chem. Commun.*, 1994, 1269-1271.

36. E. Bêche, P. Charvin, D. Perarnau, S. Abanades and G. Flamant, *Surf. Interface Anal.*, 2008, **40**, 264-267.

37. H. Lueken and B. Magnetochemie, *Leipzig (Gemany)*, 1999.

38. L. J. O'Driscoll, J. M. Hamill, I. Grace, B. W. Nielsen, E. Almutib, Y. Fu, W. Hong, C. J. Lambert and J. O. Jeppesen, *Chem. Sci.*, 2017, **8**, 6123-6130.

39. N. Darwish, I. Díez-Pérez, S. Guo, N. Tao, J. J. Gooding and M. N. Paddon-Row, *J. Phys. Chem. C*, 2012, **116**, 21093-21097.

40. Y. Li, M. Baghernejad, A. G. Qusiy, D. Zsolt Manrique, G. Zhang, J. Hamill, Y. Fu, P. Broekmann, W. Hong and T. Wandlowski, *Angew. Chem.*, 2015, **127**, 13790-13793.

41. N. Fuentes, A. Martín-Lasanta, L. Á. de Cienfuegos, M. Ribagorda, A. Parra and J. M. Cuerva, *Nanoscale*, 2011, **3**, 4003-4014.

42. C. Huang, A. V. Rudnev, W. Hong and T. Wandlowski, *Chem. Soc. Rev.*, 2015, **44**, 889-901.

43. C. Jia and X. Guo, *Chem. Soc. Rev.*, 2013, **42**, 5642-5660.

44. H. Tian, *Angew. Chem. Int. Ed.*, 2010, **49**, 4710-4712.

45. J. E. Green, J. W. Choi, A. Boukai, Y. Bunimovich, E. Johnston-Halperin, E. DeIonno, Y. Luo, B. A. Sheriff, K. Xu and Y. S. Shin, *Nature*, 2007, **445**, 414-417.

Conclusions

The aim of this thesis was to develop discrete hybrid structures containing organic and inorganic scaffolds covalently-linked through a single-metal ion. This involved the encapsulation of 4f-ions by phthalocyanine, *p-tert*-butylcalix[4]arene and monolacunary Keggin-based phosphotungstate in a double-decker structure, characterization by various spectroscopic techniques, and study of their electrochemical and magnetic behavior. The main findings are summarized below:

- For the first time, a phthalocyanine and a monolacunary polyoxotungstate were linked through a single lanthanide ion, resulting in a family of hybrid structures $[Ln^{III}(H_{16}Pc)(PW_{11}O_{39})]^{6-}$ [Ln(III) = Y, Tb, Dy]. The dysprosium analogue of this family displayed typical SMM behavior, whose energy barrier (U_{eff}) for the Orbach relaxation represented the average value of U_{eff} for both homoleptic $[Dy^{III}(H_{16}Pc)_2]^{-}$ and $[Dy^{III}(PW_{11}O_{39})_2]^{11-}$ analogues. Moreover, the periphery of phthalocyanine-ring was derivatized with electron-donor (di-*iso*-propylphenoxy) and electron-withdrawing (fluorine) groups to form $[Ln^{III}(Pc)(PW_{11}O_{39})]^{6-}$ [Ln(III) = Tb, Dy] complexes. These substituents shifted the UV-Vis spectra and redox-properties of hybrid complexes due to the changes in the energy of frontier orbitals. The fitting of magnetic ac-data revealed the choice of different relaxation channels depending on the electron-density on the Pc-ring.
- *p-tert*-butylcalix[4]arene and monolacunary polyoxotungstate were combined to form $[M^{IV}(TBC[4](OMe)_2O_2)(PW_{11}O_{39})]^{5-}$ (M = Ce and Zr), representing the first example of hybrid structures containing these scaffolds linked through a single-metal ion. The complexes displayed two reversible redox waves at positive potentials, that could be attributed to the formation of phenoxy radical and phenoxylium cation on the TBC[4] unit; this represents the first report of a redox-active calixarene mediated through a metal-ligand bond. The reversible species interchangeable by electrochemical means may offer their potential in redox-based molecular switches.

The observation of SMM behavior in $[Ln^{III}(Pc)(PW_{11}O_{39})]^{6-}$ will foster the construction of similar complexes using other lacunary POMs (Keggin and Wells-Dawson type) and paramagnetic lanthanides(III) in the case of $[Ce^{IV}(TBC[4])(PW_{11}O_{39})]^{5-}$, thus opening new avenues towards the design of diverse hybrid structures with possibly interesting electronic and magnetic properties. Additionally, the presence of organic groups, easy to derivatize, will allow the deposition of these complexes on surfaces for the understanding of fundamental single-molecule electronic and spintronic processes.

Acknowledgments

At the end of this work, I would like to express my gratitude to all the people who helped me in the realization of this thesis, on personal and scientific basis. Special thanks to Prof. Dr. Paul Kögerler for giving me the opportunity to join his group. I highly appreciate his continuous support, guidance, and encouragement throughout the time of my PhD. I would like to acknowledge the Punjab Educational Endowment Fund for the fellowship to pursue my PhD in Germany.

My sincere gratitude goes to Dr. Sergio Sanz Calvo for his valuable suggestions during the experimental work, writing of the thesis, and especially for the willingness to help whenever I needed. His pieces of advice on research as well as on career are invaluable to me.

I am highly grateful to Dr. rer. nat. Dr. -Ing. Jan van Leusen for the interpretation of the magnetic part of this thesis. I am also thankful to Dr. Natalya Izarova for her guidance in the subject of polyoxometalate chemistry.

I acknowledge Prof. Dr. Euan K. Brechin and Dr. Gary Nichol from The University of Edinburgh for the access and measurement of crystals using Diamond Light Source, Southampton. Many thanks to Christina Houben for the SQUID measurements, Brigitte Jansen for TGA measurements, and ZEA-3 Forschungszentrum Jülich for NMR, ESI-MS, and elemental analyses.

I am thankful to all current and former members of the group and the colleagues at PGI-6 Forschungszentrum Jülich for providing a nice working environment during these years. I would like to thank Dr. Jeff Rawson for introducing me to the chemistry of phthalocyanine and all his valuable guidance. Special thanks to Marvin for thoughtful discussions and his help in day-to-day issues encountered. It was my pleasure to work with Dr. Marjan Hosseinzadeh and Yushu. Many thanks to Tuba for listening, offering me advice, and sharing a great time during this journey.

Finally, I am eternally grateful to my parents and my brothers for their unconditional love and support over the years.